IMPLEMENTATION OF A TWO-STREAM-FAN IN THE CIRSTEL SYSTEM

René Heise

2006

IMPLEMENTATION OF A TWO-STREAM-FAN IN THE CIRSTEL SYSTEM

By

R. Heise

Dissertation presented for the degree Doctor of Philosophy (Mechanical Engineering) atthe University of Stellenbosch

Promoter: Prof T.W. von Backström

Department of Mechanical Engineering

University of Stellenbosch

South Africa

2006

DECLARATION

I, the undersigned, hereby declare that the work contained in this thesis is my own original work and that I have not previously, in its own entirety or in part, submitted it at any university for a degree.

Signature…… Date……16 November 2006.....

ABSTRACT

This thesis describes the design and incorporation of a twin-stream fan into the CIRSTEL tail boom. The Combined Infra-Red Suppression and Tail rotor Elimination (CIRSTEL) tail boom is a system designed to replace the tail rotor on a conventional helicopter. It relies on the Coanda effect to create circulation around the helicopter tail boom when exposed to the rotor downwash. This generates sideways-directed lift to counter the main rotor torque, and a tail thruster adds extra torque and directional control. A twin-stream fan supplies separate air streams to each of the Coanda and tail thruster sections. The first section of the study describes the experimental tests done on an 83% scale demonstrator of the twin-stream fan with the objective to verify the concept and determine the fan section efficiencies. Subsequent modifications done to the fan stator blades are also evaluated. The efficiencies of the design were shown to exceed the targets in both sections. The section concludes with design recommendations for a future fan, based on the findings of the experiments. A brief analysis of the CIRSTEL system is presented and by using optimisation techniques the predicted power demand of the system could be significantly reduced from a conventional tail rotor. The second section of the study details the conceptual design and CFD evaluation of air intakes for the fan that can be fitted to the helicopter. The objective here was to study the flow affecting helicopter intakes as well as to establish design considerations for a fan intake. A basic intake concept was developed for the Alouette III/CIRSTEL combination and modified according to results based on the CFD simulations. The intake design was evolved to the point were it was shown that the concept is feasible. These CFD simulations were an initial effort to design the fan intakes with the help of a simplified rotor flow field. The investigation was subsequently extended to investigate helicopter intake design considerations in the presence of a representative rotor, which was modelled as an actuator disk in the CFD simulations. In this investigation top and side mounted intake concepts were compared and analysed for suitability as a fan intake. Each intake concept showed its own advantages. Due to the proximity of the rotor hub to the intake, distortion and total pressure levels at the fan face are influenced negatively. The report is concluded with design recommendations for the intake as applied to the current Alouette III configuration, as well as for implementation on helicopters in general.

OPSOMMING

Hierdie tesis dek die ontwerp en toepassing van ‘n dubbelstroom waaier, in die CIRSTEL stertbuis. Die “Combined Infra-Red Suppression and Tail Rotor Elimination ” (CIRSTEL) stertbuis, is ‘n stelsel wat ontwerp is vir die vervanging van die konvensionele stertrotor op helikopters. Dit maak gebruik van die Coanda-effek, waarmee sirkulasie rondom die stertbuis opgewek word in die teenwoordigheid van die rotor se naloop stroom. Dit genereer ‘n sywaartse krag wat die hoofrotor draaimoment teenwerk. ‘n Stertstuwer gee ekstra torsie en rigtingbeheer. ‘n Dubbelstroom waaier voer aparte lugstrome na elk van die Coanda en stertstuwer seksies. In die eerste gedeelte van die studie word die eksperimentele toetse beskryf wat op ‘n 83% skaaldemonstrator van die dubbelstroom waaier gedoen is met die doel om die konsep te bevestig en die waaier effektiwiteit te bepaal. Die gevolglike modifikasies aan die waaier se statorlemme word ook in hierdie gedeelte behandel. Hierdie eerste gedeelte sluit af met ontwerpsvoorstelle vir ‘n toekomstige waaier, gebaseer op bevindings van die eksperimente. ‘n Kort analise van die CIRSTEL stelsel word aangebied en deur middel van optimeringsmetodes gebruik te maak is bewys dat kragbesparings moontlik is met die stelsel bo diè van ‘n gewone stertrotor. Die tweede gedeelte van die studie bespreek die konseptuele ontwerp en BVM-evaluering van die luginlate vir die waaier wat aan die helikopter gemonteer kan word. Die doel hier was om die vloei wat die helikopter inlate beinvloed te identifisieer en ontwerpsoorwegings te bepaal. ‘n Basiese inlaatkonsep is ontwikkel vir die Alouette III/CIRSTEL kombinasie en verder ontwikkel op die basis van die BVM resultate. Die geselekteerde basiese ontwerp vir die inlaat is gewysig tot die punt waar bewys is dat so 'n konsep wel prakties uitvoerbaar sal wees. Hierdie BVM-resultate was ‘n eerste poging om waaierinlate te ontwerp met behulp van ‘n vereenvoudigde rotorvloeiveld. Die werk is later uitgebrei om die ontwerpsaspekte van helikopterinlate te ondersoek in die teenwordigheid van ‘n meer realistiese rotorvloeiveld, wat deur middel van ‘n aksieskyf in die BVM-simulasies daargestel is. In hierdie ondersoek is sywaartse- en bo-gemonteerde inlaatkonsepte vergelyk en analiseer vir die toepaslikheid as ‘n waaierinlaat. Beide inlaatkonsepte toon eie voordele. Weens die nabyheid van die rotornaaf aan die inlaat word die vloei versteuring en totale druk vlakke negatief beinvloed. Die verslag word saamgevat deur ontwerpsvoorstelle vir die inlaat, soos van toepassing op die huidige Alouette III konfigurasie, asook vir die toepassing daarvan op helikopters in die algemeen.

To my parents

ACKNOWLEDGEMENTS

There are many people to be thanked who helped me throughout this study. Some of their actions helped directly, while others gave the necessary moral and spiritual support. These persons are too numerous for all to be mentioned individually, in what or how they helped. They know who they are. Some however deserve special mention:

Prof. von Backström, for making this PhD possible, in more ways than one,

Dr. Meyer for the actuator disk model and continued support,

Anthony for assistance with the stator design,

and all those involved in the construction and set-up of the experimental fan rig.

TABLE OF CONTENTS

LIST OF FIGURES

LIST OF TABLES

NOMENCLATURE

Symbol	Description	Units
A	Area	m^2
A_1	Rotor cyclic pitch trim	rad or deg
AR	Area ratio	-
	Aspect ratio	-
B	Experimental error estimate	-
B_1	Rotor cyclic roll trim	rad or deg
C_D	Drag coefficient	-
C_d	Discharge coefficient	-
C_L	Lift coefficient	-
C_P	Specific heat	J/kgK
	Pressure coefficient	-
c	Chord length	m
CR	Contraction ratio	-
D	Diameter	m
	Diffusion factor	-
	Drag	N
DCθ	Distortion coefficient based on a θ^o sector	-
DC60	Distortion coefficient based on a 60^o sector	-
F	Force	N
f	Loss coefficient	-
H	Fuselage height for ROBIN	-
I_{nose}	NACA profile nose radius	-
L	Boundary layer length	m
l	Thruster centre line to rotor axis	
M	Mach number	-
$\dot{m}$	Mass flow rate	kg/s
m_{ord}	Profile maximum ordinate (camber)	%
$m_{t\ max}$	Position of profile maximum thickness	%
N	Fan speed	rad/s
	Number of blades	-
	Super ellipse exponent for ROBIN	-
n	Fraction of the cross sectional duct area the mixer occupies	
P	Total pressure	Pa
p	Static pressure	Pa
p_{ord}	Position of profile maximum ordinate (camber)	%
Q	Volume flow	m^3/s
	Torque	Nm
q	Dynamic pressure	Pa
R	Rotor radius	m
r	Radius	m
Re	Reynolds number	-

T	Temperature	K
	Thrust	N
t_{max}	Profile maximum thickness	%
U	Blade speed	m/s
V	Velocity	m/s
V_a	Axial velocity	m/s
V_θ	Tangential velocity	m/s
V_t	Rotor blade tip velocity	m/s
V_r	Radial velocity	m/s
V'	Hypothetical velocity in Glauert formula	m/s
V_c	Climb velocity	m/s
v_h	Induced velocity in hover	m/s
v_i	Induced velocity	m/s
W	Power	W
	Fuselage width for ROBIN	-
w	Width	m
X	Function variable	-
x	Co-ordinate for ROBIN	m
y^+	Dimensionless distance from wall	-
Z_o	Camber height for ROBIN	m
z	Co-ordinate for ROBIN	m

Subscripts	**Description**
atm	Atmospheric conditions
B	Blade
c	Intake capture area
	Compressor
CF	Core fan
core	Core section
D	Drag
DM	Mixer (daisy mixer)
e	Engine
f	Fan
inf /∞	Far field conditions
MR	Main rotor
OF	Outer fan
S	Slot
s	Shaft
T	Thrust
	Tail Rotor
t	Intake throat area
	Turbine
	Tip
TR	Thruster
01	Compressor inlet
02	Compressor outlet
03	Turbine inlet
04	Turbine outlet

Greek Symbol	Description	Units
α	Flow angle Angle of attack	rad or deg
α_2	Effective absolute flow angle	rad
$\alpha_{required}$	Required absolute flow angle	rad
α_s	Rotor shaft andgle	Rad of deg
β	Blade stagger angle	rad
Δ	Change in quantity	-
ϕ	Polar angular coordinate for ROBIN	
Γ	Circulation strength around aerofoil	-
γ	Gas constant	-
η	Efficiency	-
φ	Function value	-
κ	Empirical rotor correction factor	
μ	Advance ratio, $\mu = V_t/V_{inf}$	-
	Inverse capture area, $\mu = A_c/A_{inf}$	-
Ω	Rotational speed	rad/s
θ	Angle	rad or deg
θ_o	Rotor collective angle	rad or deg
ρ	Density	kg/m^3
σ	Blade solidity	-
Ψ	Rotor azimuth angle	rad or deg

Acronyms	Description
CAD	Computer Aided Design
CCTB	Circulation Control Tail Boom
CFD	Computational Fluid Dynamics
CFX	Commercial CFD solver code
CFX Build	Commercial CFD meshing software
CIRSTEL	Combined Infra-Red Suppression and Tail Rotor Elimination
FOD	Foreign Object Damage
Fluent	Commercial CFD solver software
Gambit	Commercial CFD meshing software
HBM	Hottinger Baldwin Messtechnick
IGV	Inlet Guide Vane
MATLAB	Mathematical Programming Language
MTOW	Maximum Take-Off Weight
NAC	Numerical Advection Correction
NOTAR	No Tail Rotor
UDS	Upwind Differencing Scheme

CHAPTER 1

INTRODUCTION: HELICOPTERS AND COUNTER-TORQUE SYSTEMS

Flight has captured man's imagination since the earliest days, inspiring inventors to devise and develop the flying machine. Even more thrilling was the idea of being able to hover with the precision and elegance of the hummingbird. The earliest suggestions of such devices, called helicopters today, came from Leonardo da Vinci of the Renaissance area with his idea of an air-screw, depicted in Figure 1.1.

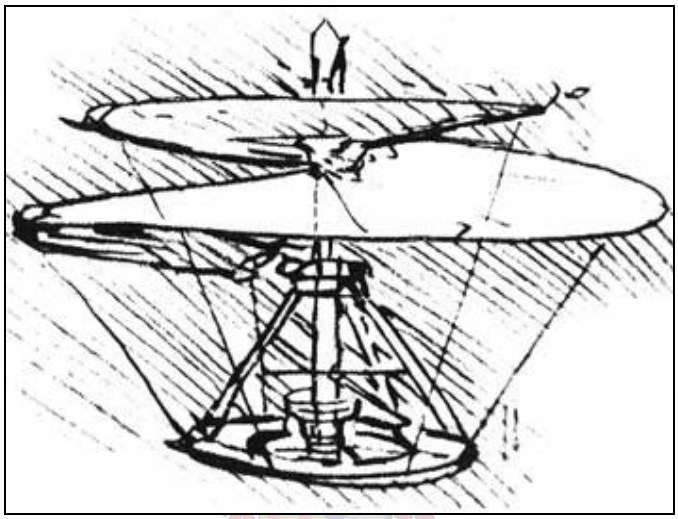

Figure 1.1 The da Vinci "air-screw"

Ever since the Wright brothers managed the first powered, heavier than air flight in 1903, there was a more concentrated effort to design and build an effective rotary wing craft. Some successes were achieved in the 1920's with gyrocopters, but these machines could not hover. Only since the exploits of Igor Sikorsky have truly practical helicopters been available, starting with the VS-300 shown in Figure 1.2.

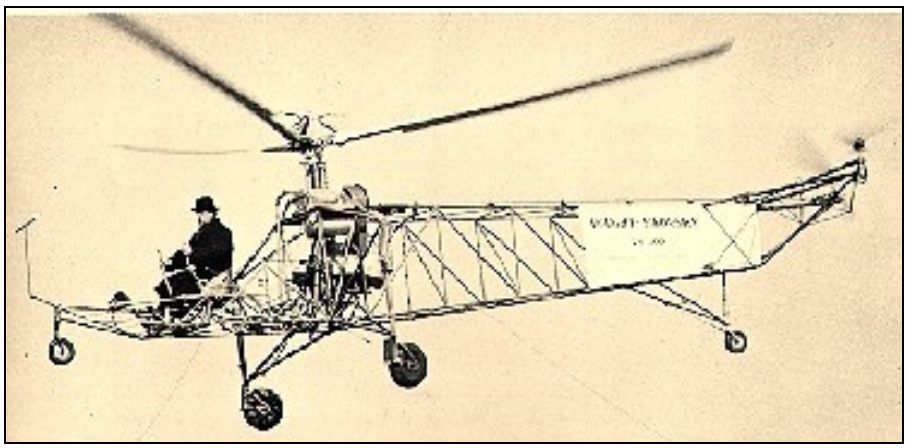

Figure 1.2 The Sikorsky VS-300, the first practical helicopter

Helicopter Designs

Sikorsky's machines had the basic layout that is common today on helicopters: a main rotor that provides lift and forward thrust, and a tail rotor that is used to counter main rotor torque, as well as for directional control (Figure 1.3a). Some other concepts do exist to cancel out the main rotor torque. The Fenestron (Figure 1.3b), although directly derived from the tail rotor, has significant advantages in noise reduction and protection over the conventional tail rotor as described by Vuillet[1]. The Fenestron is effective in the general flight envelope, but is not quite as efficient in hovering flight. Here the conventional tail rotor remains the optimum solution due to the lower through-flow velocities and the associated lower losses.

More radical concepts for helicopter layouts include the twin main rotor (Figure 1.3c) and co-axial main rotor (Figure 1.3d). Each of these concepts has its own advantages. The twin rotor is effective for large transports and the co-axial helicopters display exceptional manoeuvrability, but these types remain exceptions.

(a) Denel Oryx

(b) Eurocopter EC 120

(c) Boeing CH 47 Chinook

(d) Kamov Ka 52

Figure 1.3 Types of helicopter configurations

Tail Rotor-Less Helicopters

A problem with tail rotors is their exposed nature, which makes them susceptible to foreign object damage and tail rotor strike. By removing the tail rotor the risk of a tail rotor strike is removed, thus making the helicopter safer, as well as removing one of the primary sources of noise. In 1944 Juan de la Cierva constructed the Cierva W.9 (Lambermont[2]) which had a single main rotor and its torque was compensated by a jet thruster at the end of the tail boom (Figure 1.4), instead of a tail rotor. Air from an internal fan, which cooled the engine, was ducted through the inside of the tail boom, heated by the exhaust gases and then ejected by a controllable thruster. The pitch of the fan was also controlled by the rudder pedals which, together with the thruster, provided yaw control. The helicopter flew successfully but the project was abandoned when the helicopter crashed in 1946.

Figure 1.4 Cierva W.9, the first trials of a tail rotor-less helicopter

Another system that eliminates the tail rotor, and thus reduces the mechanical complexity of the helicopter, is the No Tail Rotor (NOTAR) system developed by Hughes (now MD Helicopters), beginning in 1976 (Logan et al.[3]).

NOTAR relies on an aerodynamic principle called the Coanda effect to create circulation around a circular tail boom with two slots along the length of the tail boom. An internal fan blows air through the slots, tangentially to the boom surface, and this air remains attached to the surface as wall jets due to the Coanda effect. This then results in the circulation effect around the tail boom. The tail boom receives the downwash from the main rotor and thus generates a sideways-directed lift vector that counters the main rotor torque. Added to the circulation control section is a tail thruster at the end of the boom and vertical stabilisers. This tail thruster directs air sideways through a nozzle to add an extra torque component to balance the main rotor torque. The tail thruster is also linked to the rudder pedals to give directional control to the helicopter. The internal fan located at the base of the tail boom compresses all of the required air to the higher pressure required for the Coanda slots. A fraction of that air is vented through the Coanda slots, while the rest is used for the tail thruster. See Figure 1.5 for a general layout of the NOTAR system.

The air venting through the thruster carries with it a lot of energy, because of its high total pressure. The fan exclusively supplies the pressure for both the tail thruster and the comparatively small flow through the Coanda slots.

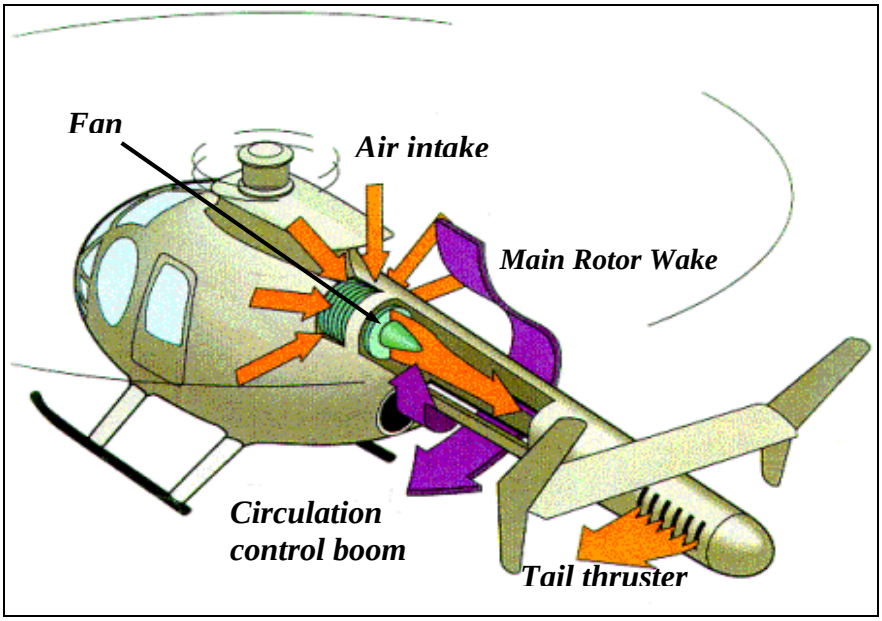

Figure 1.5 Schematic of the NOTAR system

It is here where the Combined Infra Red Suppression and Tail Rotor Elimination (CIRSTEL) has the advantage over NOTAR. CIRSTEL physically separates the circulation control andtail thruster sections and this allows each section to be optimised individually. Significant amounts of power can thus potentially be saved. Another advantage of CIRSTEL is the use of the engine exhaust gases for use in the tail thruster (Nurick[4]).

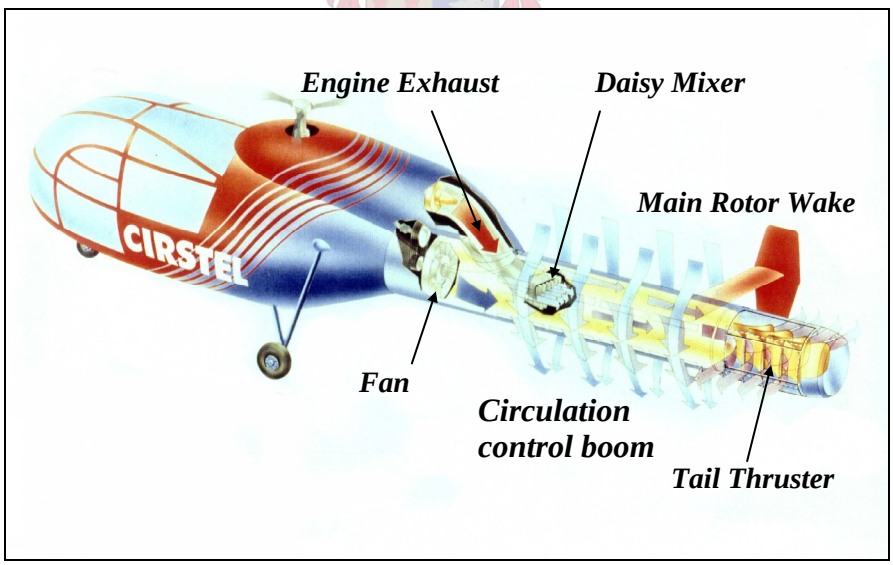

Figure 1.6 Schematic of the CIRSTEL system

In principle the CIRSTEL tail boom functions the same as NOTAR, Figure 1.6; it has a Coanda circulation control section, a tail thruster and vertical stabilisation fins. The CIRSTEL tail boom however consists of two concentric ducts that run along the length of the tail boom. The outer annulus formed by the two conduits ducts the air to the Coanda slots, while the core section is dedicated to the tail thruster. It is into this core section that the engine exhaust gases are ducted where they are injected behind the fan. Adding the exhaust gas to the core section results in a jet pumping effect, resulting in a total pressure rise for this section, and thus the load is taken off the

fan even more. The exhaust gases are also mixed with fresh air from the fan in the core section before they exit via the tail thruster. Hence the infrared signature of the helicopter is also significantly reduced. A single fan is to deliver air to both of the tail boom sections. The outer, or Coanda section, requires air of a higher total pressure than the core section, but at the same time at a lower mass flow rate.

Project Background

A prototype of the CIRSTEL tail boom was built and fitted to an Alouette III helicopter, Figure 1.7. The fan design used in this prototype had a different blade profile for the outer 17% of the blades, which supplied air to the outer section. The change in blade profile was necessitated by the higher pressure rise required for the outer section.

Figure 1.7 The CIRSTEL prototype in the original configuration

Trials on the CIRSTEL helicopter showed that the fan in the original configuration was not working to specifications. However the overall system showed promising results that warranted a continuation of the project. Two shortcomings of the design were identified during the trials. Firstly the fan was unable to deliver the required mass flows and pressure rises, primarily because no physical separation was present to split the two air streams from the rotor on. For further discussions on this topic see von Backström[5] and Heise[6].

Secondly the fan performance was hampered by the lack of suitable air intakes. The flow area of the intakes was smaller than the flow area of the fan by about 8%. This resulted in a high velocity through the intake openings (higher than the fan through-flow velocity) before the air entered a plenum chamber ahead of the fan. Separation could be expected as the air flowed through the sharp edged intake openings resulting in a high intake loss coefficient. It is estimated from momentum theory that the pressure loss coefficient of the original intake is in the order of $C_P = 1.16$.

Thesis Objectives

It was the objective of this thesis to investigate the design and performance of the fan and its intakes as part of the CIRSTEL tail boom. This thesis can thus be subdivided into two sections, the first section concentrating on the experimental fan performance evaluation, while the second part details the air intake design.

A new fan for application with CIRSTEL had previously been designed (Heise[6]). The concept for the new fan was to separate the two air streams ahead of the rotor already by means of a rotating shroud fitted to the rotor. An 83% scale concept demonstrator (Figure 1.8) based on the design had also been built and used for the experiments of the current research work.

The original objective of the intake evaluation work was to define an intake concept that could be fitted to the original Alouette III configuration. During the course of these investigations the question arose as to what the ideal position would be of such fan intakes. The layout of the Alouette III test bed precluded a top-opening intake and thus complicating the intake design, possibly also inducing higher intake losses than the simpler top-opening intake design. The research work was thus expanded to investigate different fan intake layouts on a generic helicopter fuselage configuration.

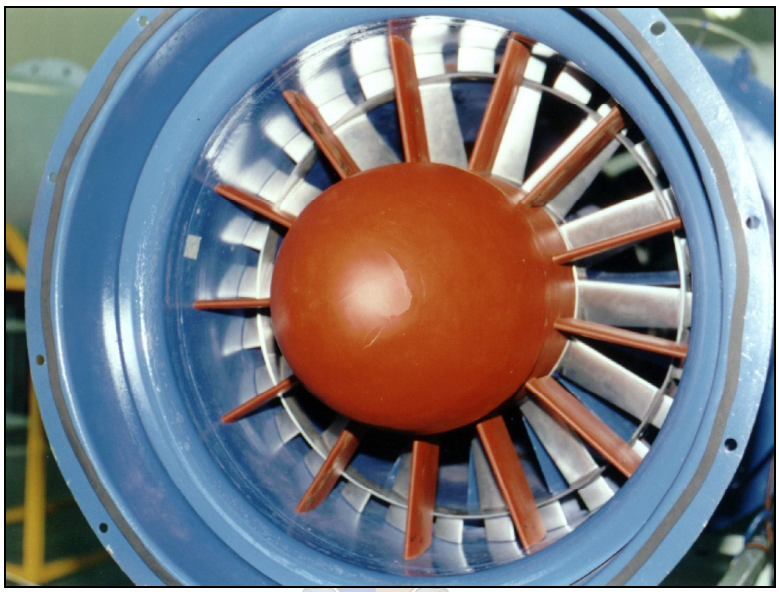

Figure 1.8 The two-stream fan demonstrator

Fan Performance Evaluation

The overall objective of the first part of this thesis was to conduct performance measurements on the 83% scale demonstrator of the two-stream fan. The question remained whether a single fan could produce two different airstreams, each at a different pressure rise as required by CIRSTEL and at the same time do so efficiently. It also remained to be resolved if the fan could be controlled by means of inlet guide vanes fitted to the fan. The concluding objective is to establish design guidelines for the design of a two-stream fan.

More specifically the method used to answer the research objectives included the following tasks:

- Conduct velocity profile measurements on the demonstrator fan. The aim here was to gain insight into the functioning of the fan and establish performance figures from the profile measurements.

- Establish performance maps of the fan sections and investigate the possibility of power turn down using inlet guide vanes. As part of these tests the effects of the sections on each other had to be investigated.

- Design and manufacture new stator blades to replace the simplified sheet metal stators in the original test rig. The stators were to be designed using the results of the first velocity profile measurements. The objective was to improve the fan by fitting new aerodynamically shaped stators and to compare the performance directly to the original performance data.

Air Intake Design

The overall objective of the second part of the thesis was to develop air intake concepts for the fan, when fitted to a CIRSTEL configured helicopter. The fan forms a critical component of the system, and hence the intakes play an important part in the overall performance of the tail boom. Thus an indication of the system sensitivity to the fan and intakes needs to be established. Design unknowns were the effects the location of the intake has on the intake performance; the location of the intake can be affected by the layout of the helicopter platform. The engine position, for example, can place constraints on the feasible design options available for the intake. Due to the size of the fan itself the practical contraction ratio that can be applied to the intake also has an upper limit. Ultimately design guidelines for similar intakes are to be established, which can also be extended to general helicopter intake design.

More specifically the work entailed the following:

- Develop a numerical model of the CIRSTEL system featuring individual sub-models of the components that make up the CIRSTEL system. The primary use for the model is to determine the mass flow rate of the fan to aid with the intake design. A secondary objective is use the model to perform a numerical optimisation of the system, with the purpose of reducing the system power demand

- Generate an initial concept for a fan intake to work effectively for the Alouette III/CIRSTEL combination. This concept has to adhere to the spatial constraints posed by the airframe.

- Develop simplified CFD models with suitable boundary conditions to simulate the effects of the rotor. This model is to be used to evaluate a suitable intake over the flight envelope and modify the design appropriately to improve its performance.

- Extend the CFD studies to investigate the fundamental issues concerning the design of intakes for helicopters. Specifically to identify the external flow characteristics, resulting from the rotor, that influence the performance of the intakes. Here an actuator disk model is to be used to simulate the main rotor and its hub.

- Investigate the performance sensitivity of the intakes to the design parameters that affect the fan performance over the forward flight envelope.

CHAPTER 2

VELOCITY PROFILE MEASUREMENTS

During a previous project a test rig for a twin flow fan demonstrator was designed and built by Heise[6], while Thomas[7] and Heise[6] conducted initial tests on the demonstrator. A new set of experiments was conducted to gain a better and detailed understanding of the twin axial flow fan system, as the previous tests left some questions open. The objective of these tests was to measure the velocity profiles at several stations in the machine in detail. The measured profiles made it possible to identify design problems with respect to the shroud concept and the sealing between the rotating and stationary parts of the shroud. A critical design objective was to meet the required efficiencies for the two fan sections. The efficiency could be determined through numerical integration of these velocity profiles. Concern was also raised over the performance of the stator blades because of their rudimentary sheet metal construction. The effectiveness of these blades was to be evaluated with the aid of the probe measurements. For the design of new stators, the measured profiles served as a design input. The new fan was subjected to an identical test to determine any improvements of the performance over the original version. A detailed comparison of the two stator versions is presented.

Test Conditions and Set-Up

The experimental apparatus used for the current tests is presented in Appendix A. The tested fan was not a true scale version of the theoretically designed fan, but a slightly distorted 83% scale version of the designed prototype fan (Heise[6]). The differences between the demonstrator and the prototype fan dimensions are also discussed in Appendix A. To get an insight into the detailed performance of the fan, velocity profile measurements were conducted. The profiles were measured with a five-hole pneumatic probe, thus providing information about static and total pressure, velocity and flow angles at the measured positions. Traverses were conducted along several stations of the fan assembly. The stations measured were in front of and behind the inlet guide vanes, behind the rotor and stators in both sections of the fan and finally at the exit of the outer diffuser, as also shown in Appendix A. The five-hole–probe was mounted in a specially constructed bracket, that allowed the probe to be traversed radially and the yaw angle to be adjusted accurately.

For the velocity profile tests the fan was throttled to deliver its designed operating pressure rise in both the core and outer section. The required pressure rise was scaled down from the original design requirements of the full size fan using the appropriate scaling laws. Two sets of tests for the profile measurements were conducted. At the operating conditions the design calls for the inlet guide vanes to be set at zero degrees, i.e. straight inflow and it is with this setting that the velocity profiles were measured. The fan RPM for the tests was selected to be at half the full-scale speed, namely 2025 rev/min. Together with a density ratio of about 120% from the design conditions and scale of 83%, this resulted in a Reynolds number, based on chord length, of $Re_c = 1.64 \cdot 10^5$. That is roughly half of the full size fan Reynolds number of $Re_c = 3.61 \cdot 10^5$. The limit consideration on the fan speed was estimated stresses in the shroud and the power limitation of the electric motor used to drive the fan in the experimental set-up.

For both of the profile tests, during which velocity profiles were measured, the fan was fitted with a standard elliptical inlet bell mouth. This ensured a uniform inlet velocity profile into the fan face.

The aim of these tests was partially to determine the maximum efficiency of the fan, which could only be determined if the fan operated under ideal conditions. A distorted profile, such as coming from an operational inlet, would naturally affect the performance of the fan.

For the tests it was important to ensure that the fan ran at its designed operating point, to be able to get representative velocity profiles and determine any potential problems. Pressure rise was used as the criterion to set the fan operating point in the lab because it could be measured directly, while the volume flow for the core section differs significantly due to the imperfectly scaled hub-tip ratio. Throttling of the outer section was accomplished by means of a set of twelve orifices. The area of the orifice openings could be adjusted for throttling purposes, while at the same time they served to measure the mass flow out of the outer fan section. A set of tests was conducted in advance to calibrate the orifices at various settings. The essence of the calibration results was to establish a relation between the C_d coefficient and orifice opening. The orifice C_d was found to be Reynolds number independent and constant in the operating range for each setting of the orifice plate.

The design requirements for the fan were given as mass flow rates and total pressure rises for each section. It is time consuming to measure the total pressure rise over a fan directly, so the wall static pressure rise was used as a reference to find the operating point. Values for the static pressure were obtained from the STFM simulations done by Heise[6]. The scaled values are given in Table 2.1 below.

Table 2.1 Scaled fan performance values

	Outer Section	Core Section
Volume Flow [m^3/s]	0.858	2.635
Mass Flow [kg/s]	1.030	3.162
Total Pressure [Pa]	744	284
Static Pressure [Pa]	555	100

Overview of Results

Substantial amounts of data were generated from traverses of the five-hole-probe. From this mapping of the velocity, pressure and flow angle profiles, the performance of each section of the fan could be determined experimentally. A station-by-station analysis is presented below. See Appendix B for plots of the profiles for both tests. The plots refer to positions behind the named element, for example the IGV measurements were taken just behind the IGV blades. The zero span position indicated on the plots is at the inner radius of each station.

Original Fan

The results discussed here are for the original fan set up that included stators manufactured from sheet metal, and thus had no airfoil shape, or variation of chord and camber with radius.

Inlet and Inlet Guide Vanes

The inlet velocity profile yielded no surprises, having a uniform profile, with the boundary layer extending over the outer 17% of the section (Figures B.1(a)). The inlet pipe length in front of the

fan inlet face was three pipe diameters long. The boundary layer on the hub was thin because of the short distance on the nose bullet over which it developed. The boundary layer on the outside wall, which spanned the outer 20% of the IGV, implied that almost the entire outer fan was operating in a boundary layer, and thus suffered from a high blockage. Pressure profiles at the inlet also showed little distortion.

The axial velocity profile behind the IGVs was slightly distorted (Figure B.4(a)). Initially it appeared as if there was a very thick boundary layer present. A noticeable inward velocity component on the outer half of the profile was measured (Figure B.6(a)), which indicated that the streamlines were diving inwards into the core-fan section. As became apparent later, the cause for this was the slight over-throttling of the outer fan, relative to the core fan. The extra resistance on the outer section reduced the mass flow into the outer section and forced more into the core section. Also, as the settings were adjusted to give the desired pressure rise, the volume flow through each section did not scale correctly. The higher hub-tip ratio of the core section, compared to that of the full scale version, meant a smaller through-flow area and this resulted in a higher axial velocity. The static pressure profile (Figure B.5(a)) was also distorted because of this phenomenon, having a higher pressure in the outside section, just in front of the outer fan, which then decreased inside of the radius at which the shroud is positioned. The total pressure remained uniform behind the IGVs, except in the boundary layer.

Core Section Rotor

The most noticeable feature of the profiles here was the distinct bulge in the total pressure profile, as seen in Figure B.7(a). This was a direct result of the simplified blade shape used in this rotor. In this section of the bulge the design simplifications gave the blade more camber and less stagger. More energy was thus added to the flow, in this region.

The velocity profiles were fairly uniform as expected, but there was a drastic change in the flow angle near the casing, Figure B.9(a). The increase in yaw in this area was as a result of the rotating boundary layer coming off the spinning shroud. This area was subject to a closer study to determine if any flow effects occurred here because of high-pressure air from the outer section blowing into the core section through the seal gap. No evidence of any detrimental effects such as pressure loss or flow distortion were found, thus the simple sealing concept used in this fan (Heise[6]) is sufficient to separate the two air streams. Of course this also means that a major potential obstacle to the concept of the twin flow fan concept is surmountable.

Outer Section Rotor

First looking at the flow angles (Figure B.12(a)), one notices a relatively high deflection of the air at the blade root and tip. The deflection angle near the centre of the blade was exactly at the required value, as calculated from the Euler turbomachinery equation to give the required total pressure rise. The absolute velocity behind the rotor (not shown) remained relatively constant, but the axial and tangential velocities on their own did vary significantly (Figure B.10(a)) hence also the extreme yaw angles. A very thin boundary layer developed behind the rotating shroud, due to the slight boundary layer suction effect in the gap between the rotating and stationary shrouds. Both the static and total pressures distributions were fairly even throughout the span of the rotor blades, Figure B.11(a).

Core Section Stators

For such simplistically built stator vanes, the results were surprisingly good. The stators were made from sheet metal, bent to give some camber and welded into position. There was no twist on the blades, so camber and stagger remained constant along the span of the blade. These stators turned the airflow coming out of the rotor to within seven degrees of the axial direction. The extreme yaw and pitch angles displayed on the outer wall were as a result of leakage from the inner probe insertion hole, which could not be blocked due to its concealed location (Figure A.2), and should be ignored (Figures B.15(a)). The axial velocity profile remained virtually the same as ahead of the stators, while the total pressure profile was flattened slightly (Figures B.13(a) and B.14(a) respectively). The average total pressure loss over the stators was 6%, thus still within acceptable limits. The static pressure profile exhibited a noticeable and constant increase towards the outside. This profile stems from the fee-vortex design of the rotor and is not a cause for concern. It did complicate conventional static pressure measurements, in that pressure tapping points were located only on the casing and not the hub. By positioning a pressure measuring point on the hub, an average and more representative pressure reading could be obtained.

Outer Section Stators

The velocity profile leaving the stators in the outer section was again surprisingly smooth, but the flow still had a very big swirl component, as can be seen from Figures B.16(a) and B.18(a). The stators were thus not working properly and needed redesigning, this time adding proper airfoil shaped blades. By turning the flow better into the axial direction a better static pressure recovery could be obtained before the flow enters the diffuser. The pressure distribution leaving the stators was also reasonably uniform, as were the flow angles.

Outer Diffuser

At the inner 17mm of the diffuser no measurements could be taken because of suspected flow separation on the inner side of the diffuser. The probe was out of range in this region, no matter what angle it was adjusted to, and thus no readings could be taken. The velocity measurements that could be taken in the rest of the diffuser revealed slightly jagged profiles, further hinting towards a stalled diffuser. The swirl component that entered the diffuser was maintained throughout the length of the diffuser, while the axial velocity was reduced significantly. Combining the two effects results in a very high yaw angle at the exit of the diffuser. It was thus clear that the stators in the outer fan section have to be carefully designed to, at worst, turn the flow to within a few degrees of the axial direction. See Figures B.19(a) to B.21(a) for the complete profile plots.

For this test case the static pressure recovery in the diffuser was relatively good, the diffuser efficiency being 75% with the IGVs set at 0^0. The total pressure loss for the same test case was less than 6%. The performance could however still be boosted with new stator vanes.

Modified Fan

The second set of results discussed here is for the tests conducted on the modified fan test rig, which included machined stator vanes, as detailed in Appendix A.

Inlet and Inlet Guide Vanes

The velocity and pressure profiles at the inlet and behind the IGVs yielded no surprises, the

profiles were almost identical to the first set of tests. Only a slightly lower average inlet velocity of 20.05 m/s, compared to 20.74 m/s, was measured which implied a lower mass flow rate. (Compare Figures B.1(a) to B.1(b))

Core Section Rotor

The inner rotor had a more uniform and higher total pressure distribution than the original model. The total pressure was noticeably higher towards the casing when compared to the previous data. Also shown in Figure B.8(b) is the static pressure, to be compared with Figure B.8(a). The static pressures were identical near the hub, but towards the casing the pressure dropped off. The swirl angles and velocities remained the same.

Outer Section Rotor

Comparing Figures B.11 show a lower average static pressure behind the second version rotor, 450 Pa compared to 488 Pa, but the area averaged total pressure remained the same. At the same time the trends in the pressure distribution remained the same. The velocity increased slightly (Figure B.10(b)), while the angles also remained the same (Figure B.12(b)).

Core Section Stators

The static pressure behind the new stators was slightly higher (Figures B.14). The pressure profile increased towards the casing, stemming from the free vortex design. The total pressure showed less rapid changes, as it did not display the sudden drop near the casing. This increased total pressure originated from the increased total pressure behind the rotor.

The swirl angle variation now was more linear (Figure B.15(b)) and it did not display the bulge of the previous design. An average swirl angle of 4^{o} remained behind the stators; this was the same average as previously. The design point of axial flow only was therefore not reached.

No distinct difference in axial velocities was detected, the average velocity was however slightly less, possibly to an inadvertently higher throttle setting. The spikes near the casing are partly due to the effects of the rotating shroud and seal that are still measured here, and partly due to leakage from the outer section through the insertion hole for the five-hole-probe. Due to the location of the insertion point it could not be sealed off effectively.

Outer Section Stators

The swirl angle leaving the new outer stators was not the designed for 5^{o}-7^{o}. Instead the flow left the stators with an almost constant swirl angle of 16^{o} (Figure B.18(b)). The stators were thus not working as effectively as anticipated. This was however a much more improved angle when compared to the 25^{o} of the old stators. The axial velocity that was measured was about 16% higher than required for a mass flow balance in the outer section. The reason for this was a high amount of blockage caused by the stalled stators, as will be discussed in more detail later in the section titled “Stator Performance Comparison”.

Static pressure recovery remained virtually the same (Figures B.17), with a uniform trend across the entire span, averaging 530 Pa. The total pressure in the measured section remained virtually unchanged at an area average of 795 Pa, and also displayed the uniform distribution as previously.

Outer Diffuser

Immediately apparent from Figures B.19 to B.21, is the un-stalled diffuser. With the initial stator blade measurements it was impossible to obtain data on the inner 16 mm of the diffuser. With the new stator design, measurements could be done over the whole width of the diffuser.

The static pressure recovery of the diffuser was less than previously (Figure B.20), but the exit static pressure was uniform. Even though the diffuser now appeared un-stalled, the diffuser total pressure turned out to be less at the exit. The average total velocity was 11 m/s and thus close to the accuracy limit of the five-hole-probe, so the data should be handled with care (Kirstein[8]). Integration of the measured velocity did for example result in a too high volume flow. However the data can still be used for comparison.

The tangential velocity component remained constant at about 5 m/s (Figure B.19), which was the same as previously, while the axial velocity displayed a slight bulge towards the outer casing. This was because the swirling flow has a tendency to remain attached to the expanding outer casing. The effective swirl angle at the exit of the diffuser remained the same.

Stator Performance Comparison

From the previous discussion it became clear that the new outer stators were not working as anticipated, and the improvement in performance of the fan did not materialise. Amongst the changes noted was the reduction of pressure recovery in the diffuser. From the five-hole-probe measurements an idea was gained of how the stators performed, when compared to the previous sheet metal stators.

Outer Stators

The outer stators were designed to give and outlet angle of 5^o to 7^o from the axial direction. The swirl angle just ahead of the stators was between 40^o and 50^o, so the stators had to turn the flow through a large angle. It was therefore not surprising that the stators stalled.

The first indication of stalled stators was the exit angle measured by the five-hole-probe. An average swirl angle of 15^o was measured, which was a significant deviation from the design angle. Oil flow experiments were also done to visualise the blade surface flow and these experiments indicated a separation point at about 80% of the chord distance.

As mentioned already, the average axial velocity was 16% higher than anticipated. This higher velocity could be attributed to the extra blockage caused by the stalled stators. The five-hole-probe was positioned exactly between the exit trailing edges of the stators; it would thus only measure the higher velocity between the blades. To gain a better understanding of the stator wakes and performance, more measurements would have to be conducted, which would cover an area of at least twice the blade pitch width. When drawing a simple sketch that plots the flow direction over the blades as in Figure 2.1 and Figure 2.2, a basic estimate of the wake thickness could be made. The wake was plotted by drawing lines parallel to the flow direction, as measured by the probe. One line started at the trailing edge, and the other line joined the blade tangentially on the suction surface. The point where this line joined on the new stators (Figure 2.1) was exactly the point where the oil flow experiments indicated the separation line. From this sketch an estimate of the blockage could be calculated, which turned out to be almost 16%, the same amount as the increase in velocity.

When doing a similar analysis with the original blades (Figure 2.2), similar results were obtained. The blockage here was only 8%, and again the same increase in axial velocity was measured. When comparing Figure 2.1 with Figure 2.2 it became apparent that the losses through the new stators might be higher. The wake width for both blades was about 4mm, using the just described method. As there were now 50 blades, instead of the original 30, the losses could be expected to be higher. Since the probe only sampled at one station in between the blades, no accurate estimate could be made of the losses. Only measurements spanning a significant sector of the annulus could reveal that information.

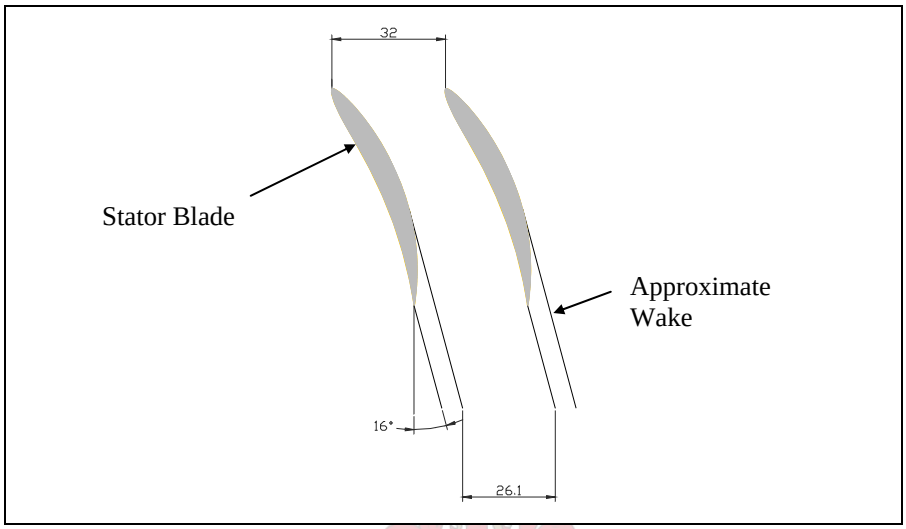

Figure 2.1 Simplified wake presentation of the new stator blades, from which the blockage can be determined

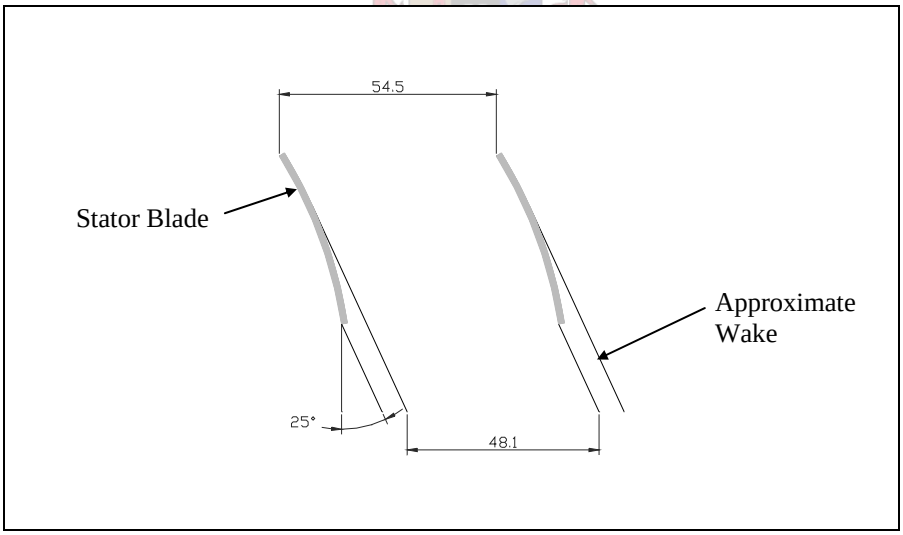

Figure 2.2 Simplified wake presentation of the original sheet metal stators. The relative blockage can be compared with Figure 2.1

From the probe data an estimate of the stator diffusion factor could be calculated. It is generally recommended in turbomachinery handbooks, as a design guideline, to limit the diffusion factor of a blade row to 0.5. Increasing this factor would run the risk of stalling the blades. The diffusion factor for stator blades is given as:

$$D = 1 - \frac{V_2}{V_3} + \frac{\Delta V_\theta}{2\sigma V_3} \qquad (2.1)$$

Here V_2 and V_3 are the inlet and outlet velocities of the stator blade and V_θ the tangential velocity, while σ is the blade solidity.

As the diffusion factor is calculated from the velocity triangle components of the blade row, an effective diffusion factor for the stators could be calculated. Figure 2.3 plots the measured diffusion factors for the original sheet metal stators and the new, machined stators. The diffusion factor for the original blades ranged from D = 0.3 to D = 0.5, ignoring the edges. The diffusion factors here were acceptable, but due to their rudimentary construction they could have been under threat of stalling. For the modified stators the diffusion factor averaged around D = 0.53, which was higher than recommended. This was more proof that the stators were stalled.

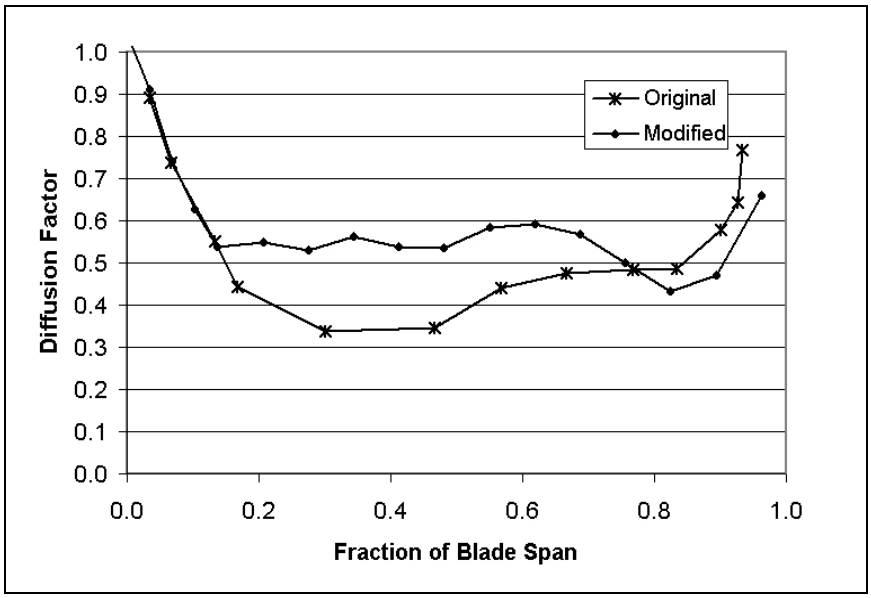

Figure 2.3 Effective diffusion factors for the two outer stator blade versions

The effect that the swirl component had on the diffuser performance remained unclear. From the five-hole-probe results it would appear that the diffuser worked better with a high entry swirl, contrary to what had been stated previously and to which the stators had been designed. It should thus be noted that the design and performance evaluation of the diffuser for this application should be the subject of further detailed evaluations.

Core Stators

The loading on the core section stators was not as severe; they had to turn the flow into an axial direction through 20^o to 30^o. Here again the original plate stators worked surprisingly well, and the new stators gave no problems.

Due to the relatively low loading of these stators the design angle was set at 0^o relative to the axial direction. As the five-hole-probe measurements however showed, a near constant swirl angle of 4^o remained behind the stators.

When comparing the diffusion factors for the old and new blades (Figure 2.4), a distinctly higher

diffusion factor for the new stators can be seen. The higher diffusion factor, especially in the outer half of the blade span, resulted in a higher average pressure recovery. Hence the higher static pressure measured behind the stator blades. The diffusion factor remained below the value of D = 0.5, it would thus be safe to assume that the stators were not stalled.

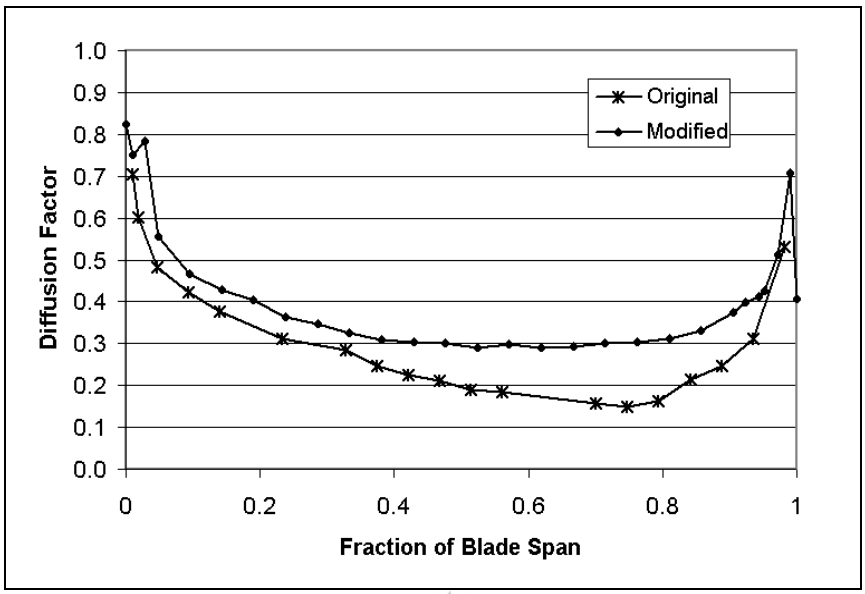

Figure 2.4 Effective diffusion factors for the two core stator blade versions

Overall Performance and Efficiency

The velocity and pressure profiles on their own reveal a great deal about the functioning of the fan and its individual components. No information on the global performance, such as power and efficiency, could be obtained directly from the individual readings. The information obtained through a single five-hole-probe was specific to a single point in the fan assembly. To obtain an overall performance estimate, the station-by-station readings were integrated numerically using the trapezium rule to obtain the area-averaged performance values.

Performance Results

As the measurements were taken behind each stage, the results from the numerical integration reveal the effectiveness of each one. Table 2.2 lists the performance figures obtained from the five-hole-probe measurements. In the previous discussion it was shown that the velocity measurements behind the outer stators were too high, specifically for the modified stators, and that the velocity readings behind the diffuser were also to be interpreted with caution. Thus the volume flow calculated from the outer rotor data was used right through in the calculations of the power absorbed by the flow. This volume flow was also within 0.8% of the value measured with the orifice plates. The figures listed here already include the performance of the outer diffuser.

Another set of power measurements was available, namely by measuring the drive shaft torque and speed. Note that the shaft power figure is the effective power that has to be delivered to the fan, as some power is required to overcome friction losses on the spinning shroud. The values presented in Table 2.3 are compensated for losses in the shaft bearings by subtracting the previously calibrated bearing losses from the experimentally measured shaft power.

Table 2.2 Fan performance figures

	Outer Section			Core Section		
	Original	Modified	Difference	Original	Modified	Difference
Volume Flow [m^3/s]	0.770	0.824	7.0%	2.621	2.570	-2.0%
Static Pressure [Pa]	674	655	-2.8%	110	120	9.1%
Total Pressure [Pa]	716	727	1.7%	378	382	0.8%
Euler Power [W]	745	842	13.0%	1209	1276	5.5%
Power Absorbed (QΔP) [W]	591	638	8.0%	1039	1 025	-1.3%
Efficiency	79.4%	75.7%	-3.7 % pts	85.9%	80.3%	-5.6 % pts

Table 2.3 Overall fan power and efficiency

	Original	Modified	Difference
Euler Power [W]	1 954	2 118	8.4%
Power Absorbed (QΔP) [W]	1 630	1 663	2.0%
Input Shaft Power [W]	2 048	1 978	-3.4%
Overall Efficiency	82.0%	79.6%	-2.4 % pts

Tables 2.2 and 2.3 also compare the performance differences of the two fan designs. The values used to calculate these values are from integration of the five-hole-probe data. The volume flows were within a few percent, typically 5%, of the values measured with the orifices and the bell mouth. However, more reliable answers are gained by using the probe data for the calculations because of the more accurate total pressure readings, which are difficult to calculate from performance data.

From Tables 2.2 and 2.3 it can be seen that there are significant differences in the overall performance between the two designs. In the outer section of the modified fan the volume flow increased, and at the same time the total pressure rise across the fan increased. Thus the Euler power and effective power also increased, but at the same time the efficiency decreased by 3.7 percentage points. This can be attributed to the reduced efficiency of the diffuser, which now had a total pressure drop of 69 Pa, instead of the 42 Pa measured on the original set-up.

The core section showed a reduced volume flow, but with a slightly higher total pressure than the original version. Hence the effective power decreased. The energy applied per unit mass to the air as calculated by means of the Euler equation was higher than before, and thus the efficiency of this section reduced by 5.6 percentage points.

Comparison of the total effective absorbed power and delivered shaft power in Table 2.3, showed

an increase in the absorbed power while a decrease in shaft power is measured on the modified fan. The overall efficiency however reduced for the modified fan when calculating the efficiency from the effective and shaft power by 2.4 percentage points.

Scaling

The model fan on which the tests were done was a slightly distorted 83% scale model and results obtained from this model were satisfactory. From these small-scale figures an estimate had to be made to get an indication of what the full size fan would deliver and compare that to the original specifications supplied.

Scaling Laws

The standard scaling laws used in turbomachinery cannot be used directly here, because the standard equations are based on an exact geometrical similarity. The new scaling equations have to take into account different flow areas and relative tip speeds of the distorted fan. The important variables used when applying the Buckingham pi theorem to this fan are diameter (D), fan speed (N) and volume flow (Q). First the dimensionless groups are identified.

Dimensionless group based on velocity:

$$\Pi_1 = \frac{Q/D^2}{ND} \tag{2.2}$$

Dimensionless group based on pressure:

$$\Pi_2 = \frac{\rho g H}{\rho N^2 D} \tag{2.3}$$

Dimensionless group based on power:

$$\Pi_3 = \frac{W}{ND\left(\rho N^2 D^2\right)D^2} \tag{2.4}$$

From these groups the scaling laws could be rewritten to the following set of equations. They are not different from the standard equations, instead the equations are written in a more detailed format by treating the D^2 term as the flow area A, and thus forming a separate term. The equation to scale volume flow rate could be written in terms of the flow area of each section as follows by using the first dimensionless group (Equation 2.2):

$$\frac{Q_2}{Q_1} = \frac{N_2}{N_1}\frac{D_2}{D_1}\frac{A_2}{A_1} \tag{2.5}$$

Similarly to scale pressures the group Π_2 (Equation 2.3) was used:

$$\frac{p_2}{p_1} = \frac{\rho_2}{\rho_1}\frac{N_2^{\,2}}{N_1^{\,2}}\frac{D_2^{\,2}}{D_1^{\,2}} \tag{2.6}$$

And finally from the third group (Equation 2.4) the scaling law for power was derived:

$$\frac{W_2}{W_1} = \frac{\rho_2}{\rho_1}\frac{N_2^3}{N_1^3}\frac{D_2^3}{D_1^3}\frac{A_2}{A_1} \qquad (2.7)$$

Scaled Performance Figures

When scaling the performance figures, it was assumed the section efficiencies remain the same for the full size fan. A density change was also accounted for in the scaled figures, as the design conditions specify the operational environment to be at 2500m above sea level. The atmospheric density at which the tests were conducted was roughly 1.2 kg/m^3, while the design density is 0.963 kg/m^3. The approximate scale of the model fan, based on the outside diameter, is 1:1.21. The scaled figures are compared with the original specifications issued by Denel Aviation in Tables 2.4 and 2.5.

Table 2.4 Outer fan: scaled performance

	Design Specification	Scaled (original)	Difference from Spec.	Scaled (modified)	Difference from Spec.
Mass Flow [kg/s]	2.68	2.41	-10.1%	2.57	-4.1%
Total Pressure Rise [Pa]	3500	3368	-3.8%	3 420	-2.3%
Efficiency	70%	79.4%	9.4 % pts	75.7%	5.7 % pts

Table 2.5 Core fan: scaled performance

	Design Specification	Scaled (original)	Difference from Spec.	Scaled (modified)	Difference from Spec.
Mass Flow [kg/s]	10.41	10.35	-0.6%	10.15	-2.5%
Total Pressure Rise [Pa]	1400	1865	33.2%	1 884	34.6%
Efficiency	80%	85.9%	5.9 % pts	80.3%	0.3 % pts

Original Fan

Here again it can be seen that the mass flow rate and total pressure rise in the outer fan of the original set up fell short of the required values, while the efficiency target was exceeded. The core fan had a much better performance than required, providing some reserves or chances to bring the power consumption down. The core fan reserves might however still be required once an air intake, representative of those eventually fitted on the helicopter, is used.

Modified Fan

When compared to the design specifications the mass flow through the outer section of the modified fan was still 4.1% less than required, along with a total pressure that does not reach the targeted value by 2.3%. The efficiency, though lower than for the first design, still exceeded the design requirements. It would appear that with a better stator design and carefully designed diffuser the design requirements can be met. Despite a lower than required mass flow, the core fan total pressure rise leaves sufficient reserves to cope with additional losses, like those losses

incurred around the daisy-mixer which will be fitted behind the core fan in the helicopter.

Table 2.6 Scaled fan power

	Design Specification[#]	Scaled (original)	Difference from Spec.	Scaled (modified)	Difference from Spec.
Outer Fan Power [W]	13 400	11 368	-15.2%	12 850	-4.1%
Core Fan Power [W]	18 170	24 470	34.7%	25 824	42.1%
Total Power [W]	31 570	35 838	13.5%	38 674	22.5%

Value calculated from required volume flow, pressure rise and minimum efficiency. Max power available 40kW.

The core section in both fan versions uses an excessive amount of power (Table 2.6) due to the 33 to 35% higher pressure rise it delivers. Assuming that a fan can be designed with the same efficiencies, an estimate can be given of its required power consumption if it delivers the correct mass flow at the correct pressure. Calculating the QΔP power and dividing it by the experimentally determined efficiencies, the total power requirement is 30 485 W. This power figure consists of 12 867 W for the outer fan and 17 618 W going to the core section.

Comparing the performance of the fan on the basis of power reveals that there are some reserves left on the maximum supply power. The power of the outer fan is also less than originally estimated, but this figure could rise once this fan section is adjusted for a higher mass flow. As promising as the core fan appears to be, improvements can still be made. If the core fan would not produce the higher measured pressure rise, the total consumed power could reduce to approximately 29 kW.

It would also be useful to scale the same experimental data using the standard scaling laws. Since the mass flow of the outer section has been shown to be too low, and the demonstrator had a higher flow area when scaled directly, better results can be gained when retaining the demonstrator geometry.

The pressure is not affected by the distorted scaling, so the pressure values remain the same when using the scaling laws. The outer section mass flow did increase for both versions (Table 2.7), thus from this example it can be seen that there is some advantage gained by increasing the flow area of the outer section to allow for blockage effects, and thereby increase the mass flow.

Table 2.7 Outer fan: directly scaled performance

	Design Specification	Scaled (original)	Difference from Spec.	Scaled (modified)	Difference from Spec.
Mass Flow [kg/s]	2.68	2.63	-1.9%	2.82	5.2%
Total Pressure Rise [Pa]	3500	3368	-3.8%	3 420	-2.3%
Efficiency	70%	79.4%	9.4 % pts	75.7%	5.7 % pts

The through-flow area of the core fan reduces from the intended full-scale area when using the standard scaling laws and hence the core mass flow is less than the design requirement (Table 2.8). Due to the lower mass flows but equal pressures, the Euler power decreased to 35.2kW and

38.7kW for the respective fans, both less than the 40kW available.

Table 2.8 Core fan: directly scaled performance

	Design Specification	Scaled (original)	Difference from Spec.	Scaled (modified)	Difference from Spec.
Mass Flow [kg/s]	10.41	9.62	-0.6%	9.43	-9.4%
Total Pressure Rise [Pa]	1400	1865	33.2%	1 884	34.6%
Efficiency	80%	85.9%	5.9 % pts	80.3%	0.3 % pts

Conclusions

The tests to measure the velocity profiles at various stations in both fan sections were successful in gaining a detailed performance analysis of the two fan versions near its operating point. Through these tests a direct comparison could be made of the changes in the fan performances. The fan sections performed well achieving the efficiency targets and coming close to matching the mass flow and pressure demands.

The effectiveness of the sheet metal stator vanes in the core section was surprisingly good, but it was clear that much could be gained by fitting carefully designed stators to the outer section. Firstly, new aerodynamically profiled stators can turn the flow more effectively, which would result in a better diffuser performance to reduce total pressure losses. Secondly, the stators with their sharp leading edges are under threat of stalling.

The five-hole-probe measurements revealed that the new machined stators of the outer section were stalled. As a result not enough turning took place before the flow entered the annular diffuser fitted directly behind the stators. Through these experiments it became clear that the stators have to be carefully designed, as they have to turn the flow by a great deal. Additionally the diffuser will also have to be designed in conjunction with the stators. From the probe and performance tests it would appear that the diffuser is sensitive to inlet swirl, which will have to be taken into consideration when designing the stators.

No problems appeared with the sealing of the rotating shroud. The only evidence it left was the rotating boundary layer on the casing of the core fan. A small amount of leakage would even assist the outer fan, by sucking away the boundary layer from the outer fan.

CHAPTER 3

FAN PERFORMANCE MAPPING

Thus far, all the tests conducted had the fan operating at one specific operating point close to its designed operating conditions. The design of the CIRSTEL tail boom was such that the resistance against which both fans have to work is constant throughout the flight envelope, the idea being to prevent the fan of having to run up and down its performance curve, as this could lead to the directional control reaction lagging behind the control inputs. Despite the fixed operating point, testing of the performance of the fan at different extremes of its capabilities was still required, to determine the overall range and limitations of the fan.

The performance range tests were conducted to determine the pressure and power curves up to the fan stalling point and to obtain an indication of the fan operating capability and range. These tests were repeated several times, each time with a different inlet guide vane setting. Here the aim was to investigate the fan's off-load performance in more detail, this time by taking measurements at three different IGV settings. A performance curve was also plotted with the vanes set for an overloaded condition. Another test objective was to establish a measure of how much each fan section influences the other at different throttle settings in terms of mass flows and pressures. Power reduction and control of the fan by means of deflecting the IGVs were some of the possibilities being considered. The power map gave a good indication of the extent to which this could be achieved and how the IGVs have to be designed to gain the desired effects.

Test Set-up

During the performance mapping tests only static pressure, mass flow and power readings were taken. No other data, such as velocity profiles, were recorded. The test rig was not altered from the previous velocity profile measurement experiments. Throttling of the core fan section was achieved by the standard throttle plate fixed at the end of the core duct. The throttle plate assembly included a diffuser that allowed the fan exit pressure to be lower than atmospheric conditions when set at the fully open position. The outer fan was throttled with the previously calibrated and adjustable orifices. Mass flows were again determined with the orifices and the inlet bell-mouth for outer and total mass flows, respectively.

MATLAB software was developed to automatically sample the pressures from eight different stations spread between the inlet, outlets and both fan sections (See Figure A.3, Appendix A). A single pressure transducer was used together with a switching box that allowed switching between the individual sampling points. The switching box was driven by the sampling software, which at the same time took torque and fan speed readings to compute the delivered power.

Performance Curves of the Original Fan

Two separate performance maps were plotted, one for each fan section. While the one section was throttled to test its performance curve, the other section was left at its operational setting. By continuing to take measurements in the "static" section, the effect that the two sections have on each other while at off-design conditions could be quantified. No total pressures were measured during the performance tests. Thus the performance curves plot the casing static pressure versus mass flow.

Outer Fan

The most interesting and important results are the performance curves of the critical outer fan. The curves of static pressure rise versus mass flow, taken for the outer fan, are presented in Figure 3.1. The pressures shown are the static pressures behind the diffuser of the outer fan (Station 8, Appendix A).

The outer fan had a very distinct and sudden stalling point on each speed line as can be seen from the curves in Figure 3.1. The points named OP are the operating points and indicate the points at the design setting of the fan. It can be seen that the operating point for each resistance curve was relatively close to the stalling point.

The performance lines are moved up or down along the fan resistance lines by deflecting the inlet guide vanes. In the unloaded condition the lines are moved to the bottom left, while in the loaded condition they are moved upward and to the right. Deflecting the IGVs to give a negative pre-swirl, resulted in both a pressure and mass flow drop, as desired, to conserve power. At the maximum negative IGV deflection of -40^{o}, the pressure rise decreased from the operating condition by 29.9% and the mass flow by 14.9%. A 5^{o} over loaded setting did not move the stall point any closer to the operating point, so the fan could still be safely operated in an over loaded condition for manoeuvring and emergencies.

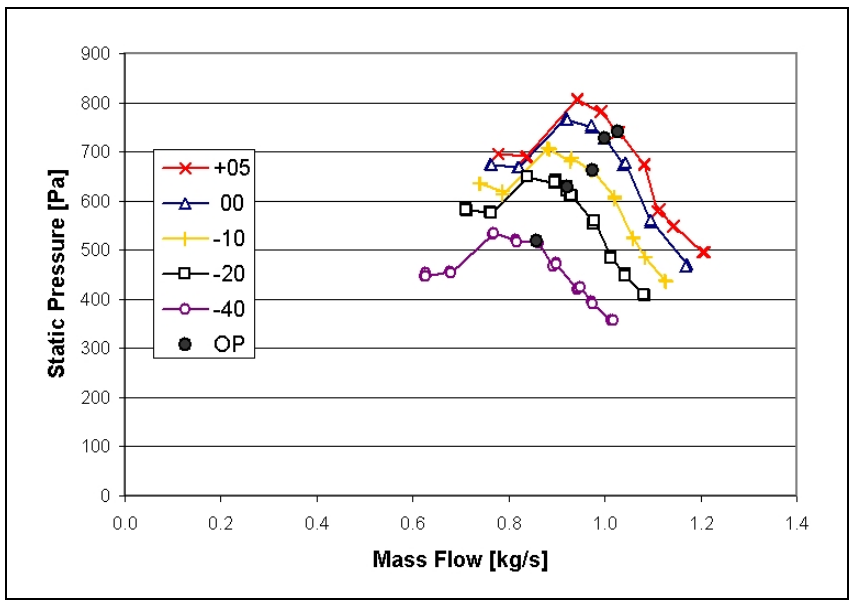

Figure 3.1 Outer fan performance curves for different IGV angles

Despite the suggestions of the previous experiments that good isolation exists between the two fan sections due to the rotating shroud, the coupling between the two sections was not conclusively determined. When throttling the core section, the inlet velocity profile would be distorted and this would have some effect on the outer fan section. This effect might be most severe when the core section is stalled.

Figure 3.2 shows the percent changes in mass flow and static pressure rise from the normal operating conditions. At small deflections of the inlet guide vanes, the variations in the outer section that result from the core fan throttling are small, less than 5% in either direction. Only at larger IGV deflections, from -20^{o}, a coupling effect is noticeable, the biggest effect being noticed with the -40^{o} test case, which is however not detrimental. Mass flow and pressure rise increase

from the normal as the core fan is throttled, because now more air is forced into the outer section. Only when the core fan is stalled does the pressure drop by more than 10%. For most of the time, the outer fan remained very close to its required operating condition. Generally, the variations followed a sloped line through the origin, indicating a definite trend. The coupling of the sections is however negligibly small and the core fan section could be safely run at a different setting without severely affecting the outer section.

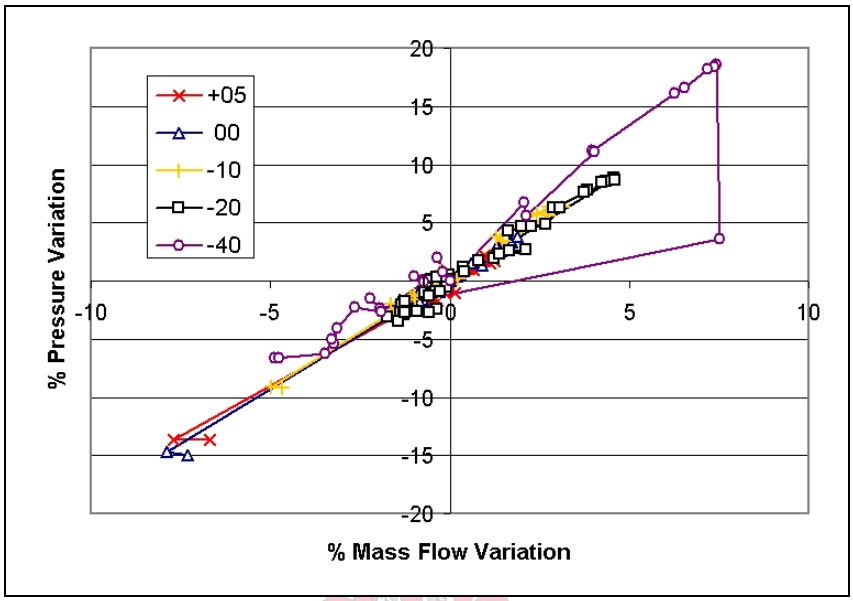

Figure 3.2 Variations in the outer section when the core fan is throttled for each setting of the IGVs

Core Fan

The fan core section is not as highly loaded as the outer section, but its performance characteristics are still important, as this section of the fan is used for directional control and the cooling of the exhaust gases. The pressures used in the performance plots that follow are those of Station 7 (See Appendix A), behind the core stator vanes.

Here again the points named OP in Figure 3.3 is the operating points of the fan core section. The operating points were far from the stall points, so there is still a safety margin should the operating conditions change in this section. This section should thus be able to handle a variety of conditions, such as the distorted inflow as a result of the airflow around the fuselage. Curious to note are the irregular positions of the stall points for each IGV setting. For small deflections of the guide vanes around the zero setting, the stall point remains on the same resistance line. When deflecting the guide vanes more there is a definite drop in the stall margin of the fan. Tufting experiments indicated the IGVs to be stalled at bigger deflections (below-10^{o}). The losses through the inlet guide vanes then became significant, which lowered the inlet total and static pressures. This resulted in the fan stalling earlier, relative to the normal stalling margin.

The stalled inlet guide vanes added less pre-swirl to the flow than intended and thus the fan was not unloaded as much as expected with the un-stalled IGVs. This effect can clearly be seen with the curves from the -10^{o} and -20^{o} settings, and hence also the jump of the operating line. The two curves lie on top of each other, only the stall points differ for reasons already mentioned. The swirl added to the flow from the stalled guide vane was the same as for the attached flow case resulting

in the same curve. The losses through the IGV row caused the drop in pressure on the -20° setting relative the -10° setting on the operating line.

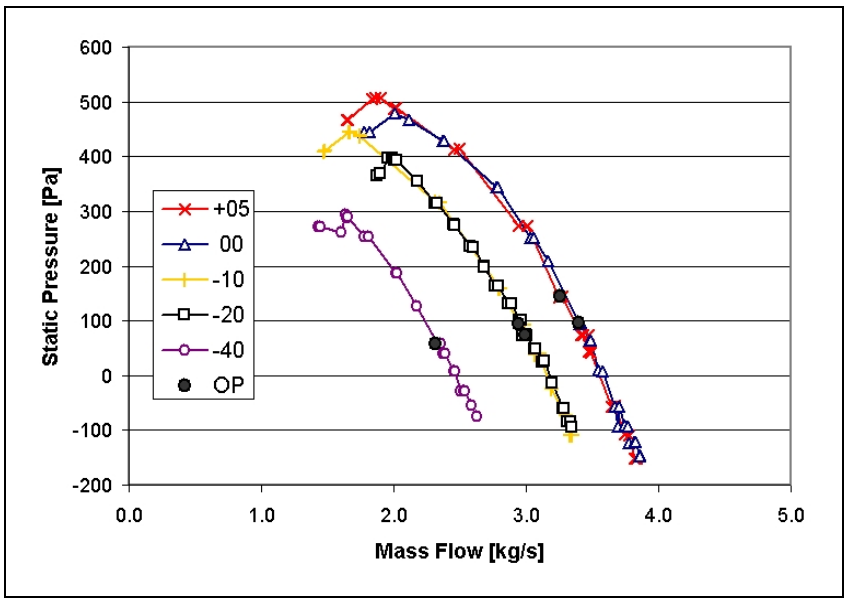

Figure 3.3 Core fan performance curves for different IGV angles

Pressure and mass flow reduced by 39.4% and 31.8% respectively at the maximum negative IGV deflection angle. Although the guide vanes appear to be working more effectively again at very high deflection angles, more carefully designed guide vanes would work better in reducing the core fan's power consumption. Controlling the fan by means of the IGVs in their current configuration will also be difficult, as can be seen with the –10°/-20° case. There is an ambiguity in the setting of the vanes and their effect around this area of the fan envelope. This can cause difficulties with the fan control system, or cause instabilities in the entire CIRSTEL system.

The effect of the outer fan section on the core fan was also monitored when being run up and down a performance line. Figure 3.4 plots the measured data. As can be seen here the changes never exceed 5% for either pressure or mass flow. These small changes are not surprising as the mass flow fraction of the outer section is small and will thus only have a limited effect on the core fan, even in the stalled condition. In addition, no trend is visible in the changes; the points centre themselves around the zero point.

Power

Another performance parameter that was charted during the tests was the overall power demand. During these measurements one section was throttled while the other section was held at a constant setting. The curves are shown in Figure 3.5 for the throttled outer section and in Figure 3.6 for the core section throttled, both plotted against the total mass flow of both sections. From these figures it can be seen by how much the power can be reduced in each section with adjustment of the inlet guide vanes.

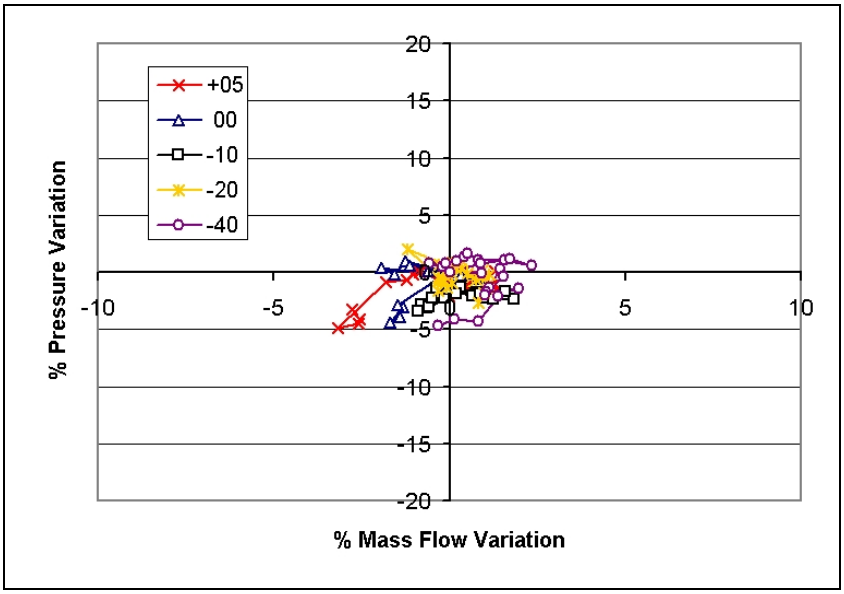

Figure 3.4 Changes in the core section when the outer fan is throttled

There was a visible difference between the –10° and –20° power lines. However, the difference between them was not as much as between the other test cases, owing to the stalled inlet guide vanes. The power difference between the two lines on the operating line was about 177 W, or 8% of the operating power. This was less than for other test cases where the difference in IGV deflection angle was the same. Success had been achieved in reducing the power consumption of the fan by adding pre-swirl to the flow with inlet guide vanes. At the maximum deflection of –40° the shaft power is reduced by 30%. The design of the guide vanes is however not refined enough to allow for effective and reliable operation to consistently bring the power down. More turn down would also be possible if the stators are more effective in the outer section.

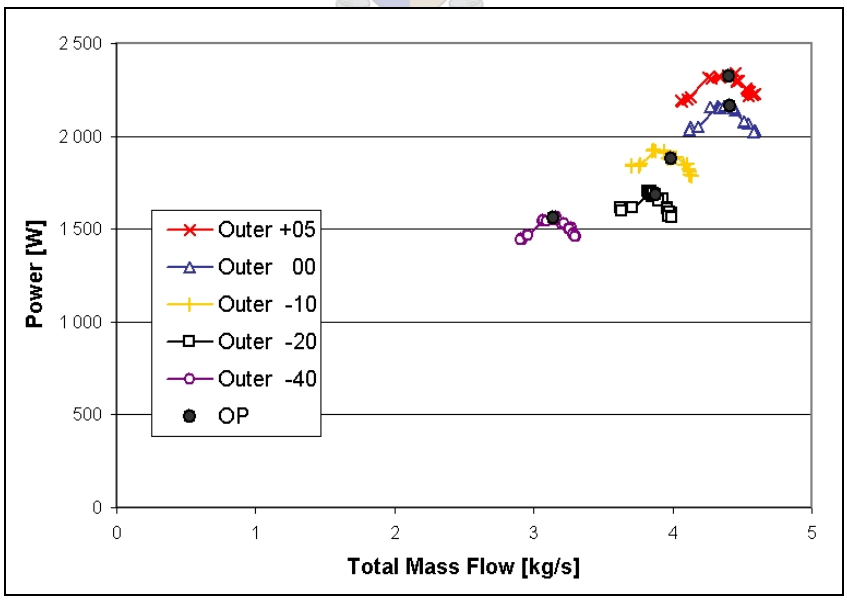

Figure 3.5 Total power chart of the fan for a range of IGV settings while throttling the outer section

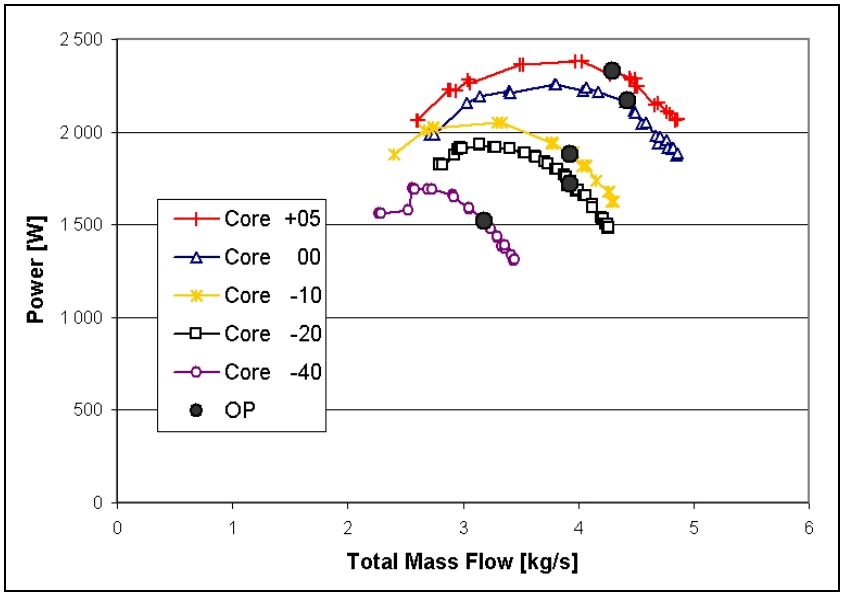

Figure 3.6 Total power chart of the fan for a range of IGV settings while throttling the core section

Performance of the Modified Fan

Similarly to the tests done on the original model, performance curves were established for the fan with the modified stators. Only the performance curves for an IGV angle of 0^o were plotted and compared to the corresponding performance curves of the original fan version.

Outer Fan

Directly comparing the performance curves taken behind the diffuser (Figure 3.7) shows the reduced performance of the modified fan compared to the original design. From the operating point of about 1kg/s to the stall point the pressure rise is less than for the original set up. This prompted an analysis of the pressure data at the stator exit (Figure 3.8). This data showed that the new performance curve generally lies above the original curve. Near the design point the increase in static pressure is only marginal, though noticeable at higher mass flows. At pressures just above the design point the new curve dips slightly below the original curve. Also apparent is the higher stall margin the fan displayed with the new stators. After stalling the fan curve now dropped off smoothly, unlike the sharp drop experienced previously. The lower static pressure at the diffuser exit also confirms the loss in diffuser performance previously mentioned in Chapter 2.

Core Fan

No diffuser was fitted to the core section, thus measurements were only made behind the stators. From Figure 3.9 it is evident that the static pressure recovery with the modified core stators was less than with the sheet metal stators for the same mass flow. This was already shown with the five-hole-probe measurements. Even though the modified fan curve was positioned below the original curve, the stall point was significantly higher.

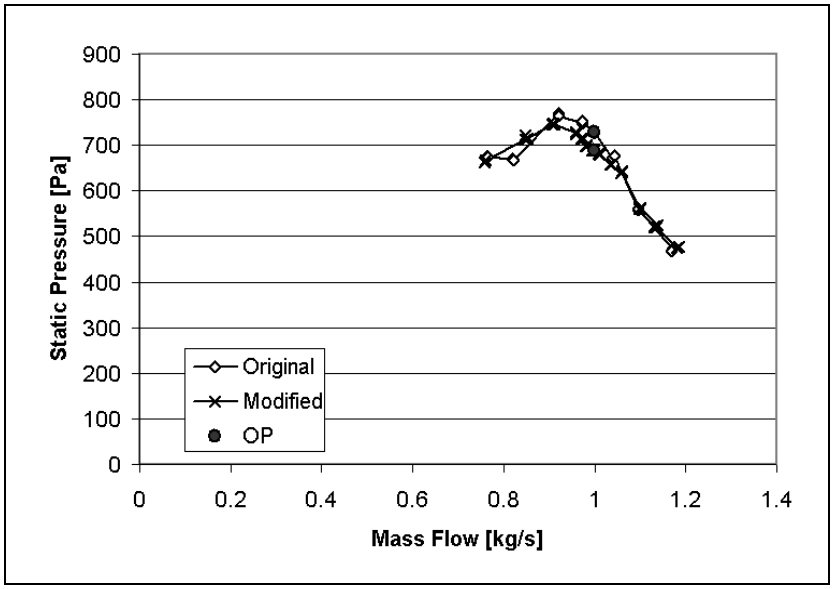

Figure 3.7 Performance curve for the outer section when measured behind the outer diffuser

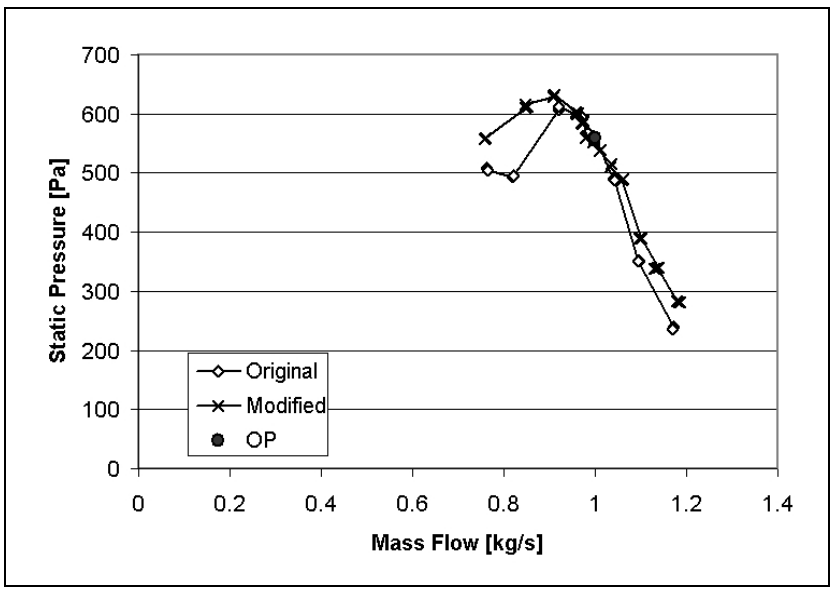

Figure 3.8 Performance curve for the outer section when measured behind the stator row

Scaling

The distorted scaling of the demonstrator makes it problematical to obtain a properly scaled estimate of the power requirement, because only the total power reading could be taken. As shown in the previous chapter, using the standard scaling laws underestimates the power requirement by about 2%, which is not a significant difference. Thus the standard scaling laws could be used to get a good enough estimate of the overall power demand.

Figure 3.10 shows the power curves scaled from the data measured during the performance tests. The scaling parameters used here were the design density of 0.963 kg/m^3, fan outer diameter of 0.666m and fan speed of 4050 rev/min.

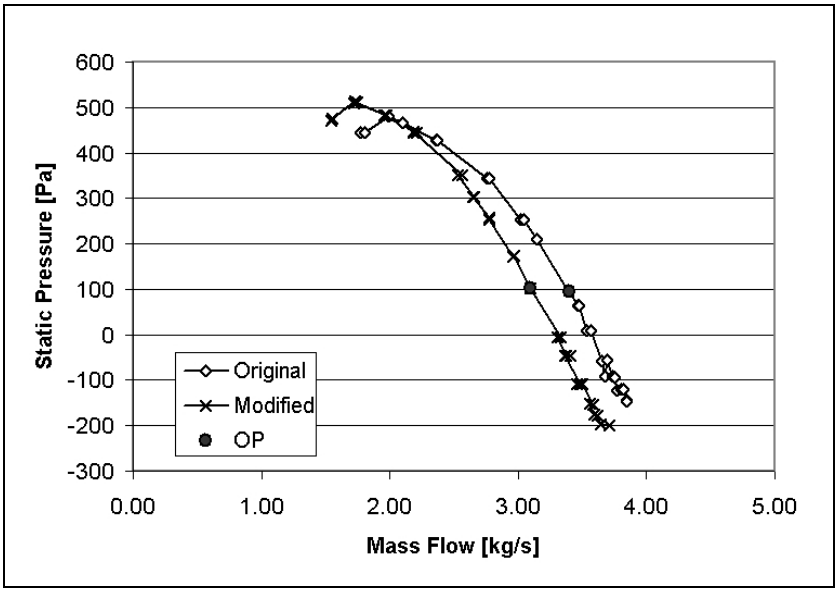

Figure 3.9 Core section performance curve

From the figure it becomes clear that the fan reaches the 40 kW limit only in the overloaded condition, and then only at a higher throttle setting than the design point. At the design operating point the fan requires about 36 kW. This includes losses like the bearing friction and shroud losses, and hence this value is slightly higher than the Euler power stated in the previous chapter. Adding 2% to compensate for the distorted scaling, this value increases to 36.7 kW, which is still less than the quoted power limit. On maximum turndown the shaft power reduces to 26 kW, or 26.5 kW when compensating for scale effects. Table 3.1 lists the power demand and mass flows for the five tested inlet guide vane settings using the standard scaling laws only at the design throttle setting.

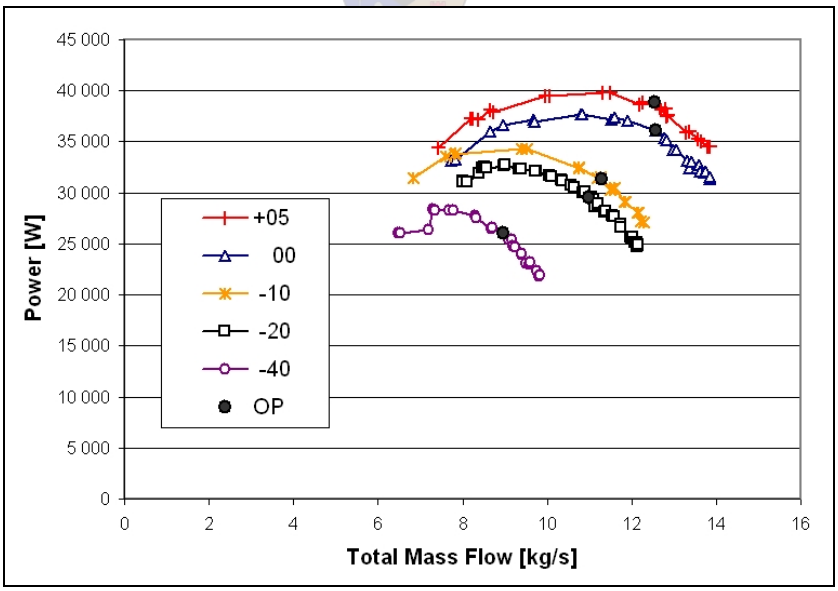

Figure 3.10 Scaled power curves for the fan when throttling the core section, using standard scaling laws

Table 3.1 Scaled mass flows and power demand

IGV setting	Outer Mass Flow [kg/s]	Core Mass Flow [kg/s]	Power [W]
5^o	2.93	9.62	38 838
0^o	2.85	9.73	36 113
-10^o	2.77	8.51	31 373
-20^o	2.66	8.33	28 111
-40^o	2.44	6.51	26 046

Fan Performance Relating to Flight Envelope

The operational phase in which there is the highest reliance on the fan is in hover and low speed flight, until enough directional stability is supplied by the vertical stabilisers. In low speed flight the Coanda effect on the tail boom is the most effective and hence it is here that the outer fan section has to work at its design point. In the survey by Fonternel et al.[9] it was noted that from the tests conducted by Hughes on the OH-6A helicopter fitted with the first NOTAR system, the circulation control effect reduced to zero at forward speeds higher than 25.8 m/s. This reduction in lift was attributed to the reduction of the rotor downwash over the tail boom, as well as the movement of the downwash off the tail boom, with the increase of forward flight speed.

It is still uncertain to what extent this effect is present with CIRSTEL, but it can be assumed that the lift reduces similarly with increasing flight speed. Thus while flying at higher speeds power could be saved by unloading the fan, or at least the outer section. When operating at design conditions the outer section of the fan consumes about 42% of the total fan power. By reducing the power demand of only the outer section in forward flight with the IGVs, the total power demand will drop noticeably. The tail thruster is used for pilot applied directional control throughout the entire flight envelope. This thruster is to be fed by the core fan air and turbine exhaust gas mixture and thus air from the core section has to be continuously supplied, not only for directional control, but also to cool the exhaust gases. At the higher flight speeds, mass and pressures could be reduced slightly because some directional control is gained from the vertical stabilisers, but mass flow quantities must remain high enough to sufficiently cool the exhaust gases.

Conclusion

Through these performance tests an idea was obtained of the behaviour of the fan over a wide range of conditions and how close the operating requirements are to the limits of each fan section.

One point that became apparent from the tests was the sudden and distinct stalling point of both sections of the fan when fitted with the original sheet metal stators As already discussed the blades could stall suddenly due to their sharp leading edges. During high throttle settings the stators would stall abruptly; the distorted flow field would then also cause the rotor to stall, thus causing the drop in pressure and mass flow. These stators however appeared to work well in their un-stalled condition. From a performance point of view the sudden stalling point it is undesirable as no warning of the impending stall is given, as it would have been if the curve first flattened off before the stall point. When the core section stalled a significant performance change could be detected in the outer section, but otherwise the two sections remained largely uncoupled.

When scaling the power consumption and compensating for the distorted scaling, the total power demand remained less than the power limit of 40 kW set in the design specifications. A significant power turndown of 28% could be achieved by deflecting the IGV blades. The power reduction in the outer section, where most of the power is to be saved, was not effectively achieved due to the low solidity of the IGVs at the outer section. If the IGVs are to be effectively used, a more refined design has to be implemented.

In general the performance of the fan did not improve significantly with the new stators fitted. The stalling characteristics however improved in that the stall was more gradual than previously and the stall margin for both sections also increased. Volume flow and pressure rise in the critical outer section also improved, however the design targets were still not met, primarily due to the low diffuser performance. The outer section efficiency decreased with the new stators due the loss in diffuser performance, but the design efficiency was still exceeded.

The core section did not gain much from the new stators. The exit static pressure decreased and a lower mass flow was measured, though the total pressure did increase as shown by the five-hole-probe measurements. Mass flows in the core section remained consistently lower and thus the new performance curve for the core section was positioned below the original curve.

CHAPTER 4

FAN DESIGN RECOMMENDATIONS

In the previous two chapters the tests done on the two-stream-fan demonstrator were described, and based on these results performance estimations were made. This was the first two-stream-fan to be built and tested. During the course of this project a first design modification was implemented on the fan by installing redesigned stator blades behind the rotor. From the measured changes in performance, and the fan characteristics determined from the experiments, design guidelines can be set up to assist in designing a future fan.

Outer Section

For the current application the outer section forms a thin annulus around the core section perimeter. The width of the outer section annulus is determined from the required mass flow through each section. In the design of the demonstrator it was assumed that the inlet velocity profile is uniform, and no blockage was considered. As has been shown from the five-hole-probe measurements, some blockage exists due to boundary layer growth, and it is in this boundary layer that the outer fan operates. Over the entire inlet to the fan the blockage was 6.8%, but when considering only the outer section the same blockage increased to 25%. Because the outer fan section has a relatively high inner-to-outer radius ratio the outer wall boundary layer blockage at its inlet causes a large reduction in the effective flow area for this section of the fan. As will be shown in the following chapters, practical intakes that would be fitted to the helicopter can result in even higher blockage on the outer perimeter. This is an important effect that has to be considered in the design of the outer section,

Rotor Design

Points that should be considered when designing the outer section rotor are as follows. Due to the non-uniform inlet velocity and total pressure distribution that can be expected ahead of the rotor it is advisable to position the shroud at a smaller radius than calculated with the assumption of uniform inlet profiles. The exact value that the shroud radius is to be reduced must be determined from the expected flow and pressure conditions at the fan face of the intake. Reducing the shroud radius will allow a higher volume flow through the outer section and will include more of the higher total pressure inlet flow. Another advantage of repositioning the shroud is that the outer blade length is increased, and thus losses associated with very low aspect ratio blades can be reduced.

The blade loading on the current demonstrator was high, due to the high pressure rise required. As a result the blades operate relatively close to their stalling point, and the inlet distortion will only reduce the stall margin more. Thus enough of a stall margin will have to be provided in this critical section. An advantage here is that the fan intakes can be designed in conjunction with the fan itself, thus the fan can be adapted to the limitations of a practical intake that is to be fitted to the helicopter.

Currently the number of blades in the outer section of the demonstrator is double the number of blades in the core fan; the number was limited on the grounds of structural considerations. The blade loading thus increased to almost the practical limit of a diffusion factor of D = 0.5. It is possible to design effective blades with a high loading as described by Wennerstrom[10], but another option would be to fit three outer blades for each inner blade instead of two, to reduce the

outer blade loading. This would also allow the increase of the blade aspect ratio to improve blade efficiency.

Fitting three sets of blades does require a detailed structural analysis. Investigations have to be done to determine if the shroud can support the extra blade without serious deflections. However, at the same time the extra blade can stiffen the shroud by increasing the shroud's moment of inertia.

Stator Design

Due to the high pressure rise required, the swirl angle leaving the rotor is in the region of 40^{o}. The stators now have to turn this flow into the axial direction before it enters the diffuser. From a weight perspective it would be desirable to have a single stage fan. Thus the stators have to turn the flow axially again. A two-stage fan will compress the flow incrementally, and thus the stators are not required to turn the flow through such large angles. But from the preceding discussion it was shown that the stators could stall easily. The stator design thus has to be considered carefully. Also the diffuser performance is directly dependent on the stator performance due to the amount of swirl entering the diffuser.

It is now suggested to use a double set of stators that work in tandem, either as a slotted flap arrangement or as a double set working on their own. With this design more slender blades can be used, unlike the low aspect ratio currently installed in the demonstrator. Added to this is a considerable weight saving. Other design concepts, such as insertion of splitter plates, can also be considered.

Diffuser Design

It has also been shown that the diffuser is sensitive to inlet swirl. Careful consideration is required in the design of the diffuser, also in conjunction with the stators. Something that has up to this point not been simulated, but must be included in the design is the duct from the engine, to transport the exhaust gases to the core section, which ducts diagonally through the diffuser. From the foregone experiments it would appear that the inlet swirl could be an advantage, but this effect was not quantified. The presence of the exhaust duct could however seriously impair the diffuser, whether swirl is present or not, unless the design is carefully considered. It is not clear how much swirl can be allowed at the exit of the diffuser before the performance of the Coanda slots is impaired. It could be of advantage if the intended exit swirl is in the direction of the tail boom circulation, so that the air enters the Coanda slots without a major change in direction. In the current application of CIRSTEL the fan turns in the required direction, so this option of using the exit swirl to reduce losses through the Coanda slots can be considered.

Core Section

The core fan is a vital, yet less critical, part of the system. Air from the core fan is used for directional control by means of clamshell valves located at the end of the tail boom, as well as to cool the engine exhaust gases.

Rotor Design

The design of the core section is quite straightforward, due to the lower load on this section. Points that do however have to be considered are the inlet distortion and stall margin. With practical intakes some inlet distortion will be present, thus a sufficient stall margin should be allowed.

The core section draws the most power, so a high efficiency is required. A high efficiency can be obtained, as has been shown, due to the shroud that splits the incoming air and thus the fan is not

subjected to blockage effects and blade tip clearance losses. However, the fan efficiency is also subject to the performance of the shroud seal.

Stator and Diffuser Design

The core stators do not have to work as hard as in the outer section, so their design is also straightforward. Exit swirl is subject to the diffuser and daisy-mixer downstream. Any exit swirl would result in more losses when the air flows past the mixer, if the mixer retains its current geometry. Thus as little swirl as possible should remain behind the stators. The design of the mixer might however also be changed to take advantage of exit swirl, which can be used to mix the exhaust gases with the fan air. Spatial constraints due to the daisy-mixer might require a dump diffuser to be fitted behind the hub.

Inlet Guide vanes

A set of inlet guide vanes was fitted to the fan. The addition of IGVs was a means of controlling the fan, primarily to reduce power consumption. During some phases of the flight profile, such as in forward flight, the demand on the fan is not high. In the forward flight for example directional control and stability can slowly be transferred from the tail boom to the vertical tail fins. The effectiveness of the Coanda effect also reduces, and thus the outer section of the fan is not required in forward flight. By shutting off the outer section significant power savings can be achieved. The core fan section however still requires a considerable through-flow to cool the exhaust gases. One way of achieving a power reduction while still allowing the core fan to pump air, is by means of inlet guide vanes.

It was shown experimentally how the IGVs reduce the power consumption of the fan and their effects on the mass flow through each section. In these tests inlet guide vane blades were used with a constant chord, thus the blade solidity reduced towards the casing. As a result not enough turning was obtained on the outer section where the power was to be saved. What would thus be required are inlet guide vanes that provide a significant amount of turning in the outer annulus while only slightly providing turn down for the core section. One more concept that that could be considered is a set of independently adjustable IGVs for the inner and outer section. In general the core section should not be unloaded by much, but the fan intake design discussed in the following sections provides a significant total pressure rise at forward flight speeds.

Structural Design

The current demonstrator structural design was based on simplified calculations using point masses and beam theory. A basic FEM analysis of the rotor has since been conducted, the results showing the shroud to be stiffer than anticipated and the stresses in the rotor being below the yield point at a fan speed of 4050 rev/min. Here are some points that have to be considered on the structural side of the design:

Rotor

Regardless of whether one or two extra sets of blades are used for the outer rotor, a detailed structural analysis is required to assess the structural properties of the rotor. FEM solutions will aid in the material selection for the rotor; possible materials are aluminium or carbon fibre composites. The demonstrator fan was machined from a single block of aluminium, which was an efficient solution for a once-off product. It also proved to be structurally sound. For further production it is however advised to use composites in the production of the fan, as it would be easier to produce, structurally better suited and less prone to catastrophic structural failure if damaged.

It should also be investigated what the optimum position is of the outer blades relative to the core blades. Aerodynamically there is no effect due to the relative position of the blades, so the positioning is purely due to structural constraints. The thickness of the shroud should also be optimised, but it must be noted that the shroud must extend forward and backward of the blades. The leading edge of the shroud must be shaped to allow for effective splitting of the incoming air, while the trailing edge has to form part of some form of seal.

Stator

The stators, apart from their aerodynamic function, also have to support the bearing at one end of the fan drive shaft. Added to that the stators will most probably have to form part of the tail boom carrying structure. Due to the Coanda slots that split the outer shell of the tail boom and thus weaken the structure, it would be advisable to have the inner duct carry the tail boom loads. A logical point this duct can be fixed to would be the stator blades and hence structural integrity would be required of the stators.

Seal design

This is an important part of the fan. An insufficiently performing seal can seriously impair the efficiency of each of the fan sections. For example the leaking seal would allow air from the high-pressure side to the core section, thus reducing the mass flow in the outer section and possibly causing extra blockage in the core section. Some small amount of seal leakage can howeveraid the outer fan, by sucking away the boundary layer and this should not impair the core section.

The current seal fitted to the demonstrator was formed by simply tapering the trailing edge of the rotating shroud to a sharp edge. This edge ran close to the stationary part of the shroud, thus forming a gap small enough to prevent air from turning around the sharp trailing edge to enter the core section. This seal performed sufficiently, but should it be required to use a different design, it is important to ensure that no rubbing between the two seal sections takes place. Any rubbing will increase the torque considerably, because of the large radius of the shroud. For some alternative seal concepts see Heise[6].

General Comments

The fan for this application calls for a high efficiency design, due to the obvious power limitations. For this reason it was decided to increase the flow area of the fan by as much as possible, when compared to the first fan fitted to CIRSTEL, to reduce the through flow velocity. By reducing the hub-tip ratio of the fan the flow area was increased, and thus a lower velocity was obtained. The reduced velocity would then reduce the incurred losses. Also the design shaft speed was reduced to reduce blade losses and fan power demand. Additionally, mechanical advantages were gained from a lower speed.

Aerodynamically the two sections can be designed separately; the shroud effectively isolates the two sections. Even during off-design conditions the effect the sections had on each other was minimal, as shown by the experiments. Some consideration has to be given to the conditions upstream of each section, such as the presence of IGVs and velocity profiles.

Finally a control strategy has to be detailed. This would mainly concentrate on the adjustment of the IGVs in flight to adapt to the current flight conditions for power savings. It must also be considered whether overloaded conditions should be allowed, and when, and the IGV role during manoeuvring.

CHAPTER 5

CIRSTEL SYSTEM MODELLING AND OPTIMISATION

This chapter details the development and results of a one-dimensional numerical model to simulate CIRSTEL equipped helicopters in hover. The model was used to perform a simple numerical optimisation of the system, with the objective of minimising the power requirement of the system. The model can be adapted to optimise other performance parameters such as the thruster exhaust temperature. Total pressures required for the system from the twin-flow-fan were the main variables used in the optimisation process. Secondary variables were the geometric dimensions of the tail boom. Previously the analysis methods used for the system did not allow for a numerical optimisation routine; also the effect the tail boom had on the engines has previously not been considered in sufficient detail. The current model thus incorporates an engine model to check and define parameters that minimise any effects the system may have on the engine. Two case studies were completed with the model, namely on a single- and twin-engine light helicopter of similar size. The results from this chapter flow into the design and analysis of the intakes discussed in Chapter 9.

The Numerical Model

The CIRSTEL tail boom system consists of 5 main components as shown in Figure 5.1; the outer Circulation Control Tail Boom section (CCTB), the core section with the mixer/nozzle, tail thruster, a fan and finally the helicopter engine, as this forms an integral part of the system. The twin flow fan supplies air to both the core and outer section circulation control section. The CCTB has two Coanda slots through which the air vents to set up a circulation around the tail boom in the presence of the main rotor downwash. In the core section the engine exhaust gases are mixed with fresh air supplied by the fan and exit the tail boom via the tail thruster. The model simulates each of the components individually, and then inter-links the individual component parameters to give the global performance of the tail boom. Figure 5.2 is a flowchart of the numerical model showing the structure and flow of the parameters between the different components of the system. The shaded fields in the figure are the main optimisation variables, while the double-framed parameters present the required global tail boom performance solutions. To close the solution it is also required to balance the main rotor torque with that generated by the tail boom, as well as ensuring the power demand of the rotor and fan can be met by the engine output. Refer also to Appendix C, where a detailed sample calculation of the system calculation and optimisation procedure is given.

1. Main Rotor

Added to the model of the five components is a routine that models the helicopter main rotor and conventional tail rotor performance. The tail rotor is simulated for comparison purposes to evaluate the tail boom relative to an equivalent tail rotor

The main rotor is modelled using a suitably modified momentum theory to include the effects of a finite number of blades and tip losses. The required thrust can be increased by a small amount to compensate for the extra downwash induced drag on the fuselage. To account for a non-uniform induced velocity and tip losses an empirically determined correction factor of $\kappa = 1.18$ is used to modify the average downwash velocity, as described by Seddon[11]. For the rotor blades NACA 0012 blade profile (Riegels[12]) data was used when calculating the power required to overcome blade drag. In none of the consulted literature is the total downwash velocity of $(V_c + v_i)$ used to

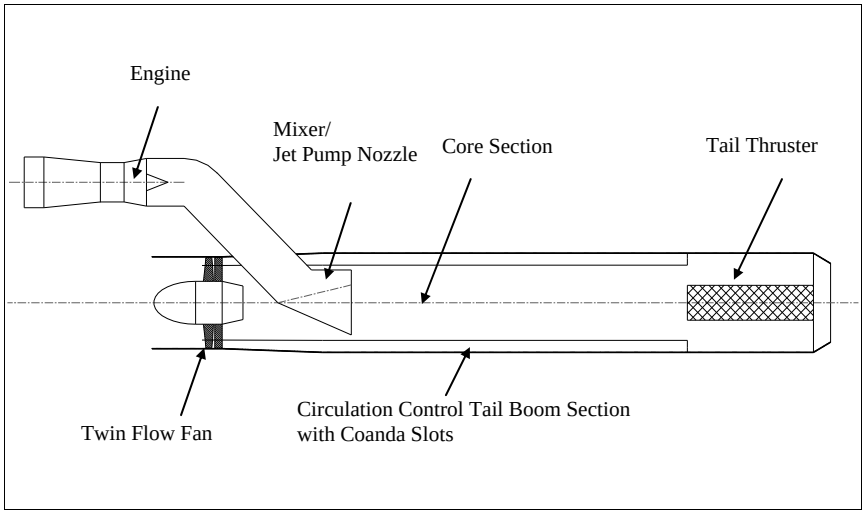

Figure 5.1 Schematic of the CIRSTEL tail boom

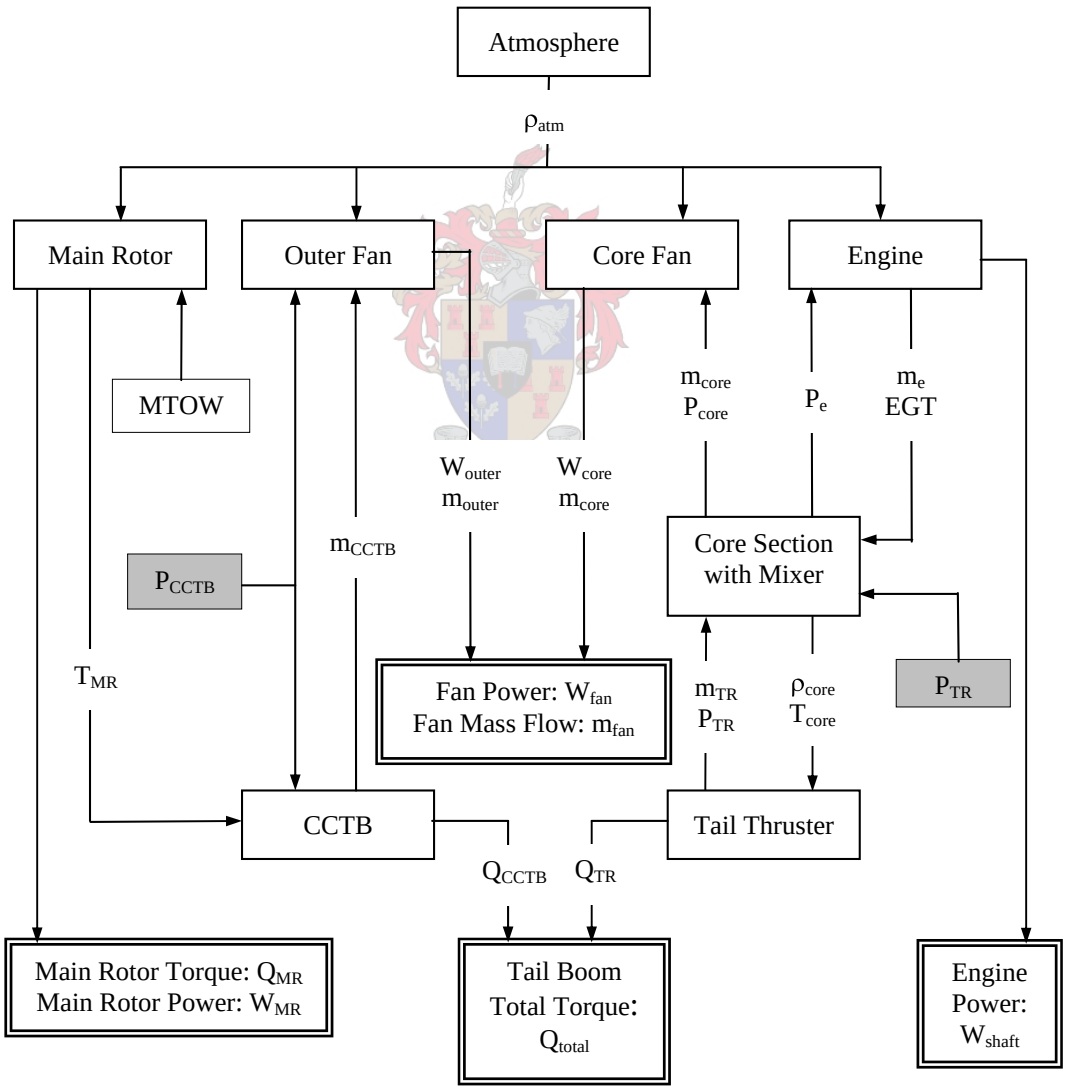

Figure 5.2 Flowchart of the numerical model for the CIRSTEL tail boom

predict the profile drag; generally the climb and induced velocities are ignored. For the current application a new equation is derived. Starting with the incremental power of a blade section,

$$dW_D = \frac{1}{2}\rho C_D V^3 c dr \qquad (5.1)$$

the equation can be integrated for the whole blade length and number of blades to give, after some simplification (for more details see Appendix C):

$$W_D = \frac{1}{8}\rho C_D A_B \left(V_t^2 + \left(V_c + v_i\right)^2\right)^{\frac{3}{2}} \qquad (5.2)$$

Gessow et al.[13] do state that the commonly used equation is limited to hover and low-speed climb. Equation 5.2 however provides better answers when compared to published performance data of helicopters. From the calculated power the amount of torque acting on the fuselage is determined, and the performance of an accompanying conventional tail rotor can be determined using the same momentum theory

2. Engine

To date the engine has never been completely included in any analysis of the CIRSTEL system (Lippert et al.[14]). As an integral part of the system the modelling of the engine is critical to monitor the effects on the engine caused by the tail boom, primarily as the turbine backpressure can change with the design of the mixer. By increasing the backpressure on the turbine the surge margin is reduced, and a reduction in delivered power will occur as well. The current model allows for the design to be optimised such that the backpressure on the engine is reduced to zero.

The engine is modelled as a single shaft, constant speed engine with a diffuser after the turbine. The exit area of the diffuser is the same as that of the mixer and is thus one of the design and optimisation parameters. Since the engine is a constant speed unit the volume flow through the engine is constant. Hence the mass flow can be determined from the ambient atmospheric conditions once a mass flow is known at given atmospheric conditions. The standard thermodynamic relationships for the compressor and turbine are used, with the combustor exit total temperature fixed at a specified 1100K for this study. A pressure ratio for the compressor is determined for the selected engine along with the section efficiencies.

The engine is tied into the rest of the tail boom by the value of the static pressure at the exit of the diffuser/mixer, which is the static pressure in the core section of the boom. For the turbine performance the diffuser exit dynamic pressure can be determined from the known mass flow, density, exit area and diffuser efficiency, which then together with the static pressure gives the exit total pressure of the engine. A problem arises in determining the exhaust density, which again is dependent on the static pressure in the tail boom and thus forming a circular reference. To circumvent this problem an exit density is guessed with which the calculations are continued. In the solving phase of the program the error between the guess and calculated value is then kept zero by changing the guessed density.

Finally the engine power output is determined, and modified to include gearbox losses. The shaft power available is then compared to the total demand from main rotor and fan and the gearbox rating. If required the total takeoff weight can be modified to keep within the limits of the engine and gearbox.

3. Core Section with Mixer

The core section with its mixer where the engine exhaust gases are injected is essentially a jet pump. This effectively unloads the fan if carefully designed and thus allows an effective power reduction mechanism over conventional systems. A control volume momentum analysis is used to set up a quasi one-dimensional model of the mixer and duct. To make the equations useful for the design of the current tail boom, they were derived such that the entry and exit streams can have different densities and the total pressures of each stream can be specified. Total pressures are used in the equations as the total pressures in the sections of the tail boom drive the solution.

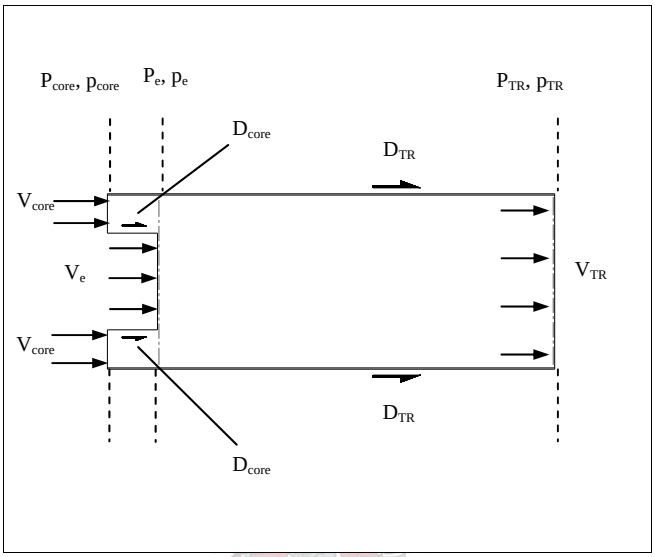

Figure 5.3 Control volume for the core section

Figure 5.3 shows the control volume of the core section for purposes of the momentum analysis. The duct has a constant diameter, thus the mixer exit opening occupies a fraction n of the cross-sectional area A, with the fan duct area being (1-n)A. The sum of forces on the control volume can then be written as

$$\begin{aligned}\sum F &= D_{TR} + D_{core} + D_e + Ap_{TR} - nAp_e - (1-n)Ap_{core} \\ &= \dot{m}_{core} V_{core} + \dot{m}_e V_e - \dot{m}_{TR} V_{TR}\end{aligned} \qquad (5.3)$$

At the entrance and exit to the control volume the streams will exhibit some momentum deficiencies due to wall friction and form drag. These are accounted for in the D_x terms and take the form of

$$\begin{aligned}D_x &= f_x \rho_x V_x^{\,2} A \\ &= f_x \dot{m}_x V_x\end{aligned} \qquad (5.4)$$

Here the loss factor f is equivalent to half the drag coefficient based on the cross-sectional area of the flow. The losses in the duct that are accounted for in the D_{TR} term are effectively duct friction losses and are calculated using pipe flow theory. The duct loss calculation used here is an approximation, as the flow patterns in the core section will be more complicated than the fully developed flow on which the theory is based. A more accurate solution will require a more detailed study of the three-dimensional flow pattern. The loss coefficient associated with the engine air is estimated to be $f_e = 0.05$ for a 95% diffuser efficiency. From Hoerner[15] the drag coefficient of the

mixer is estimated to be $C_D = 0.2$ which would make $f_{core} = 0.1$. This value was later adjusted to $f_{core} = 0.12$ when comparing results to some limited experimental data (Bouwer et al.[16]). After some simplification the final result of the momentum analysis yields the following equation:

$$A(P_{TR} - P_{core}) = \dot{m}_{core} V_{core}\left(\frac{1-2n}{2(1-n)} - f_{core}\right) + \dot{m}_e V_e(1-f_e) - \dot{m}_{TR} V_{TR}\left(\frac{1}{2} - f_{TR}\right) \quad (5.5)$$

This is the desired function with the section mass flows as the required input variables and the core fan total pressure as the output. This equation can now easily be applied for the system calculations. Refer to Appendix C for a detailed derivation of equation 5.5.

The experiments on the CIRSTEL jet-pump done by Bouwer et al.[16] were for a fixed value of the mixer/duct area ratio, thus that data cannot easily be used for design purposes. That data was however used to calibrate the loss factors in Equation 5.5. Care has to be taken when interpreting the results by Bouwer et al. as it can predict unrealistic total pressures from the fan at low mass flow ratios; this is due to insufficient data being available in that region.

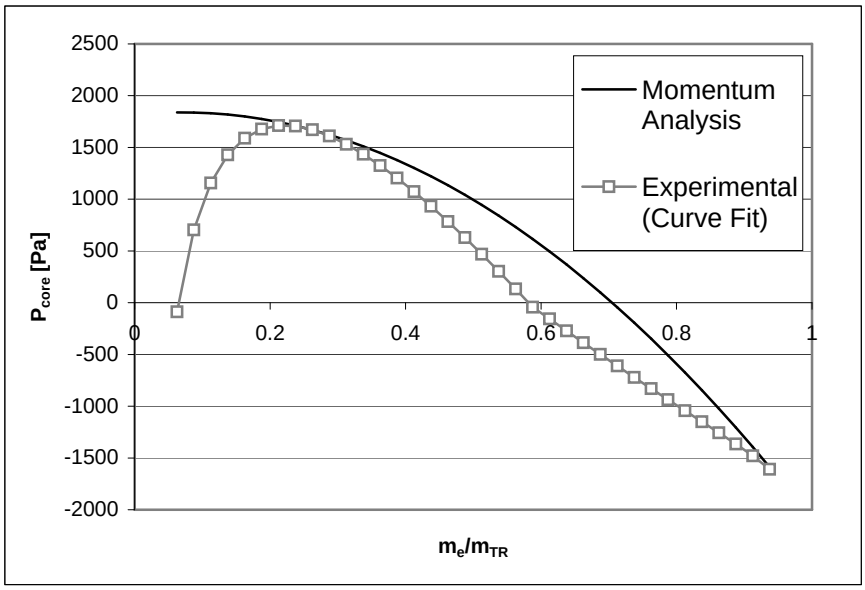

Figure 5.4 Momentum analysis and experimental result comparison for the core section

Figure 5.4 compares the experimental data of Bouwer et al.[16] to the results obtained by the momentum equation, all to achieve a total exit pressure of 1200 Pa and 1.6kg/s mass flow, with a nozzle area ratio n = 0.469. The figure shows the pressure contribution that the fan has to deliver in order to achieve the desired exit pressure for a range of engine mass flow fractions of the total required exit mass flow. As can be seen from the figure, the theoretical results follow the experiment comparatively well for mass flow ratios larger than 0.2. At the lower values the experimental curve-fit indicates a negative pressure to be supplied from the fan to achieve the desired total pressure rise at the thruster end of the duct, which is unrealistic as the fan at that ratio has to deliver virtually the entire pressure rise on its own.

4. Tail Thruster

The performance of the tail thruster is based on the theory developed by Nurick[17] for a clamshell thruster, with experimentally determined thrust and power coefficients used for the calculations. The thrust delivered by the thruster is a function of the thrust coefficient, exit area and the total pressure supplied to the thruster. Similarly the mass flow is dependent on the power and thrust coefficient, exit area, density and total pressure. Here the total pressure is calculated from the momentum theory for the core section. Once the total core section mass flow is known the amount the fan has to contribute can be calculated by subtracting the engine mass flow from the total flow.

As shown by Nurick[17] the static pressure can be determined from the thruster coefficients, geometry and total pressure alone. The density in the tail boom can not be calculated because the specified total pressure influences the static pressure, mass flow and hence the mixed air flow temperature in the duct, which are all needed to calculate the density. This results in a circular reference, and again a density is estimated from which the calculations are continued, and this estimated density is then adjusted during the solving phase to equal the actual value in the final solution. Knowing the two mass flows entering the core section the mixture temperature can be calculated, from which finally the actual mixture density can be calculated.

5. Circulation Control Tail Boom Section

Fonternel et al.[9] give a summary for the theory on the circulation section, while more recently Nurick[18] conducted further investigations specifically for the CIRSTEL system. The torque that the circulation section provides in hover is a function of the supplied total pressure, main rotor thrust and the tail boom geometry. A similar geometry is used in the simulations as the geometry used by Nurick, for which the produced torque is given by

$$Q_{CCTB} = 0.101\left(\frac{P_{CCTB}}{T_{MR}/\pi R^2}\right)^{\frac{1}{2}} T_{MR} D \qquad (5.6)$$

This equation is valid for a round and flap-less tail boom. Two Coanda slots are used for this boom; one at a location of 60º from the top, with the second slot located 120º form the top of the tail boom. The Coanda slots extend to the radius of the main rotor with a total length of 2.75m. To calculate the mass flow through the two Coanda slots, they are modelled as a nozzle with a discharge coefficient of C_D = 0.802. The discharge coefficient is derived from experimental data (Nurick[18]).

6. Fan

The fan used for the CIRSTEL system is unique in that it has the ability to supply each section of the tail boom with a separate air stream of the required pressure and mass flow rate. As part of the general research effort into the CIRSTEL system such a fan has been tested experimentally (Chapter 2 and 3). Results from these tests are incorporated into the current simulation program in that it has been shown that the inner and outer sections of the fan do not influence each other significantly, regardless at which operating point each section is working. Secondly the fan efficiencies determined during the experimental trials are used here to determine the power requirements of the fan. Since the required mass flow and total pressure rises are known, and hence the required fan power, the corner stone for the fan design is provided as well.

7. Global Tail Boom Performance

The torque that each of the circulation control and tail thruster sections develops is added to give the total delivered torque of the tail boom. The total power required by the fan is the sum of the

inner and outer section power demands, and is an important result to monitor. This value is required for monitoring of the total power requirement of the helicopter and to compare to the power demand of the conventional tail rotor to highlight any power savings or differences. Finally the total mass flow requirement of the fan is required for the design of the air intakes for the fan.

Optimisation Method

As well as facilitating an easy design process, the simulation program was also designed to be utilised with a numerical optimisation scheme. Added to that, by monitoring the performance of the individual components during the optimisation process, the most critical components could also be identified. Standard numerical optimisation techniques, such as the simplex method (Vanderplaats[19]) with constraints, were employed to find optimum dimensions and parameters for this tail boom. For simplicity the current program was written for a spreadsheet, which allowed a better visibility and control of the parameters during the search for convergence.

The objective of the optimisation process is to minimise the power required by the fan, while the tail boom still delivers the required torque to balance and control the helicopter. The primary constraint on the optimisation process is thus the percentage of main rotor torque that the tail boom has to counter, including the reserves required for manoeuvring. Once an optimum for a selected design point is found, the solution has to be checked for other parts of the hover envelope by scaling the fan performance with the appropriate fan scaling laws.

Any reductions in the total power requirement over the standard tail rotor have their obvious advantages; if the requirement increases the feasibility of the system reduces, though the tactical and safety advantages of the system remain.

Input variables used are primarily the geometric features of the tail boom, such as boom diameter, mixer area and thruster exit area. The total pressures in the two conduits of the tail boom drive the solution, and thus are the two primary variables in the optimisation, as these have the most direct influence on the performance of the boom and the fan. The fraction of the total torque delivered by each of the two sections can also be limited.

Optimisation Constraints

Two helicopter design configurations were studied, namely a single- and a twin-engined helicopter in the light utility helicopter class. Both helicopters have the same overall dimensions with a main rotor diameter of 11m. The single engine helicopter is modelled as having an engine based on the Artouste IIIB delivering 500kW, while the twin-engined helicopter has engines each delivering 480kW, which in turn are based on the Arrious 2K1 engine. For the single engine helicopter the power limit is the engine output, while for a twin-engined helicopter the limit is usually defined by the main rotor gearbox rating and the corresponding limit is set in the program. As a design point the maximum take off weight is selected for the atmospheric conditions of 85 000 Pa and 25ºC for both versions. The upper design limit chosen is a maximum all up weight which can be maintained with available power plus an extra margin of the fan power to allow formanoeuvring.

Engine performance degrades with altitude and temperature, which was also included in the analysis. Due to the nature of the CIRSTEL system the backpressure on the engine can change from normal atmospheric conditions, which in turn will change the engine output due to a difference in the pressure drop across the turbine. These effects of the changing backpressure were also included in the analysis of the system. A higher backpressure on the turbine will reduce the power output and reduce the surge margin. A lower backpressure would thus seem to be a better solution, but this can lead to overloading of the engine, and thus the backpressure should be kept close to zero through careful selection of the mixer area. Though not explicitly included in the

optimisation routine, the engine backpressure was monitored during the optimisation process to remain close to zero.

Further constraints that were experimented with are the thruster exit area and tail boom diameter. These variables however quickly converged to unrealistic values; the tail boom diameter increased to a size that could not be installed on a helicopter and the thruster exit area also ended up as being too large to practically fit on the tail boom. These two dimensions thus had to be fixed to practical values and did not form part of the numerical optimisation process. The exit area of the mixer was chosen such that the engine(s) would experience a close to zero backpressure, yet the mixer performed sufficiently as a jet pump nozzle for both test cases. When allowing the optimisation routine to size the nozzle area the tendency is to reduce the area and increase the backpressure on the engine unless the backpressure is explicitly constrained. Further, a larger nozzle exit area is more desirable to allow for better mixing of the hot gasses inside of the core section duct.

The fraction of the torque delivered by the circulation control section is limited to below 48%; this is to ensure an effectiveness of the tail boom at slow speed flight, when the effectiveness of this section is reduced due to the decrease in downwash from the main rotor and more reliance is placed on the tail thruster. Since the circulation control section is more efficient at creating torque the fraction it contributes is always close to the maximum limit. A secondary effect of this limit is the temperature of the gases exiting the thruster; by increasing the workload of the core section more cold air is demanded from the fan, and thus the thruster temperature is reduced.

Optimisation Results

In both test cases the power required by the fan reduced noticeably to below that of a conventional tail rotor. The fan power was below 5.6% and 8.4% of the main rotor power, for the single- and twin-engined helicopters respectively, as opposed to the 9 to 10 percent of the conventional tail rotor. The reduction in power can mainly be attributed to the jet pump effect in the core section and the ability to optimise the tail thruster and circulation control section separately. The jet pump has a dominating effect on the performance of the tail boom, and is thus a critical component in the design of the system. Through a careful selection of the nozzle size the backpressure on the engine(s) is controlled. The nozzle size was not included in the current optimisation as a parameter because the parameter continuously settled at the constraint value assigned to it. With the current selected nozzle size the backpressure on the engine was less than 20% of the engine exit dynamic pressure for both versions. Table 5.1 gives the detailed results of the simulations for the two case studies.

The relatively small power saving for the twin-engined helicopter stems from the high engine compressor pressure ratio of 9.5 versus the pressure ratio of 5 used for the single-engined helicopter. As a result it has a small mass flow through the engine for the power the engine produces and the fan then has to supply enough air to power the tail thruster. This can also be seen by the low thruster exit temperature of 149ºC. The power saving is therefore a trade-off, amongst others, between the type of engine used and the thruster exit temperature required that has to be considered at the start of the design process.

Finally the thruster exhaust temperature was reduced to well below the 170ºC threshold for both test cases, which will make it difficult for infra-red sensors to pick up (Lippert et al.[14]). In the calculations complete mixing of the exhaust gas is assumed due to the limitations of the one-dimensional model. Incomplete mixing will not significantly affect the momentum analysis, but a distinct degrading of the IR suppression will occur if incomplete mixing takes place. It is thus imperative that the design of the mixer is carefully considered.

Also worthwhile noting here is that the total pressure in the outer CCTB section is lower than the pressure supplied to the thruster. The fan however has to deliver a higher pressure to the outer

CCTB section than to the core section; the remainder in the core section being made up from the energy supplied by the engine exhaust gas.

Table 5.1 Optimisation results for 110% of main rotor torque

	Single 2070kg T/O mass	Twin 3500kg T/O mass
Total Fan Power [kW]	17.1	51.1
Equivalent Tail Rotor Power [kW]	27.2	61.2
% Saving	37.2%	16.5%
Thruster Gas Temperature [ºC]	164	149
Total Torque [Nm]	9159	16634
Total Pressure Supplied to Thruster [Pa]	2182	3840
Total Pressure Supplied to CCTB by the Fan [Pa]	1639	3398
Total Pressure Supplied to Core Section by the Fan [Pa]	1312	2765
% Contribution by Circulation Control Section	46.3%	46.6%
Fan Diameter [m]	0.550	0.550
Tail Boom Diameter [m]	0.720	0.720
Tail Thruster Area [m^2]	0.4655	0.4655
Core Section Diameter [m]	0.650	0.650
Nozzle Area (Fraction of Core Section)	0.235	0.230
Mass Flow Fraction	0.277	0.246

A sensitivity analysis of the objective function to small perturbations of the two optimisation variables is presented in Table 5.2. For this sensitivity analysis one variable was perturbed by 5% of its optimum variable, while the other variable remained at the optimum value. The results show the objective function to be significantly more sensitive to perturbations of the total pressure in the core section of the tail boom by a factor of about 11 for both cases. The 48% torque contribution constraint placed on the CCTB section was not violated.

Conclusion

The results of this optimisation study show that the system offers a potential power demand reduction over a conventional tail rotor by up to 37%, while reducing the exhaust gas temperature to below 170°C. The calculations also confirmed that through careful designing and sizing of the mixer nozzle the effects on the engine can be small, with the backpressure on the engine being less than 20% of the exit dynamic pressure, while still boosting the performance of the tail thruster.

Table 5.2 Sensitivity analysis of the objective function

	P_{TR} [Pa]	P_{CCTB} [Pa]	$\Delta W_{fan}/\Delta P$ [kW/Pa]
Single-Engined Helicopter			
P_{TR} perturbed	2291	1639	1.460
P_{CCTB} perturbed	2182	1748	0.136
Twin-Engined Helicopter			
P_{TR} perturbed	4032	3398	3.240
P_{CCTB} perturbed	3840	3590	0.292

CHAPTER 6

HELICOPTER INTAKES

Gas turbine engines have found wide application as power plants in helicopters. Naturally these engines are sensitive to pressure and flow distortions at their compressor faces. Although helicopter flight speeds are low in comparison to fixed wing aircraft flight speeds, the intake performance is still critical to deliver quality air for maximum engine performance. However, there are some fundamental differences between helicopter intakes and fixed wing aircraft intakes. Most important is the change in flow environment, from the straight downwash in hover to the relatively horizontal flow at maximum speed. The most critical part of the flight envelope is hover and transitional flight, where the power demand is the highest. Here the intake design is most difficult, as traditionally this requires the air to turn through almost 90 degrees, corresponding to a very high angle of attack and/or static running conditions in conventional aircraft.

A Survey of Helicopter Intakes

For helicopter engines the mass flows are relatively small because helicopters rely on the developed engine shaft power, rather than the engine thrust. This allows the intakes to be physically small and due to the low flight speeds experienced there is nothing to be gained by a diffusing inlet duct. Thus the intakes usually exhibit a large amount of contraction, which helps their performance in the complex flow field. Due to the small mass flows there is space available in the fuselage structure for high contraction ratio inlet ducts.

Some of the traditional intake designs, shown in Figure 6.1, are the Pitot intake (for example the Eurocopter EC 725 Super Puma), forward facing side intake (Bell 430), flush mounted side intake (Agusta A109) and radial inflow/bell mouth type intake, as seen on most Russian helicopters (Mi 24). To a large extent the detail of the intake position is determined by the engine position relative to the main rotor gearbox. Engines that have their drive shaft extending forward have to be located behind the gearbox, thus this design is usually characterised by side intakes. Rear-end drive shaft engines offer the advantage of placing the engine in front of the gearbox and thus allowing the intakes to be far forward and open directly to the front.

Often the afore-mentioned intake versions are used in conjunction with a plenum chamber, to allow the air to settle before entering the engine. Intakes also have to give some form of foreign object damage (FOD) protection from dust, rain and birds. Available devices range from inertial separation ducts and screens to complicated sand filters, but these will not be considered in detail here.

Each of the mentioned designs have their own advantages. The Pitot type intakes show good pressure recovery, as shown by Seddon et al.[20] (Figure 6.2), but require installation in front of the gearbox. Side intakes have the disadvantage of ingesting the fuselage or cowling boundary layer. The forward facing version also acts like the Pitot type with a performance close to the Pitot type at low flight speeds, as again seen in Figure 6.2. Flush mounted intakes offer a natural protection against FOD, due to inertial separation, but have a bad pressure recovery performance. However, if these inlets can be extended to open upwards over the upper part of the engine cowling the potential pressure recovery in hover could be beneficial.

(a) EC 725 Super Puma: Pitot intake

(b) Bell 430: side mounted intake

(c) Agusta A109: flush side intake

(d) Mill Mi 24: radial inflow intake

Figure 6.1 Examples of four types of helicopter intakes

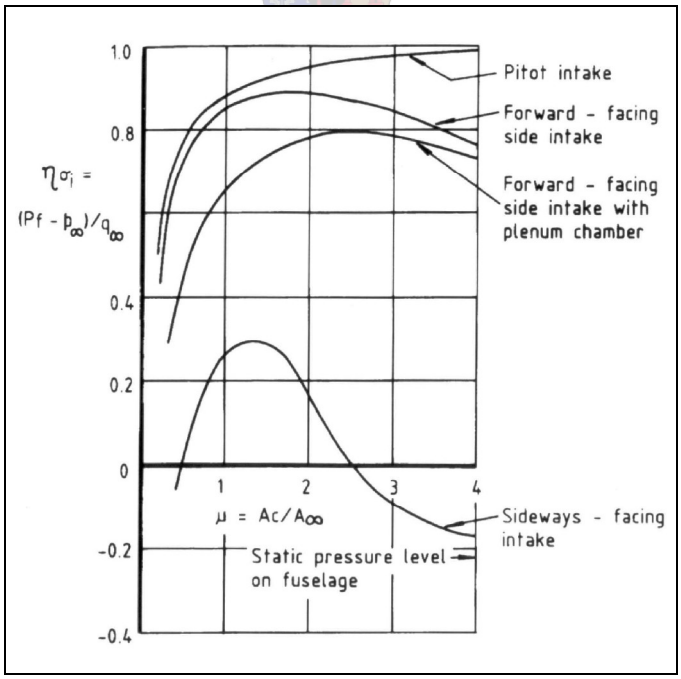

Figure 6.2 Typical pressure recoveries of helicopter intakes (from Seddon et al.[20])

Tail Rotor-Less Helicopter Intakes

To date only two tail rotor-less designs are on the market, those being the MD Helicopter products of the MD530/600 series and the MD Explorer. Of these only one, the MD Explorer, was designed from the beginning as a pure NOTAR helicopter. The MD 530/600 was developed from the original Hughes 500, with the NOTAR tail boom being an "add-on" (Figure 6.3).

Due to the high mass flow required for the NOTAR tail boom and correspondingly large fan, the intake becomes a dominant part of the fuselage structure. It thus becomes impractical to have an inlet of the same shape and contraction ratio as the engine inlets. It would simply be too large. The inlets to the fan are thus facing upwards, to capture the rotor downwash. The air then gets turned internally through roughly 90 degrees before entering the fan.

The design of both helicopters allows the intakes to be on top, the single engine MD530/600 have their engines in the fuselage below the main gearbox and thus out of the way of the fan and intake. The MD Explorer is twin-engined, thus allowing the intake and the fan to be located in between the two engines as is visible in Figure 6.4.

Figure 6.3 The MD 530 NOTAR with its top mounted fan intake

Figure 6.4 MD Explorer showing the fan intake between the two engines

Review of Design Methods

No generalization in the design of helicopter intakes is as yet possible; intakes are more likely to be custom designed for each application, so nothing significant has been published regarding the design of helicopter intakes and no fixed design guidelines exist. This is also partly due to the complex flow fields and the fact that tools to analyse the designs efficiently are only now becoming available. Thus none of the consulted literature sufficiently accounted for the rotor effects on the intakes. It is here where the current investigation is aimed at studying the flow phenomena affecting helicopter intakes.

Hermans et al.[21] describe the experimental approach used for designing the engine intakes of the NH90 helicopter. Various scale models of up to 1:3 scale were manufactured and extensively tested in wind tunnels to design, study and optimise the engine intakes. Most of the models utilised powered rotor hubs and for some tests full rotor models were used. Though experimental trials generally give good results, it is a time consuming and expensive task. Approximately 1900 wind tunnel hours were used for the NH90 program, of which significant portions went to the study of the intakes alone.

Limited works are available that theoretically assist in the design of helicopter intakes. Holdø et al.[22] studied the flows generated by the interaction of an inlet and a cross-flow, which gives a basic understanding of flows that can occur around helicopter and VTOL intakes.

Boizard[23] describes the analysis of the AS 350 Ecureuil and Dauphin intakes with the aid of a three-dimensional panel method program. Here however only the intake ducts with helix separator are modelled and the boundary conditions employed do not account for any rotor downwash.

Vuillet[24] discusses the importance, problems and objectives of the aerodynamic design of engine air intakes. Basic design principles of helicopter engine intake design are presented, both in type selection and geometrical design.

Seddon et al.[20] dedicate only a small section of their work to helicopter intakes, though the design principles for fixed wing aircraft intakes discussed throughout the book are applicable to the detail design of helicopter intakes. Goldsmith et al.[25] extend the discussion of intake design by presenting practical solutions to specific intake design problems.

Design Requirements and Objectives

Vuillet[24] summarises the design objectives for engine intakes as follows:

- Reduction of power losses and reduced fuel consumption
- Improved surge margin
- Protection against FOD
- Ease of installation and service

For the current study the focus will only be on the first two points. Even though the remainder requires equal attention, they are secondary to the current research issue and application to the CIRSTEL fan.

In the paper by Vuillet it is also suggested to prioritise the design parameters/features when it comes to designing efficient intakes. In order of identified priority the design features are:

- Position of the capture area A_c on the fuselage
- Size of the capture area, also implying the intake contraction ratio
- Angle of incidence
- FOD protection devices
- Relative thickness of the intake lips
- Duct design
- Lip shape

For the current investigation, which focuses on the fan intake, a similar approach is used as described by Vuillet, however further constraints need to be applied here.

Spatial constraints primarily limit the size of the intake, the fan having a large diameter compared to normal engine sizes, and thus the intake will form a significant component of the fuselage. Also due to the large mass flows and size of the fan intake, any internal duct particle separators are precluded. The fan should however itself exhibit a large amount of FOD tolerance due to the relatively slow speeds at which it operates. Thus no explicit attention will be given here to particle separation.

Secondly the layout of the CIRSTEL system limits the options regarding the type of intake possible. The fan has to be positioned at the base of the tail boom and with the fuselage in front the intakes have to open to the sides, top or bottom of the fuselage.

The objective of this investigation was to develop effective air intake concepts for the Alouette III/CIRSTEL combination. This was to be done using CFD with unsophisticated boundary conditions, based on rotor momentum theory to enforce the rotor flow field. The study then also expanded to study alternative intake geometries for a generic helicopter fitted with the CIRSTEL system. Here positioning of the intake, as well as duct design, was studied in the presence of a realistic rotor flow field. The rotor for these CFD simulations was implemented by the use of an actuator disk model to give a time-averaged solution of the rotor flow field. The investigations also considered the effects of the rotor hub on the performance of the intake. Basic phenomena of the flow field underneath the rotor affecting the intakes are explored and discussed.

Design of the Intakes

Critical cases for these intakes are the hovering condition and very low forward speeds (rearward and sideways flight is not included in the present analysis). This condition is similar to static or high angle of attack flows for standard aircraft intakes. Here the intake flow is dominated by its behaviour around the intake lip. At high angles of attack there is the added complexity of unsymmetrical flow in and around the intake. Also, the stagnation point varies significantly around the inlet perimeter, depending on the flow ratio and incidence of the intake. It is also not easy to define the flow approaching flow field for the intakes in this case. Data and ideas from studies of these cases for conventional intakes can however be used to shape the fan intakes. As may be expected, the losses in the intake can to a large extent be attributed to the shaping of the inlet lips and how the air flows over these, especially at high angle of attack.

Duct Design and Contraction Ratio

The spatial constraints that are typical for the current installation into the CIRSTEL system dictate a short duct length. This will have a positive effect on the thickness of the duct boundary layer entering the fan, but at the same time the duct turns will have to be tight which can result in high losses. Thus Gerlach shaping (described by Seddon et al.[20]) should be implemented where possible. Gerlach shaping reduces the radial pressure gradient in a duct bend by increasing the outer wall velocity and decreasing the inner wall velocity of a duct bend.

The most effective method of controlling duct losses is however a high contraction ratio. The inlet contraction ratio, $CR = A_c/A_t$, has a major effect on the total pressure loss in the intake, especially if lip separation is present due to a high angle of attack. Here A_c is the capture area and A_t is the throat area of the intake. Seddon et al.[20] shows the effect of a high contraction ratio on the total pressure loss (Figure 6.5). Even if separation does occur, a high contraction ratio reduces the severity of the effect of separation. The intakes for CIRSTEL are thus to be designed with an as large as possible contraction ratio. As an example, the AS 350 Ecureuil uses an engine intake contraction ratio of 6.0, but due to the size of the CIRSTEL fan it will be impractical to fit an intake with a similar contraction ratio.

Lip Shape

The flow incidence variation for helicopters is significant. Ignoring rearward flight, the angle of incidence varies from 90 degrees at hover to angles in the order of 5 degrees at maximum forward speed. As already mentioned, the lips have a dominant effect on the effectiveness of the inlets; the lips should thus be adapted to the changing flow conditions by thickening the windward lip (the lip which is on the side of the inflow angle), which will ease the flow into the duct. A further improvement can be gained by cambering the windward lip outwards into the direction of the

incoming flow. The effects of these detail changes to the lips are shown in Figure 6.6, taken from Seddon et al.[20].

The intakes here are to incorporate both these concepts, high contraction ratio and lip shape. Generally a 2:1 ratio of the lip ellipse cross section is considered the optimum and should be implemented here. Vuillet[24] also suggests the intake lips to have a thickness of 25% of the intake diameter if the intake is of the Pitot or forward facing type.

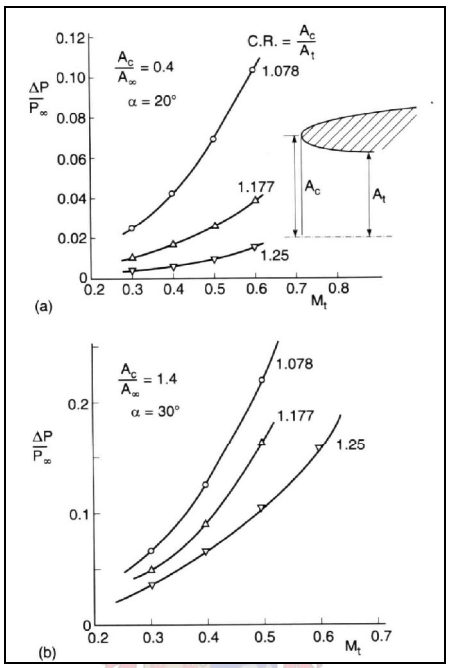

Figure 6.5 Effect of contraction ratio on pressure losses (Seddon et al.[20])

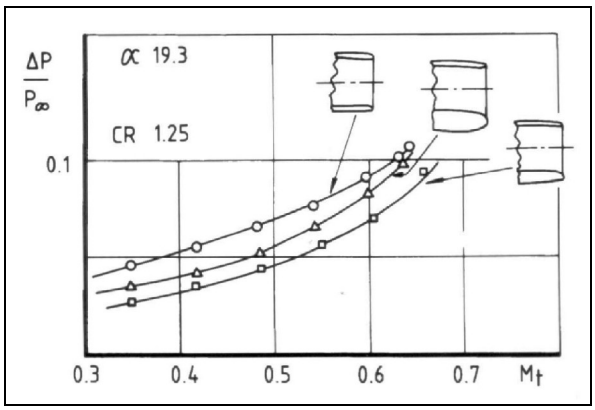

Figure 6.6 Effects of lip geometries on total pressure losses (Seddon et al.[20])

Intake Lip Stagger and Intake Shielding

Lip stagger is the backward or forward sweep of the intake entry plane between the highlight points and the normal of the axis of the duct. Seddon et al.[24] shows in Figure 6.7 that at low forward speeds (small inverse capture ratio) and high angle of attack no significant gains are made by adding lip stagger. Lip stagger for these intakes should however still be investigated at a later

stage, due to the (at this stage unknown) complicated flow field around the fuselage and engine cowling that might hold advantages to lip stagger. A scoop can also be added on the bottom half of the side opening inlets to form an intake shield. The scoop is intended to capture the downward flowing air and guide it into the intake, as also described by Seddonet al..

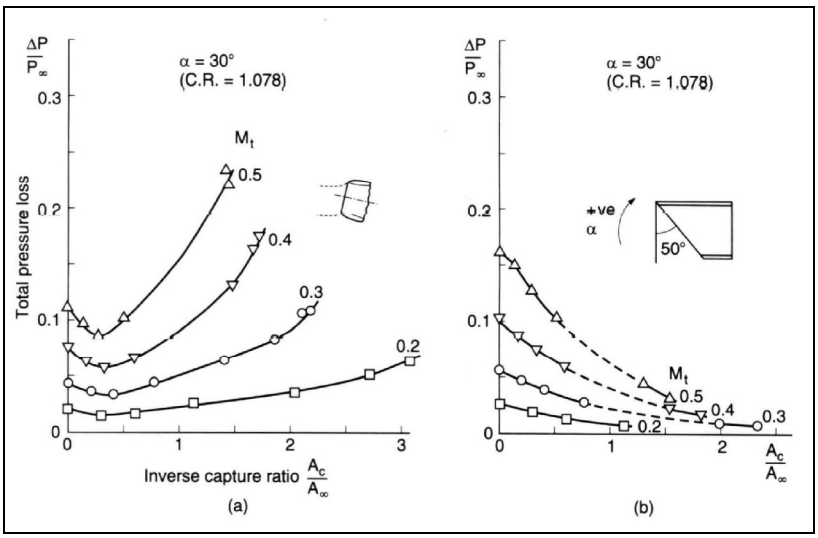

Figure 6.7 The effects of lip stagger on the performance of intakes (Seddon et al.[20])

CHAPTER 7

ALOUETTE III/CIRSTEL INTAKE DESIGN AND EVALUATION

Helicopter intakes, in contrast to those of fixed wing aircraft, feature an important change in the flow environment: the intakes are exposed to a straight downwash in the hover to the almost horizontal flow at maximum speed. In this chapter a concept for intakes for the Alouette III/CIRSTEL combination is developed and analysed using CFD methods. The design evolved, based on the CFD results, to yield improvements in the performance.

Concept Development

For the design in the current CIRSTEL application there are further spatial constraints due to the utilisation of an existing airframe. The fuselage structure of the Alouette III test bed may not be modified; it consists of a space-frame structure in the rear section of the fuselage to which the tail boom is attached (Figure 7.1). But the single most limiting factor is the position of the engine. The single engine is positioned almost directly above the intended fan position, and thus the air intakes have to open sideways or downwards. There is also a limit as to how far back the fan and its diffuser can be installed and still allow the engine exhaust ducting and daisy-mixer to be installed. Into this space the fan drive shaft and pulley assembly will also have to be fitted in. Combined, this gives a spatial constraint of a 600mm wide vertical band behind the fuselage where the intakes can be installed. Furthermore there are three attachment points where the tail boom is fixed to the fuselage space frame that have to be considered.

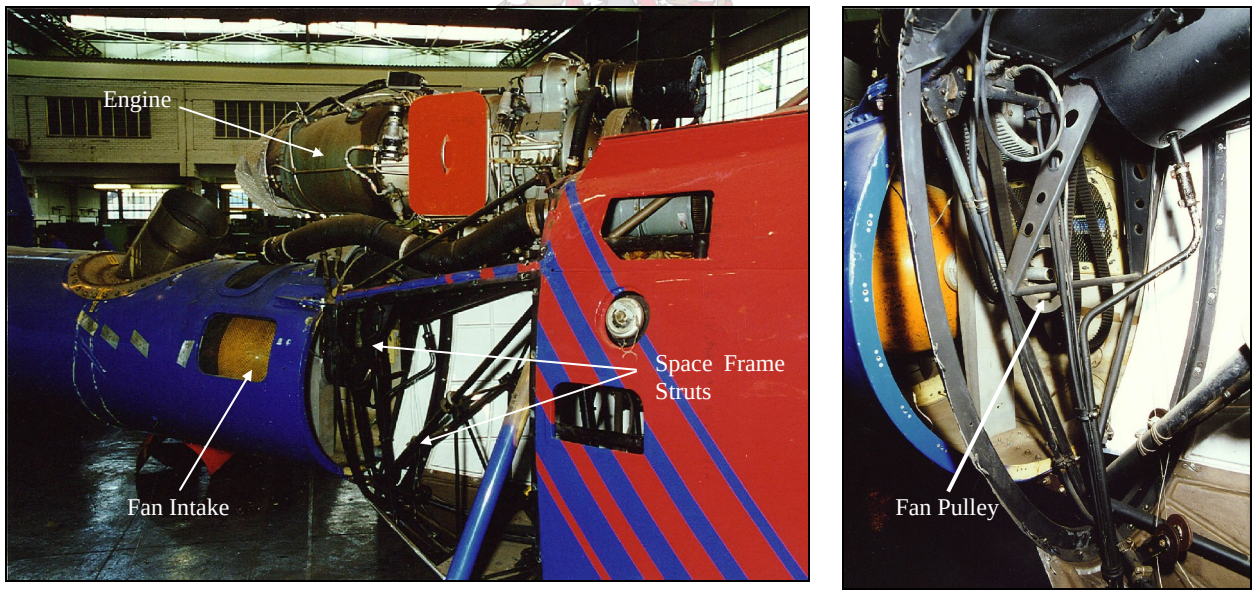

Figure 7.1 Details of the original Alouette III/CIRSTEL helicopter, showing fan intakes, space frame and fan pulley assembly

A practical trade-off study showed that the only realistic option would be side intakes as shown in Figure 7.2, that make optimum use of capturing the incoming air, especially the rotor downwash. Seddon et al.[20] showed that side opening intakes have the worst efficiency of the four intakes studied, thus the objective is now to design intakes that exhibit enough properties of the Pitot type to make the design feasible.

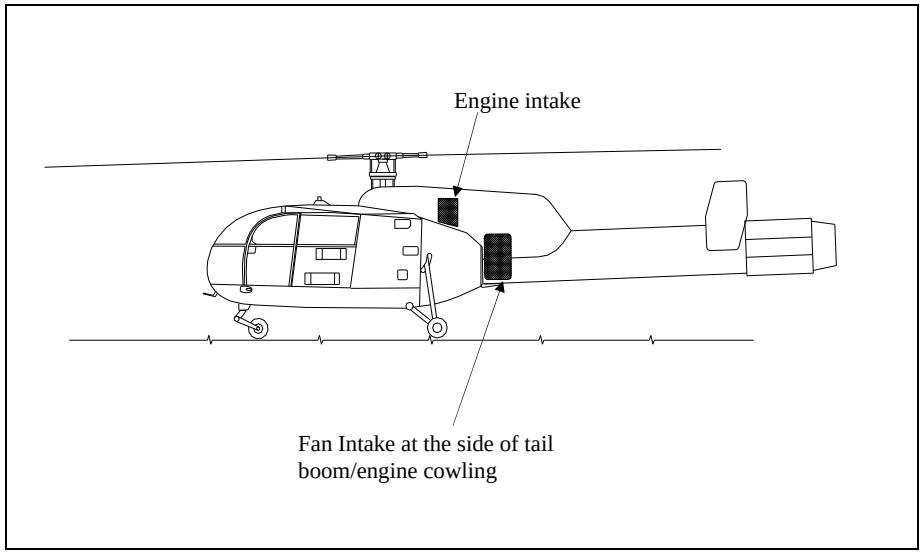

Figure 7.2 Selected concept for the Alouette III/CIRSTEL intakes; the openings are located on the side of the tail boom/engine cowling

Intake flow is dominated by the behaviour around the intake lips, and to a large extent the losses in the intake can be controlled with the shape of the lips (Seddon et al.[20]). Here, data and designs for conventional intakes under static or high angles of attack were used to shape the fan intakes. Seddon et al.[20] also discuss the effect of a high contraction ratio, $CR = A_c/A_f$, on the total pressure loss; the current intakes were thus designed with as large a contraction ratio as possible.

To account for the changing flow conditions the lips were adapted by thickening the windward lip (for this case the upper section of the intake) to ease the flow into the duct. The position selected for the inlet openings would require the duct to open to both sides of the tail boom. A semicircular inlet profile cross section was selected for simplicity, the idea being to have half a bell mouth on either side of the tail boom that will allow the capture of air at forward speed (ram air effect), while still being effective in the hover. The inlet opening is to be placed close to the fan, thus creating a short duct and thus thin boundary layers, which are critical for the outer fan section. Although this makes the fan visible from some angles, the IGVs do shield the fan to a great extent and for the current application it was considered to be sufficient.

An intake scoop was added at the bottom half of the inlet. It was intended to capture the downward flowing air and guide it into the intake. Fairings were placed around the engine, fuselage and its structure to integrate the intake into the airframe. These fairings were to be fitted, without modification to the engine and fuselage, while at the same time still giving maintenance access to the engine and structure. For the case of hover and slow forward flight the air will first flow over the engine cowling before entering the intakes. The fairing that covers the engine and gearbox thus had to be shaped to allow the air to flow smoothly over it without separation. The engine cowling extends to blend in with the rear end of the fuselage to give a continuous blended surface. The end of the Alouette III fuselage is bulged outwards and the intake fairings were designed to give a blended transition from the fuselage panels into the fan air intake. The intake panels end with sharp a trailing edge inside the intake duct, just ahead of the IGVs. The fan diameter and flow quantities used were those originally specified.

Structurally the tail boom is mounted to the fuselage space frame at three points. The upper two attachment points initially precluded any possibility of allowing the intake openings to face upwards and increase the contraction ratio. It was then decided to first ignore the attachment points and then later add a strut with an airfoil profile that is aligned to the local flow conditions.

Eventually this strut could also be used as an inlet guide vane to the intake to increase its performance in a hover.

Flow Modelling

Since this was an initial study of the problems involved with designing intakes for the fan, the complex flow of the rotor was not modelled in detail. Studies done by Leishmann et al.[26] of the flow through a rotor with an attached fuselage give an indication to the nature of the complex flow field, while Berry et al.[27] also give an indication of the difficulties involved in numerically simulating the rotor with the varied lift distribution and tip vortex structure. Instead, for these studies, the incoming flow was specified as uniform, with the flow velocity and incidence angle derived from momentum theory. Glauert's modified actuator disk theory[11] was used here, which draws an analogy between the rotor and an elliptically loaded circular wing. He suggested that a mean induced velocity can be defined from momentum theory, from which the following equation can be deduced, which relates the induced velocity by the rotor to V and v_h:

$$\left(\frac{v_i}{v_h}\right)^4 + \left(\frac{V}{v_h}\right)^2 \left(\frac{v_i}{v_h}\right)^2 - 1 = 0 \qquad (7.1)$$

Though no formal proof exists, it was pointed out that this momentum theory is accurate enough for performance predictions. To provide some verification a video of a flight test of an Alouette III, equipped with tufts mounted on the tail boom, was used. Even though the tufts did not give an indication of the local velocities, the angle they made relative to the flight direction gave a good indication to the plausibility and accuracy of the calculated values using momentum theory.Figure 7.3 plots and compares the calculated and experimental angles, and it is clear from the graph that a reasonable correlation exists. From the flight tests two sets of data were obtained, one for the left hand side (LHS) and one for the right hand (RHS) side of the helicopter. The theoretical correlation was obtained with a helicopter weight of 20kN. Free stream velocity values and wake angles as calculated by momentum theory for the Alouette III helicopter are given in Table 7.1.

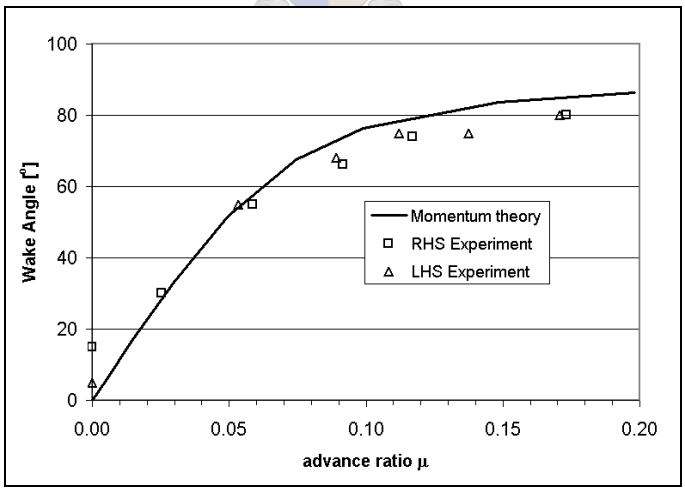

Figure 7.3 Calculated and measured wake angles

The computational flow domain (Figure 7.4), only included one side of the helicopter. The simple modelling of the rotor wake in this CFD model did not include any swirl, thus symmetry could be used to reduce the control volume, and thus the number of mesh nodes. The flow domain extended one fuselage length ahead of the helicopter, one fuselage height above and two fuselage heights below the helicopter. The total length of the domain was three and a half fuselage lengths long and one fuselage length wide. The mesh generated in CFX Build for these computations was an

unstructured mesh of tetrahedral elements. The surface mesh length of the fuselage was set at 75mm with the height of the first element perpendicular to the surface being set to 0.2mm to form a prismatic boundary layer mesh. Mesh resolution for the intake was 20mm with a first element height of 0.1mm.

Table 7.1 Calculated free stream velocities for the Alouette III helicopter

μ	0.000	0.005	0.015	0.030	0.050	0.074	0.099	0.149	0.198
V_{MR} [m/s]	10.04	10.06	10.27	10.97	12.75	16.23	20.59	30.19	40.08
Wake Angle [^{o}]	0.0	5.7	17.0	33.2	51.7	67.5	76.3	83.7	86.4

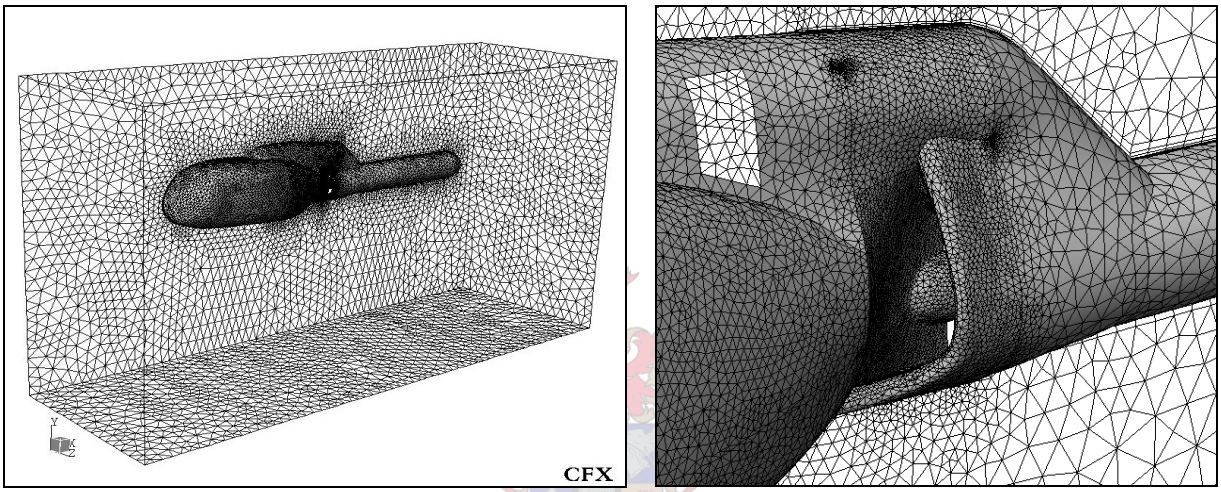

(a) **(b)**

Figure 7.4 Flow domain surface mesh (a) with detail of the mesh around the intake (b)

The top and front faces of the flow domain were used to enforce the momentum theory flow conditions on the control volume. These were defined as inflow boundaries. The rest of the control volume surfaces were defined as pressure boundaries, except the symmetry planes. The fan was modelled as a single mass flow boundary, as a result of acceptable results obtained from earlier test cases (See Appendix D). A progressively finer mesh was used near and in the intakes, the element size being limited to 20 mm in the intake duct and the intake lips.

Calculation of the boundary layer thickness on the fuselage was done using the velocities calculated with momentum theory and the average boundary layer travel distance to the intakes. The fuselage was broken into sections that were analysed separately, according to what influence each section would have on the intake. Sections located above the intake would naturally only affect the intakes in hover and low speed flight. Here the velocities experienced during hover were used, while calculations for the forward fuselage used the high-speed flight velocities. These calculations were then used to determine the required near wall mesh size. Conditions for the hover dictated the smallest boundary layer grid, using the $y^+ < 11$ criterion, around the intake panels. Thus the calculated boundary layer mesh parameters for the hovering case were used, resulting in a first element height of $\Delta y = 0.1$ mm.

The commercial CFX 5.5 solver was used to solve the flow in the domain, using an implicit formulation to solve the Navier-Stokes equations with a second order discretization scheme. The steady, viscid and incompressible computations took approximately 300 iterations to converge.

Intake Distortion

In the design of intakes the effect that the intake will have on the compressor have to be considered; the combination has to remain compatible. When matching a fan or compressor to an intake, a measure is necessary that will relate the intake performance to that of the compressor. A significant parameter is the total pressure distribution and magnitude at the fan face. The most commonly used distortion coefficient is the DC60 coefficient, and this coefficient was used to evaluate the intake designs, and is defined as follows:

$$DC(\theta) = \frac{P_f - P_\theta}{q_f}; \ \theta = 60^o \qquad (7.2)$$

The DC60 factor describes the fan face distortion by subtracting the mean total pressure of a 60^o sector with the lowest mean total pressure of the fan face from the average total pressure over the entire face and then dividing that result by the mean dynamic pressure over the face[20]. No detailed testing for distortion sensitivity of the two stream fan have been done, but it is fair to assume that this fan will be affected by distortion and hence the intake distortion levels should be limited. The design criteria suggested by Cumpsty[28] is to limit distortion on the fan face to a DC60 value below 0.5. The distortion factor was evaluated separately for the inner and outer sections of the fan. A MATLAB routine analysed the CFD results and gave the DC60 factors, along with average total pressures. Figure 7.5 displays the DC60 factors obtained for the outer sections of the three designs studied.

Intake Design 1

Based on the DC60 results, the first intake design (Design1, Figure 7.7(a)) failed the design criteria suggested by Cumpsty[28] for both the inner and outer fan sections. At $\mu = 0.00$ the distortion was unacceptably high in the outer section, but dropped off quickly as the advance ratio (flight speed) increases. It then increased slightly again to a value of 0.5. This behaviour was due to a strong flow separation area forming at the top of the inlet duct. It would appear that the separation zone resulted from a stagnation zone forming in the channel above the inlet (Figure 7.7(a)), which is formed by the inlet itself and the engine cowling, and the low pressure region in the upper corner of the intake duct (Figure 7.8 (a)). As the flight speed increased, the separation zone quickly became weaker and at the same time moved down along the intake side. At $\mu = 0.05$ the separation vortex was small, but then increased again with increasing air speed, due to the separation now occurring at the lip of the scoop. Core section distortion values (Figure 7.6) remained within limits and thus the core section was not under threat of stalling. The rise of the DC60 factor at high advance ratios is a result of the fuselage boundary layer now being ingested into the fan.

Intake Design 2

The second design (Figure 7.7 (b)), although exhibiting the same features as Design 1, was a complete redesign. However, the engine cowling remained the same as before. The biggest change characterising the second design is a very thick lip on the top section of the intake, while at the same time the upper intake section was blended in more smoothly with the engine cowling. A thick lip would guide the air more easily into the intake, while reducing the risk of separation due to the low-pressure region in the upper corner of the duct. A spin-off of the thicker lip was the blending in of the intake to the engine cowling, which eliminated the previous channel in which the vortex formed. The capture area also increased with the addition of this feature. The intake lips were cambered outwards by 8^o more than in the previous design. The intake duct was also extended forward by 50mm, to allow the flow more space to straighten out before entering the fan.

Considering the outer section, Figure 7.5, the DC60 values started off at a very high value of 1.25, then gradually reduced with increasing advance ratio. Compared to Design 1, the DC60 factors were now worse for advance ratios below $\mu = 0.15$. This was due to a separation zone inside the

duct that spanned a wider sector than previously. Hence the high DC60 factors, and the distortion did not reduce as quickly due to the slow disappearance of the separation zone. An improvement was however noticed in the core section over the entire range of flight speeds,Figure 7.6.

It would appear from these results that the new intake design hardly offered improvements over the first design. However further studies of the CFD results highlighted some more deficiencies in the design, as well as revealing that some sections of the intake worked acceptably. Most notable here was the lack of a strong separation zone at the top of the intake, as is visible in Figure 7.8 (b). Investigating where the losses in the intake originated from revealed that the losses were confined to the outer side of the intake, starting from the intake lips. The separation zone was thin, but occupied a large sector of the circumference and thus affected the downstream flow significantly. Extending the duct forward inadvertently caused the cross-sectional flow area inside the duct to first increase, before reducing again due to the nose bullet. This increase in flow area contributed to the separation the intake lip. Secondly, the results showed the stagnation line to be far on the outside of the intake lips for most flight speeds. From these plots it became clear that the radially inflowing air around the rear end of the fuselage was not taken into account properly, even though the lips had been angled outwards already.

Intake Design 3

A new design was created from Design 2 by simply adapting the intake geometry parametrically as shown in Figure 7.7 (c). The changes that were applied were as follows. The intake lips were moved back by 50 mm and thickened by 20% to reduce risk of separation, especially under hover conditions. Also the lips were flared out even more to allow a better flow alignment to the local flow conditions.

The apparent improvements in the performance of the design were immediately visible, when the CFD results were processed and compared to the first two sets of results. Firstly the low pressure region that was dominant in the first two designs was removed, as can be seen in Figure 7.8 (c). Also the DC60 factors showed a marked improvement over the whole range of flight speeds. The worst distortion was again encountered at $\mu = 0.00$, with a DC60 factor of 0.427 in the outer section (Figure 7.5), and thus well within the acceptable limit. For advance ratios higher than $\mu = 0.03$ the factors remained below 0.2, except at very high speeds, and thus the outer fan section should have no problems with a decreased surge margin. Distortion in the core section (Figure 7.6) remained very low; up to $\mu = 0.10$ the DC60 factor was around DC60 = 0.03. Only at higher speeds, where the fuselage boundary layer was ingested, did the DC60 values increase, but they remained well within limits.

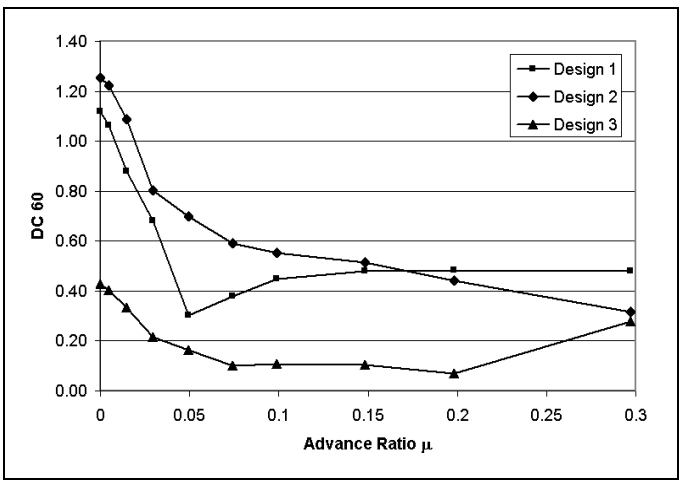

Figure 7.5 Outer fan distortion coefficients

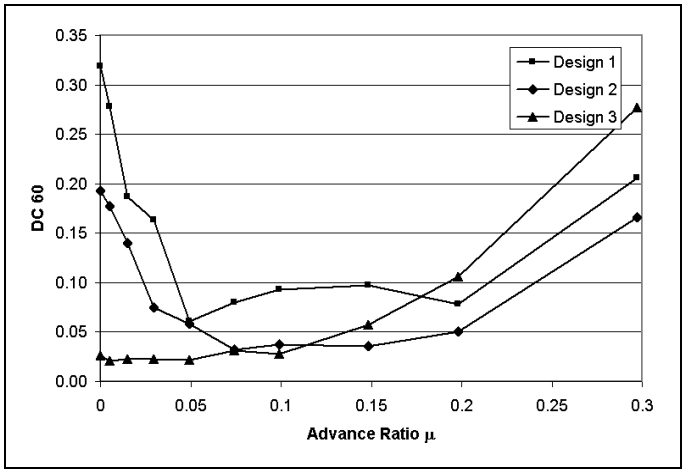

Figure 7.6 Core fan distortion coefficients

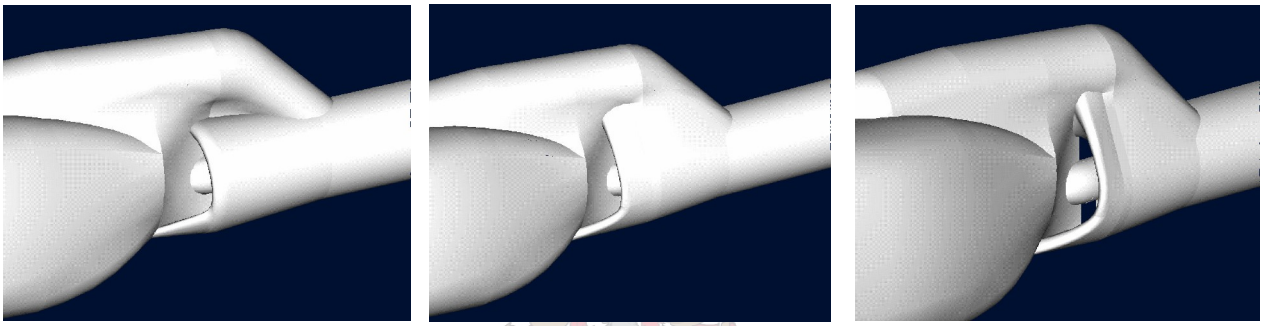

(a) Intake Design 1 **(b) Intake Design 2** **(c) Intake Design 3**

Figure 7.7 Evolution of the intake design

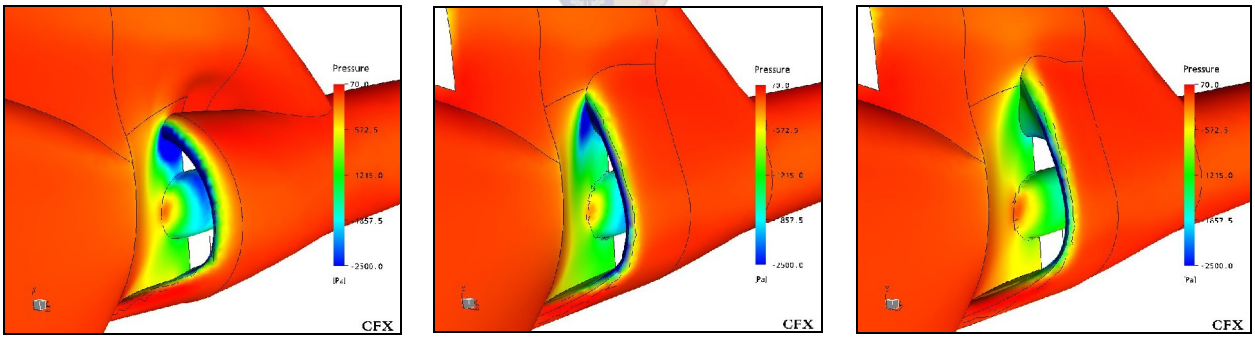

(a) Intake Design 1 **(b) Intake Design 2** **(c) Intake Design 3**

Figure 7.8 Static pressure distribution on the fuselage and intake during hover. The low pressure region (blue) on the upper corner of the intake is visibly reduced through the design evolution

Intake Total Pressure and Efficiency

For the current application the power available to the fan is limited to that usually consumed by the tail rotor. To make the system truly effective the fan should use less than this limit while still delivering the correct total pressure rise. It is thus crucial that the total pressure loss in the intake duct is minimal to yield a good efficiency curve.

For Design 1 the average total pressure (Figure 7.9) at the outer fan face was well below the ambient stagnation pressure. It started out at C_P = -1.65 (Translating into –1170 Pa) and rose

steadily with an increase in flight speed. Only at advance ratios of above $\mu = 0.23$ did the total pressure exceed atmospheric pressure. Therefore, only at these higher flight speeds, where the outer fan performance is not critical, was any use being made of the increase in dynamic pressure resulting from the flight speed. The core fan started off with a total pressure deficiency of $C_P = -0.2$, or 400 Pa, which reached positive values at an advance ratio of $\mu = 0.11$, Figure 7.10. With respect to Design 2, the average total pressures did not improve significantly for both sections. Even a lower pressure in the outer section is indicated when compared to Design 1 at speeds in excess of $\mu = 0.05$.

The average total pressure over the outer section of Design 3 gave a 52% to 46% improvement over the first two designs, respectively, in hover. The average total pressure coefficient was now $C_P = -0.02$ (–565 Pa) at hover, with positive values being achieved at around $\mu = 0.16$, see Figure 7.9. The average total pressure at the core fan face was –25 Pa at hover, with positive pressures being maintained virtually throughout, with the aid of the ram-air effect (Figure 7.10). The core fan should therefore work well with this design of intake.

Figure 7.11 is a plot of the intake efficiency versus advance ratio (note that this is not the inverse flow ratio, $\mu = A_c/A_{inf}$, as used in Figure 6.2). The efficiency is defined as the average total pressure drop over the entire fan face divided by the free stream dynamic pressure, Equation 7.3. The dynamic pressure is calculated from momentum theory for the rotor to avoid division by zero at $\mu = 0.00$. This is unlike the figures given by Seddon et al.[20], but gives a better performance comparison for intakes fitted to rotorcraft.

$$\eta = \frac{P_f - P_\infty}{q_{MR}} \qquad (7.3)$$

It is clear that the efficiency of the intake at low advance ratios was too low. Even though it increased rapidly it only reached positive values at $\mu = 0.15$, corresponding to a flight speed of 30 m/s. The intake efficiencies for Design 2 in Figure 7.11 show a slight improvement at low μ values. But still the efficiency remained undesirably low.

However, the overall intake efficiency for Design 3 improved significantly with respect to Designs 1 and 2. At low speeds the efficiency was still not as desired in the light of figures given by Seddon et al.[20], but the results are promising and could be improved with further design iterations.

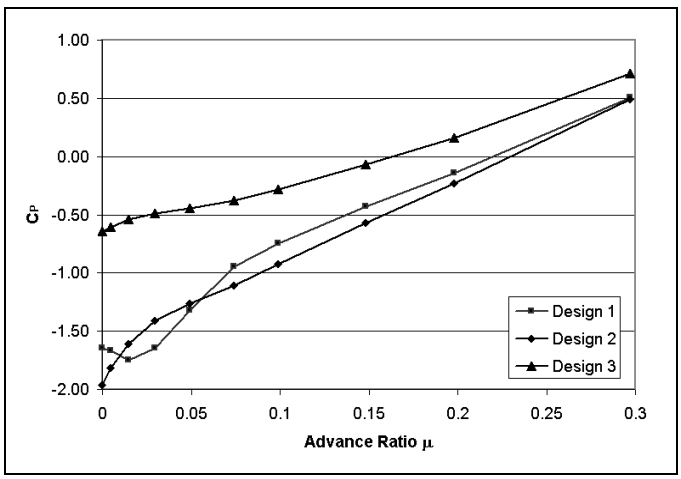

Figure 7.9 Average total pressure coefficient, outer fan

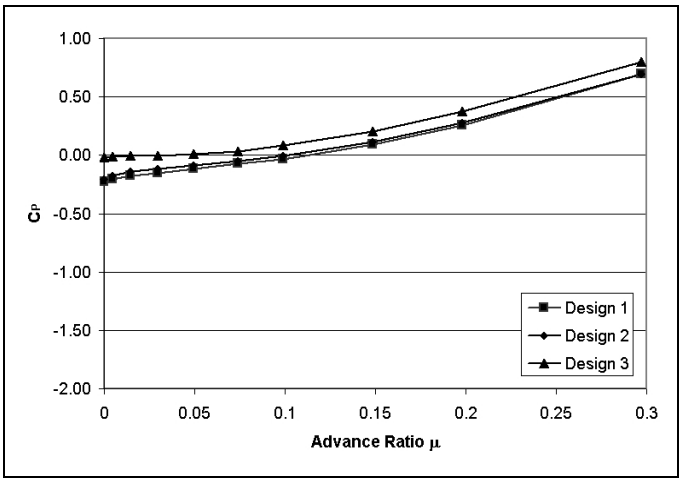

Figure 7.10 Average total pressure coefficient, core fan

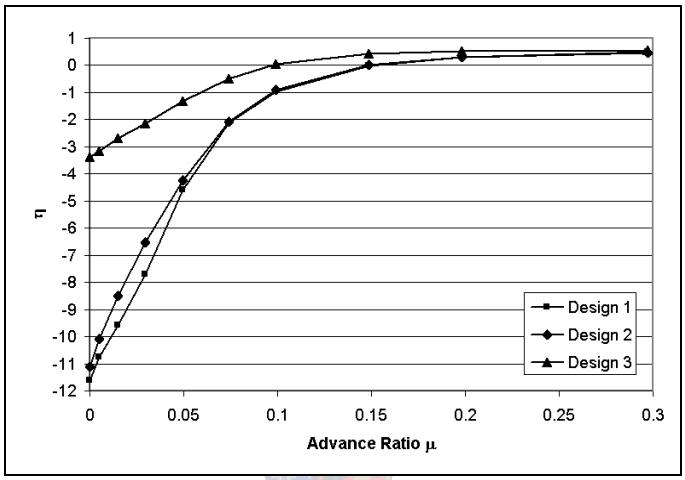

Figure 7.11 Overall intake efficiencies for Designs 1,2 and 3

Conclusion

The objectives of the intake design were to develop practical intakes for the two-stream fan when fitted to the CIRSTEL/Alouette III combination. Studies were done to determine suitable options that can be implemented to improve the intake's performance, primarily during hover. It was important to consider the effects that the intakes would have on the outer fan during hover and low speed flight, as it is in this part of the flight envelope where there is the most dependence on the CCTB section of the tail boom to which the outer fan delivers its air stream.

It was found that during the hovering phase the DC60 coefficients for the outer and core sections of Design 1 were 1.1 and 0.325 respectively. The outer distortion factor was too high; a factor of DC60 = 0.5 is considered the limit, and thus two further design iterations of the concept were completed. For the last iteration the DC60 factors dropped to 0.4 and 0.02 for the outer and core sections. Over the entire tested flight envelope the performance and efficiency of the latest design improved to acceptable levels. Some improvements on the design are still possible, and critical design parameters were identified. Most importantly the position and shape of the intake lips in the upper and side sectors of the intake have to be carefully considered. The upstream flow conditions and presence of any bodies like the fuselage, fairings or rotor hub also have to be considered when designing the intakes. The location of the intake opening on the helicopter also contributes to the feasibility of the entire concept and thus the helicopter configuration should be chosen carefully. In Chapter 9 this problem is evaluated in more detail, while in Chapter 10 the design and modification procedures for the intake with its implications are discussed.

CHAPTER 8

CFD EVALUATION OF HELICOPTER AERODYNAMICS

This chapter presents the findings of simulating a helicopter fuselage in the presence of a rotor, using computational fluid dynamics. The objective is to verify an actuator disk model for use as the main rotor, as a more realistic flow field was sought than the uniform inflow used up to now. An actuator disk model was selected as this saves computing resources by not having to model individual rotor blades with moving grids. Additionally this work served to form a basis for the simulations of the intakes, presented in Chapter 9. The analysis presented here was conducted on the ROBIN configuration, as substantial experimental data is available on this configuration such as by Mineck et al.[29]. Initially a trial series was conducted on a fuselage-only configuration. This served to develop confidence in the mesh and turbulence models eventually used on the full rotor and fuselage simulations. Here use was made of the Fluent commercial CFD software suite. The fuselage and rotor combination was modelled being mounted in a 14- by 22- foot wind tunnel as in the experiments. The actuator disc model used for the simulations is different to the standard approach in that it calculates the section angle of attack by referencing to flow velocity values a finite distance upstream and downstream of the rotor disk, where standard models tend to reference to the flow inside the disc. Thus more accurate answers can be obtained, even for skewed inflows (Hotchkiss et al.[30]). The rotor hub was also included in the simulations, also modelled as an actuator disk, to simulate the effects of the rotor hub on the aerodynamics around the fuselage. It was thought that the hub modifies the flow patterns significantly, though no direct references could be found.

Actuator Disk

Much development has been done on actuator disks for applications in helicopters, either for rotor performance analysis or fuselage aerodynamics, with various degrees of success having been achieved (Chaffin et al.[31], Lee et al.[32], Ruffin et al.[33]). An actuator disc model is sufficient if a non-transient solution is sought that requires the modelling of the passage of the blades and associated tip vortices over the helicopter fuselage. The current study investigates the agreement of numerical solutions with experimental data, to form a basis for further aerodynamic studies, such as intake performance.

To account for the different velocity field occurring in the actuator disk from the 2D flow field on which the blade section lift and drag coefficients are based, the section angle of attack is calculated by the average flow vectors ahead and behind the blade element (Thiart et al.[34]). However, air approaching an airfoil experiences an up-wash ahead of the airfoil, and thus the forward flow vector must be measured a finite distance upstream of the airfoil section, as suggested by Meyer et al.[35]. This concept has been shown to give very good results when compared to the overall experimental performance data of skew inflows to industrial fans (Hotchkiss et al.[30]). These results gave confidence to use the same code to model helicopter rotors, as the global performance should at least be similar to that of a real rotor.

The actuator disk forms a volume in the flow domain that is normally occupied by the rotor into which the momentum sources are introduced, with an identically meshed volume upstream and downstream of the rotor volume (Figure 8.1). The upstream volume is placed about one blade chord length directly above the actuator disk, with a sufficiently fine mesh in between to capture the spin-up of the incoming flow. The error of the blade section angle of attack formed by placing the upstream disk not strictly upstream with the skewed inflow is assumed to be small; at least at

slow advance ratios, flow vectors do not change significantly for a given small region that affects a given blade section. This could however be a problem at high advance ratios. The actuator disk for the current application does not include any coning or tilt of the tip path plane, but blade pitching was modelled using the standard abreviated Fourier harmonic series (Seddon[6]):

$$\theta = \theta_o - A_1 \cos\psi - B_1 \sin\psi \qquad (8.1)$$

Balancing of the rotor for zero pitching and rolling moments around the hub was done on a manual iterative basis, with the assumption that the response to the pitching coefficients is linear. The section lift and drag coefficients for the blades were defined for a NACA 0012 profile, shown in Figure 8.2. The data was interpolated from Riegels[12].

Added to the actuator disk model that simulates the rotor blades was a second actuator disk (volume) that modelled the rotor hub blade roots, as shown in Figure 8.1. Here the section lift and drag properties for the hub were defined as those of a 2D cylinder in cross flow for the calculation of the source terms. A constant lift coefficient of $C_L = 0.0$ and drag coefficient of $C_D = 1.2$ was defined for the section properties. Due to the complexity of the hub volume, no reference planes could be implemented for this actuator model. The flow vectors thus have to be determined inside the hub volume itself. The rotor hub was modelled on that of the 2m rotor used by Mineck et al.[29]. In general the presence of the hub is often neglected in similar simulations; it is thought that the presence of the rotor hub can have a noticeable effect on the aerodynamics of the fuselage, especially in the region of the gearbox cowling.

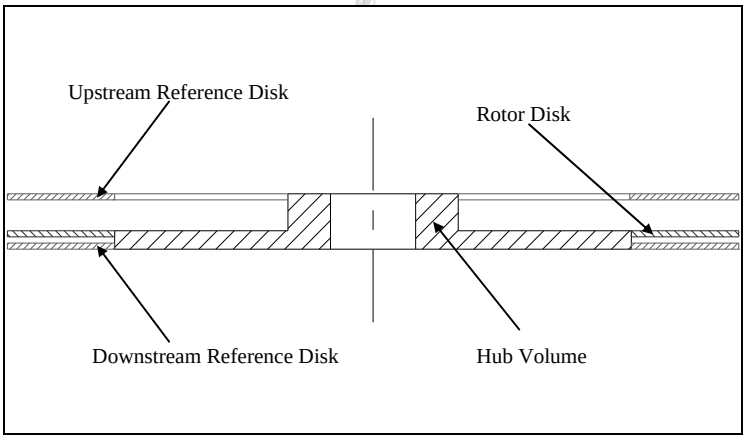

Figure 8.1 Schematic cross section of rotor disk and hub volume, with the location of the referencing disks

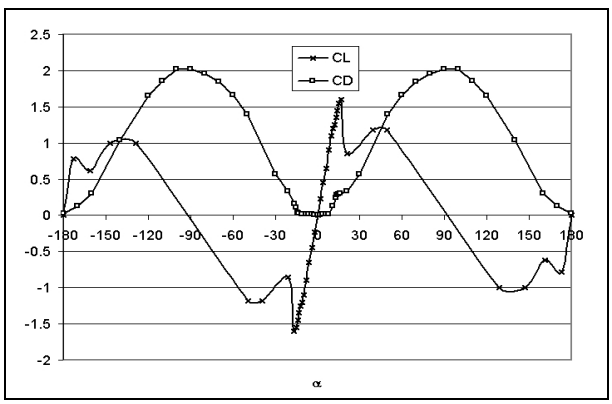

Figure 8.2 Rotor blade section lift and drag coefficients

Fuselage Only Simulations

In preparation the ROBIN fuselage (Mineck et al.[29]) was evaluated without the rotor to define mesh sizing and compare turbulence models. Experimental data based on the work by Freeman et al.[36] is available for a ROBIN fuselage-only configuration in a wind tunnel. For this test case the fuselage was modelled at an angle of attack of -10^o with zero yaw. Due to the symmetry only one half of the flow domain was simulated. The experimental data is however not exactly symmetrical. The experimental data is in the form of pressure measurements taken at several stations on the fuselage surface, which are compared to the CFD data.

The near wall mesh was constructed to give y^+ values below 4 for the expected flows around the fuselage. A y^+ value of 4 or less was selected so that the laminar sub layer would be resolved for better results from the turbulence models. An estimate for the height of the first element can readily be determined from basic boundary layer theory along with the thickness of the boundary layer itself. It was further aimed to keep at least 10 elements in the estimated boundary layer for sufficient resolution of the entire boundary layer. The mesh near the wall consisted of prismatic elements, and for this specific application of the 2m ROBIN fuselage the first element had a height of 0.05mm. After reducing the surface mesh length to 15mm (0.75% of fuselage length) grid independence was obtained. This is of the same order as the mesh used by Chaffin et al.[31] for similar studies. Full use was made of the unstructured mesh capability of Gambit to allow the elements away from the fuselage surface to grow to the selected volume mesh size. Four volume mesh sizes were used and tested for grid convergence; namely 35, 30, 25 and 20mm. For all sizes good agreement with the experimental data was obtained, with the change from 25 to 20mm not yielding any significant improvements. The coarser 35mm mesh is still useful as sufficiently accurate answers are still obtained and less computing resources are required.

Fluent was used to solve the Navier-Stokes equations on the hybrid mesh. The steady, viscid and incompressible flow equations are solved using the SIMPLEC pressure-velocity coupling algorithm. A second order discretisation scheme was implemented for the pressure variable, while the second order upwind discretisation scheme was specified for the remaining variables to ensure stability of the numerical solution.

Consecutive tests were done on all the grid sizes to select a turbulence model. Turbulence models that were evaluated were the k-ε (Launder et al.[37]), k-ω (Wilcox [38]), Shear Stress Transport (SST) (Menter[39]), Spalart-Allmaras (SA) (Spalart et al.[40]) and Detached Eddy Simulation (DES) (Cokljat et al.[41]) models. Surface pressures were compared along four cross-sectional stations as indicated in Figure 8.3 to Figure 8.6. The data presented here is for the 25mm volume and 15mm surface mesh. The pressures are non-dimensionalised with the wind tunnel free stream conditions, which for this case is 21.2m/s at standard atmospheric conditions.

The data on the cross sectional stations is presented as a function of ϕ, the polar angular coordinate used for the definition of the ROBIN body. The use of ϕ instead of the commonly used z coordinate allows for a better presentation and comparison of the data on the upper and lower surfaces of the fuselage.

Reasonable agreement with the experimental data is obtained for all the models over most of the cross sections. At the first station from the nose at x = 0.350R (Figure 8.3) the k-ω model gives an unrealistically high pressure on the upper surface ($\phi = 90^o$) along with a too low pressure below the fuselage. At the station just behind the cowling (Figure 8.4) most turbulence models give good answers, with the SST and k-ω models lying closest to the experimental data. The Spalart-Allmaras and DES models give almost identical results, which results from the near wall treatment of the DES model with the Spalart-Allmaras model and the fact that no significant flow separation occurs to modify the global flow pattern. All models however under-predict the pressure on top of

the fuselage ($\phi = 90^o$), which could be a result of the over-prediction of the wake of the cowling. The difference between experimental and numerical data at the bottom of the fuselage is a result of the wake of the model support strut, which is not modelled in the CFD simulations. The last two stations from the nose at x = 1.135R and x = 1.540R (Figure 8.5 and Figure 8.6) show a separation point on the side of the fuselage at around the $\phi = 60^o$ radial, which can be seen by the sharp reversal of the pressure plot. None of the evaluated turbulence models captured the separation point exactly, with the SST model coming closest. The k-ω model however predicts the pressure distribution on the bottom half the best. The discrepancy between the numerical and experimental data at the last two cross sections is assumed to be, in part, due to an insufficiently fine surface mesh that cannot capture the separation point correctly.

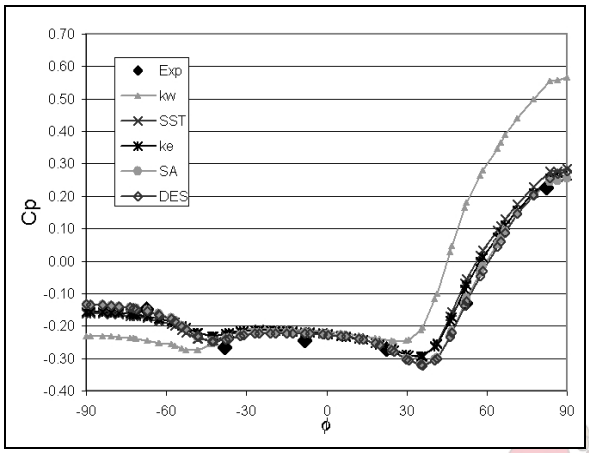

Figure 8.3 Pressure distribution, fuselage only, x = 0.350R

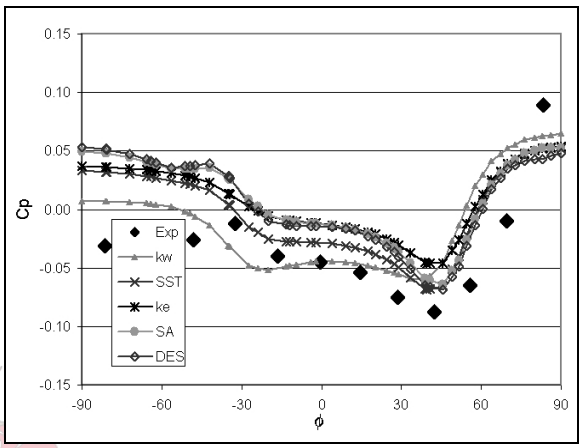

Figure 8.4 Pressure distribution, fuselage only, x = 1.170R

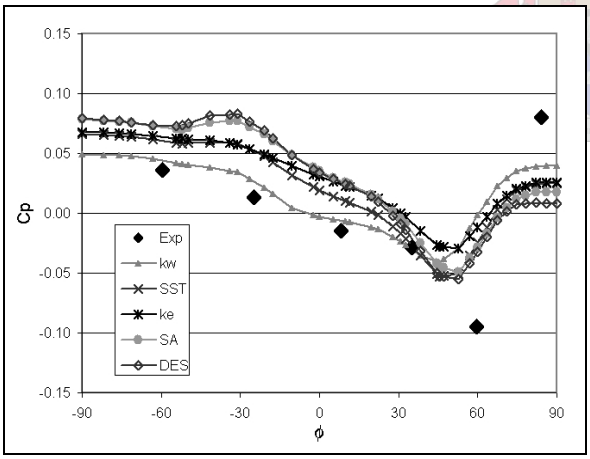

Figure 8.5 Pressure distribution, fuselage only, x = 1.350R

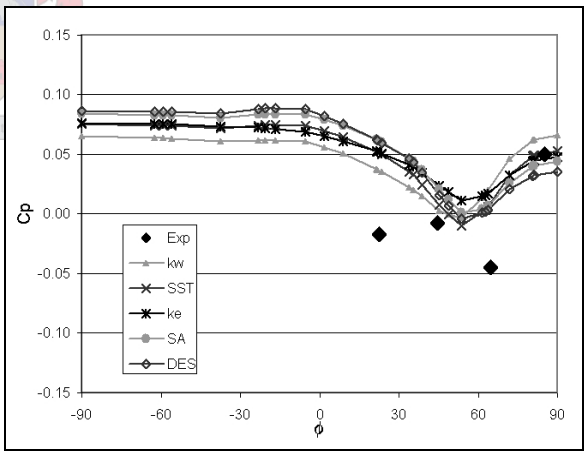

Figure 8.6 Pressure distribution, fuselage only, x = 1.540R

For the range of turbulence models tested, on average, the SST model performs the best over the range of compared experimental data. It is thus the model selected to be used for the full rotor and fuselage simulations. These CFD simulations were conducted using Fluent 6.1. Subsequent simulations with the later release, version 6.2, yielded better answers than the older results, the 35mm mesh giving more accurate results than the 20mm mesh on the 6.1 solver. This follows from the improved numerics in the solver for better spatial accuracy, especially for tetrahedral meshes such as used for the current application (Fluent News[72]). For consistency only the results of the 6.1 solver are shown.

Rotor and Fuselage Simulations

For the initial validation process of using the actuator disk as a helicopter rotor presented here, the simulation was done for one advance ratio and thrust coefficient only. A case from Mineck et al.[29] was selected with an advance ratio of $\mu = 0.05$ and a thrust coefficient of $C_T = 0.00636$. A low advance ratio case was chosen; as in such a case the rotor wake impinges on most of the fuselage and the inflow into the rotor is sufficiently skew to test the capabilities of the actuator disk as a helicopter rotor. The rotor and fuselage combination was again modelled as being in the 14 by 22ft wind tunnel. The mesh was based on the results of the previous fuselage only trials, this time however the entire flow domain with a mesh for the rotor was included to capture the 3D flow effects from the rotor (Figure 8.7).

Two sets of experimental data are available for the selected test case, namely from Mineck et al.[29] and Freeman et al.[36]. The CFD model was defined to mimic the Mineck tests. The difference between the Mineck experiments and that of Freeman is the use of a smaller rotor, with a rotor radius of only 86% of the rotor radius R defined for the ROBIN geometry and with a solidity of $\sigma = 0.098$ compared to the solidity of $\sigma = 0.0871$ of the Freeman experiments. However both data sets are used for comparison as they show the same trends of the pressure distribution.

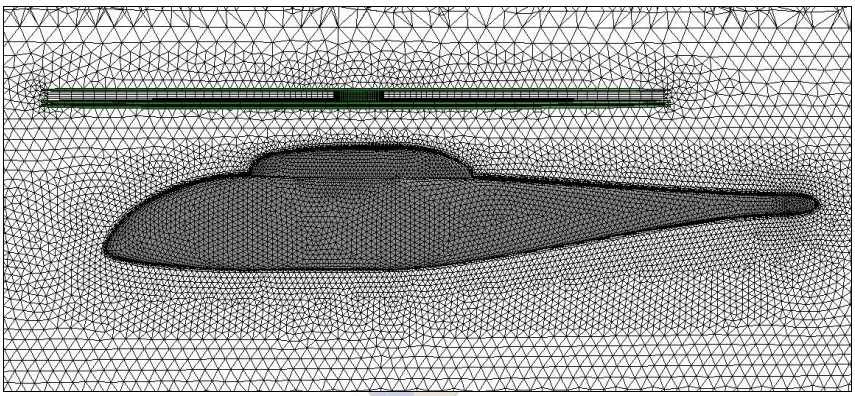

Figure 8.7 Mesh configuration for ROBIN with rotor and hub

Qualitative analysis

When qualitatively comparing the CFD data to the oil flow experiments done by Mineck et al.[29] in Figures 8.8 and 8.9 it is noticeable that the streak lines for the selected experimental thrust coefficient of $C_T = 0.00687$ do not follow the experimental streak lines closely. The angle of the numerical streak lines is too shallow, almost suggesting that the thrust coefficient used is too low. Based on this assumption a run was conducted for twice the specified thrust coefficient, and for this case the streak lines compare better with the experiments.

Figure 8.8 graphically compares the two cases to the experimental results on the advancing side of the fuselage; the dark streak lines are from the numerical simulations. On the nose and centre sections the streak lines are better predicted by the high thrust case. The streak lines on the cowling are also better captured with the high thrust case, as well as the wake of the hub at the trailing edge of the cowling and the convection of this wake down the starboard side that is evident from the experiments. None of this is seen in the standard case, the streak lines again only conforming rearwards of the cowling.

On the retreating side shown in Figure 8.9 the nose forward of the rotor wake the streak lines predicted by the double thrust case are again much better predicted, similar also in the mid-fuselage section. The influence of the hub-wake, which is evident in the experiments, is also only presented in the high thrust case. Only towards the rear of the fuselage behind the cowling do the

original results again compare well with the experiments. On the cowling the streak lines are not well represented.

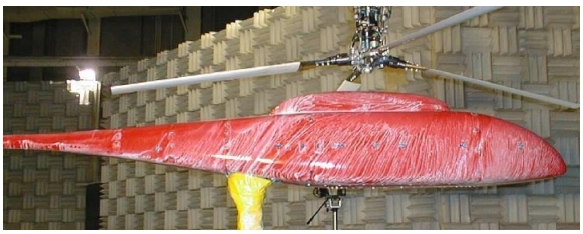

(a) Original Experiment, form Mineck et al.[29]

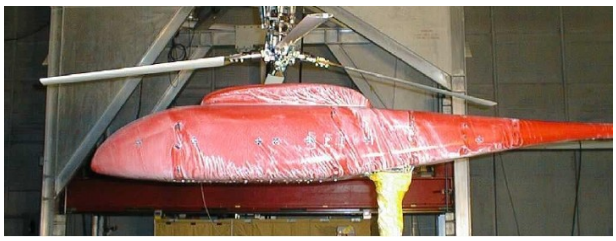

(a) Original Experiment, form Mineck et al.[29]

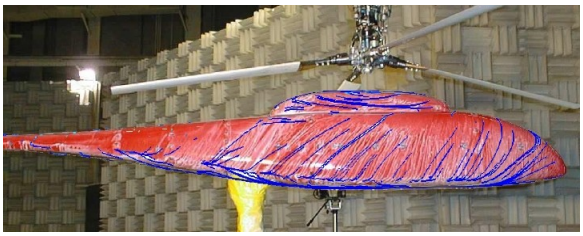

(b) CFD results superimposed, C_T = 0.00687

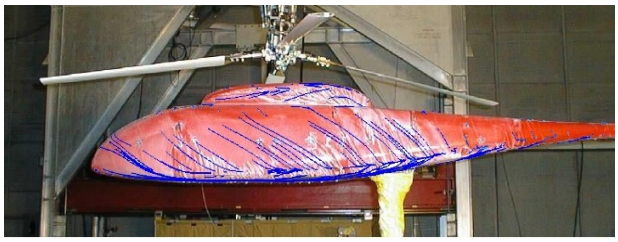

(b) CFD results superimposed, C_T = 0.00687

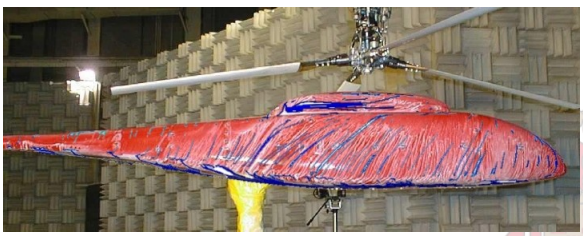

(c) CFD results superimposed, C_T = 0.0134

Figure 8.8 Streak lines, experimental vs. numerical on advancing side

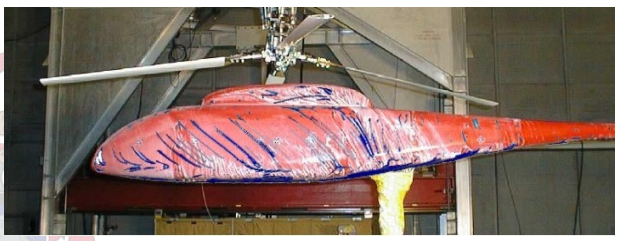

(c) CFD results superimposed, C_T = 0.0134

Figure 8.9 Streak lines, experimental vs. numerical on retreating side

Quantitative Analysis

The rotor was iteratively balanced to have a zero moment about the hub. Table 8.1 shows the collective and pitch angles obtained for the two cases, along with the experimental values from Mineck et al.[29]. The difference between the experimental and numeric values for the C_T = 0.00636 conditions can, amongst others, be attributed to a lack of coning of the rotor actuator disk.

Table 8.1 Trimmed pitch conditions

Case	θ_o	A_1	B_1	α_s
Mineck et al.[29], C_T = 0.00636	11.9°	-1.3 °	1.3 °	0.0 °
CFD, C_T = 0.00687	8.35 °	-2.11 °	1.25 °	0.0 °
CFD, C_T = 0.0134	14.72 °	-1.73 °	2.70 °	0.0 °

Mineck et al. supplies time averaged data for 12 points measuring transient pressures on the upper surface of the centre line. First comparing the pressures on the centre line shows that the standard C_T = 0.00636 case predicts the pressure on the top of the fuselage well; for most of the fuselage length the predictions lie close the experimental values, except for the nose section and behind the cowling (Figure 8.10).

The pressure distribution for the double thrust case is too high by a factor of two. There are however two sections in which that data predicts the trends well. The first is the nose section; although the pressure is predicted too high, the data predicts the higher pressure ahead of the cowling leading edge, which is not shown in the standard case. This higher pressure corresponds to the leading edge impact point of the rotor wake, which is correctly predicted by the double thrust case, as is also evident from the streak lines.

The second area where the double thrust case predicts the trend well is at the trailing edge of the cowling. Though not exactly captured, the low-pressure region is as a result of the rotor hub. For the standard case no evidence of the hub wake is seen.

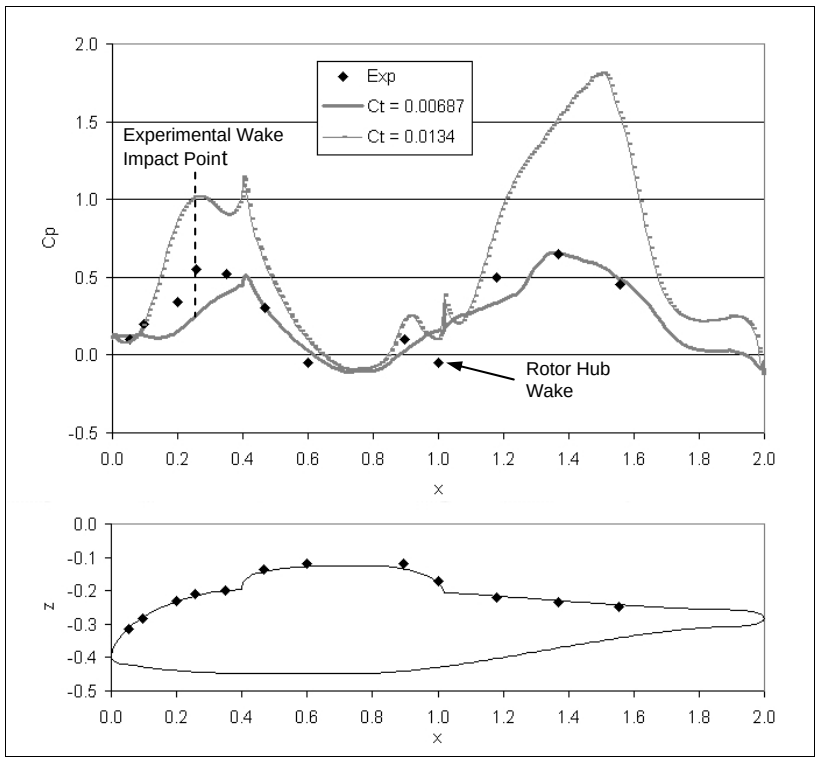

Figure 8.10 Pressure distribution on centre line, upper fuselage

Comparing the pressure distributions at the four cross-sectional stations shows that, in general, the better the pressure on top of the fuselage is predicted (essentially the stagnation point) the better the pressure distribution around the fuselage is predicted. Data from Mineck et al. [29] is represented by "Exp 1" in Figures 8.11 to 8.14, while data from Freeman et al.[36] is represented by "Exp 2".

For the station at x = 0.350R (Figure 8.11) neither of the two cases predicts the pressure distribution around the fuselage correctly, though the double thrust case again captures the trend better by displaying the low-pressure at the $\phi = -40^o$ position on the advancing side. This is as a result of the rotor wake passing that position which does not occur in the standard thrust case. The pressure contour on the upper half ($0^o < \phi < 90^o$ on advancing, $-90^o < \phi < 0^o$ on retreating side) on both sides is however sufficiently well predicted by the standard case. On the plot for the retreating side the predictions of Chaffin et al.[31] (C&B on the legend) are plotted as well. Their predictions show a pressure trough at the $\phi = 40^o$ position in Figure 8.11 (b) which is not evident in the experiments. This is attributed to a lack of prediction of the separation point on the lower corner of the fuselage in their simulations. Thus the current simulations are a small improvement of what has been achieved till now.

At the section x = 1.170R (Figure 8.12) the double thrust case predicts the stagnation pressure well, and following on this the general pressure distribution is well presented. The low-pressure spike, (which is especially well presented by the Freeman[36] data, $\phi = 40^o$ on the advancing side) is a result of the hub-wake influencing that point. The shallower angle the hub-wake forms for the standard case means that the wake does not have such a strong influence, as seen by the CFD data. The low-pressure trough on the upper surface ($\phi = -40^o$) on the retreating side is however not captured by any of the two cases. None of the troughs on the retreating side are captured by the Chaffin et al.[31] results. To note here is also the differences in the two experimental datasets.

For the last two sections at x = 1.350R and x = 1.540R (Figure 8.13 and Figure 8.14) both cases give reasonable answers, though the standard case on average again gives more accurate results on the upper section of the fuselage, as already discussed, whereas the double thrust case over predicts the pressures, but clearly follows the trends.

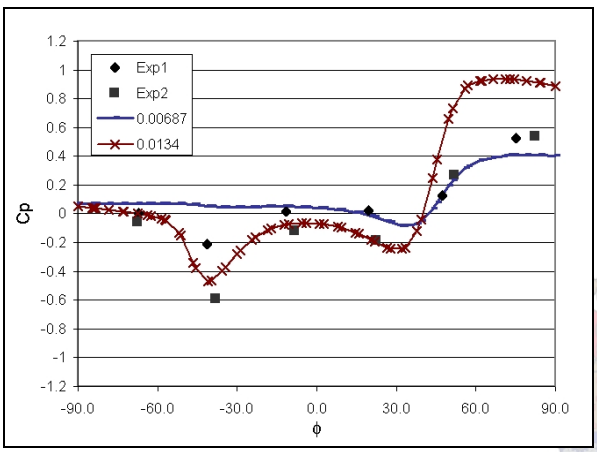

(a) Advancing

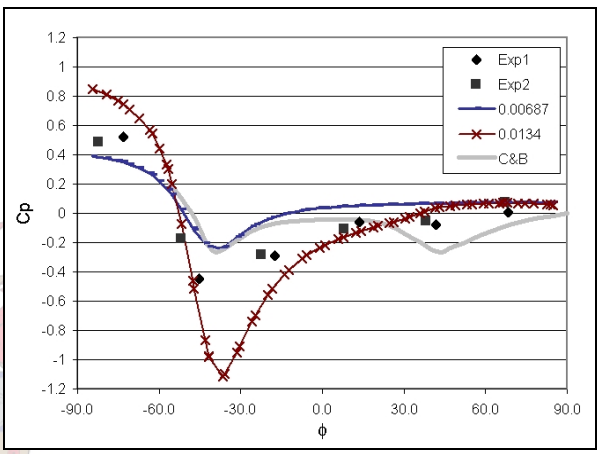

(b) Retreating

Figure 8.11 x = 0.350R

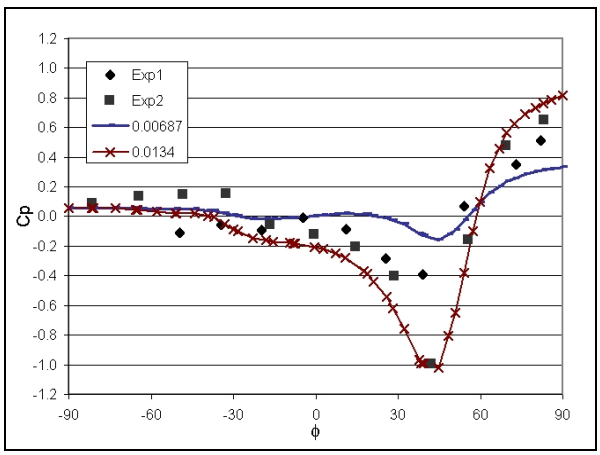

(a) Advancing

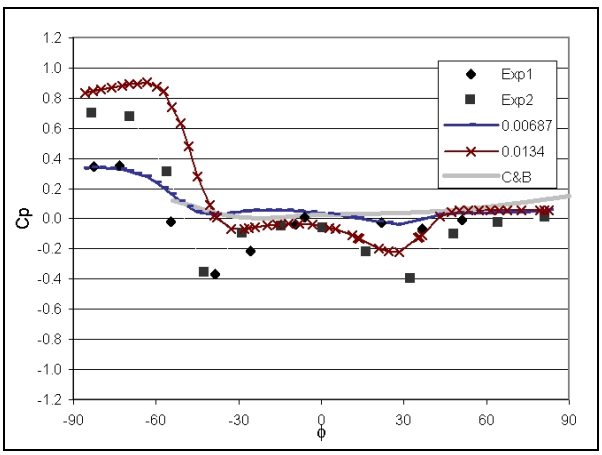

(b) Retreating

Figure 8.12 x = 1.170R

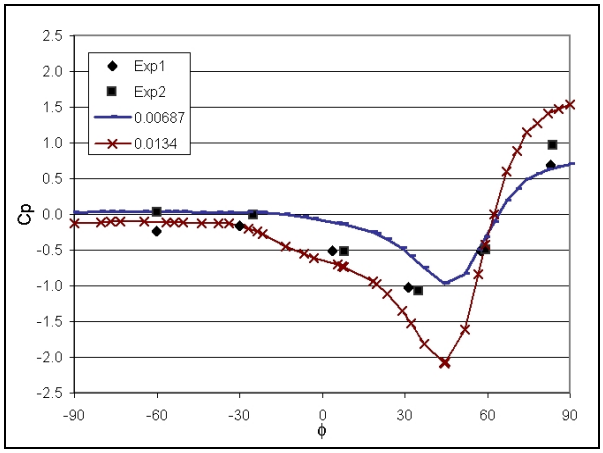

(a) Advancing

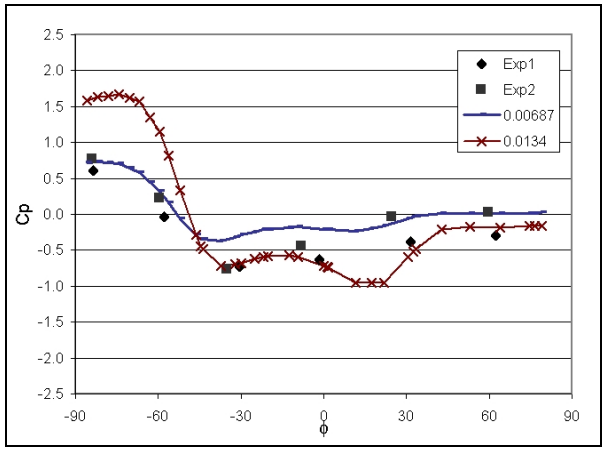

(b) Retreating

Figure 8.13 x = 1.350R

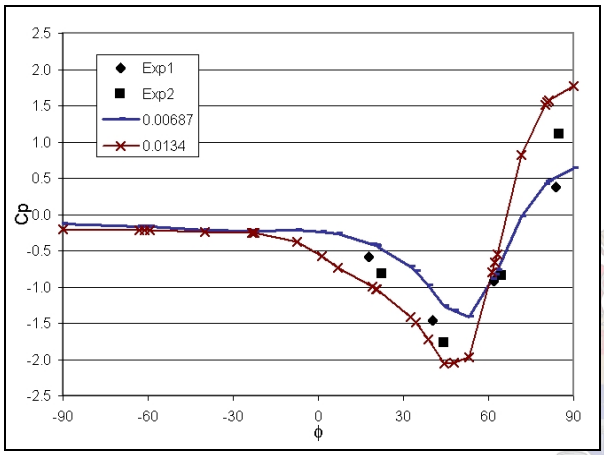

(a) Advancing

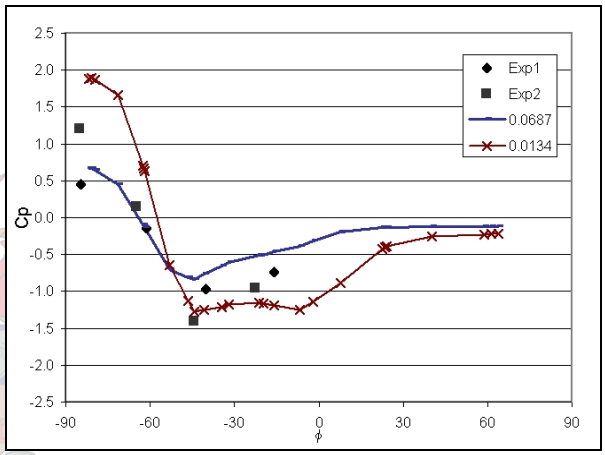

(b) Retreating

Figure 8.14 x = 1.540R

Effect of the Rotor Hub

The pressure measurements are of insufficient resolution to trace the effects of the rotor hub sufficiently; the only evidence being on the top surface just behind the cowling (Figure 8.10). The inclusion of the hub in the simulations could thus not be quantified explicitly. Qualitatively, the streamlines from the hub are compared in Figure 8.15; (a) shows the streamlines through the hub with hub actuator model included and (b) hub actuator model switched off. Clearly visible are the streamlines forming a helix on the advancing side of the fuselage. This flow pattern is not present in the hub off case; the flow field is thus noticeably changed in the lee of the hub, which has important effects on the local aerodynamics of the fuselage. The hub wake also influences the trimming of the rotor. Also, due to the backwards "paddling" of the hub on the retreating side the airflow is modified on that side.

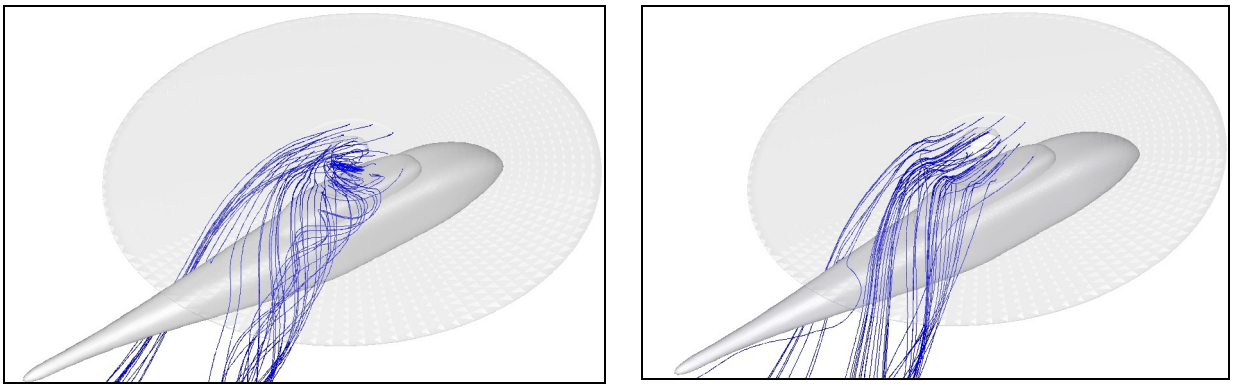

(a) Rotor hub included **(b) Rotor hub excluded**

Figure 8.15 Streamlines comparing the effect of the rotor hub on the flow patterns in the simulations

Conclusion

Ruffin et al.[33] already indicated that the load distribution of the rotor disk has an important effect on the pressure distribution on the fuselage. In the current application the pressure distribution of the disk was not prescribed as applied by Ruffin et al.; rather the load distribution resulted from the trimming of the rotor disk with the pitching coefficients. Thus the pressure distribution predictions are improved. This is also the case when comparing the current results to the predictions of Chaffin et al.[31].

From the analysis so far it would appear that a significant contribution to the differences of the numerical data is the angle of the rotor wake relative to the fuselage. Using the average induced velocity from the CFD results in a basic momentum analysis confirms that the actuator disk does produce the specified thrust. Further comparing the load distribution of the rotor for the two cases shows that the rotor with the high thrust setting has a higher loading at the leading and trailing rim of the rotor; the standard thrust case even has a significant portion of the rotor leading edge experiencing an up-wash through the rotor. This will have a significant effect on the downwash structure; a higher loading at the leading edge forces more air downwards at the leading edge.

Further reasons identified for the difference between the numerical and the experimental downwash distribution is the lack of coning and the tilt of the tip path plane. Both these factors influence the load distribution on the rotor and hence the rotor-wake.

Also, the method of determining the blade section angle of attack can introduce some error at the leading edge of the disk. In the trial done by Hotchkiss et al.[30] with this method a shrouded fan was modelled. Unlike that fan the current rotor is not shrouded and this allows the flow pattern to change noticeably between the upstream reference disk and the actuator disk itself, especially at the leading edge of the rotor.

As already stated, the aim is to develop a method by which rotorcraft intake aerodynamics can be evaluated, and the hub with its control rods can have significant effects on the local aerodynamics around the intakes. All the simulations here were done on a PC desktop machine. The computational effort is low and thus the method forms a useful evaluation tool. Useable results have been obtained from these simulations, with the actuator disk showing promising results that can be improved with fine-tuning on the basis of the points discussed above. In general the wake angle and downwash have to be predicted correctly for the pressure distribution around the fuselage to be correct. It is shown here is that the pressure distribution on the upper fuselage surface is correctly predicted apart from the leading edge and the trends of the pressure distribution around the fuselage are captured if the wake angle is closer to the experimental.

CHAPTER 9

CFD EVALUATION OF TOP AND SIDE MOUNTED INTAKES

The fan intake analysis in Chapter 7 was for side mounted intakes only. It is thought that top mounted intakes might offer advantages over side mounted intakes by being able to capture the rotor downdraft better in hover and slow flight conditions. Side intakes require the flow to turn both inwards and rearwards before entering the fan, while for the top intakes in general only one rearwards turn is required. Thus side intakes could incur higher losses compared to the top intakes. The positioning of the intakes could also offer advantages over the entire flight envelope by capturing air of higher total pressure and less distortion. In addition to comparing the two intake concepts, the effects of the rotor hub on the performance of the intakes were also investigated.

To investigate the two different intake concepts, CFD studies were done on a generic helicopter fuselage configuration that included an actuator disk to represent the main rotor. The top intake would be suitable for a twin-engine helicopter, while a single engine helicopter would require side intakes, for a standard layout where the engine would be mounted in the centre line above the fan. The size selected for the helicopters is of the light utility helicopter class already described in Chapter 5. The two system designs of Chapter 5 are implemented here for the intake evaluations.

The analysis of the intakes presented here follows a different path and is more detailed than that presented in Chapter 7. To better understand the design issues of the intakes, the performance as a whole is not investigated as such. Instead, individual design aspects of the intakes are analysed, such as positioning of the intake opening and duct losses.

Fuselage

A generic fuselage configuration was used for the investigation of the intake concepts. This fuselage was based on the ROBIN configuration (Mineck et al.[34]), modified here to be representative of a tail-rotor-less helicopter fuselage, with a constant diameter tail boom of diameter 0.13R for the circulation control section. The main fuselage is identical for both versions. The cowlings were modified to be representative of a single- and a twin-engine helicopter. The single-engine version, shown in Figure 9.1, had the gearbox cowling extended from the original to accommodate the exhaust duct into the tail boom. The twin-engined helicopter on the other hand had the gearbox cowling shortened, with an additional cowling added to form the engine bay cowling, shown in Figure 9.2. Both fuselages have an R = 11m rotor diameter in order to represent the helicopters described in Chapter 5. For details and coefficients describing the two fuselage configuration dimensions refer to Appendix E.

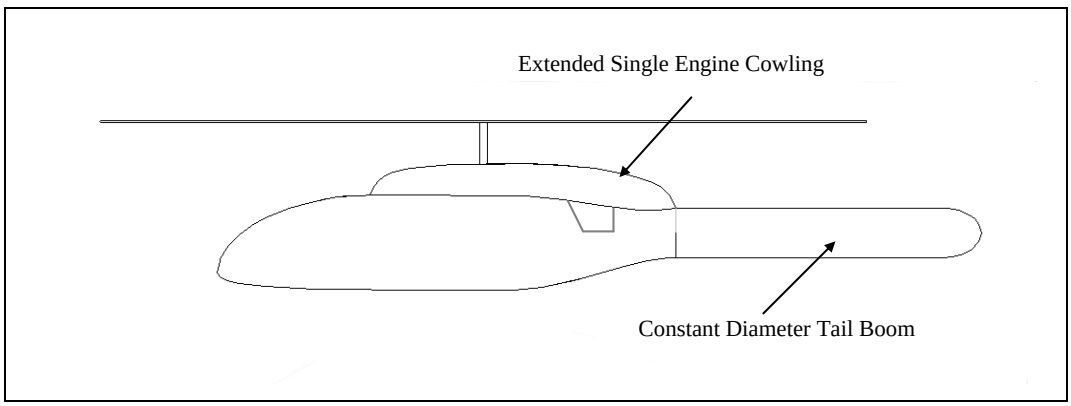

Figure 9.1 Modified single engine ROBIN fuselage

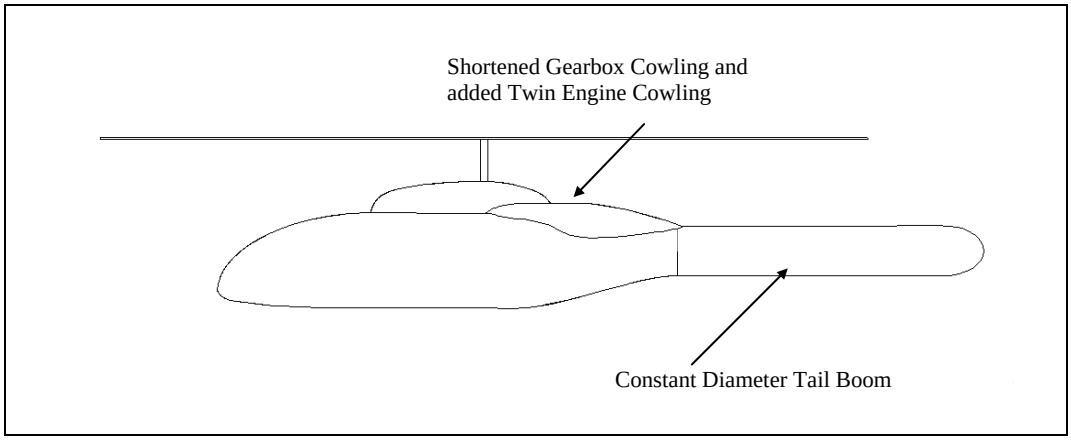

Figure 9.2 Modified twin engine ROBIN fuselage

Intakes

The intakes were designed with the spatial constraints of the fan and its diffuser, as well as engines and gearbox, in mind. The fan has a diameter of 550mm for both versions, with a duct housing of 300mm in length. This excludes the fan diffuser. The rear end of the fan was placed 410mm ahead of the start of the circulation control section of the tail boom, the space in between being designated for the diffuser. The axis of the fan is tilted upwards, to point the drive shaft directly at the main gearbox. A limit for the forward end of the intakes was also set, this being 1800mm forward of the tail boom base.

Three contraction ratios were investigated for both fan intake versions, namely contraction ratios of 2.5, 3.0 and 3.5. The inlet opening/capture area (A_c) was varied to obtain the specified contraction ratios. At 30% down the length of the intake duct, the duct cross section was also specified, along with the cross sectional area. Here the area was specified to be 1.5 times the fan area, and remained constant for the different contraction ratios used. The dimensions of the inlet capture area were scaled linearly to obtain the required contraction ratio.

Side Mounted Intakes

The side mounted intakes are designed for fitment to the single-engine helicopter. In the general layout of the single-engine helicopter the engine is mounted above the fuselage to the rear of the rotor gearbox. Thus the intakes have to open to the side here, similar to the design for the Alouette III discussed in Chapter 7. The intakes were designed by applying the design principles discussed in Chapter 6; also the insights gained from the Alouette III intakes flowed into the current design. These side intakes for the generic fuselage are located at a position similar to that of the intakes for the Alouette III.

Inherently the side intakes form a complicated duct; the incoming flow has to turn towards the intake, turn inwards to enter the duct and then rearwards toward the fan face. As in the final design of the Alouette III intakes, the intakes feature thick lips on the upper rear corner of the inlet opening and a smooth transition of the cowling surface into the intake duct. Here a scoop is also included at the bottom of the intake. The capture area of the intake is a 3D curved surface, thus the duct entry is also a complicated 3D surface as can be seen in Figure 9.3. Design features of the intake include the following:

- Entry area faces slightly upwards, to capture downdraft.
- Scoop included at the lower side of the intake opening to aid in capturing air.
- Elliptical intake lips at the rear and bottom sides of the intake.

- Blended surface from duct to the fuselage at the front and top.
- Duct entry is facing 57.0^{o} sideways from forward to allow efficient capture at intermediate flight speeds. Duct then turns axially to guide the air into the fan.
- Fan axis tilted upwards by 7.0^{o}.
- Duct cross section changes from rectangular at capture area to double-elliptical to semi-circular, before joining up with the opposing side duct ahead of the fan. Due to the short duct length no effective Gerlach shaping (described by Seddon et al.[20]) could be implemented, as this would cause a too distorted duct shape. The double-elliptical section at the duct bend is however elongated for better flow turning, as described by Sawyer[43].
- Fan has an elliptical hub nose cone.

Details of the intake duct cross section geometry are given in Figure 9.4 along with Table 9.1.

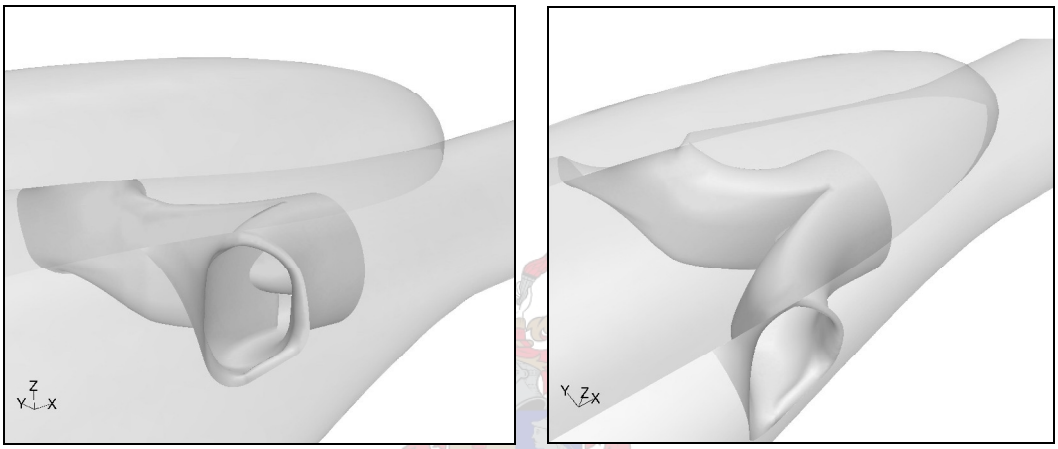

Figure 9.3 Side intake duct (fuselage displayed semi-transparent)

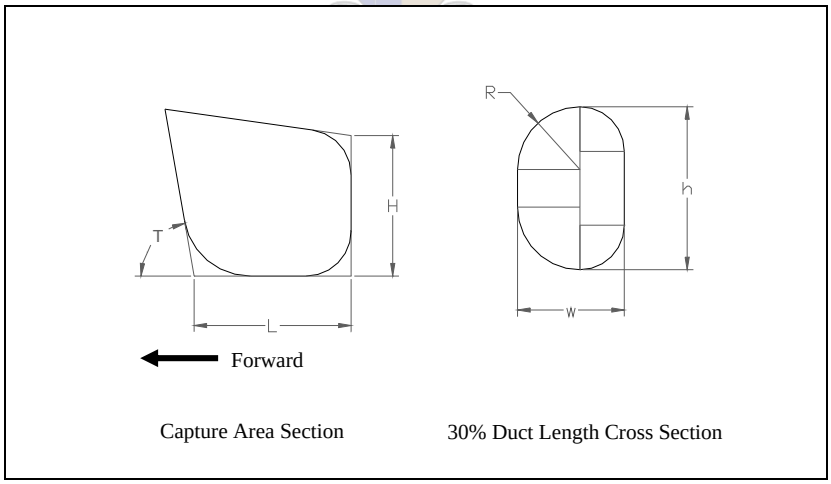

Figure 9.4 Side intake duct cross sections

Table 9.1 Dimensions for Side Intake Cross Sections

Contraction Ratio	2.5	3.0	3.5	Common to all Contraction Ratios	
H [mm]	383	419	452	h [mm]	486
L [mm]	430	471	510	w [mm]	320
T [^{o}]	100^o	100^o	100^o	R [mm]	187

Top Mounted Intake

The top mounted intake is designed for the twin-engine helicopter for fitment between the two engines. This requires that the engines be spaced far enough apart for the intake to fit in between them. For the top intake, air enters the intake duct from the top of the fuselage and is then turned rearwards towards the fan (Figure 9.5). Design of this type of intake is simpler, since effectively only one turn of the flow is required once it has entered the duct. This layout requires the fan drive shaft to extend from the fan across the intake duct, resulting in some disruption of the intake flow. Design features of the top intake include the following:

- Entry area of the intake is on top of the fuselage, facing upwards for ideal capture of the downdraft.
- Intake located behind gearbox cowling and between the two engines.
- Elliptical intake lips of large radius form the transition of fuselage into the duct.
- Duct entry centre line is slanted 55.0^o upwards from the horizontal axis. The forward slant of the intake is to allow for an efficient capture of the air in forward flight.
- Intake flow is turned into the fan. The fan axis is tilted upwards by 16.0^o from the horizontal axis.
- The shape of the capture area is derived from streamline patterns of a cross flow entering a hole on a flat plate, as described by Holdø et al.[22]. The intake capture area is shaped to allow for a smooth inflow of the air from the stagnation zone behind the intake and saddle points on the side of the opening.
- A similarly shaped cross section is used to describe the duct shape before transitioning to circular ahead of the fan. The intermediate cross section is elongated for better flow turning, as described by Sawyer[43].
- The fan is fitted with an elliptical nose cone from which the shaft extends.

Details of the intake duct cross section geometry are given in Figure 9.6 along with Table 9.2.

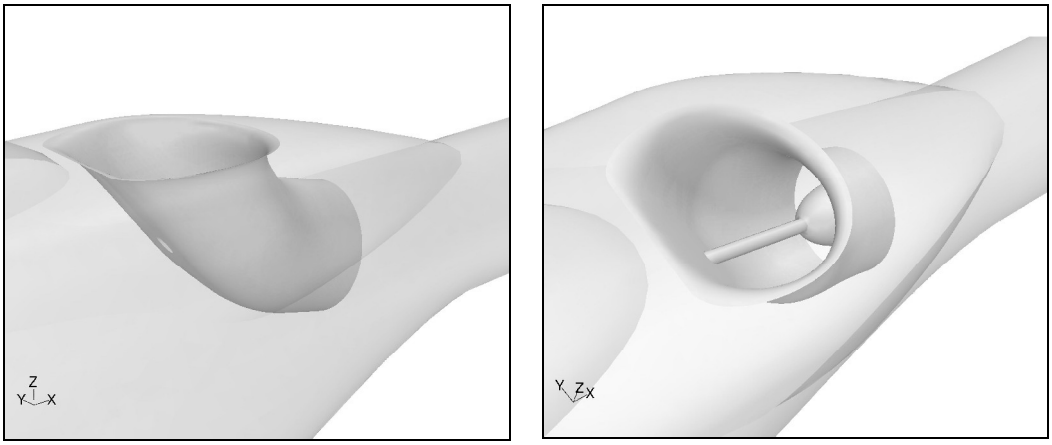

Figure 9.5 Top intake duct (fuselage displayed semi-transparent)

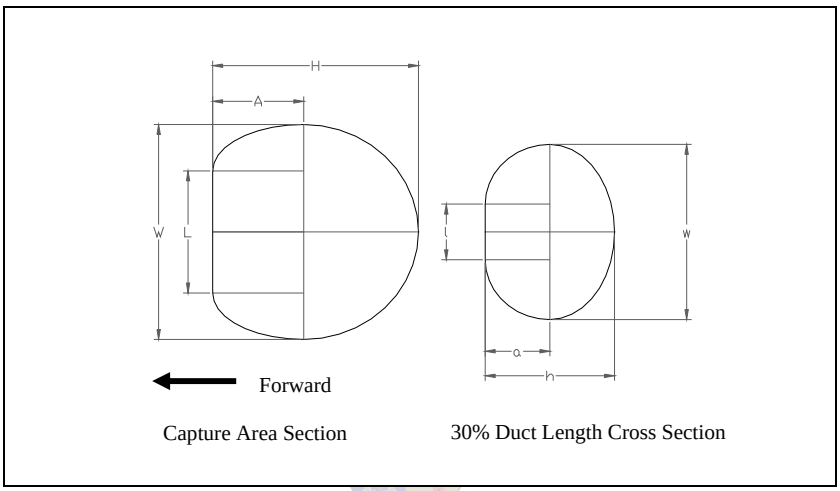

Figure 9.6 Top intake duct cross sections

Table 9.2 Dimensions for Side Intake Cross Sections

Contraction Ratio	2.5	3.0	3.5	Common to all Contraction Ratios	
H [mm]	712	780	843	h [mm]	490
W [mm]	740	810	876	w [mm]	660
A [mm]	315	345	373	a [mm]	245
L [mm]	420	460	497	l [mm]	210

CFD Model

The mesh used here for the simulations is of a similar resolution to that developed in Chapter 8, except that here the full size helicopter dimensions are used. The flow domain defined was 3.32 rotor diameters wide, extends 2.56 diameters upstream and 5.06 diameters downstream from the

rotor centre. The domain was 2.21 diameters high, with the rotor origin located at two-thirds height. This is a scaled up version of the dimensions used in the verification case. For the low speed flights of $\mu = 0.000$ and $\mu = 0.015$ the domain was shortened downstream, but extended upwards by 0.5 diameters and downwards by 1.5 diameters. This is to prevent boundary condition effects and reduce recirculation of flow into the flow domain.

The mesh was a combination of hexahedral and tetrahedral mesh elements, generated with the commercial code Gambit. The mesh for the rotor disk and hub was constructed from hexahedral cell elements, while the rest of the domain was constructed with tetrahedral elements. Use was made of the unstructured mesh to have a finer mesh resolution near the fuselage. The boundary layer mesh was made from prismatic elements, with a surface length of 82mm. The first element of the boundary layer mesh was 0.1mm high, with a growth rate of 1.6 for the following 8 elements. In the immediate vicinity of the fuselage the volume mesh size was 192mm, increasing to 300mm. For the far field element size went up to 1375mm. See Figure 9.7 for a general view of the meshed domain and details of the hub mesh

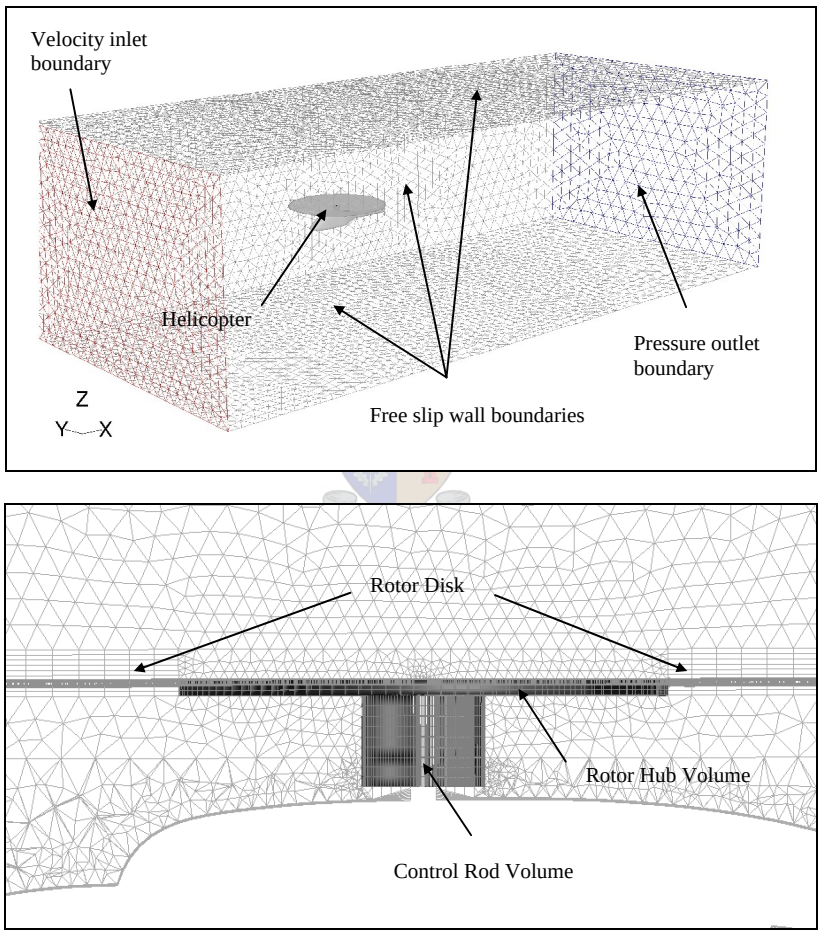

Figure 9.7 General mesh configuration and detail of the rotor hub mesh

A separately built mesh for the intake ducts was used for simplicity and then interfaced with the main mesh. The interface between the two meshes is the capture area of the intake. The mesh resolution for the duct was 22mm, with boundary layer elements being 0.05mm high at the wall, growing at a rate of 1.6 for a total of 9 elements. Total count for the combined mesh was 1.54 million elements. This also formed the practical upper limit for the resources available to do the simulations.

Boundary conditions applied were free slip walls on top, bottom and side domain boundaries, with a constant velocity boundary at the inlet of the flow domain to enforce the air speed. The exit of the flow domain was set as a constant pressure boundary. The required mass flow through the intake, and thus the fan demand, was set with a velocity boundary of the average specified flow velocity in the duct. This boundary condition was applied five fan diameters downstream of the fan to prevent boundary interferences. The split in the fan was not simulated. Flow density and pressure were defined to simulate the atmospheric conditions used in the system calculations of Chapter 5.

The commercial CFD solver Fluent was used to resolve the flow in the domain, using an implicit formulation to solve the Navier-Stokes equations on the hybrid mesh. The flow equations are solved using a second order discretization scheme with a SIMPLEC pressure-velocity coupling algorithm. The steady, viscid and incompressible computations took between 700 and 1500 iterations to converge, depending on the case simulated. Due to the flow recirculation through the domain boundaries during the hovering and slow speed flight simulations, the simulations took more than double the number of iterations to converge than that of the high-speed flight simulations. Convergence was obtained when the continuity and turbulence residuals for the global flow field reached the specified numerical accuracy of $1 \cdot 10^{-5}$. The recirculating flow field of the slow flight speed simulations prevented the global continuity residuals to reduce to below $1 10^{-3}$.

The actuator disk models used in Chapter 8 were used here again for the rotor and hub. For the current simulations the hub volume was modified to also include the control rods, as shown in Figure 9.7, so that the same actuator disk also models these control rods. The trimming of the rotor had to be done manually as a trimming routine is not implemented in the actuator disk code. A process was however followed that systematically searched for the correct trimming coefficients within 4 to 5 runs of the simulations. For the first run pitch and trim coefficients (θ_o, A_1 and B_1) were calculated analytically (Prouty[44]). From that first solution a prediction for the second set of trim coefficients used for the next run could be made. With the solution of the first and second runs a linear interpolation of the three coefficients was done to predict the next set of trim coefficients. The process is repeated for the next few runs, until the rotor is acceptably trimmed to the desired thrust and moment settings. If the initial solution is already converged, the coefficients can be changed after 100 time steps iterations already, without the requirement of a fully converged solution. The steps described here can be implemented as a subroutine in the actuator disk code to automatically trim the rotor to the desired trim settings.

The specifications of the rotors of the two helicopter versions were different, though both had the same diameter with a 24% root cut out. Additionally the respective thrust coefficients also differed. Thus each rotor had to be trimmed separately to obtain a zero rolling and pitch moment about the hub as well as the correct thrust setting. The trim conditions for the two rotors are given in Table 9.3 and Table 9.4. Rolling and pitch moment balance errors were below 0.45% and 1.0% respectively from zero (percentage of rotor thrust times rotor radius) and the thrust error was below 1.2% of the specified thrust values for the range of advance ratios selected.

Table 9.3 Single-engine helicopter rotor details

$C_T = 0.00555$	R = 5.5 [m]	Twist = -1.66 [°/m]	RPM = 350	# Rotor Blades = 3
μ	0.000	0.015	0.050	0.149	0.198
θ_o	10.211	10.273	9.653	7.649	7.400
A_1	0.000	-0.606	-1.900	-1.339	-1.082
B_1	0.000	0.665	1.500	2.849	3.562

Table 9.4 Twin-engine helicopter rotor details

C_T = 0.00668	R = 5.5 [m]	Twist = -1.66 [°/m]	RPM = 384	# Rotor Blades = 4
μ	0.000	0.015	0.050	0.149	0.198
θ_o	8.926	8.991	8.541	5.984	5.833
A_1	0.000	-0.399	-1.762	-1.675	-1.258
B_1	0.000	0.339	1.237	2.131	2.647

Side Intake Evaluation

Results discussed in this section are for the side intakes of the single-engine helicopter for the three contraction ratios over the selected range of advance ratios. Comparison is also made of the effects that the inclusion or non-inclusion of the rotor hub has on the performance of the intakes and fan. The split between the inner and outer fan sections was taken at a diameter of 516mm. This is not the same diameter as that where the fan shroud would be located for a uniform inflow velocity, but was based on a 4% outer wall duct blockage of the flow approaching the fan. The blockage has a large effect on the available flow area of the outer fan section, but only a small effect on the core section.

Capture Area Pressure Coefficient

Here the total pressure at the opening, or capture area, of the intake is presented, normalised with the free stream dynamic pressure, as defined by Equation 9.1. The figures presented here are thus essentially a measure of the effectiveness of the position of the intake. The free stream velocity used to calculate the dynamic pressure is based on the average velocity through the rotor disk, as calculated by momentum theory (Seddon[11]). This avoids the division by zero at μ = 0.00 if the flight speed is used. Additionally it provides a better measure for normalisation as the intakes are significantly affected by the rotor downwash. Free stream values as calculated by momentum theory for the single engine helicopter are given in Table 9.5.

$$C_P = \frac{P_C - P_\infty}{q_{MR}} \qquad (9.1)$$

Table 9.5 Free stream velocities for the single-engine helicopter

μ	0.000	0.015	0.050	0.149	0.198
V_{MR} [m/s]	10.62	10.83	13.21	30.27	40.01

Figure 9.8 shows the average total pressure coefficients at the capture plane of the side intakes over the range of tested advance ratios. At μ = 0.00 there is a small difference between the hub and the no-hub results: the hub results have a 0.1 higher C_P value for all contraction ratios. The hub therefore has a small positive influence. The contraction ratio has a noticeable effect at low advance ratios; a higher contraction ratio, and thus a larger net capture area, gives a better performance.

At μ = 0.015 the hub included results are decidedly worse, indicating a strong influence of the hub at that advance ratio. As can be seen by the streamlines entering the intake in Figure 9.9 the flow first passes through the hub, and thus is subjected to significant losses. Increasing the contraction ratio again helps, but no significant improvement is found above a contraction ratio of CR = 3.0.

For advance ratios higher than $\mu = 0.050$ the difference between hub and no-hub results becomes smaller because the hub wake is convected past the inlet area. Above $\mu = 0.050$ the effects of the contraction ratio also becomes smaller.

At $\mu = 0.050$ the C_P value is larger than one due to the majority of the flow entering the intake no longer being subjected to the losses of the hub at this advance ratio. Instead that flow passes through the rotor blades and work is done on the flow, increasing its total pressure from the free stream conditions. The non-uniform load distribution on the rotor causes some of the flow to gain a higher total pressure when compared to the disk average, which thus can result in a pressure coefficient above unity as the average dynamic pressure of the rotor disk is being used to calculate the coefficient. For this specific case the total pressure at the intake entry plane exceeds the average due to the captured flow first passing through a highly loaded sector of the rotor, resulting in the C_P above unity.

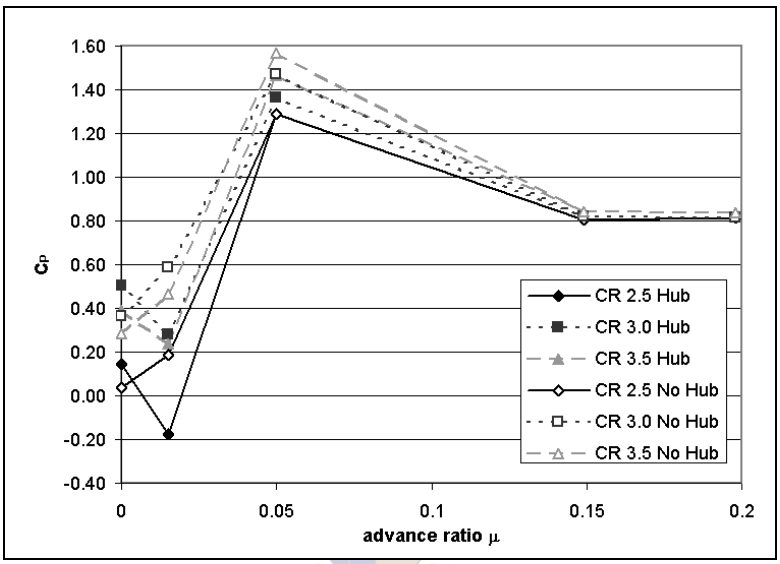

Figure 9.8 A_c total pressure coefficients, side intakes

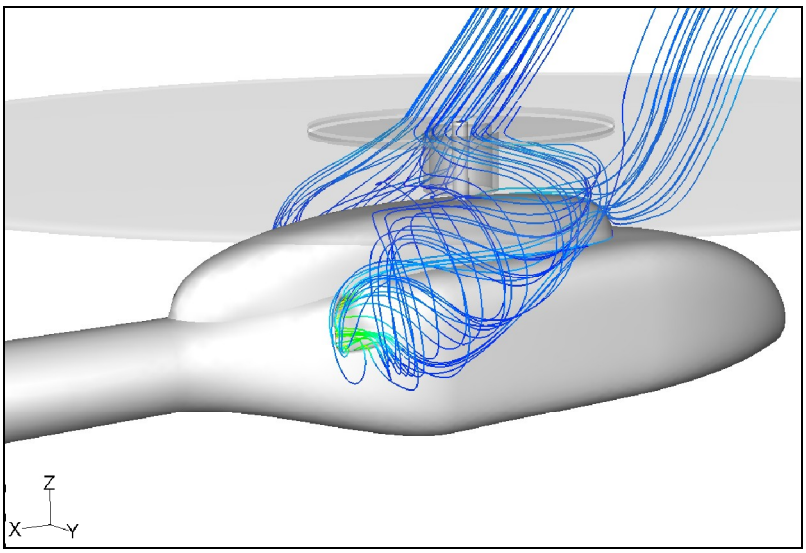

Figure 9.9 Streamlines entering the intakes on the advancing side at $\mu = 0.015$ (CR = 3.0)

Intake Efficiency

The overall intake efficiency is presented in Figure 9.10: it is defined as the average total pressure over the entire fan face divided by the fee stream dynamic pressure, as already given by Equation 7.3. Again the dynamic pressure as calculated with rotor momentum theory is used to avoid division by zero at $\mu = 0.00$. This is unlike the figures given by Seddon et al.[20], but this gives a better performance comparison for intakes fitted to rotorcraft.

In Figure 9.10 there is a distinct difference visible in the intake efficiencies with respect to the different contraction ratios. A higher contraction ratio gives a better performance, as already indicated by Seddon et al. Also noticeable is the relatively small advantage of the CR = 3.5 over the CR = 3.0 intake when compared to the CR = 2.5 intake. The effect of the rotor hub is small for each of the respective contraction ratios, similar as discussed in the previous section, with the influence on the efficiency being negligible above $\mu = 0.05$.

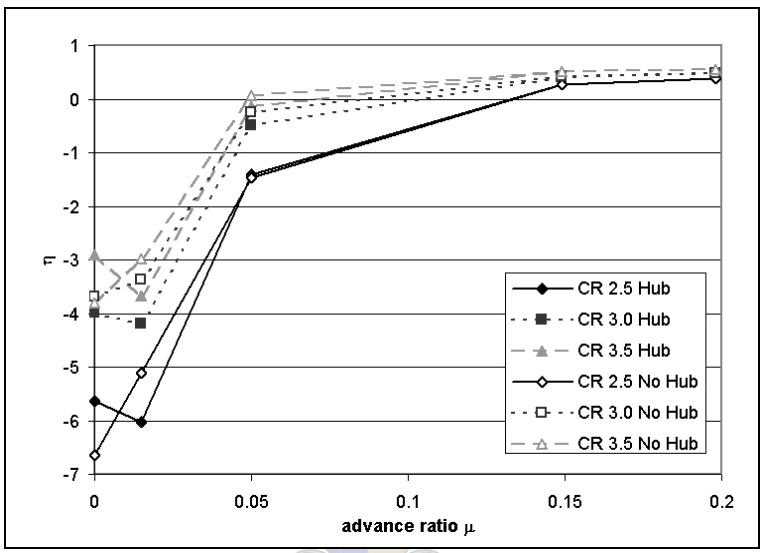

Figure 9.10 Intake efficiency, side intakes

Duct Losses

Figure 9.11 shows the duct losses of the side intakes when considering the average total pressure of the fan face. Intake duct losses are defined as the total pressure loss of the air inside the intake duct, normalised with the dynamic pressure at the fan face (Equation 9.2). This gives a measure of the effectiveness of the intake duct, and thus of the design of the intake.

$$\Delta C_P = \frac{\Delta P_d}{q_f} \qquad (9.2)$$

The effect the contraction ratio on the duct losses is immediately apparent. The two higher contraction ratios show significantly lower losses over the entire range of advance ratios, with up to 30% lower losses. Again the difference between CR = 3.0 and CR = 3.5 is not as significant as that between CR = 2.5 and CR = 3.5. The relative influence of the rotor hub is small on the duct losses, slightly improving the performance at $\mu = 0.00$, with the trend reversing at $\mu = 0.015$. No difference is detected at higher advance ratios.

Looking at just the outer section of the fan (Figure 9.12), the losses remain remarkably constant throughout the flight envelope. Below $\mu = 0.01$ the two higher contraction ratio intakes fare marginally better, possibly due to the thinner duct boundary layer that strongly affects the outer

fan. Comparing the loss of the outer fan to the average of the entire fan face, the losses here are up to three times higher than the average.

The trends of the core fan (Figure 9.13) are identical to the average of the fan face, for the same reasons already stated. The losses are however lower due to the exclusion of the boundary layer flow, which enters the outer fan.

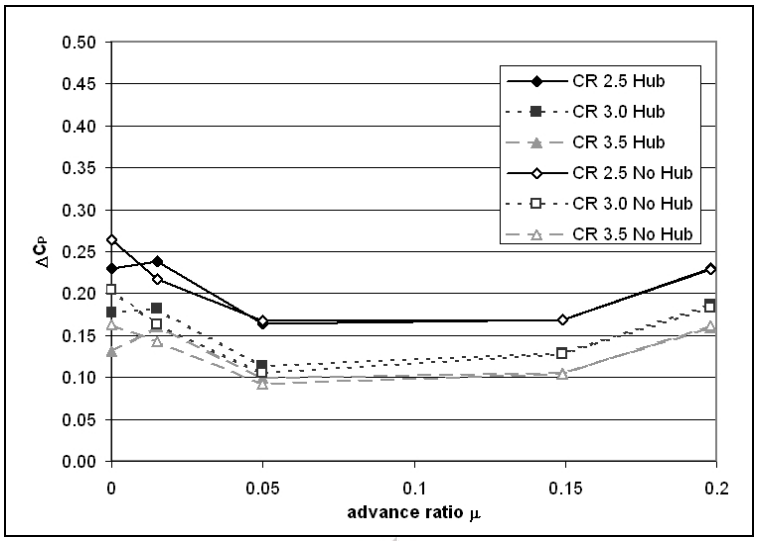

Figure 9.11 Duct loss, side intakes

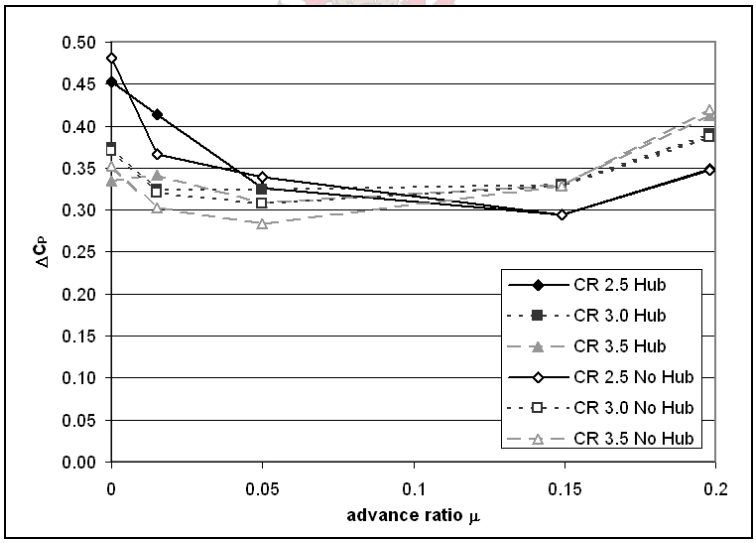

Figure 9.12 Outer fan duct loss, side intakes

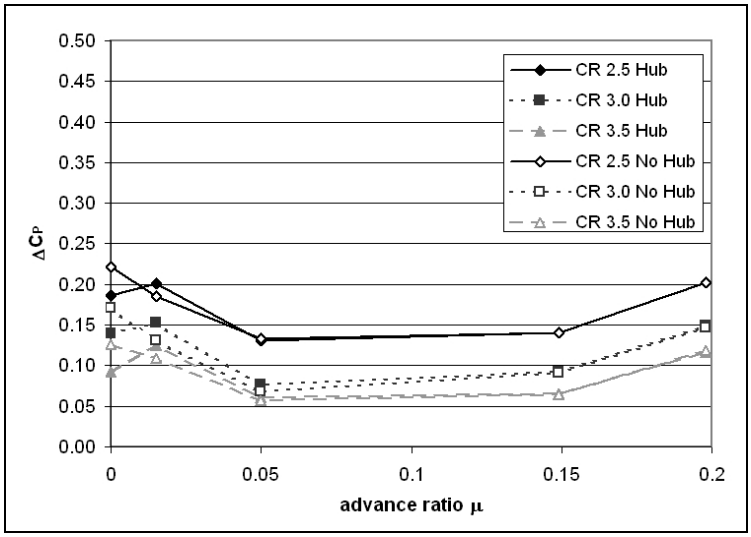

Figure 9.13 Core fan duct loss, side intakes

Distortion

The DC60 factor as described by Equation 7.2 is again used to quantify the distortion on the fan face. The distortion on the entire fan face is lower than the DC60 = 0.5 limit suggested by Cumpsty[28], as can be seen in Figure 9.14. Also, the distortion is significantly lower than the lowest DC60 = 0.4 value of the best design discussed in Chapter 7. At hover the distortion on these intakes is mildly sensitive to contraction ratio, but again not much different above CR = 3.0, with the lowest distortion being DC60 = 0.04. At the low advance ratios of $\mu = 0.00$ and especially at $\mu = 0.015$, the inclusion of the hub has a significant influence; the distortion is lower with the hub included at $\mu = 0.00$, but higher again at $\mu = 0.015$. At $\mu = 0.015$ the rotor hub creates a helix flow pattern (also visible in Figure 9.9), predominantly on the advancing side, that gets ingested by the intake on that side and thus causes the higher distortion. For advance ratios above $\mu = 0.05$ the hub has little or no effect on the distortion, as its wake is convected past the intakes.

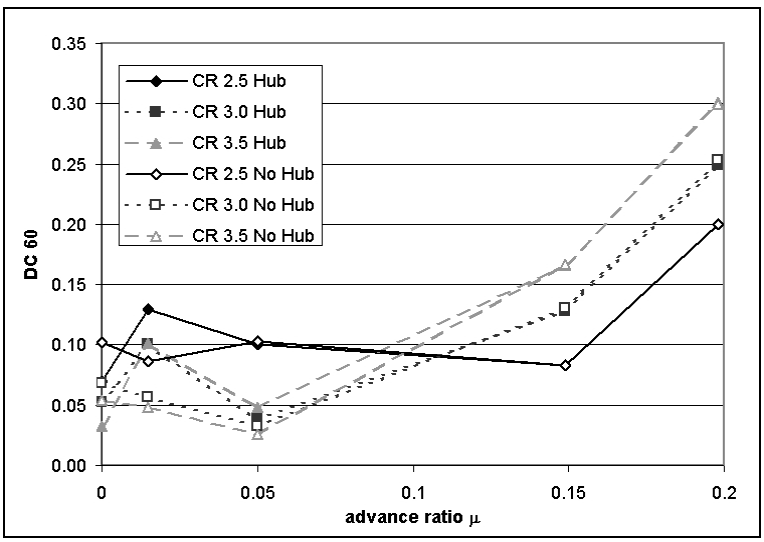

Figure 9.14 Fan face distortion values, side intakes

The outer fan section shows higher distortion values compared to that of the fan face average (Figure 9.15); this is due to the separation cells inside the duct affecting primarily the outer sections. At the very low advance ratios the trends are similar to those for the entire fan face, for the same reasons.

At $\mu = 0.05$ the distortion is higher again with the rotor hub. This is because the hub causes a small amount of reversed flow to enter on the retreating side intake (top rear corner of intake as shown in Figure 9.16) and this causes the higher distortion, as that air flows directly to the outer fan section. The larger contraction ratio intakes draw in more of the reversed flow, hence the increasing difference for larger contraction ratios. This seems to be a design specific issue, which might not be generalised for all side intakes.

The trends in the distortion on the core fan (Figure 9.17) are again identical to the average of the fan face, for the reasons already stated. The distortion is however lower due to the exclusion of the boundary layer flow and some of the separation regions that occur inside the duct.

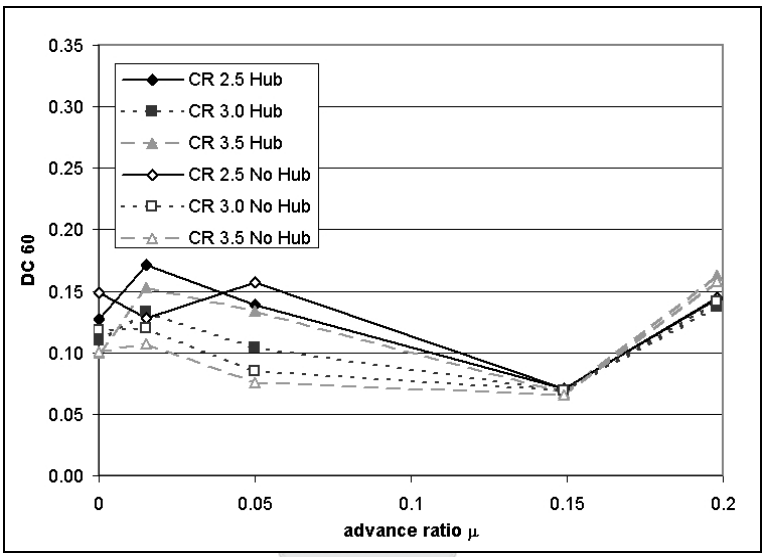

Figure 9.15 Outer fan distortion values, side intakes

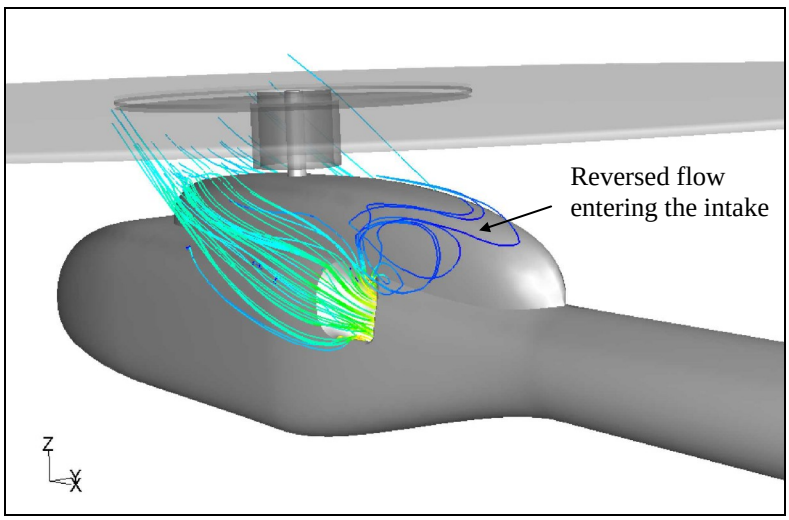

Figure 9.16 Streamlines entering the retreating side intake at $\mu = 0.050$ (CR = 3.0)

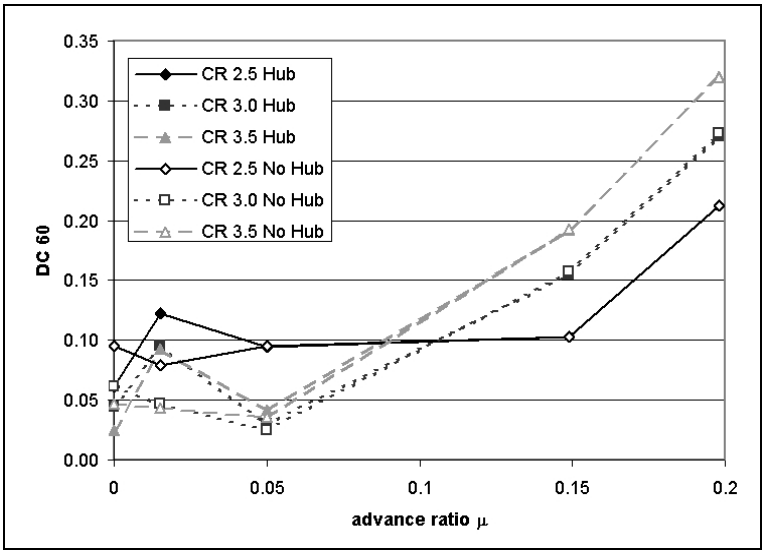

Figure 9.17 Core fan distortion values, side intakes

Contours of total pressure at the fan face for the five advance ratios are shown in Figure 9.18, looking at the fan face in the downstream direction (Note the different scale for each plot). The plots are for the CR = 3.0 side intake with rotor hub included only, but show the trends in distortion patterns that are evident for all contraction ratios. At hover, $\mu = 0.000$, there are two low pressure cells at the 3 and 9 o'clock positions. As the flight advances to a low speed of $\mu = 0.015$, the swirl in the rotor wake entering the intake causes the low pressure cells to migrate to the 2 and 8 o'clock positions respectively. At $\mu = 0.050$, where the rotor wake is already convected past the inlets, the cells return to the original positions while at the same time reducing in strength. Distortion values then pick up again at $\mu = 0.149$ to $\mu = 0.198$, due to separation at the lower intake lips.

Top Intake Evaluation

The alternative design of the top mounted intake was also evaluated for the same three contraction ratios and the advance ratios. A comparison is again made between results that include and exclude the rotor hub. The split of the two fan sections was taken at a diameter of 516mm, based on a 4% duct blockage of the flow approaching the fan.

Capture Area Pressure Coefficient

The C_P value in Figure 9.19 presents the average total pressure of the intake capture area, normalised with the free stream dynamic pressure, as already defined for the side intakes in Equation 9.1. The free stream velocity is again calculated from momentum theory for the specific load conditions used in this simulation, given in Table 9.6.

Table 9.6 Free Stream Velocities for the Twin Engine Helicopter

μ	0.000	0.015	0.050	0.149	0.198
V_{MR} [m/s]	12.78	13.00	15.35	33.32	43.95

At $\mu = 0.00$ the effect of the inclusion of the rotor hub is small; the hub only slightly reducing the total pressure available to the intake by a maximum of approximately 0.1. For the conditions at $\mu = 0.015$ most of the flow entering the intake first passes through the rotor hub and is thus subjected to the drag losses of the rotor hub. See also Figure 9.20 for the path lines entering the

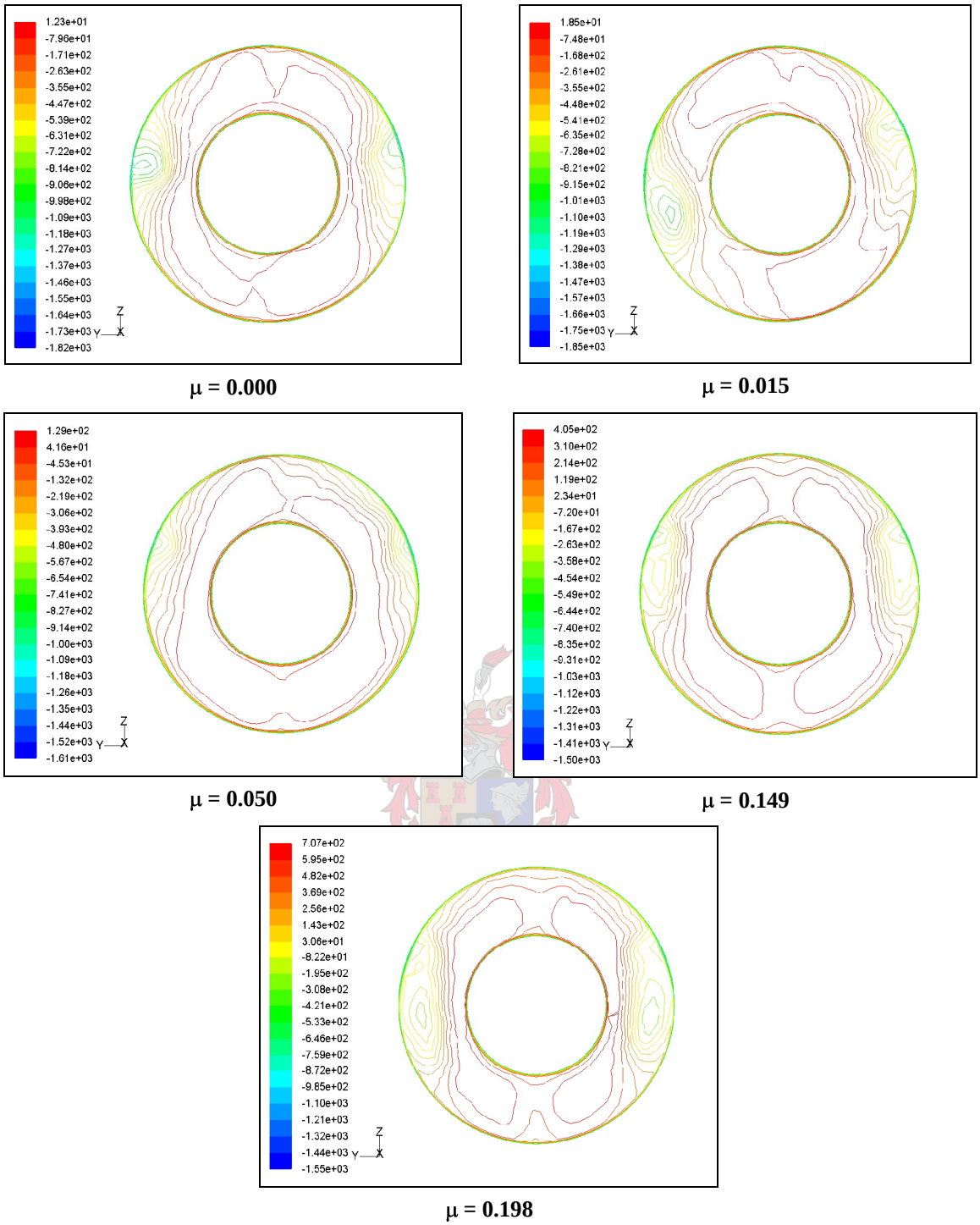

Figure 9.18 Fan face total pressure contours, side intakes (CR = 3.0)

intake. At μ = 0.015 (Figure 9.19) the CR = 3.5 intake shows a significant advantage above the other contraction ratios with a $C_P = 0.21$ versus $C_P \approx 0$ of the other intakes that include the hub. For the cases where the hub was not included there is no significant drop in the available total pressure at the entry plane from hovering conditions.

Increasing the contraction ratio does again show some advantage. At μ = 0.05 the flow entering the intake is still strongly affected by the rotor hub and the flow patterns it creates. But the flow itself does not pass through the hub volume first and hence the losses are less than at μ = 0.015, as can be seen from the C_P values of approximately 0.45.

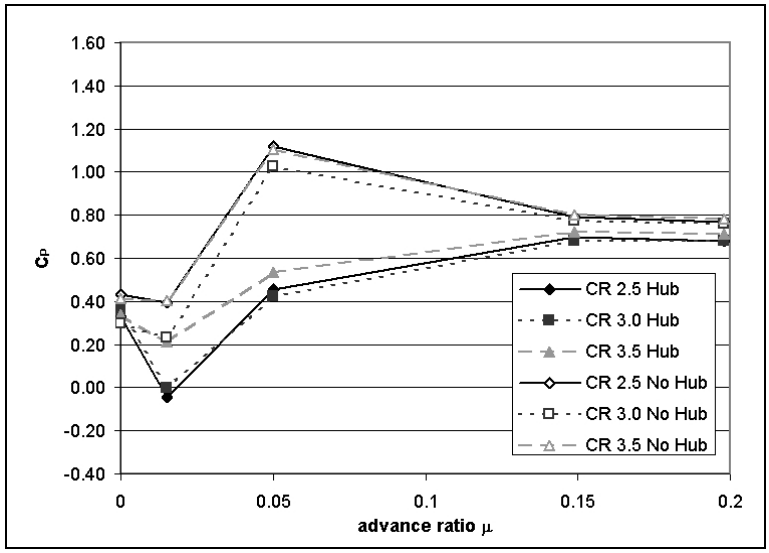

Figure 9.19 A_c total pressure coefficients, top intake

The C_P values for the no-hub case are again above unity at $\mu = 0.05$, for the same reasons as explained for the side intakes. Apparent at $\mu = 0.05$ is also the effect that the hub has on the intake. There is a difference in the C_P-values of approximately 0.6 between the hub on and off cases, indicating the strong effect the hub has on the intake at this advance ratio. At the higher advance ratios the hub does not have a dominating influence anymore, a difference of approximately 0.1 being predicted. Important to note is that at the high advance ratios the wake of the cowling is ingested into the intake.

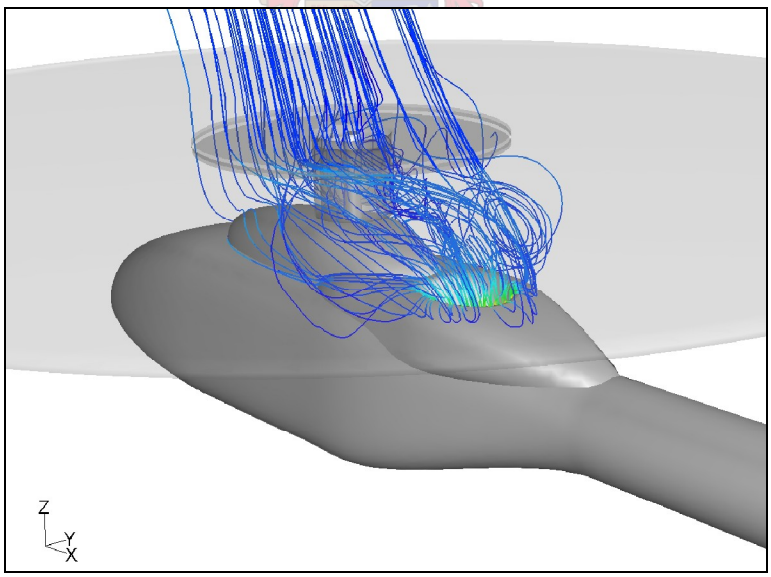

Figure 9.20 Streamlines entering the top intake at $\mu = 0.015$ (CR = 3.0)

Intake Efficiency

Using the definition of intake efficiency of Equation 9.1, the overall intake efficiency for the top intake is shown in Figure 9.21. Unlike the side intakes, the rotor hub has a distinct effect on the efficiency of the intakes. The effect is small at low speed flight, but has a dominating influence at the advance ratio $\mu = 0.05$, with the difference contributed by the hub being about 1.5 efficiency points for all contraction ratios. Increasing the contraction ratio has a significantly positive effect

on the efficiency performance of the intake, but again not much is to be gained from a higher contraction ratio than 3.0.

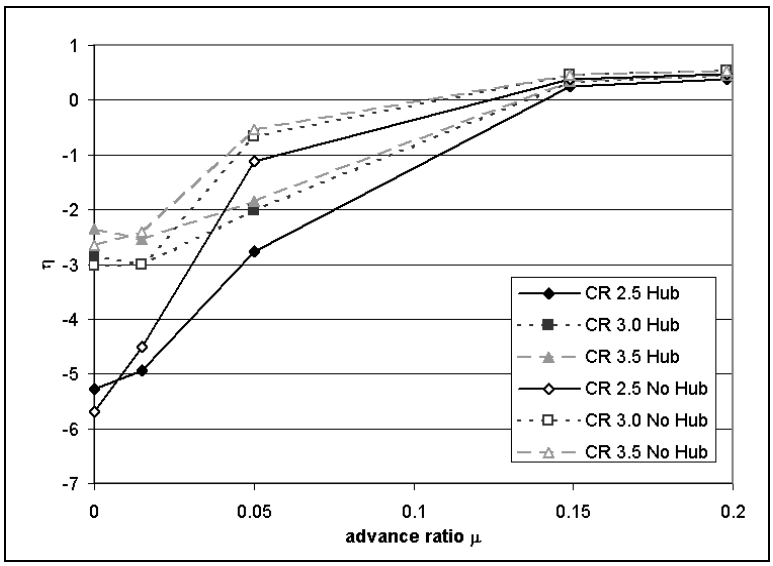

Figure 9.21 Intake efficiency, top intake

Duct Loss

In Figure 9.22 the average duct loss of the top intake is shown; again normalised with the average dynamic pressure on the fan face, as described by Equation 9.2.

Evident is again the effect an increasing contraction ratio has on the losses of the duct, with the relative improvement of a contraction ratio above 3.0 being small. At hover the difference in the duct loss between CR = 2.5 and CR = 3.0 is roughly 0.07, with the remainder of the results varying by approximately 0.01 from each other. For the higher contraction ratios the losses also remain relatively constant around 0.08. A difference of the hub and no-hub results can be seen at $\mu = 0.05$, as this is the advance ratio where the hub wake has the most significant effect on the intake. Similar duct losses for all intakes at high advance ratios indicate a low dependence on contraction ratios.

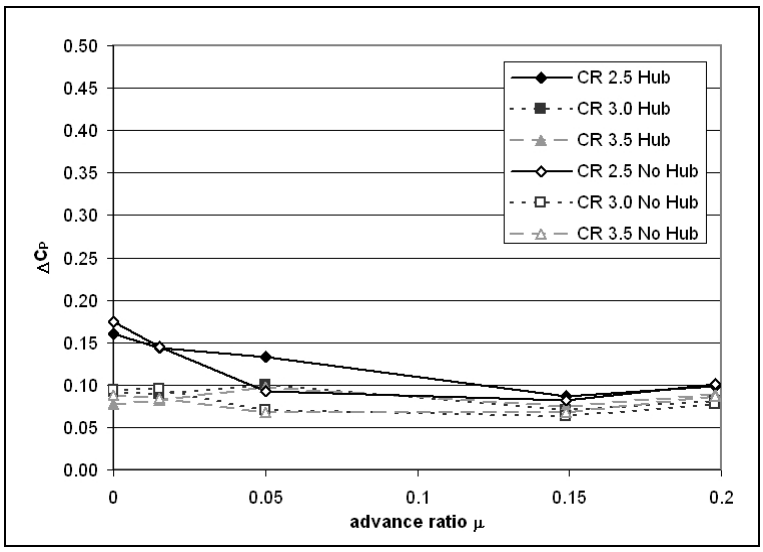

Figure 9.22 Duct loss, top intake

Over the range of advance ratios the losses for the outer fan are virtually constant, and about three times higher than the average loss for the entire fan face (Figure 9.23). This is however only true for the two higher contraction ratio intakes; and both have the same loss coefficient. A small influence of the rotor hub is detected at $\mu = 0.05$ for the two higher contraction ratio intakes; for the remainder the results are identical. A noticeable and almost constant effect of the rotor hub is found over the entire flight envelope for the CR = 2.5 intake. The loss of the core fan section (Figure 9.24) is again identical to the loss of entire fan face as it makes up 88% of the entire flow area.

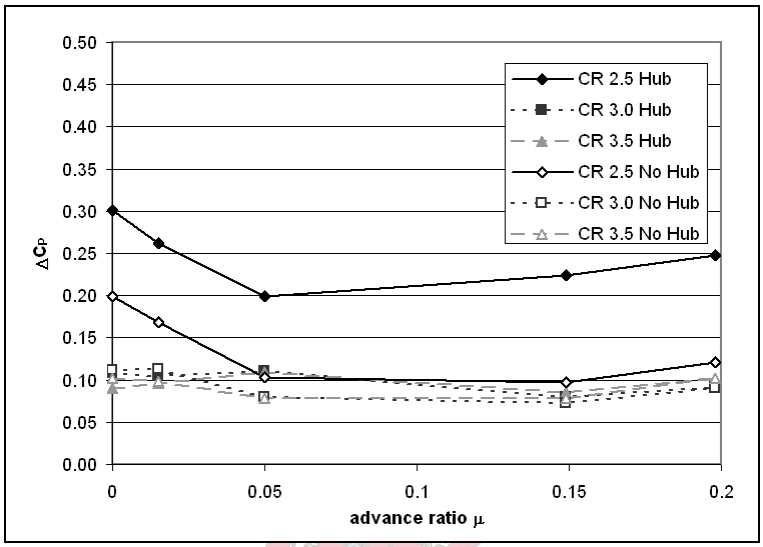

Figure 9.23 Outer fan duct loss, top intake

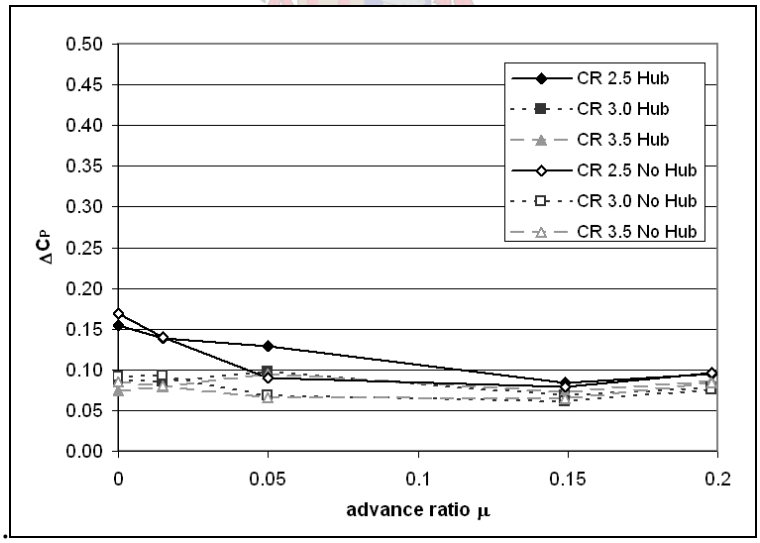

Figure 9.24 Core fan duct loss, top intake

Distortion

The fan face flow distortion of the top intake is distinctly sensitive to the contraction ratio, as can be seen in Figure 9.25. The larger contraction ratios give lower distortion values at the low advance ratio end of the flight envelope, though the trend reverses at $\mu = 0.149$, where the CR = 2.5 intakes shows slightly better results. Similar to the same trends as before, there is not a drastic difference in distortion between the CR = 3.0 and CR = 3.5 intakes when compared to the CR = 2.5 intake. Interesting to note is that the inclusion of the hub improves the DC60 values

notably at μ = 0.015 for all contraction ratios. The trend is however reversed dramatically at μ = 0.050.

The reason for the low DC60 values at μ = 0.015 is as a result of the rotor hub feeding air into the intake from the retreating side (this does not happen in the no-hub case), and only a little of the swirling flow on the advancing side is ingested; this results in a better flow quality at the fan face. The reversal in the trend follows from a change of side from which air gets inducted; between μ = 0.015 and μ = 0.050 the incoming flow switches from the retreating to the advancing side of the fuselage. The flow patterns that are formed by the hub on the advancing side(Figure 9.26) now get ingested into the intake and increase the fan face distortion.

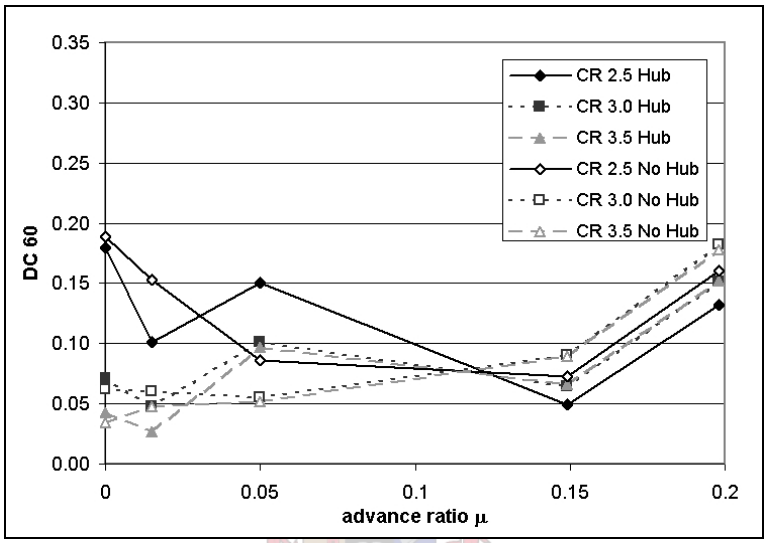

Figure 9.25 Fan face distortion values, top intake

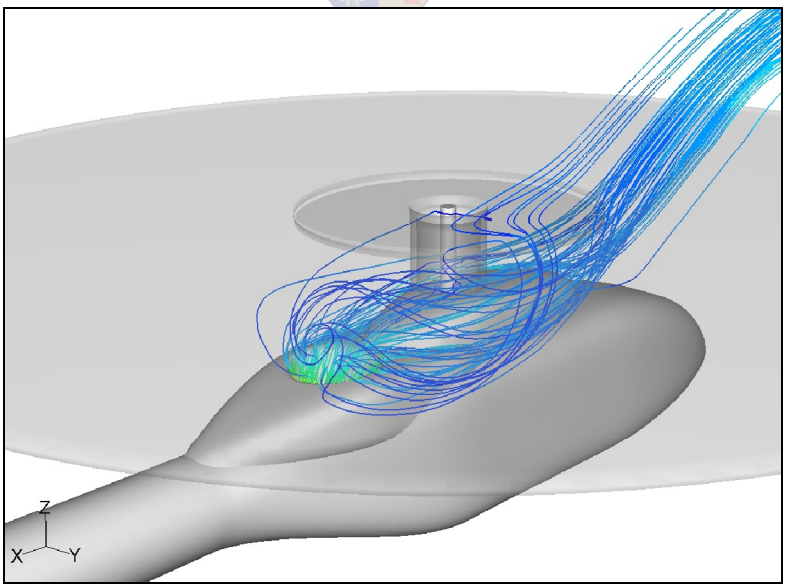

Figure 9.26 Streamlines entering the top intake, predominantly from the advancing side, μ = 0.050 (CR = 3.0)

Separation zones that form inside the intake duct again strongly influence the distortion in the outer fan section. Due to a small but strong separation cell on the inside of the duct bend, the DC60

factors are relatively high at low advance ratios. As the advance ratio increases the separation in the duct decreases and thus the DC60 values continually improve (Figure 9.27). The rotor hub has little influence on the distortion, but increasing the contraction ratio improves the distortion noticeably, bringing the DC60 down to as low as DC60 = 0.2 at hover for the CR = 3.5 intake. Trends in the core section performance, measured on distortion, are again similar to that of the entire fan face, as shown in Figure 9.28.

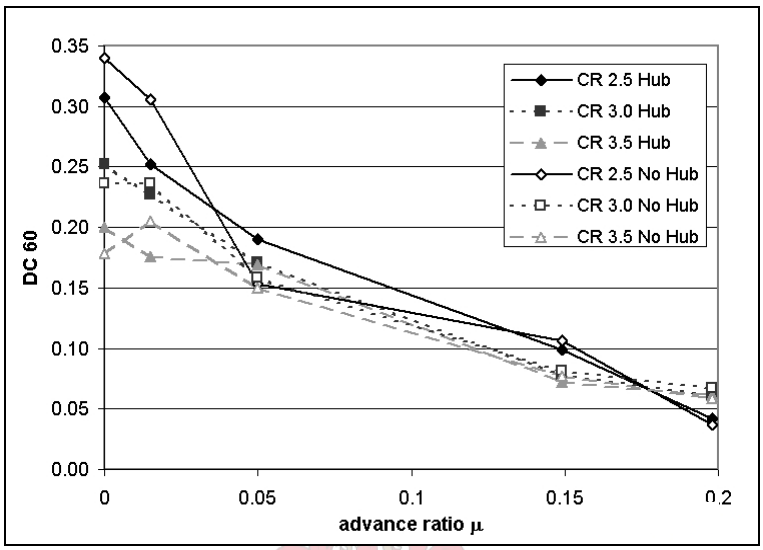

Figure 9.27 Outer fan distortion values, top intake

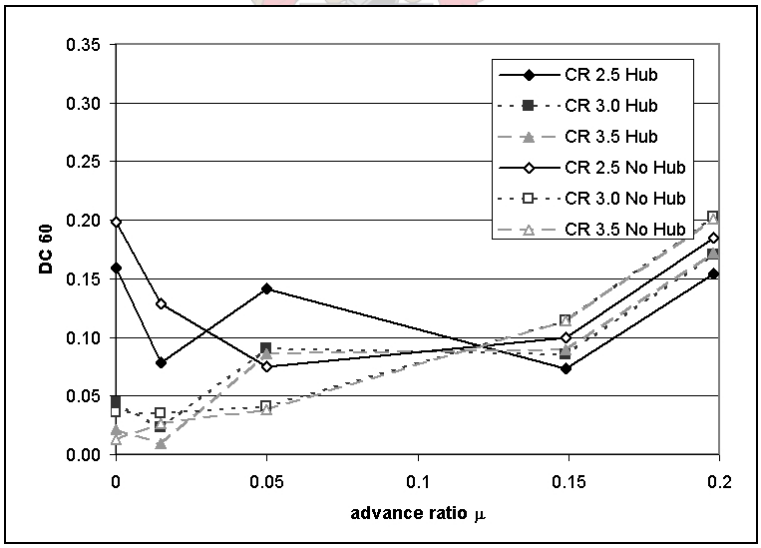

Figure 9.28 Core fan distortion values, top intake

Contours of total pressure at the fan face for the five advance ratios are shown in Figure 9.29, looking at the fan face in the downstream direction (Note the different scale for each plot). The plots are for the CR = 3.0 top intake with rotor hub included only, but show the trends in distortion patterns that are evident for all contraction ratios. At hover, $\mu = 0.00$, there is a single low pressure cell at the 12 o'clock position which is as a result of separation inside the duct bend. As the flight speed increases to a low speed ($\mu = 0.015$) another low pressure cell appears at the 7 o'clock position due to the fan shaft wake. Swirl from the rotor wake causes a slight anti-clockwise shift of

the low pressure regions at μ = 0.05. At μ = 0.149, where the rotor wake influence on the inlets is small, symmetry of the pressure contours is restored. Distortion values then pick up again slightly at μ = 0.198, a result of cowling wake and the effects of the intake operating at a high incidence.

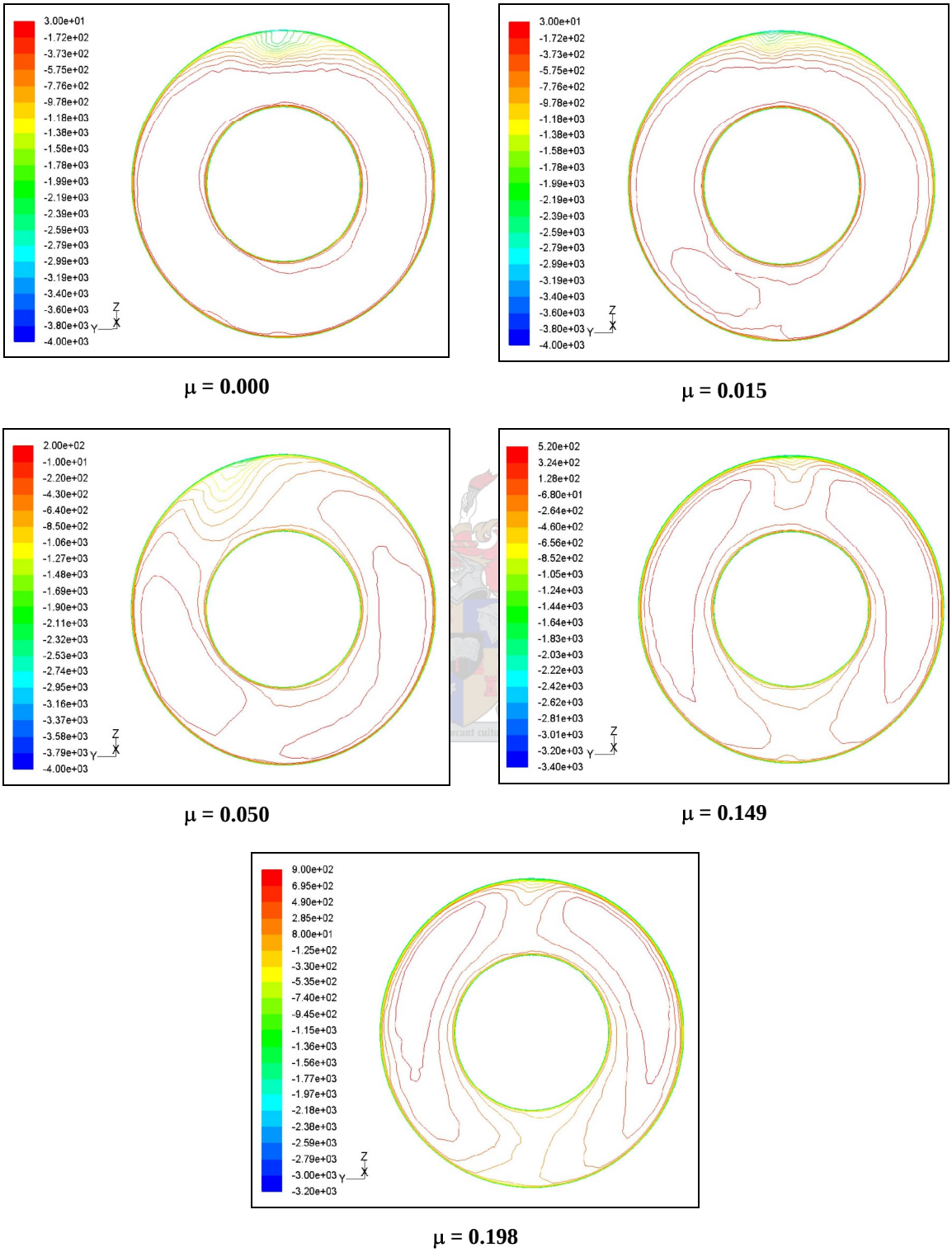

Figure 9.29 Fan face total pressure contours, top intake CR = 3.0

Comparison of Side Mounted vs. Top Mounted Intakes

Here a side-by-side comparison of the two intake concepts is presented to give a better indication of the relative advantages each concept presents. Results used here for the comparison are only from the rotor hub inclusive cases, but for all three contraction ratios. The comparisons are made according to the same parameters used for discussion in the previous sections on the individual designs.

Capture Area Pressure Coefficient

A beneficial direct comparison between the two intakes can be made by looking at the average total pressure available for each concept at the capture plane. Here any sub-optimal designs of the duct itself are excluded, allowing for analysis of the design specific issues that need to be considered for the location of the intake. The C_P values in Figure 9.30 are again normalised with the free stream dynamic pressure as per Equation 9.1.

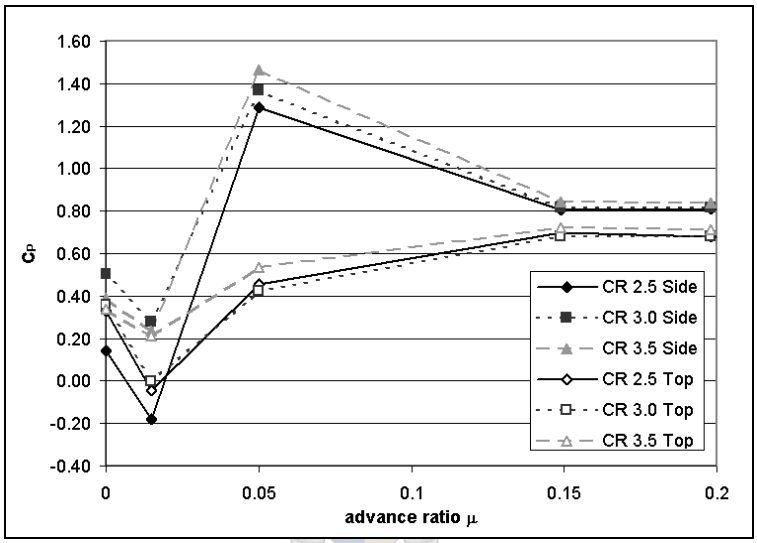

Figure 9.30 A_c total pressure coefficients

At hover the average total pressure at the capture plane is virtually the same, except for the CR = 2.5 and CR = 3.0 side intakes, which show slight variations. Consequently no preferred location of the intake opening at hover can thus be established, as long as a contraction ratio of at least 3.0 is used.

For $\mu = 0.015$ the rotor hub influences both designs negatively, more so for the top intake. But as can be seen in Figure 9.30, a larger capture area (and resultantly bigger contraction ratio) helps to improve the top intake performance.

In the intermediate speed range of $\mu = 0.050$ the side intakes have a clear advantage. Here the hub wake is already convected past the side intakes, while the top intake still inducts air that is strongly affected by the hub. At the high flight speeds the total pressure available to the intakes is similar, however the top intake is now located in the wake of the gearbox cowling and thus has a slight pressure deficiency.

Intake Efficiency

With regard to the intake efficiency (Figure 9.31) at hover the position does not have a significant influence, with the top intake faring only slightly better. A more significant parameter through which the performance can be obtained is the contraction ratio. This is also true for the intake performances at $\mu = 0.015$. In the mid speed range the initial total pressure deficiency (Figure 9.30) of the top intake causes a lower overall efficiency compared to the side intakes, until at higher

speeds the efficiency values are again equal. The efficiency is additionally also dependent on the losses in the intake duct, which are discussed next.

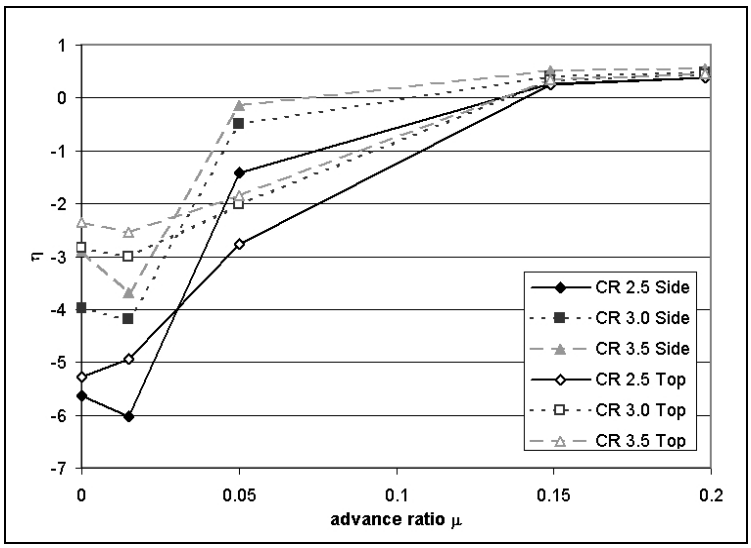

Figure 9.31 Intake efficiencies

Duct Loss

Comparing the duct losses for the two concepts in Figure 9.32, it is clear that the top intakes perform noticeably better at low speeds, especially the two intakes featuring the higher contraction ratios. This is primarily as a result of the simpler/cleaner duct shape that is possible with the top intake, while on the other hand the side intakes require a series of complex three-dimensional S-bend turns in a confined volume. These rapid changes in the duct cause losses which are evident by the high losses of up to $\Delta C_{\Delta P} = 0.25$ for low flight speeds. Here a large contraction ratio helps to bring the losses under control. The two higher contraction ratio top intakes show an almost constant ΔC_P not exceeding $\Delta C_P = 0.1$ for the entire range of flight speeds. It should be noted here that for a straight duct of similar size to the intake duct, the pressure drop is $\Delta C_P = 0.045$, which is about half of that displayed here. At higher speeds the duct losses increase as a result of the intakes now operating at a high incidence.

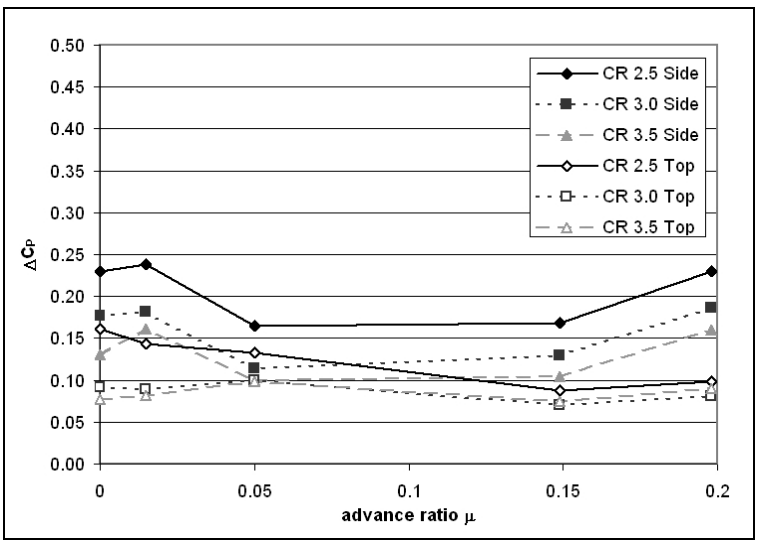

Figure 9.32 Duct losses

When considering the outer section of the fan (Figure 9.33), the losses are relatively constant over the range of advance ratios, especially for the higher contraction ratio intakes. Here the top mounted intakes have a clear advantage over the side intakes. The CR = 3.0 and CR = 3.5 intakes give the same performance, which is superior to all the other designs. Also, the loss coefficient of approximately 0.1 is virtually the same as that of the average of the entire fan face.

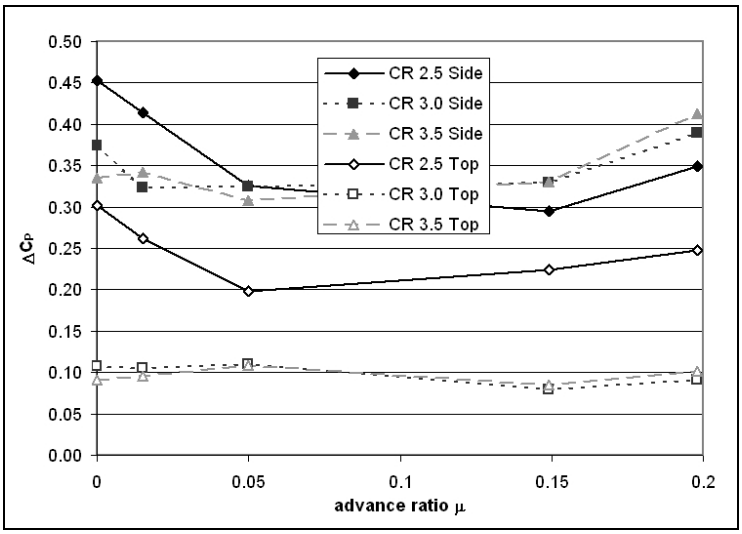

Figure 9.33 Duct losses, outer fan

Figure 9.34 shows the performance of the core section, that is, as before, similar to the duct loss measured for the entire fan face, spare the slight improvements due to the removal of the duct boundary layer.

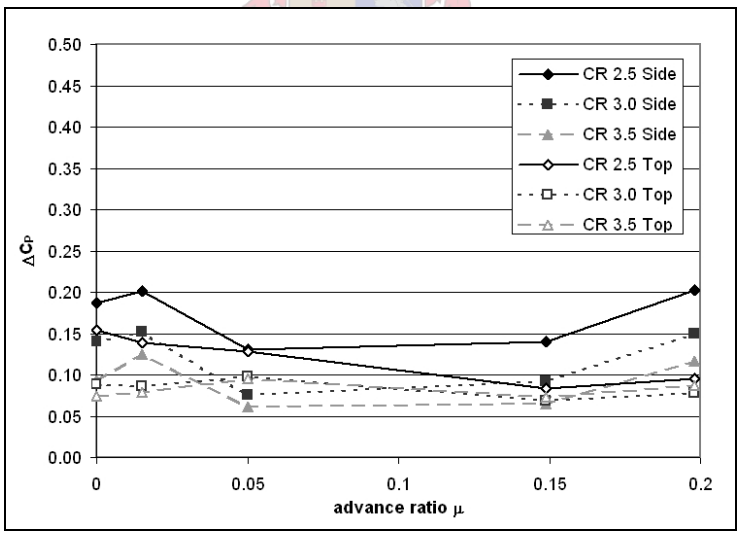

Figure 9.34 Duct losses, core fan

Distortion

According to the comparison of the DC60 factors (Figure 9.35) for the two concepts there is no clear advantage. For the entire fan face most of the designs have a similar distortion value of about DC60 = 0.04 to DC60 = 0.06, except the CR = 2.5 top intake. As the flight speed increases, the rotor hub negatively influences the side intakes; the DC60 value increases to almost double the value at hover. The trend is reversed at $\mu = 0.050$ where the top intakes takes the brunt of the hub wake. Beyond $\mu = 0.050$ there is a gradual increase of the DC60 factors for all intakes as they start

to operate at progressively higher angles of incidence. The comparatively higher DC60 values of the side intake are partly due to the intake shaping that is optimised to work at low advance ratios.

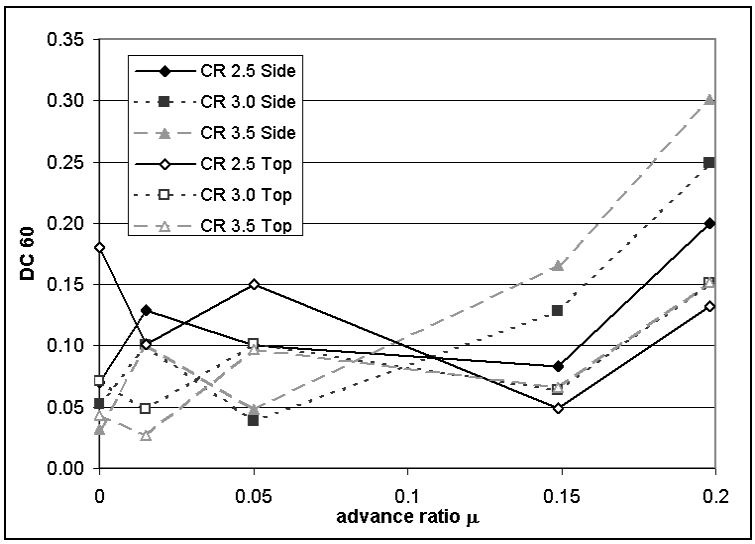

Figure 9.35 Fan face distortion values

The DC60 values for the outer fan section (Figure 9.36) start off with comparatively high values at hover for the top intake. This is as a result of the separation bubble that forms on the inside of the bend of the top intake. As soon as the separation bubble starts to disappear the distortion values approach that of the side intakes. Except at $\mu = 0.00$ and $\mu = 0.198$, both CR = 3.5 intakes show similar results for the outer section. The increase in distortion for the side intakes is as a result of the intake shaping that is optimised for slow flight; specifically the lower intake lips that are designed to capture the downdraft. At higher flight speeds the flow separates off these lips, causing the distortion as seen in Figure 9.37.

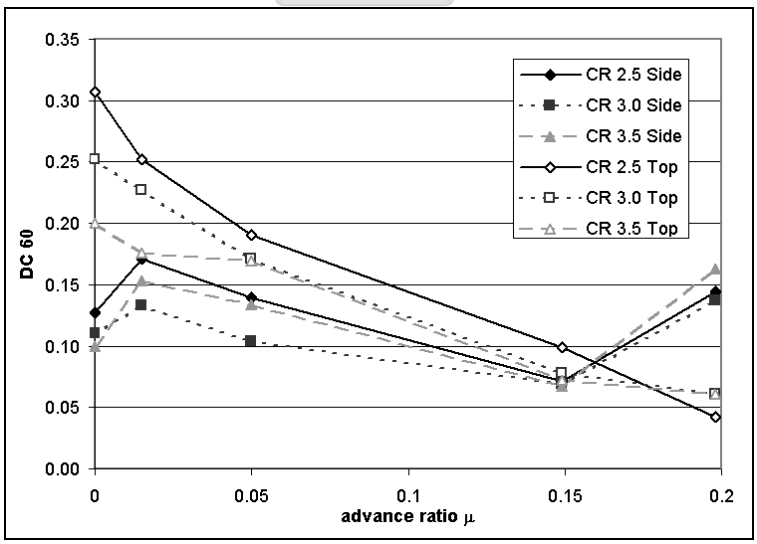

Figure 9.36 Outer fan distortion values

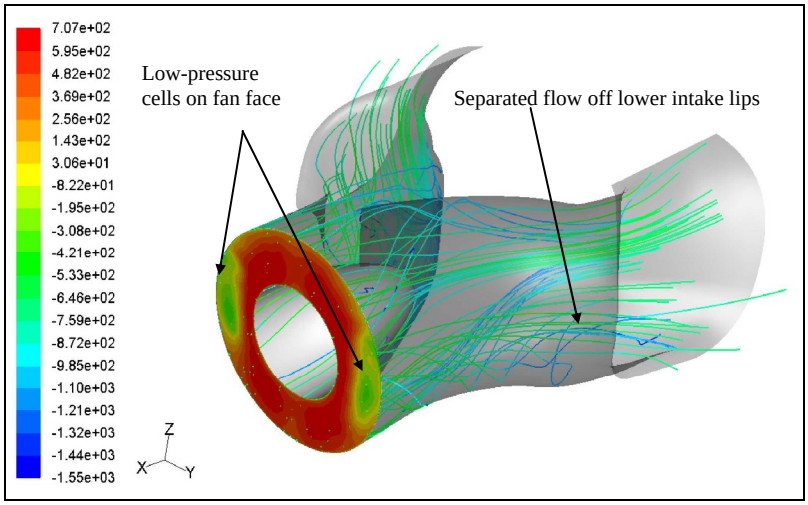

Figure 9.37 Separation in side intakes, μ = 0.198

Figure 9.38 shows the distortion performance of the core section, that is, as before, similar to the distortion on the entire fan face, spare the slight improvements due to the removal of the duct boundary layer and parts of the separation zone wakes.

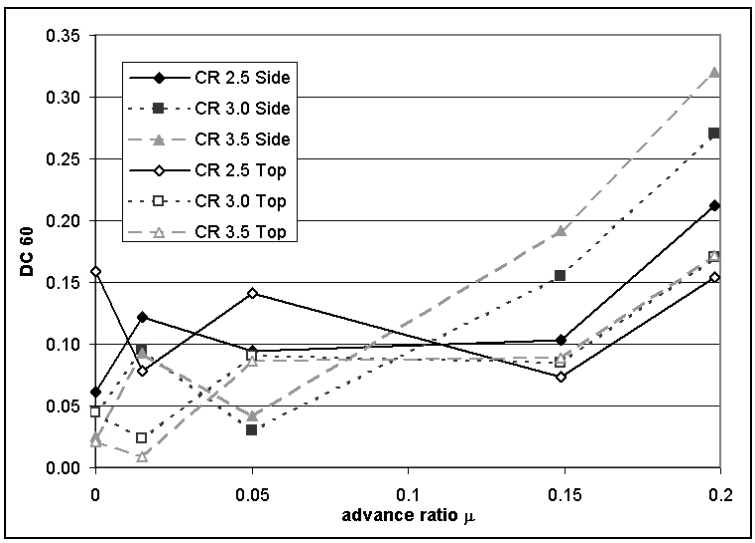

Figure 9.38 Core fan distortion values

Conclusion

The objective of the intake evaluation was to analyse two intake concepts for the two-stream fan. A generic fuselage configuration was used. The studies concentrated on the evaluation of design parameters such as intake location, contraction ratio and the role the rotor and its hub have on intake performances. Consideration was also given to the effects the intakes would have on the outer fan over the range of advance ratios.

It was found that the rotor and hub flow fields influence the side and top intakes at different advance ratios and varying strengths. A side-by-side comparison showed the advantages of the intake concepts, though no overall preferred concept could be established. The contraction ratio proved to be an efficient design parameter through which intake losses and distortion could be controlled. In Chapter 10 a review of the designs issues affecting the intakes is presented, together with procedures for intake design and the effects on the fan performance.

CHAPTER 10

INTAKE DESIGN: DISCUSSION AND RECOMMENDATIONS

In the previous four chapters the design and CFD evaluation of the intake concepts were discussed. The results were analysed and the intake performance extrapolated to give an indication of the fan performance. An intake concept for the Alouette III/CIRSTEL was shown to be feasible, based on intake efficiencies and distortion coefficients at the fan face. From the initial concept and geometry the design was evolved into a workable solution, based on CFD evaluations. Additionally side and top mounted intake concepts on a generic fuselage were evaluated with the aim of expanding the understanding of helicopter air intakes.

Alouette III/CIRSTEL Intakes

The CFD evaluations helped to modify the intake geometry to improve efficiency and reduce the total pressure distortion at the fan significantly throughout the entire flight envelope. With regard to the average total pressures over the entire face, the intakes still require some further work. For example, the intakes could benefit from further outwards cambering of the lips, as previously mentioned, to reduce lip separation. This work highlighted the most important issues that have to be considered in the design of helicopter intakes, namely the contraction ratio and lip design, similar to the suggestions by Vuillet[24].

Through the course of the modifications to the intakes the contraction ratio was increased, which in part resulted in the better performance of the design iterations. The first intake design had a contraction ratio of CR = 2.3 and the final design CR = 2.8.

It was also shown that the lips have a significant role in the performance of the intakes, as lip separation can easily occur if the lips are designed without proper anticipation of the local flow conditions. The upper lip has to be thick to give a good rounded entrance into the intake during hover conditions, while the remainder of the intake lip has to be flared out sufficiently to account for the incoming flow during these conditions. It appears that the lip thickness and shape play a considerably more important role on these intakes than what Vuillet[24] suggests, judging by the effect the changes to the lip had on the current intake performance.

Though the CFD simulations for the Alouette III/CIRSTEL intakes were simplified studies in that a uniform flow field was implemented to simulate the rotor flow, the results did give a good indication of the intake performance under realistic conditions. When comparing the work of Chapter 7 with that of Chapter 9 where better flow conditions were enforced through the use of an actuator disk, the trends of intake efficiency and distortion remained similar, specifically for the side intakes.

Side and Top Intakes

The intakes for the generic fuselage (described in Chapter 9) were designed based on the lessons learnt in Chapter 7. Here however the position of the intake on the fuselage was changed for the specific purpose of determining the advantages of the two positions of the intake openings.

Initially it was hoped that positioning the intake on top of the fuselage would allow it to capture the rotor downwash, and thus have flow of a higher total pressure enter the intake. This did not prove to be the case. This can firstly be attributed to the reduced downwash velocity near the centre of the rotor, compared to the average of the rotor disk, and secondly to the losses the rotor

hub adds to the flow entering the intake. In this respect the advantage of the top over the side intakes intake in hovering conditions is therefore small.

Another point of consideration for the top intake is the wake of the gearbox cowling and rotor hub that constantly affect the intake, specifically between $\mu = 0.05$ to 0.15 in the current configuration. It is thus advised to streamline the cowling, even using strakes or vortex generators to deflect the wake away from the intake where possible.

A factor that affects both intakes is the change of side of the incoming intake flow, particularly at low speed. At advance ratios below $\mu = 0.015$ the flow gets induced predominantly from the retreating side; above $\mu = 0.015$ it changes to the advancing side.

The side intakes again exhibited a thick inlet lip at the upper and rear sector and a scoop on the lower sector. At the same time the lips were significantly more cambered outwards than on the Alouette III intakes, which distinctly reduced the amount of lip separation.

No direct performance comparison could be made with the top intake, but from the previous analysis it became clear that particular attention has to be given to the geometry of the rearward intake lip. During hovering and slow flight speeds the stagnation line is still far outside of the intake and thus the flow will accelerate around the lip into the intake duct. If the lip is too thin its pressure distribution will cause flow separation, along with the associated losses at the fan face. This was also evident for the CR = 2.5 top intake which has a relatively thin rear sector lip from which the flow did separate during hovering conditions.

Controlling duct losses has been shown to be more difficult with the side mounted intakes, due to the intricate duct shape. Increasing the contraction ratio proves to be an effective method to control the losses, as well as to limit the distortion on the fan face. Through all investigated performance parameters the trend was consistent, namely that increasing the contraction ratio above 3.0 does not yield significant performance improvements.

The rotor hub has a predominantly performance reducing effect on the intakes. The rotor hub adds losses to the incoming flow while at the same time the flow pattern it creates cause a higher distortion on the fan, particularly during the slow flight phase. It is thus important to always model the hub with performance evaluations of the intakes.

In general there is no distinct advantage to either intake. Below advance ratios of about $\mu = 0.03$ the top intake does appear to be the better choice due to its higher overall efficiency, lower losses and low distortion coefficients for the entire fan face. A reversal of these advantages then occurs between $\mu = 0.03$ and $\mu = 0.150$, where the side intakes have the advantage due to the hub wake already being convected past the intake openings. At the high speed end of the flight envelope the side intakes suffer from high distortion levels, due to the design being optimised for low speed flight by adding the scoop on the lower sector of the inlet opening. This scoop and the experienced high angle of attack of the intake at high advance ratios cause some separation at the duct entrance resulting in the pressure and flow distortion. Additionally, the flow entering the side intakes (streamlines shown in Figure 10.1) first flows along the side of the fuselage and is thus subject to the losses in the fuselage boundary layer.

The top intake design does not display these characteristics to the same extent even though it is also operating at high angles of attack at this high speed stage of the flight envelope. By placing the intake on top of the fuselage less turning of the incoming flow is required, while at the same time less of the flow entering the intake is affected by the fuselage/cowling boundary layer. It also appears that the presence of the gearbox cowling reduces the local angle of attack, as some of the flow is already turned downwards toward the intake before the entry plane as can be seen by studying the streamlines shown in Figure 10.2.

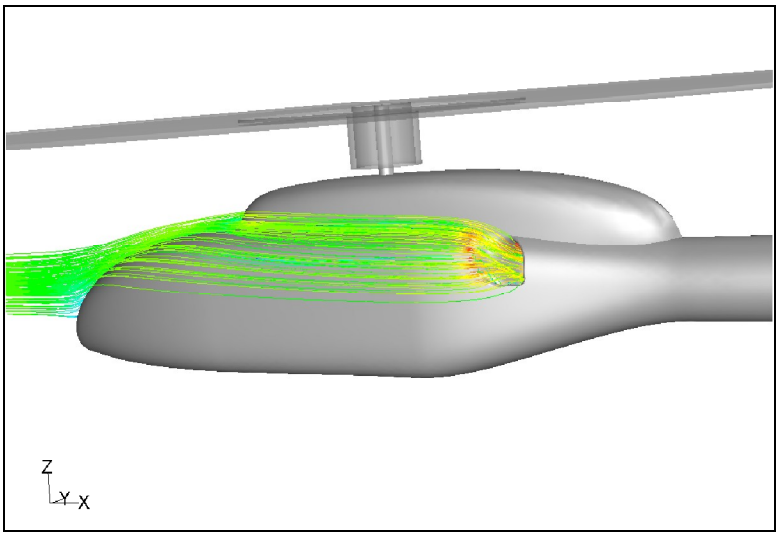

Figure 10.1 Streamlines entering the side intakes at μ = 0.198

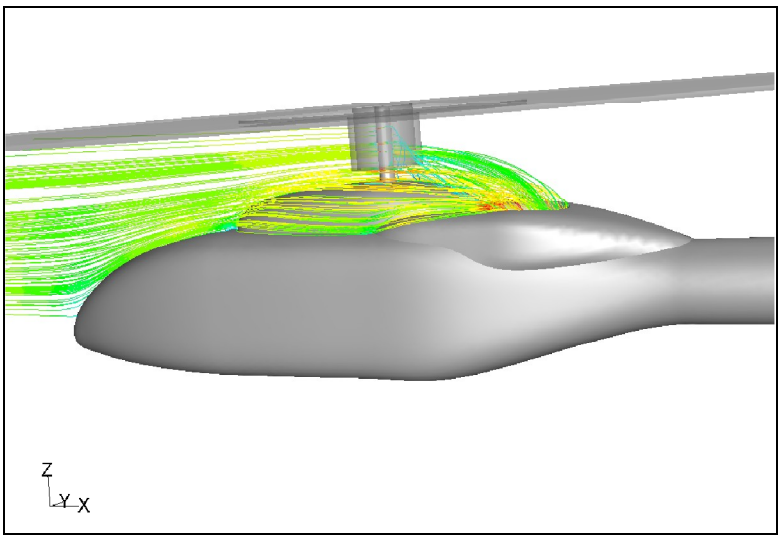

Figure 10.2 Streamlines entering the top intake at μ = 0.198

As a general design guideline it is suggested here to design these intakes with specific focus on hovering conditions. The current intakes were designed with a compromise between hover and high speed flight by angling the entrance of the intake duct forward by up to 35^{o}. This resulted in the reduced intake performance that was shown at low and high end of the advance ratio range. In the mid speed range, where the relative angle of attack of the intakes is low, both intake versions showed a good performance. Use should thus rather be made of the increased dynamic pressure at higher advance ratios of the incoming flow to offset a reduced intake performance.

Effects of the Intake on the Fan Design

The effects of a distorted inlet flow will also have to be considered in the design of the fan. As has been seen in the CFD simulations, the flow over lips were prone to separation, and hence the losses concentrated on the outer annulus. It is exactly in this area where the outer fan is located and has to operate. To ensure minimal losses and to increase the average total pressure the intake will have to be properly designed, in order to reduce the load on the outer fan. Increasing the pressure rise of

the outer fan could counter the problem, but this would of course increase the power demand of the outer fan in proportion to the total pressure rise.

Judging from tests on the demonstrator fan the core section worked better than expected. Combined with the demonstrated acceptable intake performance in the core section, power could be saved here and used on the outer section. At higher advance ratios the fan is assisted by the increase of dynamic pressure of the incoming air (especially in the core section). Thus the IGVs can be used for turn down of the air entering the fan to reduce power consumption while the higher incoming dynamic pressure still boosts the core section of the tail boom for an overall constant performance.

Another feature that needs consideration is the lower than designed for axial velocity in the outer section of the intake due to the blockage. The effect of this is a reduced mass flow into the outer section and this reduced mass flow would degrade the performance of the Circulation Control Section. Here a simple solution can be used to increase the mass flow; by simply reducing the radius of the shroud, and thus increasing the flow area, the mass flow could be adjusted. Another spin-off would be longer blades for the outer section, which would again help in reducing secondary blade losses.

Distortion will occur for any practical intake, thus the fan must have a fair tolerance to inlet distortion. Even though no detailed tests have been done to establish the sensitivity of the two-stream fan to total pressure distortions, some tests done by de Villiers[45] did consider the performance of the fan with some inlet distortion. These tests were done on the fan demonstrator with more practical intakes, as opposed to a bell mouth inlet, and velocity profiles were then taken ahead of the fan with a five-hole-probe. Although the resolution of the measurements was not fine enough to determine DC60 factors, a qualitative comparison could be made to CFD evaluations. When comparing contour plots of axial velocities, it appeared the distortion on the experimental intakes was much worse than for the intake designs discussed here. With this distorted inlet flow the mass flow of the fan sections decreased by 7.7% for the inner and outer sections, while fan pressure rises reduced by 14% in the outer section and 9.7% for the core section. The performance reduction did thus not grow to critical levels.

To gain an idea of the compensation that is required from the fan if a realistic intake is fitted, a fan performance calculation with the intake CFD results is given here. Taking the best performing intake at hover (CR = 3.5 for the respective helicopter versions) and adding the extra pressure rise required to overcome the intake pressure loss, the power required by the fan is given in Table 10.1. The mass flows through the two sections remains the same as for the ideal case. These calculations are for steady hovering conditions at the design atmospheric conditions. The power increases by 13.1% and 6.8% for the single- and twin-engine helicopter respectively. This higher power demand from the fan with the intakes is however still below the power requirement of the conventional tail rotor. This also shows that by optimising the entire CIRSTEL system an overall power saving can still be achieved, even if it is not possible to obtain perfect performance values for all the subsystems.

Requirements and Considerations of the Design

From the performance of the intakes, based on the CFD results, it is suggested the intakes should exhibit the following features or the following design points should be considered. Specific emphasis here is on the fan intakes; for engine intakes attention should also be given to dust protection.

Table 10.1 Fan Performance with simulated intakes for 100% of main rotor torque

	Single 2070kg T/O mass	Twin 3500kg T/O mass
Total Pressure Supplied to Outer Section by the Fan [Pa]	1316	2796
Additional Pressure Rise for Outer Section [Pa]	361	517
Total Pressure Supplied to Core Section by the Fan [Pa]	1054	2275
Additional Pressure Rise for Core Section [Pa]	112	107
Total Fan Power with Ideal Intakes [kW]	12.7	38.8
Total Fan Power with Real Intakes [kW]	14.5	41.5
% Power Increase	13.1%	6.8%
Equivalent Tail Rotor Power [kW]	23.7	53.0

Fuselage Position and Local Air Flow Conditions

The local airflow conditions are the starting point for the design of the intakes. The flow conditions that have to be taken into account are the conditions enforced by the rotor and the rotor hub. Also, the nature of the incoming flow at the location of the intakes has to be considered. For example the flow patterns resulting from the fuselage, engine cowling, gearbox cowling and position of the engine intakes (to name a few), have to be properly accounted for. Removed doors and any other disturbances of the upstream flow also have to be considered. Below advance ratios of about μ = 0.03 the top intake concept performs better than the side intakes after which the side intakes have the advantage due to the hub wake already being convected past the intake openings.

One of the objectives of the NOTAR and CIRSTEL systems was to reduce the noise emissions from the helicopter. The first OH-6 helicopter, fitted with the first version of the NOTAR tail boom also had its fan intakes facing sideways. Observers on the ground could thus clearly hear the fan, with the overall noise reduction being virtually nil. This was one of the reasons why the intake was then modified to only face upwards. As a result the fan noise was then radiated upwards, away from possible observers. Thus for the side intakes the fan noise can be expected to be significant. Furthermore, the sideways facing and open nature of the intakes does not shield the fan well from any battle damage or FOD damage.

Contraction Ratio and Intake Duct Design

Intake contraction ratio has shown to be a fundamentally important design parameter through which intake losses and distortion can be controlled, provided the duct cross-sectional area decreases consistently. Conversely, an increase of the cross-sectional duct area will cause a potential performance reduction due to possible separation in the now diffusing duct.

Boundary layer control inside the duct is important to limit the degradation of the outer fan section. Though not evaluated with the CFD simulations, a sudden contraction of the intake duct just ahead of the fan can thin the boundary layer that affects the outer fan section. If so desired active boundary layer control methods can also be applied, as for example outlined by Seddon et al.[20] and Goldsmith et al.[25].

Intake grids will have to be fitted to give the fan some form of protection from FOD. Unlike engine intakes, sand filters are not recommended. Sand filters will add to the complexity and losses

experienced by the intake; the fan itself should thus rather exhibit a tolerance to small FOD particles.

The angle of incidence on the intake varies considerably throughout the flight envelope. For the CIRSTEL system the intakes must be optimised for hover and low speed flight, as this is the part of the flight envelope where there is a principal reliance on the fan. For the rest of the forward flight envelope the increased dynamic pressure can be utilised to boost the intake/fan performance.

Lip Shape

Along with the intake contraction ratio, lip shaping is the most critical part of the design. Factors that have to be considered are the thickness, aspect ratio and cambering of the cross-section for the lips. Generally an elliptic cross-sectional profile is used for incompressible flow intakes, and can also be used here. Commonly an aspect ratio of 2:1 is used for the elliptical cross-section, which was found to give good results. (Reddy[46]). Vuillet[24] suggests a lip thickness of around 25% of the intake diameter. For the side intakes it is however suggested here to use significantly thicker lips on the upper sector of the intake to prevent separation during hover. Camber angle should be determined from the anticipated local flow conditions; emphasis should be on hovering conditions. If required, slotted intake lips, such as those applied on the Harrier (Goldsmith et al.[25]), can also be used to suppress intake losses.

Intake Scoop

The idea of adding an intake scoop to the side intakes appeared to work well. Streamline plots of the air entering the fan show how the scoop captures air at low advance ratio conditions. The size of the scoop should however be limited as its presence is detrimental to the intake performance in high-speed flight.

Conclusion

The evaluations of the intake designs, one for the Alouette III fuselage and two for a generic fuselage, were performed and the results show that the intake designs studied here are feasible. The flow phenomena affecting the intakes are identified, the primary design difficulty being the dynamic flow fields affecting the intakes from hover to flight speed. Intake efficiency, losses and distortion have been shown to be controllable by the selection of intake position, contraction ratio and lip shape. It is advised to design the intake primarily for hovering conditions. The study included only numerical trials of the flow phenomena affecting the intake. It thus remains to quantify the performance figures experimentally to gain confidence in the results presented in the preceding chapters.

CHAPTER 11

CONCLUSION AND RECOMENDATIONS

The objectives set for this thesis in the introduction have been achieved, and the following conclusions can be drawn on the fan performance, intake design and the CIRSTEL system in general

Fan Performance Evaluation

The objective of the performance evaluations was to conduct experiments on a demonstrator of the twin-stream fan. Specifically, velocity profile measurements and performance mapping tests were done on the original set up and an evolved version of the demonstrator. The results of these tests are given in Chapters 2 to 5, while design recommendations are give in Chapter 6. This section sums up the findings of the experiments.

The profile measurements conducted in Chapter 2 showed that the fan sections worked, in principle, to the design specifications. Mass flows and pressures measured were close to the required quantities. However, some deficiencies of the design could be identified from these measurements. The performance of the outer section did not match the design requirements completely, as the mass flow fell short by 10% and the total pressure by 4%. Factors that contributed to the reduced performance were the high inlet blockage on the outer section, which was not considered in the design of the demonstrator, and the rudimentarily constructed stators. The stators could not turn the flow back to the axial direction, which caused the diffuser to stall. The core fan total pressure exceeded the design requirements by 33%, and the efficiencies for both sections were found to exceed the design requirements. The measured efficiencies were 79% for the outer and 86% for the core section. When scaling the performance data the power consumption scaled to 36kW, which was less than the allowed 40kW. The concept of the rotor shroud was also found to work well.

New stator blades were designed and built based on the findings in the previous experiments. It was hoped that the aerodynamic stators would improve the overall performance of the fan, especially the outer section where a better diffuser performance was envisaged. However the improved performance did not materialise completely, primarily due to a reduction in the diffuser performance, despite less inlet swirl to the diffuser. Upon further investigation it was found that the modified outer stators were stalled, and a 16^{o} swirl angle remained, due to a too optimistic blade design that pushed the diffusion factor higher than the advised value of 0.5. As a result the fan efficiencies decreased.

In Chapter 3 the results of the performance mapping tests are presented. The effects of the adjustable IGV blades on the power turn down in each section were tested and at a maximum IGV deflection of -40^{o} the total power reduced by 30%. It was found that the design of the IGV blade was not refined enough to result in an effective power reduction of the outer section. Only small coupling effects were measured between the two sections, typically less than 5%, of which none were detrimental to the performance of the fan. Abrupt stall characteristics of the fan were detected, which could be attributed to the original stator construction. The modified stators did alter the stalling characteristics to a gradual transition into stalled conditions.

The inclusion of a shroud fitted to the rotor was shown to be a practical solution for the generation of two different air streams. The design of the stators is critical as the diffuser performance depends directly on the amount of inlet swirl. The use of two-stage stators should be considered for the outer section, as a single row of stators cannot turn the flow sufficiently. Reducing the radius of

the shroud position can have positive effects, such as increasing the mass flow through the outer section and increasing the inlet total pressure. Increasing the IGV solidity, especially near the fan casing so that a constant solidity is maintained, will ensure better flow turning and more effective fan power reduction.

Air Intake Design

The objectives of the intake design were to develop practical intakes for the two-stream fan when fitted to the Alouette III/CIRSTEL combination. Using a commercial CFD code an intake concept was evaluated and modified for improved performance.

Concepts were developed in Chapter 7 with consideration for the spatial constraints posed by the Alouette III fuselage structure and the aerodynamic conditions that would be experienced from hover to maximum forward flight. Studies were done to determine suitable options that can be implemented to improve the intake performance, primarily during hover.

A simple model was developed to emulate the effects of the rotor downwash, using momentum theory, which was used in defining the boundary conditions of the CFD models. The CFD evaluations simulated the helicopter in flight, from an advance ratio of $\mu = 0.00$ to a maximum of $\mu = 0.3$. From the simulation results distortion factors were calculated which occur at the fan face for the outer and core sections of the fan. The initial intake design proved to have too high distortion values, and thus two further design iterations of the concept were completed. For the last iteration the DC60 factors dropped to 0.4 and 0.02 for the outer and core sections. Over the entire tested flight envelope the performance and efficiency of the third intake design iteration improved to acceptable levels. An important design consideration for the intake is the effects it will have on the outer fan during hover and low speed flight, as it is here where there is the most dependence on the outer fan section.

Some improvements are still possible on the design, and critical design parameters were identified. Most importantly the shape of the intake lips in the upper and side sectors of the intake have to be carefully considered. The upstream flow conditions and presence of any bodies like the fuselage or fairings have to be considered when designing the intakes. The location of the intake opening on the helicopter also contributes to the feasibility of the entire concept and thus the helicopter configuration should be chosen carefully.

The studies were extended to include a more detailed analysis of helicopter aerodynamics specific to the design of intakes. For these studies an actuator disk was used to model the main rotor. The rotor hub was also modelled here as it was found to modify the flow field around the fuselage significantly and thus affected the intakes.

Two fan intake concepts were evaluated and compared for a generic helicopter fuselage. The side and top mounted intake concepts for the fan showed that each design has itsown advantage, but no preferred concept evolved out of the studies. An intricate duct shape characterises the side intake that can lead to excessive losses if not carefully designed. The top intake, on the other hand, is easier to design for minimal duct losses. Location of the intake capture area is an important factor as this determines the flow quality available to the intake. In the intermediate flight range between $\mu = 0.03$ and $\mu = 0.15$ the rotor hub strongly affects the top intake as it ingests a significant portion of the hub wake. Only below $\mu = 0.06$ are the effects of the rotor hub appreciably felt on the side intakes.

Intake contraction ratio can be used to limit losses and distortion, but for these type of intakes a contraction ratio of 3.0 appears to be the optimum, since larger contraction ratios do not show significant improvements. Highlighted here again is the important role that the rear sector (and for the side intakes upper sector) intake lips play in limiting the intake losses. The intake lips must

display a minimum/significant thickness and be designed for hover and very low speed flight conditions.

The CIRSTEL System

This thesis focused on two components of the CIRSTEL system, namely the fan and the intakes for the fan. Through the work presented here these two components are characterised for a range of conditions that will be experienced during flight. The system model that is discussed in Chapter 5 is valid for hovering flight only, since the characterisations used for the Circulation Control Section is derived for hovering conditions only. Nevertheless the system model showed that through optimisation the power demand of the system could ideally be reduced over conventional tail rotors by up to 37%. An uncertainty in the exact performance of the mixer remained, resulting in the modelling of this component being done with momentum theory that is adjusted to the limited experimental results available. It is however suggested to investigate the performance of such a mixer/ejector combination in more detail to gain confidence for the system modelling. Also, scope exists for further advanced research on the stability and flight dynamics of a helicopter fitted with CIRSTEL, along with control methods and characteristics of the system. The composition of the three directional torque control methods that make up the CIRSTEL tail boom during different flight phases and its effects on control methods will have to form part of future research efforts.

REFERENCES

1. Vuillet, A., (1989), *Operational Advantages and Power Efficiency of the Fenestron as Compared to a Conventional Tail Rotor*, Vertiflite, Vol. 35, No.5, July/August 1989, pp. 24-31.
2. Lambermont, P., (1958), *Helicopters and Autogyros of the World*, via http://avia.russian.ee/helicopters_eng/cierva_w9-r.html
3. Logan, A.H., Morger, K.M., Sampatacos, E.P., (1983), *Design, Development and Testing of the No Tail Rotor (NOTAR) Demonstrator*, Paper No. 67, 9th European Rotorcraft Forum, Stresa, Italy, September 1983
4. Nurick, A., (1997), *Evaluation of the Performance of a CIRSTEL System Fitted to an Alouette 316B Helicopter*, Denel Aviation Report, 95F0000RL0001, October 1997
5. von Backström, T.W., (1999), *Fan Conceptual Design*, ITM/VB9903, Department of Mechanical Engineering, University of Stellenbosch, South Africa.
6. Heise, R., (1999), *Development of a Twin-Flow Axial Fan*, Final Year Project, Department of Mechanical Engineering, University of Stellenbosch, Stellenbosch, South Africa.
7. Thomas, K. (2000), *Testing of a Twin Flow Axial Fan*, Final Year Project, University of Stellenbosch, South Africa.
8. Kirstein, C. (2001); *Flow Through a Solar Chimney Power Plant Collector-to-Chimney Transition Section*, MSc Thesis, University of Stellenbosch, South Africa.
9. Fonernel, M.A., Nurick, A., (1990), *The Use of Circulation Control on the Tail Boom of a Helicopter: A Survey*, Report No 93, University of the Witwatersrand.
10. Wennerstrom, A.J. (2000), *Design of Highly Loaded Axial-Flow Fans and Compressors*. Concepts ETI, Vermont, USA.
11. Seddon, J. (1990), *Basic Helicopter Aerodynamics*, AIAA /Blackwell Science.
12. Riegels, F.W., (1961), *Airfoil Sections*, Butterworths, London
13. Gessow, A., Myers, G.C., (1983), *Aerodynamics of the Helicopter*, Frederic Ungar Publishing, New York
14. Lippert, A.M., Martins, J.C.F., Nurick, A., (1994), *CIRSTEL Conceptional Design: Input Parameters and Optimisation Process*. CSIR Report AERO 94/199.
15. Hoerner, S.F., (1965), *Fluid-Dynamic Drag*, Hoerner Fluid Dynamics.
16. Bouwer, P., Nurick, A., (1994), *An Experimental Investigation of a ½ Scale Combined Helicopter Anti-Torque And Engine Exhaust Gas Cooling Model*, CSIR Report AERO 94/099.
17. Nurick, A., (1995), *An Experimental Investigation of the Characteristics of Helicopter Thrusters*, Aeronautica Meridiana, Vol. 12, pp. 14-35.
18. Nurick, A., (1992), *Experimental Investigation of a Helicopter Circulation Controlled Tail Boom*, Journal of Aircraft, Vol. 38, No. 3, May-June 2001, pp. 528-535.
19. Vanderplaats, G.N., (1999), *Numerical Optimisation Techniques for Engineering Design*, 3rd Edition.

20. Seddon, J., Goldsmith, E.L. (1999), *Intake Aerodynamics*, Second Edition, Blackwell Science.

21. Hermans, C., Hakkaart, J., Panosetti, G., Preatoni, G., Mikulla, V., Chéry, F., Serr, C., (1997), *Overview of the NH90 Wind Tunnel Test Activities and the Benefits to the Helicopter Development*, American Helicopter Society 53rd Annual Forum, Virginia Beach, Virginia, April/May 1997.

22. Holdø, A.E., O,Brien, M., Calay, R.K., (2000), *Flows Generated by the Interaction of an Inlet and a Cross-Flow*, Journal of Wind Engineering and Industrial Aerodynamics, Vol. 88 (2000), pp. 1-23.

23. Boizard, B., (1984), *Three-Dimensional Calculation of the Flow in Helicopter Air Intakes*, Vertica Vol. 8, No. 3, pp. 243-253.

24. Vuillet, A., (1980), *Aerodynamic Design of Engine Air Intakes for Improved Performance*, 6th European Rotorcraft and Powered Lift Aircraft Forum, Bristol, England, September 1980.

25. Goldsmith, E.L., Seddon, J., (1993), *Practical Intake Aerodynamic Design*, Blackwell Science.

26. Leishman, J. G.; Bi, N-p (1989), *Aerodynamic interactions Between a Rotor and a Fuselage in Forward Flight*, Journal of the American Helicopter Society 1990, v.35, n.3, pp. 22-31.

27. Berry, J; Bettschart, N (1997); *Rotor-Fuselage Interaction: Analysis and Validation with Experiment*; 53rd Annual Forum Proceedings of the American Helicopter Society.

28. Cumpsty, N.A. (1989), *Compressor Aerodynamics*, Longman Scientific & Technical, Essex, UK.

29. Mineck, R.E., Althoff Gorton, S., (2000), *Steady and Periodic Pressure Measurements on a Generic Helicopter Fuselage Model in the Presence of a Rotor*, NASA TM 2000-210286.

30. Hotchkiss, P.J., Meyer, C.J., von Backström T.W. (2006), *Numerical Investigation into the Effect of Cross-Flow on the Performance of Axial Flow Fans in Forced Draught Air-Cooled Heat Exchangers.* Applied Thermal Engineering 26 (2006), pp. 200-208.

31. Chaffin, M.S., Berry, J.D., (1997), *Helicopter Fuselage Aerodynamics Under a Rotor by Navier-Stokes Simulation*, Journal of the AHS, July 1997, v.42, no.3, pp. 235-242.

32. Lee, J-K, Kwon, O. J., (2002), *Predicting Aerodynamic Rotor-Fuselage Interactions by Using Unstructured Meshes*, Trans. Japan Soc. Aero Space Science, Vol. 44, no. 146, pp. 208-216

33. Ruffin, S.M., O'Brien, D., Smith, M.J., Hariharan, N., Lee, J-D, Sankar, L., *Comparison of Rotor-Airframe Interaction Utilizing Overset and Unstructured Grid Techniques.* 42nd AIAA Aerocpace Sciences Meeting and Exhibit, Reno, NV, January 2004.

34. Thiart, G.D., von Backström, T.W., (1993), *Numerical simulation of the Flow Field Near an Axial Flow Fan Operating Under Distorted Inflow Conditions*, Journal of Wind Engineering and Industrial Aerodynamics, pp. 189-214.

35. Meyer, C.J., Kröger, D.G., (2002), *Numerical Simulation of the Flow Field in the Vicinity of an Axial Flow Fan*, International Journal of Numerical Methods in Fluids, pp. 947-969.

36. Freeman, C.E., Mineck, R.E., (1979), *Fuselage Surface Pressure Measurements of a Helicopter Wind-Tunnel Model with a 3.15 Meter Diameter single Rotor*. NASA TM 80051.

37. Launder, B. E. Spalding, D. B., (1972), *Lectures in Mathematical Models of Turbulence*. Academic Press, London, England

38. Wilcox, D. C., (1998), *Turbulence Modelling for CFD*. DCW Industries, Inc., La Canada, California.

39. Menter F.R., (1994), *Two-Equation Eddy-Viscosity Turbulence Models for Engineering Applications*, AIAA Journal, Vol. 32, No. 8, pp. 1598-1605.

40. Spalart, P. Allmaras, S., (1992) *A one-equation turbulence model for aerodynamic flows.* Technical Report AIAA-92-0439, American Institute of Aeronautics and Astronautics.

41. Cokljat, D., Liu, F., (2002), *DES of Turbulent Flow Over an Airfoil at High Incidence*, AIAA Paper, No. 2002-0590

42. Fluent News, (2005) Vol. XIV Issue 1, pp. 34-35

43. Sawyer, J.W. (1976), *Sawyer's Gas Turbine Engineering Handbook, Vol. 1*, Second Edition, Gas Turbine Publications, Inc. 80 Lincoln Ave., Stanford, Connecticut, 06904.

44. Prouty, R.W., (1986), *Helicopter Performance, Stability and Control*, PWS Publishers.

45. De Villiers, S.H. (2001), *Development of Air Intakes for a Helicopter with an Internal Fan*. Final Year Project, University of Stellenbosch, South Africa.

46. Reddy, D.R., Reddy, E.S., Moody, R.E., (1997), *Aerodynamic Shape Optimising of a Subsonic Inlet Using Three-Dimensional Euler Computation*. Journal of Propulsion and Power. Vol. 14, No. 2, March-April 1998, pp. 225-233.

47. von Backström, T.W., (2000-2005), *Private Communication.*

48. Gannon, A.J., (2002), *Design of a Solar Chimney Turbine*, Ph.D. Thesis, University of Stellenbosch, Stellenbosch, South Africa.

49. Lewis, R.I., (1991), *Vortex Element Methods for Fluid Dynamic Analysis of Engineering Systems*, Cambridge Press, Cambridge.

50. White, F.M. (1994), *Fluid Mechanics*, Third Edition, McGraw-Hill, London.

51. Jane's All the World's Aircraft (1970).

52. CFX 5.5 Manual (2001), AEA Technology.

53. Wikipedia (2006), *Super-ellipse*, http://en.wikipedia.org/wiki/Super_ellipse

APPENDIX A

EXPERIMENTAL APPARATUS AND PROCEDURE

This section describes the experimental fan test set-up and the test equipment used here. Two types of tests were done on the fan, namely velocity profile measurements with the aid of a five-hole-probe, and global performance tests. For the performance tests, static pressures on the casings were measured, along with fan speed and torque.

Test Set-Up

The demonstrator fan in which the tests were conducted was an 83% scale model of the full-scale prototype. This demonstrator was however not a true scale model; it was slightly distorted to simplify the manufacturing process, as described by Heise[6]. Tables A.1 and A.2 list and compare the dimensions of the fan sections for the full scale prototype and scaled test demonstrator. The blade profiles were also simplified. A constant section blade was used in the outer section of the fan. The designed profile did not vary significantly over the span of the blade, the effort involved in manufacturing did not warrant a non-constant profile. The core fan blade profile did vary significantly however; instead of the designed profile values, the camber and stagger were interpolated linearly between hub and shroud.

Table A.1 Outer fan dimensions

	Hub diameter [mm]	Tip Diameter [mm]	Hub-Tip Ratio
Prototype	600	666	0.901
Demonstrator	490	550	0.891

Table A.2 Core fan dimensions

	Hub diameter [mm]	Tip Diameter [mm]	Hub-Tip Ratio
Prototype	305	594	0.513
Demonstrator	270	484	0.558

The fan consisted of an outer and core section driven by a single 3.5kW electric motor. Both sections shared the same constant chord adjustable inlet guide vanes, but were split from the rotor onwards into the two respective sections. The outer section consisted of the rotor, stator blades and an annular diffuser, while the core section consisted of the rotor and stators only.Figure A.1 shows a general view of the fan test facility.

The inner and outer sections could be throttled independently. The outer section was throttled by means of adjustable orifice plates, and at the same time these also served to measure the outer section mass flow. The core section was throttled using a standard throttle plate used for industrial fan tests. The total mass flow through the system was measured with the inlet bell mouth, while the outer mass flow was measured with the already mentioned orifice plates. Subtracting the outer flow from the total flow gave the core section mass flow.

There were 7 stations at which the velocity profiles were measured. These positions are indicated in Figure A.2. The five-hole-probe used for these tests was mounted in a specially constructed bracket that attached onto the fan casing. The bracket allowed the probe to be traversed across the

span of the fan sections. Provision was also made on the bracket to adjust the yaw angle of the probe.

There were 8 stations at which the casing static pressures were measured. The stations are indicated in the diagram of Figure A.3. There were four pressure tapping points for each station, except behind the core rotor, where there were only two tapping points that were connected to the outside via thin copper pipes.

Figure A.1 The fan test-rig set up with sampling equipment

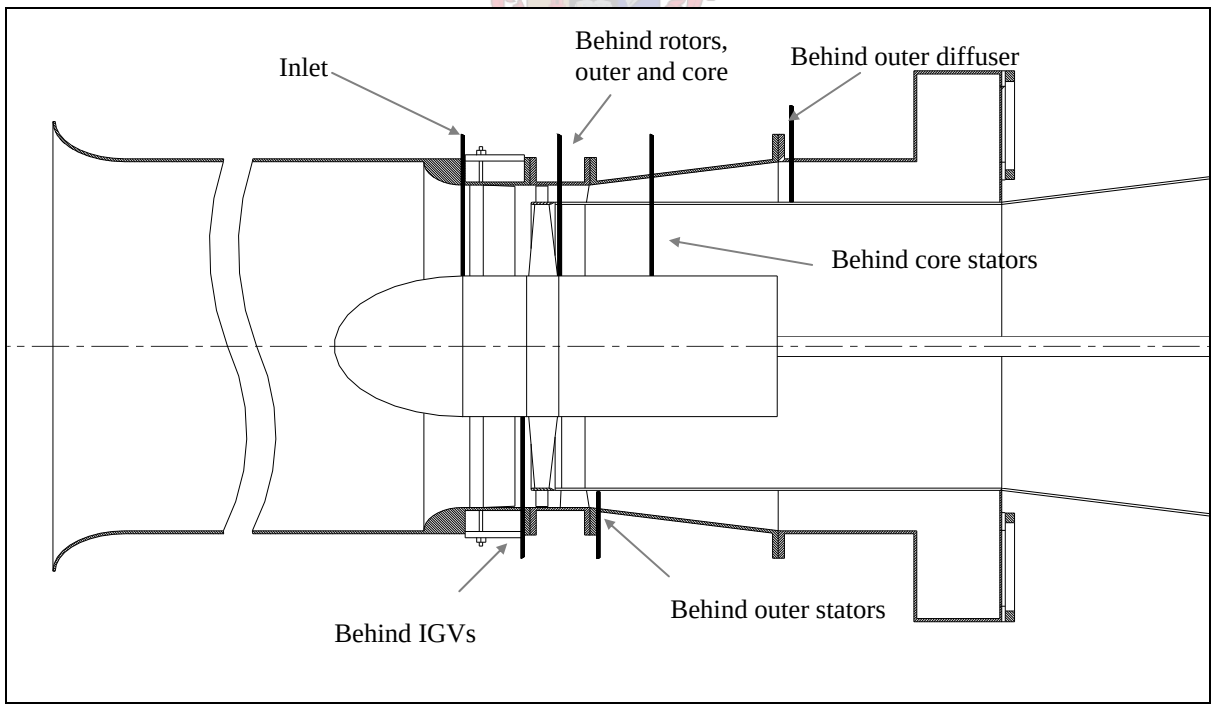

Figure A.2 Location of five-hole-probe insertion and measuring points

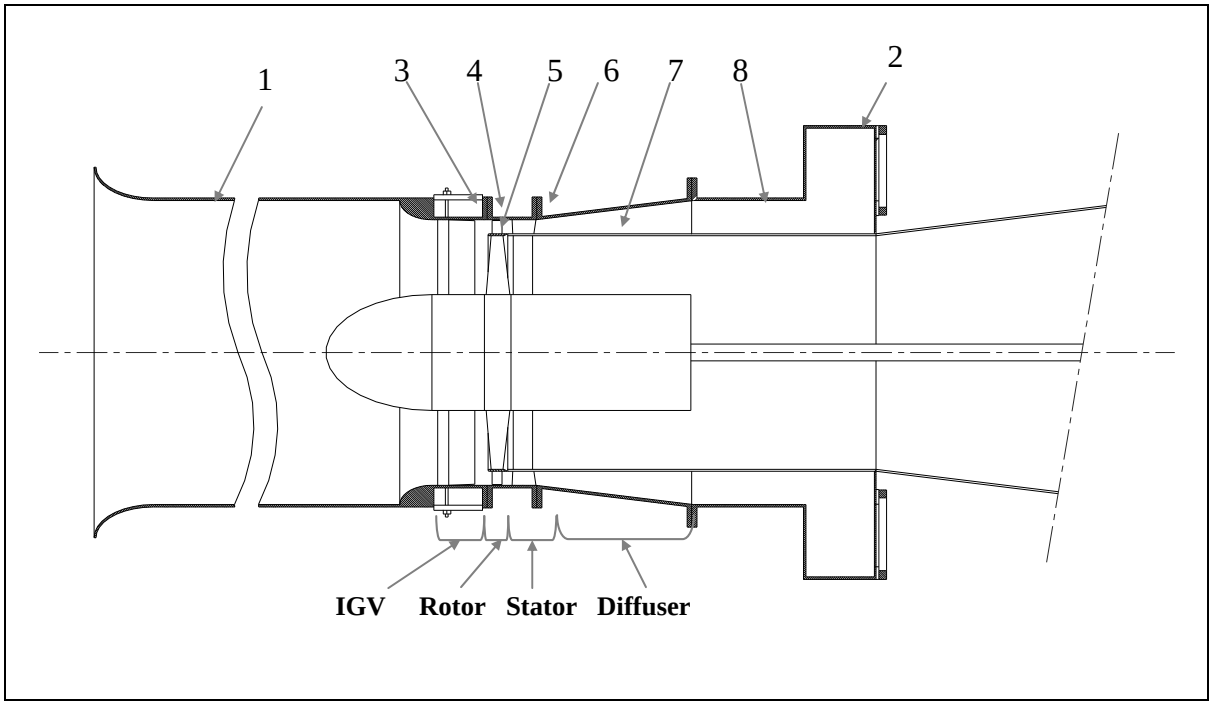

Figure A.3 Location of static pressure tapping points and fan sections

Table A.3 Description of pressure tapping points

1	Inlet bell mouth	5	Behind core rotor
2	Orifice plates	6	Behind outer stator
3	Behind Inlet guide vanes	7	Behind core stator
4	Behind outer rotor	8	Behind outer diffuser

Design and Manufacture of New Stators

The stators of the original fan test rig were made from sheet metal; plates bent to give some camber and welded into position. These rudimentary blades had neither airfoil profiles nor any variation of camber and chord. Thus the stators could not have been optimally efficient, yet the overall performance of the system was found to be acceptable.

An excessive amount of swirl did remain behind the stators in the outer section causing the diffuser to stall, while at the same time the decrease in axial velocity caused the swirl angle to increase dramatically towards the diffuser exit. As a rule of thumb, the swirl angle should not exceed the diffuser cone angle (von Backström[47]). As the fan performance was already promising, it was hoped that by adding properly designed stators the performance would improve even more.

The measured flow angles behind the rotor of the original version were the input for the blade design; with the design criteria being that the flow had to be turned completely into the axial direction by the stators. This however also being subject to secondary constraints that took into account the blade aspect ratios and blade spacing.

A code developed locally by Gannon[48] for the design of turbo machinery blades was chosen for the design work on the stators. This design code uses the surface vorticity method (Lewis[49]) to

solve the flow around the blade geometry, and then optimises the blade geometry using numerical optimisation techniques.

For the outer section the number of blades selected was 50 to limit the blade aspect ratio, as casing and shroud dimensions already fixed the blade height. Also blade spacing had to be considered to allow for machining. Twenty-five blades were chosen for the core, again half the number of outer blades, as for the rotor. Out of further construction considerations the minimum blade thickness was also limited to provide a strong blade.

Finalised characteristics of the blade profiles, based on the modified NACA 4 digit profiles, are presented in Table A. and Table A.5. It was not possible to completely turn the flow into the axial direction in the outer section of the fan. An exit swirl angle of 5^o to 7^o remained as listed in Table A., but it was less than the diffuser angle and thus acceptable. More turning is possible, but that would require a further increase of the chord. At this stage the aspect ratio of the outer blades was already at 0.44, and reducing this would further run the risk of increased losses. For this reason the pitch chord ratio on the outer blades was limited to 0.5. At the same time machining difficulty would also escalate. Due to the camber and pitch of the outer blades a very long cutter had to be used and the work piece set at an angle to the machining axis, which added to the difficulty of the machining process.

Table A.4 Blade data for the modified NACA 4 digit outer stators

% Span	Outlet angle	Stagger angle	Chord [mm]	Pitch/ Chord	m_{ord}	p_{ord}	t_{max}	$m_{t\,max}$ top/bottom	I_{nose} top/bottom
0%	6.97^o	22.48^o	61.6	0.50	0.095	0.50	0.10	0.452/0.279	3.345/0.886
50%	5.01^o	20.79^o	65.7	0.50	0.083	0.50	0.10	0.474/0.258	3.996/3.768
100%	6.97^o	26.42^o	69.8	0.50	0.110	0.50	0.10	0.433/0.285	3.791/6.202

Table A.5 Blade data for the modified NACA 4 digit core stators

% Span	Outlet angle	Stagger angle	Chord [mm]	Pitch/ Chord	m_{ord}	p_{ord}	t_{max}	$m_{t\,max}$ top/bottom	I_{nose} top/bottom
0%	0.160^o	14.43^o	51	0.665	0.0901	0.50	0.10	0.259/0.271	3.646/3.268
30%	0.602^o	13.63^o	51	0.828	0.0925	0.50	0.10	0.239/0.252	3.146/3.183
60%	0.914^o	12.39^o	51	0.991	0.0912	0.50	0.10	0.232/0.239	4.088/4.181
100%	3.178^o	10.00^o	51	1.207	0.0814	0.50	0.10	0.230/0.226	4.521/5.498

TEST EQUIPMENT

The primary parameters measured during the tests were pressures, fan torque and shaft speed. The equipment used for the tests is listed in Table A.6. A standard Pentium I, 100 MHz personal computer with an Eagle technologies Analogue-to-Digital Digital-to-Analogue card (ADDA) was used to sample the data. MATLAB programs were used to control the sampling process. The input signals from the bridge amplifier and switching box signals were transmitted to and from the PC via a connection box and the ADDA card.

To simplify the process of data sampling, software was developed that automatically sampled and processed the data. The data was then displayed numerically and graphically by the software for a quick feedback of key performance figures. Mass flow measurements had an accuracy of 1.86% with the five-hole-probe having an accuracy of 5% at flow velocities above 11m/s (Kirstein[8])

Table A.6 Test Instrumentation

Sensor	Type	Accuracy
Barometer	Mercury column	1/200th inch (127 μm)
Thermometer	Alcohol thermometer	1^{o}F (0.556 ^{o}C)
Pressure transducer	HBM PD1	1 Pa
Torque transducer	HBM T5	0.002% for a max of 50 Nm
Speed sensor	Turck MS 25-UI	0.1% of shaft speed
Bridge amplifier	HBM DA24, Model KWS 7073	-
Five-hole-probe	Pneumatic probe	5% calibrated
Switching box	FCO 91 MkII	-

APPENDIX B

FIVE-HOLE-PROBE MEASUREMENTS

On the following pages the data is plotted which was taken with the aid of a five-hole-probe. The data presented here are that for the original sheet metal stators and for the machined airfoil shaped stators of the modified fan. All measurements were conducted with an inlet guide vane setting of 0^o. The velocity, pressure and angle data is plotted against the span of the blades, presented as a fraction of the local span, with zero at the inner radius. For the diffuser the width of the diffuser annulus is used. The measurements were taken behind each station, in other words the outer rotor data was taken on a single radial line just behind the outer rotor. A detailed discussion of the plots is given in Chapter 2. For completeness all plots of the data collected are included.

INLET

Original Fan (Sheet Metal Stators) **Modified Fan (Machined Stators)**

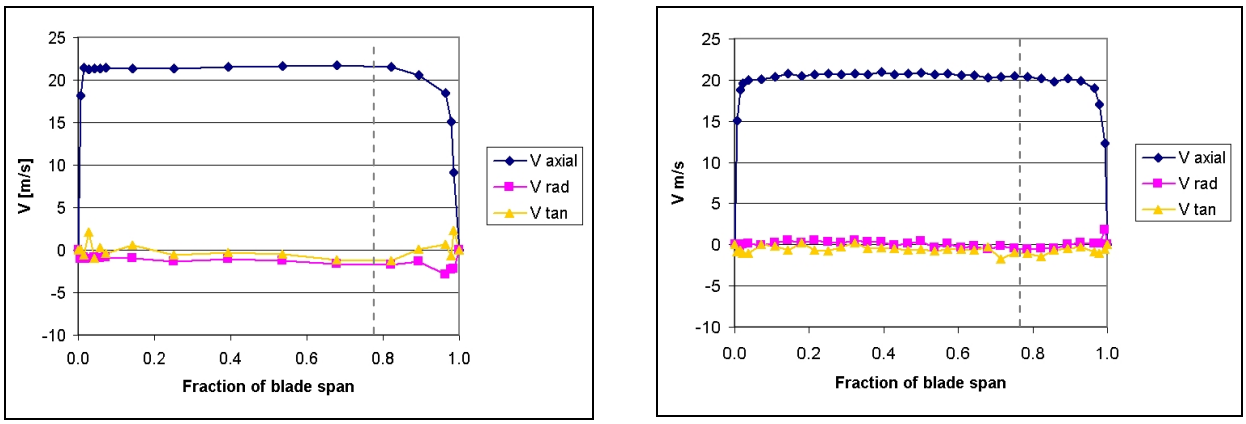

(a) **(b)**

Figure B.1 Velocity Components (Vertical line at 78% blade span indicates the radius of the shroud)

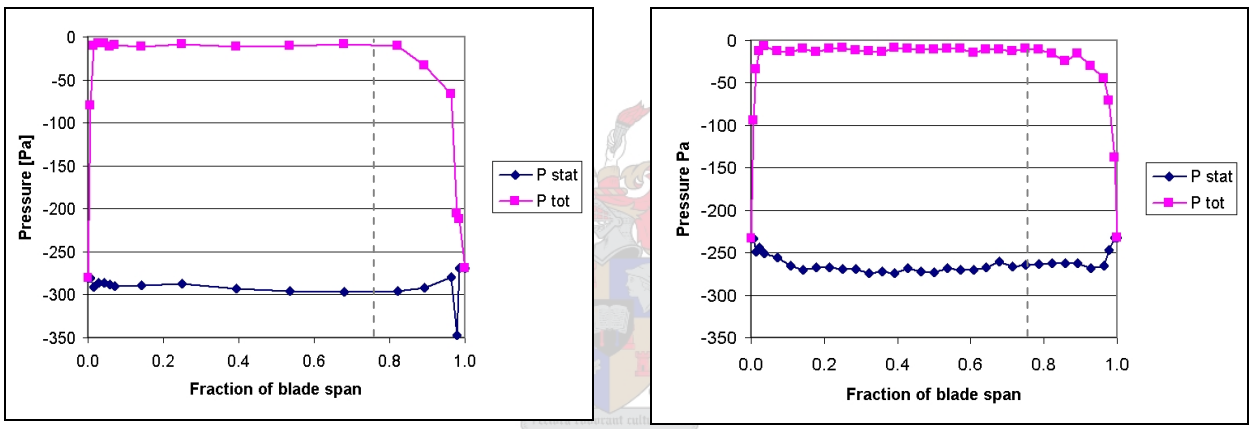

(a) **(b)**

Figure B.2 Pressures (Vertical line at 78% blade span indicates the radius of the shroud)

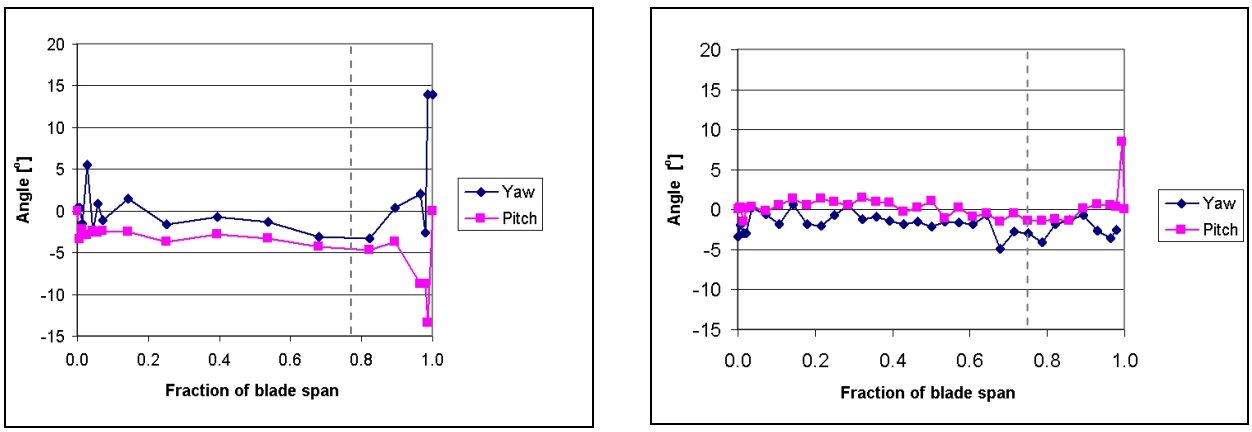

(a) **(b)**

Figure B.3 Flow Angles (Vertical line at 78% blade span indicates the radius of the shroud)

Original Fan (Sheet Metal Stators) **Modified Fan (Machined Stators)**

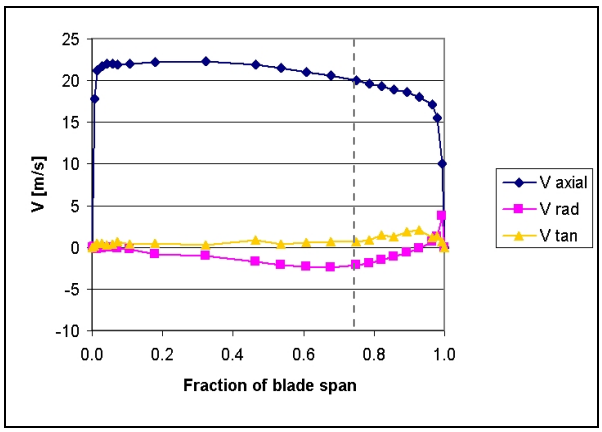

(a)

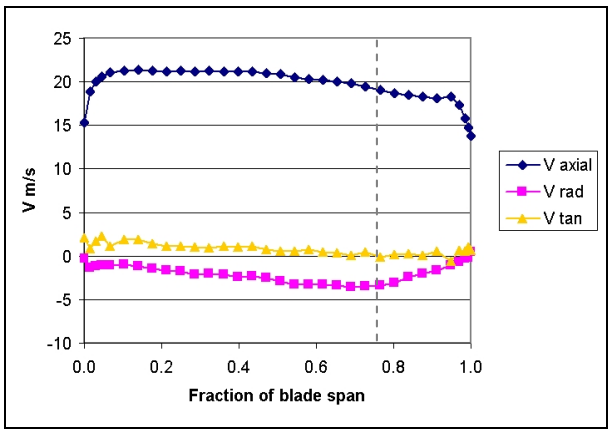

(b)

Figure B.4 Velocity Components (Vertical line at 78% blade span indicates the radius of the shroud)

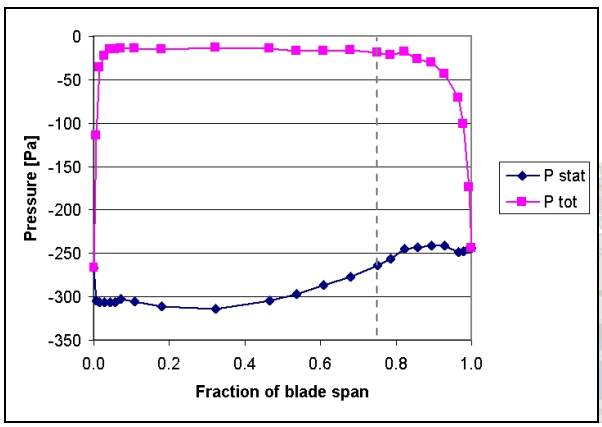

(a)

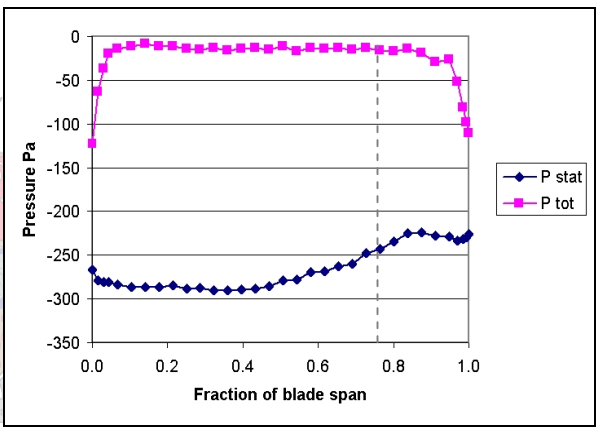

(b)

Figure B.5 Pressures (Vertical line at 78% blade span indicates the radius of the shroud)

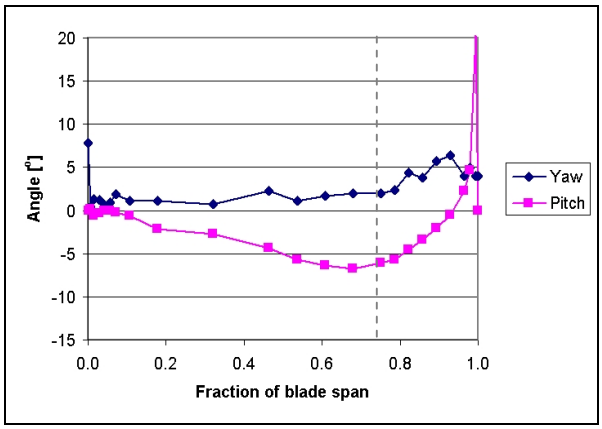

(a)

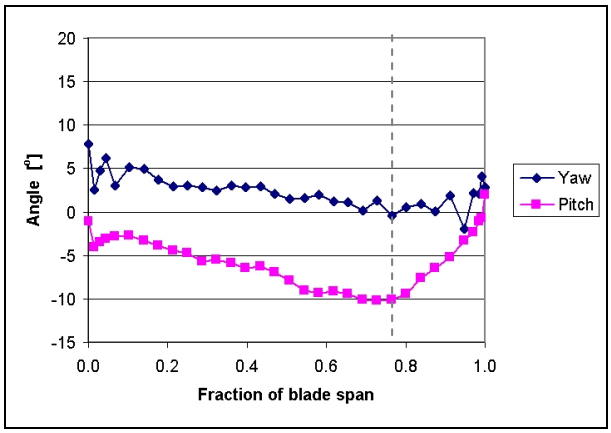

(b)

Figure B.6 Flow Angles (Vertical line at 78% blade span indicates the radius of the shroud)

CORE SECTION ROTOR

Original Fan (Sheet Metal Stators) **Modified Fan (Machined Stators)**

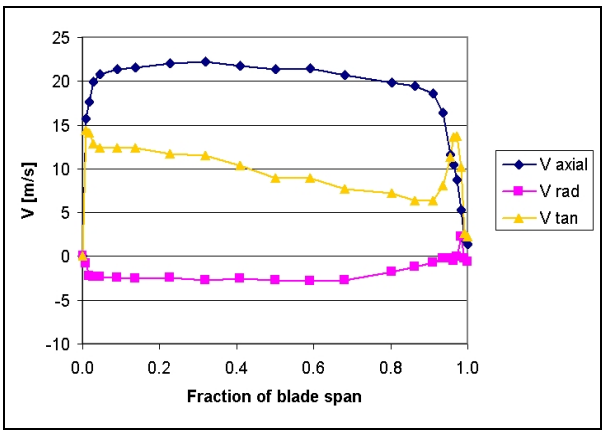

(a)

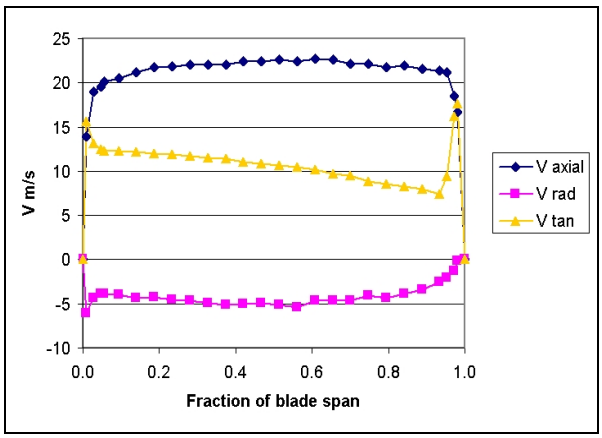

(b)

Figure B.7 Velocity Components

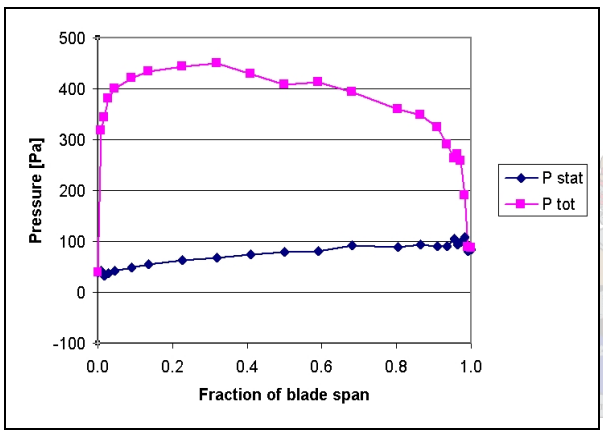

(a)

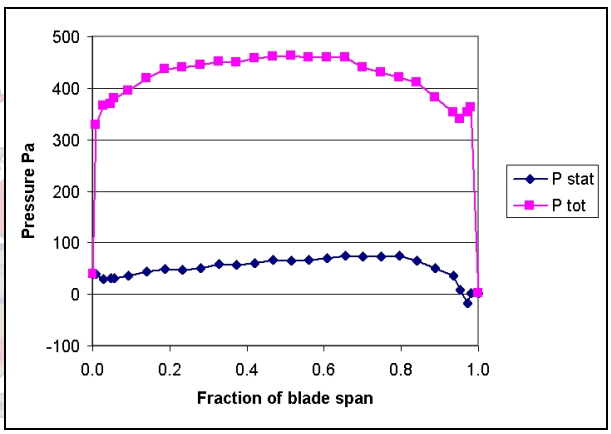

(b)

Figure B.8 Pressures

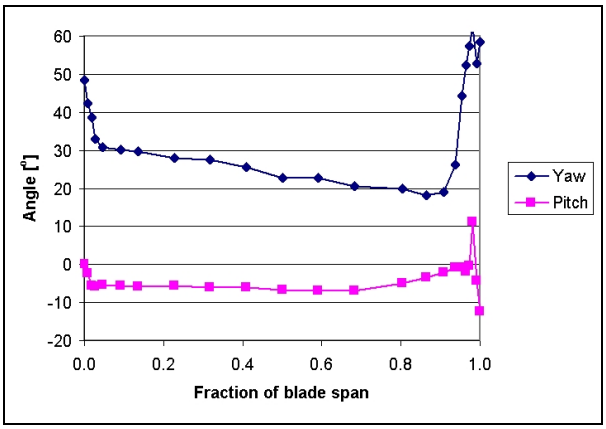

(a)

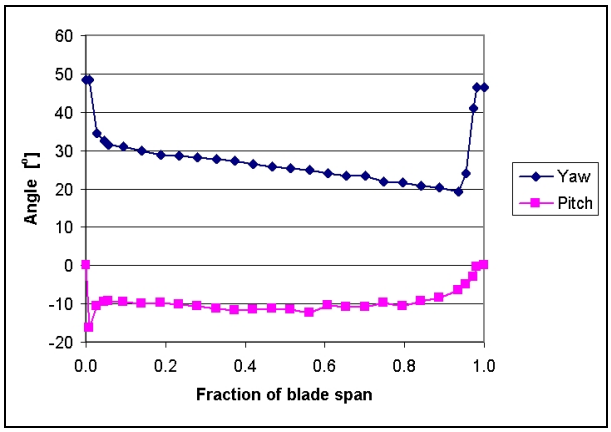

(b)

Figure B.9 Flow Angles

OUTER SECTION ROTOR

Original Fan (Sheet Metal Stators) **Modified Fan (Machined Stators)**

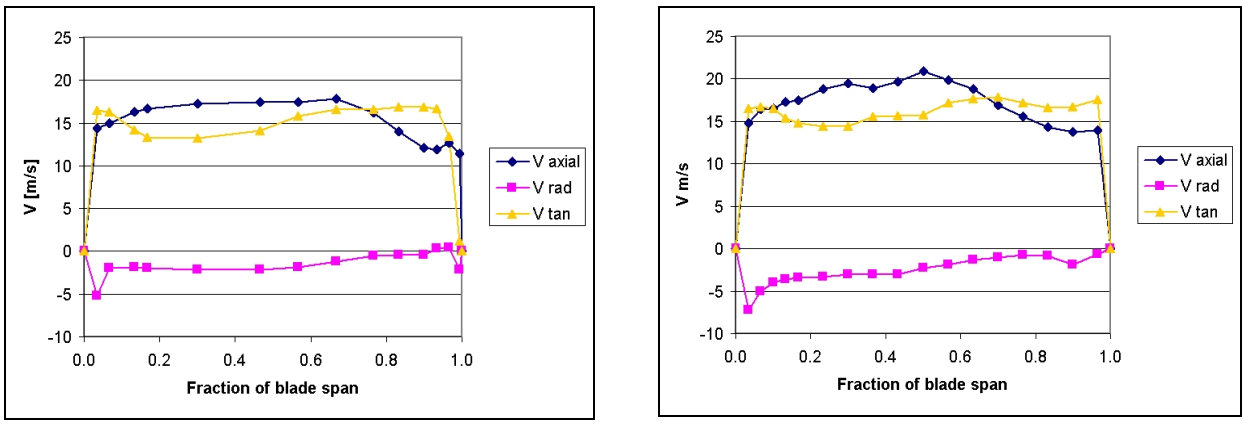

(a) **(b)**

Figure B.10 Velocity Components

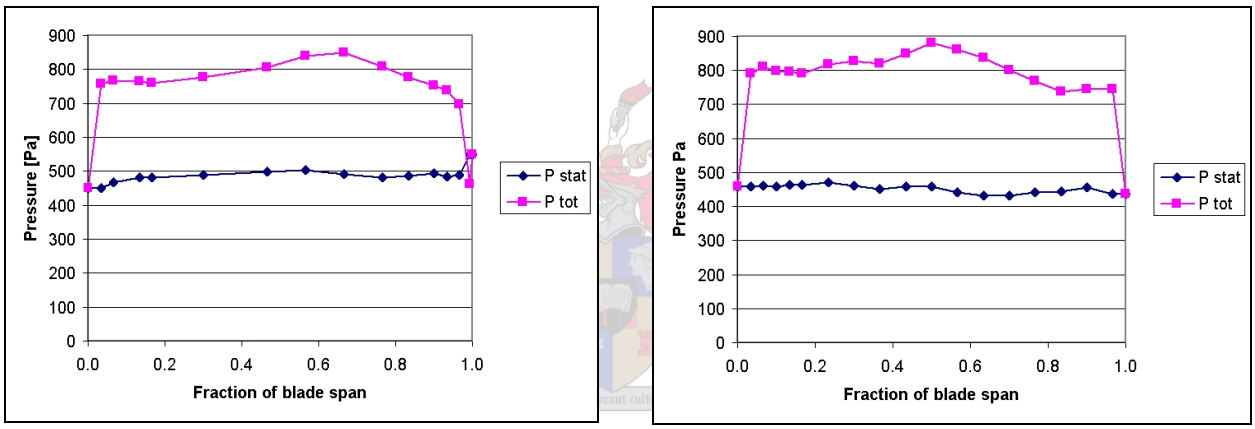

(a) **(b)**

Figure B.11 Pressures

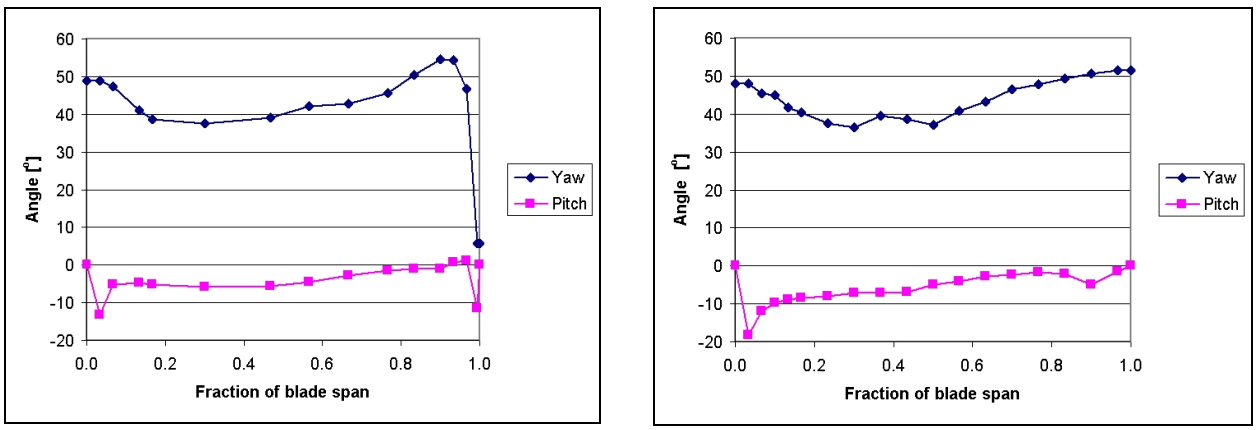

(a) **(b)**

Figure B.12 Flow Angles

Original Fan (Sheet Metal Stators) **Modified Fan (Machined Stators)**

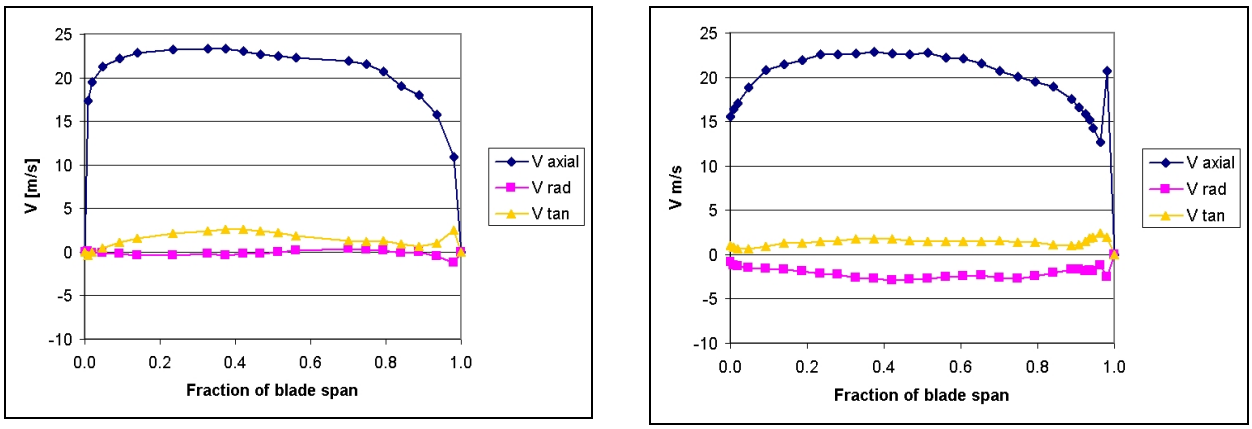

(a) **(b)**

Figure B.13 Velocity Components

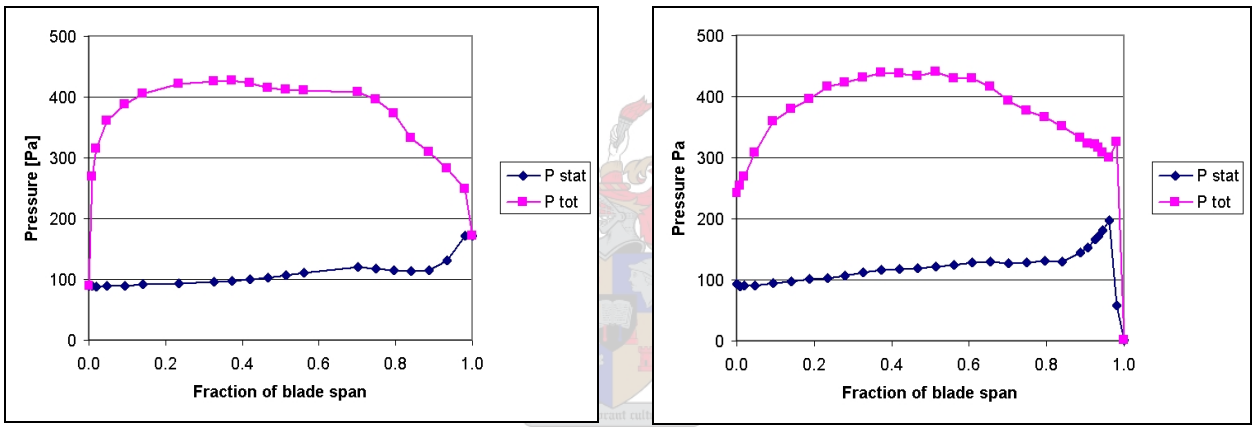

(a) **(b)**

Figure B.14 Pressures

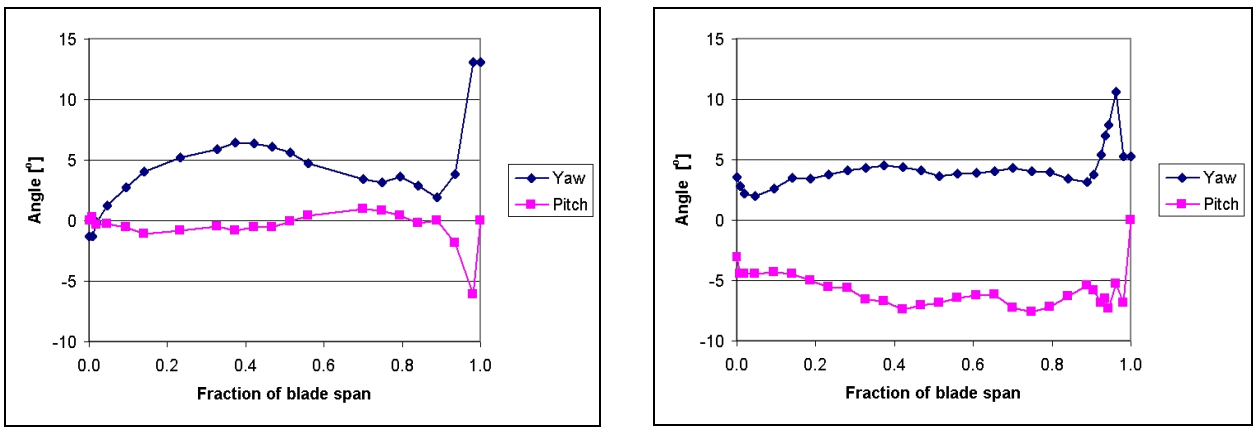

(a) **(b)**

Figure B.15 Flow Angles

OUTER SECTION STATORS

Original Fan (Sheet Metal Stators) **Modified Fan (Machined Stators)**

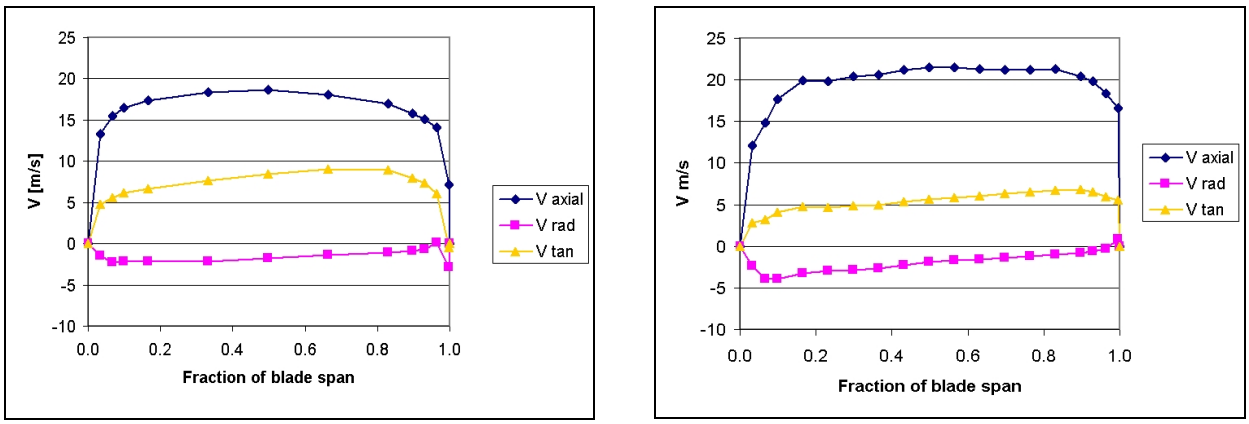

(a) **(b)**

Figure B.16 Velocity Components

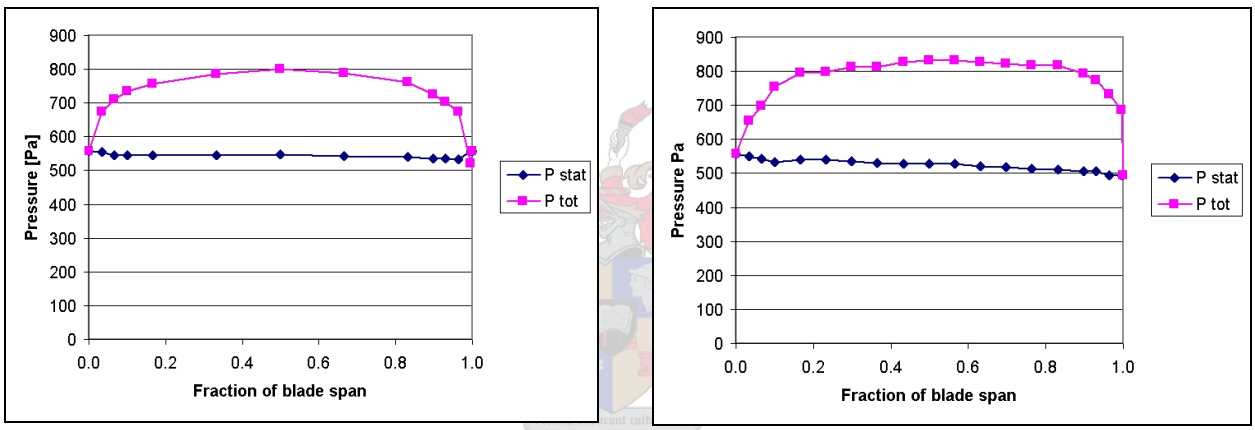

(a) **(b)**

Figure B.17 Pressures

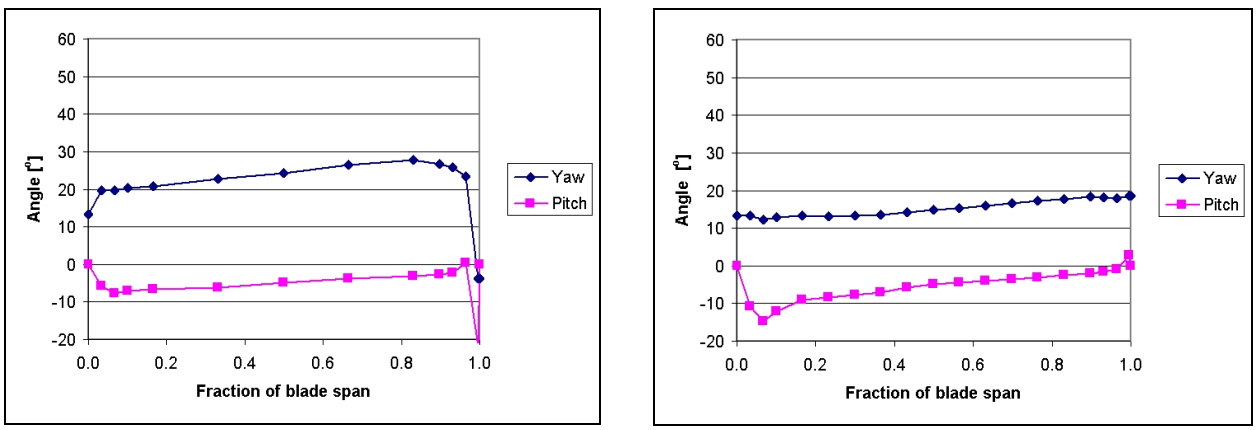

(a) **(b)**

Figure B.18 Flow Angles

OUTER DIFFUSER

Original Fan (Sheet Metal Stators) **Modified Fan (Machined Stators)**

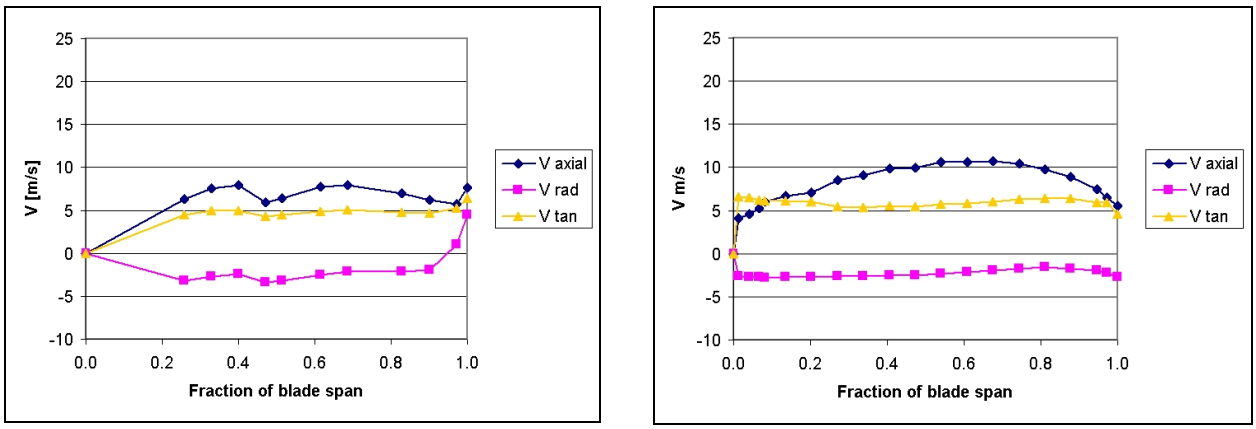

(a) **(b)**

Figure B.19 Velocity Components

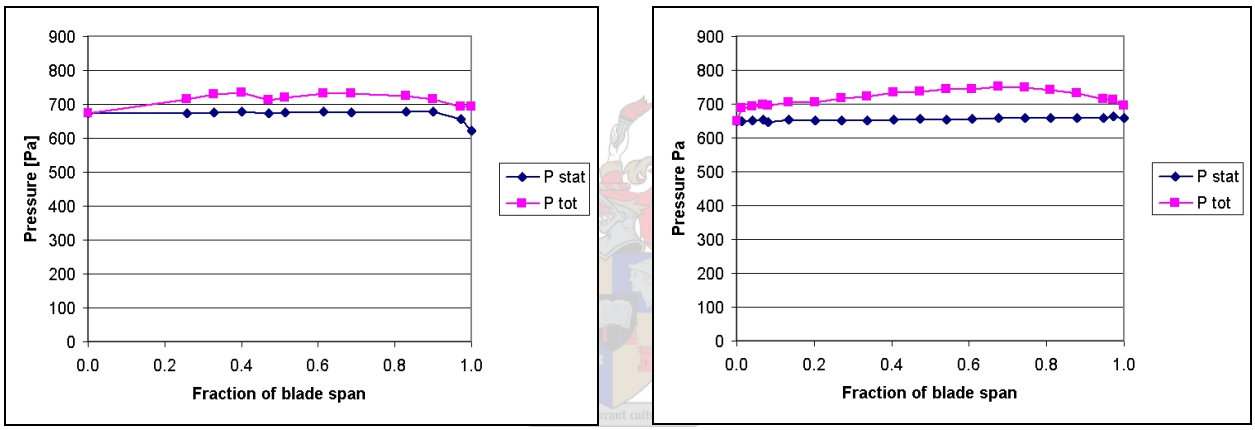

(a) **(b)**

Figure B.20 Pressures

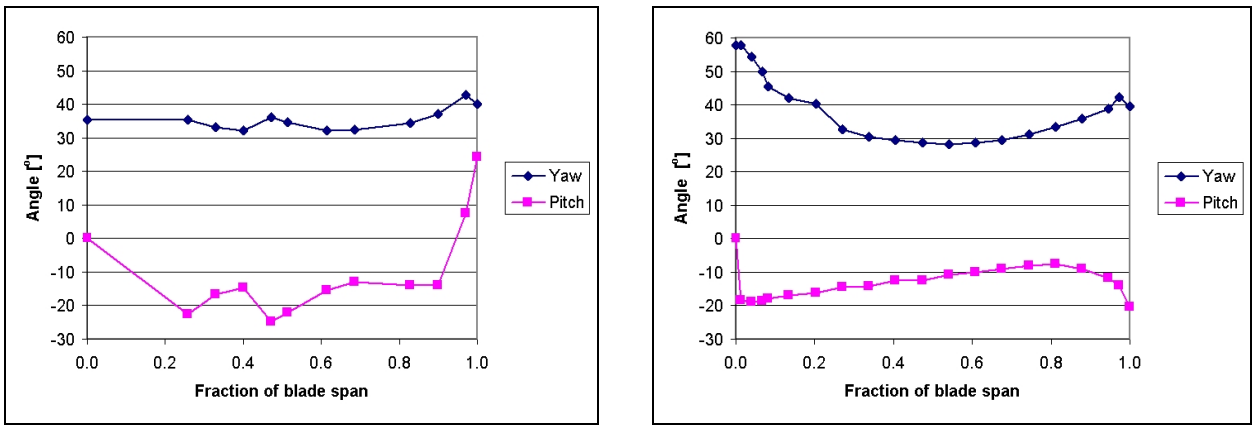

(a) **(b)**

Figure B.21 Flow Angles

APPENDIX C

CIRSTEL SYSTEM MODELLING: SAMPLE CALCULATIONS

This Appendix describes the system model, discussed in Chapter 5, that was developed to evaluate and optimise the CIRSTEL system under hover conditions. The sample calculations given here are for the single engine helicopter, though not representative of the final optimised values.

Atmospheric Conditions

Temperature	$T_{atm} = 25^{o}C$
Pressure	$P_{atm} = 85\,000Pa$
Density	$\rho = \frac{P_{atm}}{RT_{atm}}$ $= 0.994kg/m^3$

Helicopter Data and Performance

Weight of Helicopter	$F = m \cdot g$ $= 1680N$	Mass is set manually to check for MTOW
Required Main Rotor Thrust	$T_{MR} = 1.025 \cdot F$ $= 16893N$	The factor 1.025 is a correction to account for extra downwash induced drag on the fuselage (Seddon[11])

Main Rotor

Rotor Radius	$R = 5.5m$	
Rotor Area	$A = \pi R^2$ $= 95.03m^2$	
Rotor Loading	$T_{MR}/A = 177.8N/m^2$	
Number of Blades	$N = 3$	
Chord Length	$c = 0.26m$	
Blade Area	$A_B = 0.9 \cdot NcR$ $= 3.86m^2$	0.9 is to account for the root cut-out
Main Rotor RPM	350	
Main Rotor Speed	$\Omega = 2\pi 350/60$ $= 36.56$ rad/s	

Blade C_D; NACA 0012	$C_D = 0.012$	Riegels[12]
Blade Lift Slope	5.73	91.1% of the theoretical 2π
Climb Velocity	$V_c = 0$m/s	Required for general performance prediction and calibration. To be set to zero for system design since CCTB equations only valid for hover.
Induced Velocity	$v_i = -\frac{V_c}{2} + \sqrt{\left(\frac{V_c}{2}\right) + \frac{T_{MR}}{2\rho A}}$ $= 9.44\text{m/s}$	From Momentum Theory, Seddon[11]
Loss Factor	$\kappa = 1.18$	Empirical factor to account for variations in induced velocity and top losses, Seddon[11]
Induced Power	$W = \kappa(V_c+v_i)T_{MR}$ $= 188\ 162\text{W}$	
Rotor Drag Power	$dW_D = \frac{1}{2}\rho C_D V^3 c\, dr$ $= \frac{1}{2}\rho C_D c\Omega^3 \left(\sqrt{r^2 + \left(\frac{V_c + v_i}{\Omega}\right)^2}\right)^3 dr$ $\therefore W_D = \frac{1}{2}\rho C_D c\Omega^3 \int_0^R \left(\sqrt{r^2 + \left(\frac{V_c + v_i}{\Omega}\right)^2}\right)^3 dr$ $= \frac{1}{2}\rho C_D c\Omega^3 \left[\frac{1}{4} r \left(\sqrt{r^2 + \left(\frac{V_c + v_i}{\Omega}\right)^2}\right)^3 + \frac{3}{8}\left(\frac{V_c + v_i}{\Omega}\right)^2 r\sqrt{r^2 + \left(\frac{V_c + v_i}{\Omega}\right)^2} + \frac{3}{8}\left(\frac{V_c + v_i}{\Omega}\right)^4 \ln\left(\sqrt{r^2 + \left(\frac{V_c + v_i}{\Omega}\right)^2}\right)\right]_0^R$	
	$W_D \approx \frac{1}{8}\rho C_D cR\left(\sqrt{V_t^2 + (V_c + v_i)^2}\right)^3$	The last two terms of the integral can be ignored since they contribute only ≈ 0.5% to the final answer
	For the whole Rotor: $W_D \approx \frac{1}{8}\rho C_D A_B \left(\sqrt{V_t^2 + (V_c + v_i)^2}\right)^3$	

In none of the consulted literature the (V_c+v_i) term is included to predict the profile drag and power. Gessow et al.[13] do state that the commonly used equation is limited to hover and low-speed climb. The above-derived equation gives better answers when compared to published performance data.

Rotor Drag Power $W_D = 52\,606W$

Total Main Rotor Power $W_{MR} = W+W_D$
$= 316\,268W$

Main Rotor Torque $Q_{MR} = W_{MR}/\Omega$
$= 8\,629Nm$

Tail Rotor

Tail rotor calculations are done for comparison to CIRSTEL fan performance

Diameter $D_T = 1.91m$

Number of Blades $N_T = 3$

Tail Rotor Area $A_T = ¼\,\pi D_T^2$
$= 2.87m^2$

Blade Area $A_{BT} = ½\,B_T c D_T$
$= 0.029m^2$

Tail Rotor Speed $\Omega_T = 220$ rad/s — Educated guess

Required Tail Rotor Thrust $T_T = Q/l$
$= 1029N$ — l is the distance from MR shaft to tail rotor shaft; $l = 6.4m$

Tail Rotor induced Velocity $$v_{iT} = \sqrt{\frac{T_T}{2\rho A_T}}$$
$$= 13.44 m/s$$

Tail Rotor Power $$W_T = \kappa v_{iT} T_T + \frac{1}{8}\rho C_D A_{BT}\left(\sqrt{\left(\frac{\Omega D_T}{2}\right)^2 + v_{iT}^2}\right)^3$$
$$= 16\,710W$$

CIRSTEL Tail Boom Data

Tail Boom Dimensions

Tail Boom Diameter $D = 0.72$ — Value is selected on practical considerations. Can also be optimised, but this will increase the diameter beyond practical limits.

Diameter of Inner Sleeve	$D = 0.65$	Must be at least 50mm smaller than D
CCTB Section Flow Area	$A_{CCTB} = \frac{1}{4}\pi(D^2-d^2)$ $= 0.0753m^2$	
Core Section Flow Area	$A_{core} = \frac{1}{4}\pi d^2$ $= 0.3318m^2$	
Mixer Area/Core Flow Area	$n = 0.23$	This fraction is defined, as it is one of the optimisation parameters. The smaller this value the better the jet-pump effect. If however the ratio results in an exit area smaller than the engine exhaust, the engine backpressure is increased.
Mixer Area	$A_{DM} = nA_{core}$ $= 0.0763m^2$	

Fan Details

Outer Fan Diameter	$D_{OF} = 0.666m$	
Core Fan Diameter	$D_{CF} = \sqrt{\frac{\frac{D_{OF}^2}{(1-\nu^2)}}{\left(\frac{\dot{m}_{CCTB}}{\dot{m}_{core}}+\frac{1}{(1-\nu^2)}\right)}}$ $= 0.626m$	ν is the hub-tip ratio and is set at 0.5. m_{CCTB} & m_{core} are the mass flows of the two sections, to be calculated later
Core Fan Area	$A_{CF} = \frac{1}{4}\pi D_{CF}^2(1-\nu^2)$ $= 0.211m^2$	
Outer Fan Area	$A_{OF} = \frac{1}{4}\pi(D_{OF}^2-D_{CF}^2)$ $= 0.0402m^2$	
Diffuser/Outer Fan Area Ratio	$AR = A_{CCTB}/A_{OF}$	
Efficiency Core Fan	$\eta = 85\%$	As determined in Chapter 2
Efficiency Outer Fan	$\eta = 79\%$	As determined in Chapter 2

Thruster Details

Thruster Width	w = 0.950m	Value selected on maximum practical length that would fir in tail boom
Thruster Height	h = 0.510m	Optimisation parameter, eventually limited to 0.510m
Area of Thruster Opening	$A_{TR} = wh$ $0.4845m^2$	This is the total area, i.e. for both sides
Thruster Centre Line to Rotor Axis	l = 6.4m	
Mass Flow Coefficient	$K_G = 0.8121$	Nurick[17]
Thrust Coefficient	$K_T = 0.7763$	Nurick[17]
Power Coefficient	$K_P = K_G/K_T$	Nurick[17]
Thruster Area Ratio	$AR_{TR} = A_{TR}/A_{core}$ $= 1.46$	Parameter to be monitored when optimising
Total Pressure: Thruster	$P_{TR} = 1792Pa$	Primary optimisation variable. Value is changed by solver

CCTB Details

Slot Width/Tail Boom Radius	0.028	
Total Width of Slots	$w_S = 0.028D/2$ $= 0.01008m$	This is the total width, i.e. sum of both slots
L1	2.75m	Start position of slots from rotor CL, has to allow for space of fan, diffuser and mixer
L2	5.5m	End of slots. Must at least reach the end of the rotor blades
Slot Flow Area	$A_S = w_S(L2-L1)$ $= 0.02772m^2$	
Total Pressure: CCTB	$P_{CCTB} = 1\ 754Pa$	Primary optimisation variable. Value is found by solver. This is also the minimum total pressure the outer fan section has to deliver

Tail Boom Calculations

Thruster

Thruster Static Pressure	$p_{TR} = (1\text{-}0.5\ K_P^2 K_T^3 A R_{TR}^2) P_{TR}$ $= 814.23\text{Pa}$	Nurick[17]
Density of Thruster Gases: Guess	$\rho_{TR} = 0.66644\text{kg/m}^3$	
Density of Thruster Gases: Actual	$\rho_{TR} = \frac{P_{atm} + p_{TR}}{287(273 + T_{TR})}$ $= 0.66644\text{kg/m}^3$	
Error of Density	$\text{Error} = \rho_{guess} - \rho_{actual}$	The density in the tail boom can not be explicitly calculated, because the specified total pressure influences the static pressure, mass flow and hence the mixed temperature, which are all needed to calculate the density. This results in a circular reference. To overcome this a guess of the density is made, from which all subsequent calculations are made. During the optimisation process the solver monitors the error and changes the guessed density to make the error zero.
Thruster Mass Flow	$\dot{m}_{TR} = K_P K_T^{\frac{3}{2}} A_{TR} \sqrt{\rho_{TR} P_{TR}}$ $= 11.98\text{kg/s}$	Nurick[17]
Thruster duct Velocity	$V_{TR} = \frac{\dot{m}_{TR}}{\rho_{TR} A_{core}}$ $= 54.18\text{m/s}$	
Core Fan Mass Flow	$\dot{m}_{core} = \dot{m}_{TR} - \dot{m}_e$ $= 8.41\text{kg/s}$	Engine mass flow is calculated under engine calculations
Thruster Thrust	$T_{TR} = K_T P_{TR} A_{TR}$ $= 674.14\text{N}$	Nurick[17]
Mass Flow Ratio	$\dot{m}_e / \dot{m}_{core} = 0.42$	
Specific Heat	$C_{Pengine} = 1128\text{J/kgK}$	
Specific Heat	$C_{Pcore} = 1005\text{J/kgK}$	

Temperature of Thruster Flow	$T_{TR} = \frac{C_{Pe}\dot{m}_e T_e + C_{Pcore}\dot{m}_{core} T_{atm}}{C_{Pe}T_e + C_{Pcore}T_{atm}}$ $= 175.7^{o}C$	Should be less then 185°C for IR suppression
Re of Thruster Duct	$Re = \frac{\rho_{TR} V_{TR} d}{\mu}$ $= 1.87 \cdot 10^{6}$	
Moody Friction Factor	$f = \left(-1.8\log\left(\frac{6.9}{Re}\right)\right)^{-2}$	White(50)
Friction Loss Coefficient	$f_{TR} = \frac{1}{2}(L2 - L1)\frac{f}{d}$ $= 0.0221$	
Mixer Loss Coefficient	$f_{core} = 0.12$	Pressure loss coefficient across mixer, derived from Hoerner(15) and experimental data(16)
Mixer Loss Coefficient	$f_e = 0.05$	Pressure loss coefficient inside engine/mixer, derived from diffuser theory
Core Fan Total Pressure	$P_{core} = -\left(\frac{f\left(\dot{m}_e, \dot{m}_{core}, \dot{m}_{TR}\right)}{A_{CF}} - P_{TR}\right)$ $= 1189.9Pa$	Pressure rise the core fan has to deliver. The function $f\left(\dot{m}_e, \dot{m}_{core}, \dot{m}_{TR}\right)$ is derived from momentum theory, detailed later
Mixer Exit Static Pressure	$p_{core} = P_{core} - 0.5\rho_{atm} V_{core}^{2}$	
Core Fan Power	$W_{core} = \frac{1}{\eta_{core}} \frac{\dot{m}_{core}}{\rho_{atm}} P_{core}$	
Thruster Torque	$Q_{TR} = T_{TR} l$ $= 4314Nm$	

CCTB

Mass flow to CCTB Slots	$\dot{m}_{CCTB} = C_D A_S \sqrt{2\rho_{atm} P_{CCTB}}$ $= 1.31kg/s$	A C_D = 0.80168 is calculated form experimental data (Nurick(18))
Outer Fan Power	$W_{outer} = \frac{1}{\eta_{outer}} \frac{\dot{m}_{CCTB}}{\rho_{atm}} P_{CCTB}$ $= 2932W$	

Total CCTB Torque, no Flap	$Q_{CCTB} = 0.101\left(\frac{P_{CCTB}}{T_{MR}/\pi R^2}\right)^{\frac{1}{2}} T_{MR} D$ $= 4314\text{Nm}$	Equation derived by Nurick[18] from experimental data for a flap-less tail boom

Tail Boom Total

Fan Power: Total	$W_{fan} = W_{core} + W_{CCTB}$ $= 14\,778\text{W}$	
% of Main Rotor Power	$W_{fan}/W_{MR} \cdot 100\%$ $= 4.675\%$	
Total Torque	$Q_{total} = Q_{TR} + Q_{CCTB}$ $= 8\,629\text{Nm}$	
% of Torque Required	$Q_{total}/Q_{MR} \cdot 100\%$ $= 100\%$	This percentage to be set for the required amount of anti-torque
% CCTB Torque of Total	$Q_{CCTB}/Q_{MR} \cdot 100\%$ $= 50\%$	Although the CCTB Torque is the most efficient, its contribution should be limited. Otherwise the thruster temperature increases. Also control problems could be experienced in transitional flight as the effectiveness of the CCTB decreases (Lippert et al.[14])
Total Fan Mass Flow	$\dot{m}_{total} = \dot{m}_{CCTB} + \dot{m}_{core}$ $= 9.72\text{kg/s}$	
Velocity at Fan Face	$V_{fan} = \frac{\dot{m}_{total}}{\rho_{atm}(A_{OF} + A_{CF})}$ $= 56.2\text{m/s}$	

Engine Calculations

Number of Engines	$E = 1$	Defined for type of helicopter
Engine Mass Flow	$\dot{m}_e = 4.31\frac{\rho_{atm}}{1.2}$ $= 3.57\text{kg/s}$	Volume flow through the engine remains constant. ISA mass flow quoted at 4.31kg/s by Jane's[51] for the Artouste IIIB
Total Engine Mass Flow	$\dot{m}_e = \dot{m}_e E$ $= 3.57\text{kg/s}$	
Cold-End Gas Constant	$\gamma_c = 1.4$	

Hot-End Gas Constant	$\gamma_c = 1.33$	
Cold-End Specific Heat	$C_{Pc} = 1005 J/kgK$	
Hot-End Specific Heat	$C_{Pt} = 1147 J/kgK$	
Compressor Efficiency	$\eta_c = 0.766$	Estimated
Turbine Efficiency	$\eta_t = 0.862$	Estimated
Inlet Static Pressure	$P_{01} = 8500 Pa$	Atmospheric condition
Inlet Static Temperature	$T_{01} = 298K$	Atmospheric condition
Pressure Ratio	$PR = 5$	Given for Artouste IIIB
	$P_{02} = PR.P_{01}$ $= 425\,000 Pa$	
	$T_{02} - T_{01} = \frac{T_{01}}{\eta_c}\left((PR)^{\frac{\gamma_c - 1}{\gamma_c}} - 1 \right)$ $= 227K$ $\therefore T_{02} = 525K$	
Compressor Power	$W_c = C_{Pc}(T_{02} - T_{01})m_e$	
	$T_{03} = 1100K$	Given
	$P_{03} = P_{02}(1 - 0.06)$	Estimated 6% pressure loss over combustor
Dynamic Exit Pressure	$P_{dyn} = \frac{1}{2\rho_e \eta_d}\left(\frac{m_e}{A_{DM}} \right)^2$ $= 2974 Pa$	
Static Backpressure	$p_e = p_{core}$	Static pressure in core section
Error: Static Backpressure	$p_e - p_{core} = 0$	Solved to be zero by Solver by changing p_e
Exit Total Pressure	$P_{04} = P_{atm} + p_e + P_{dyn}$	
	$T_{03} - T_{04} = \eta_t T_{03}\left(1 - \left(\frac{P_{04}}{P_{03}} \right)^{\frac{\gamma_c - 1}{\gamma_c}} \right)$ $= 298K$ $\therefore T_{04} = 802K$	

a simplification equation...	$\Psi = \frac{1}{2C_{Pt}}\left(\frac{\dot{m}_e}{A_{DM}}\frac{287}{(P_{atm}+p_e)}\right)$	
EGT	$EGT = \frac{-1 \pm \sqrt{1^2 + 4\Psi T_{04}}}{2\Psi}$ $= 762.4K$	
Engine Exhaust Gas Density: Guess	$\rho_e = 0.388 kg/m^3$	
Engine Exhaust Gas Density: Calculated	$\rho_e = \frac{P_{core}}{287(EGT)}$ $= 0.388 kg/m^3$	
Error	$Error = \rho_{guess} - \rho_{actual}$	Kept zero by Solver
Exhaust area	$A_e = A_{DM}$ $= 0.0763 m^2$	
Turbine Pressure Ratio	$PR_T = P_{03}/P_{04}$ $= 4.52$	
Turbine Power	$W_t = \eta_t \dot{m}_e C_{Pt} T_{03}\left(1-\left(\frac{1}{PR_T}\right)^{\frac{\gamma_t - 1}{\gamma_t}}\right)$ $= 1\,219\,307 W$	
Engine Power Out	$W_{out} = W_t - W_c$ $= 404\,511 W$	
Shaft Power Output	$W_{shaft} = \eta_{GB} W_{out}$ $= 331\,700 W$	$\eta_{GB} = 0.82$ for gearbox losses
Total Power Available	$W_{tot} = E \cdot W_{shaft}$	
Total Allowed Power	$W_{allowed} = 410\,000 W$	Set to max rated or gearbox limits
Total Required Power	$W_{required} = W_{MR} + W_{fan}$	Must be less than "Total Engine Power Available"

Momentum Theory for the Mixer/Jet-Pump

The derivation of the equation used to model the Daisy Mixer/Jet-Pump for the core section is detailed here. Refer also to Figure 5.2 for a schematic of the control volume

The duct cross sectional areas can be defined as:

$A_{TR} = A_{core} + A_{DM}$

$= A$

$A_{DM} = nA$

$A_{core} = (1\text{-}n)A$

where n is the fraction of the cross sectional duct area occupied by the mixer.

The sum of forces on the control volume can be expressed as:

$$D_{TR} + D_{core} + D_e + Ap_{TR} - nAp_e - (1-n)Ap_{core} = \dot{m}_{core}V_{core} + \dot{m}_e V_e - \dot{m}_{TR}V_{TR}$$

where the momentum deficiency terms are:

$$D_{TR} = f_{TR}\rho_{TR}V_{TR}^{\ 2}A$$
$$= f_{TR}\dot{m}_{TR}V_{TR}$$

$$D_{core} = f_{core}\rho_{core}V_{core}^{\ 2}(1-n)A$$
$$= f_{core}\dot{m}_{core}V_{core}$$

$$D_e = f_e\rho_e V_e^{\ 2}nA$$
$$= f_e\dot{m}_e V_e$$

Also the static pressure at the mixer exit is

$$p_e = p_{core}$$
$$\therefore nAp_e + (1-n)Ap_{core}$$
$$= nAp_{core} + (1-n)Ap_{core}$$
$$= Ap_{core}$$

Thus the sum of forces equation becomes, by substitution of the equations:

$$f_{TR}\dot{m}_{TR}V_{TR} + f_{core}\dot{m}_{core}V_{core} + f_e\dot{m}_e V_e + Ap_{TR} - Ap_{core} = \dot{m}_{core}V_{core} + \dot{m}_e V_e - \dot{m}_{TR}V_{TR}$$
$$\therefore A(p_{TR} - p_{core}) = \dot{m}_{core}V_{core}(1-f_{core}) + \dot{m}_e V_e(1-f_e) - \dot{m}_{TR}V_{TR}(1+f_{TR})$$

Also the static pressures can be defined in terms of total and dynamic pressures. This substitution is done to make the equations more useable for the current application, since the total pressures are required as answers.

$$p_{TR} = P_{TR} - \frac{1}{2}\rho_{TR} V_{TR}^{\ 2}$$

$$p_{core} = P_{core} - \frac{1}{2}\rho_{core} V_{core}^{\ 2}$$

Substituting into the momentum equation and simplifying yields the desired equation:

$$A\left(P_{TR} - P_{core}\right) = \dot{m}_{core} V_{core}\left(\frac{1-2n}{2(1-n)} - f_{core}\right) + \dot{m}_e V_e \left(1 - f_e\right)_e - \dot{m}_{TR} V_{TR}\left(\frac{1}{2} + f_{TR}\right)$$

$$= F\left(\dot{m}_{core}, \dot{m}_e, \dot{m}_{TR}\right)$$

This is the desired function which can now easily be used for the system calculations

Notes on the Optimisation Process

The objective of the optimisation process is to minimise the power required by the fan, while the tail boom still delivers the required torque.

The Solver function of Excel was used as the optimisation algorithm; employing the Newton search method with a forward approximation of the derivative.

The primary constraint is thus the fraction of main rotor torque the tail boom has to deliver; values used here were 100% for steady hover and 110% with manoeuvre reserves.

The primary variables are the total pressures in the two sections of the tail boom. This has the most direct influence on the fan power.

During the optimisation process the error functions are also forced to be zero.

The fraction of torque delivered by the CCTB section must be limited; the limit set here is 48% to ensure sufficient authority of the tail thruster as the CCTB section effectiveness decreases in forward flight. Since the CCTB is the most efficient torque creating section, the supplied fraction tends to be close to the maximum allowed.

Further constraints that were experimented with are the thruster opening area, tail boom diameter, and daisy mixer area. However these variables quickly converged to unrealistic values, and were thus fixed at practical values. The mixer area was set to virtually eliminate backpressure on the engine. The thruster exhaust temperature was also monitored, though not explicitly constrained to be below the advised 185^{o}C.

APPENDIX D

CFD VERIFICATION STUDY

To start the CFD analysis a short verification process was done to determine methods of constructing grids on complex geometries using an unstructured mesh, as well as comparing the CFD results of a second order advection scheme to experimental data.

A commercial CFD code was used for the evaluations and also for the analysis of the air intakes, namely CFX 5.5. The code uses an unstructured mesh, and thus it is capable of handling complex geometries without major user intervention in setting up the flow domain grid. The mesh is generated using the Advancing Front and Inflation (AFI) method[52]. The code allows for inflation of the surface elements to form prismatic volume elements near wall surfaces, rather than the usual tetrahedral volume elements. The inflated elements have a small length perpendicular to the surface that allows the capture of the steep flow gradients in the boundary layer.

One of the difficulties associated in the definition of a grid for optimal performance of the solver is the selection of the element size. Mesh element lengths have to be fine enough to represent the underlying geometry accurately while not resulting in an excessive number of cells. For the turbulence models to resolve the boundary layer well enough at least five elements should be in the boundary layer. Depending on the turbulence model used, the first node from the wall should lie near a y^+ value of 5. This places the node in or near the laminar sub-layer, and more accurate results can be obtained. However, this will result in small elements that are not always practical, so a y^+ value of 30 is sufficient, as this still close to the start of the overlap log-law.

Estimations can be made of how thick the boundary layer will be at a certain point of interest by using methods used to analyse flat plate flow. Using the definition of y^+ and turbulent friction coefficient, it can be shown that the height of the first node as a function of the desired y^+ value is:

$$\Delta y = y^+ L \sqrt{80}\, Re_L^{-13/14} \qquad \text{(D1)}$$

Equation D1 is also a function of the downwind position of the node as well as the free stream velocity, which enters the equation through the Reynolds number. It is thus a simple matter to determine an appropriate first element height by estimating the free stream velocity and the boundary layer growth distance. The turbulence model used for the test cases was the shear stress transport model (SST). The capabilities of the two-equation turbulence model have been illustrated by Menter[39]. For the current test case no other turbulence models were used.

Test Geometry

The geometry used for the validation was the bell mouth and inlet section, including IGVs, of the test rig used to test the demonstrator fan for which the air intakes of the helicopter are to be investigated. The geometry was complex enough to test the meshing process and good experimental data was also available for comparison to the CFD data. A unique feature of the fan design is that the air is split ahead of the fan rotor into two streams (an inner and outer stream) for use in the different sections of the tail boom. Two mass flow boundaries were thus incorporated to model the two separate air streams. The mass flow quantities enforced at the fan face were airflow quantities measured by the inlet bell mouth and orifice plates located at the exit of the outer stream.

Results and Discussion

In the following figures (Figures D.1 to D.4) some of the CFD results are compared with the experimental data. Two stations were selected to extract the data from the CFD results. The data was collected along radial lines, one at the inlet, just in front of the inlet guide vanes and the other behind the IGVs of the fan. The spatial position of these radial lines corresponds exactly to those positions on which data was taken with a five-hole-probe in the experiments.

Overall the results for the test case appeared promising, the values being close to the experimentally determined flow values. Important to note is however that only the second order advection scheme predictions of are shown, as they are closer to the experimental values than the first order advection scheme results.

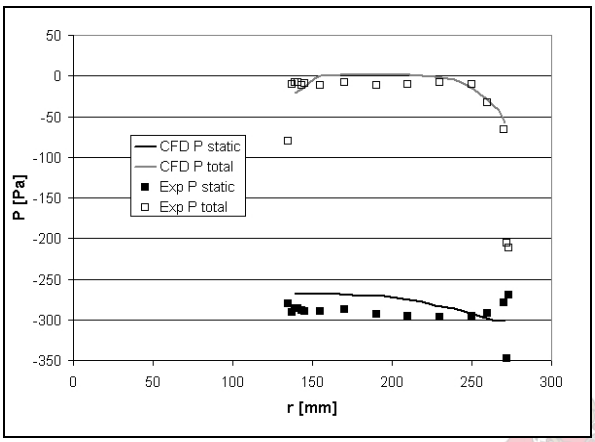

Figure D.1 Inlet pressures: Experimental and CFD

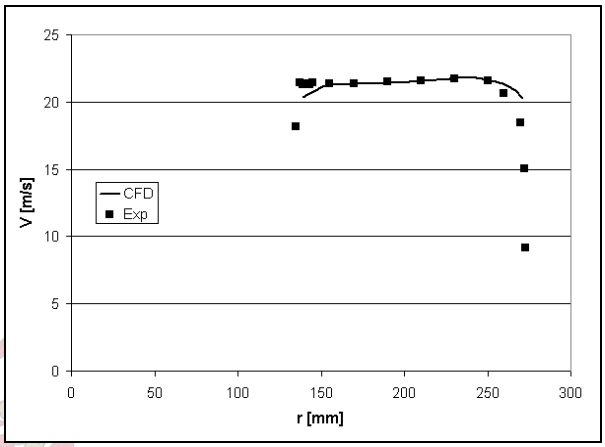

Figure D.2 Inlet velocities: Experimental and CFD

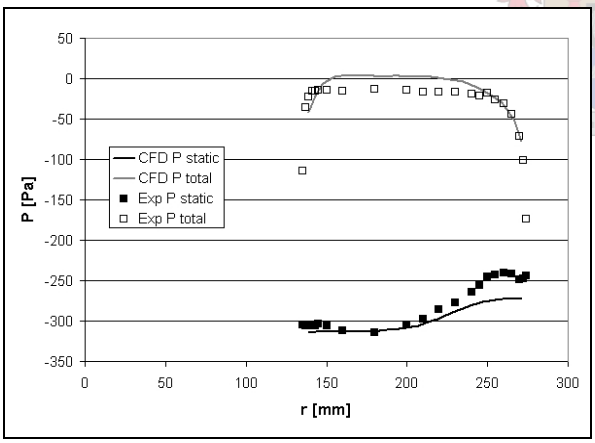

Figure D.3 IGV pressures: Experimental and CFD

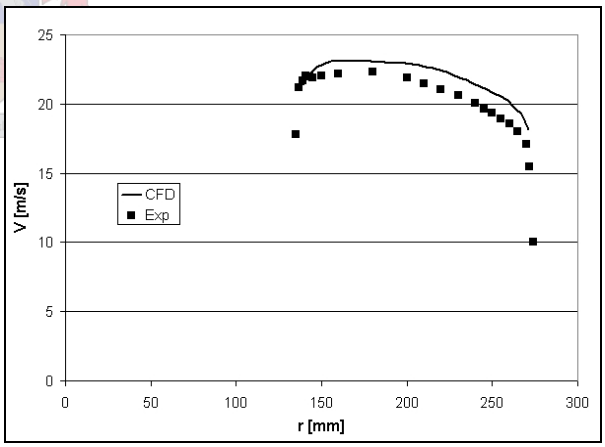

Figure D.4 IGV velocities: Experimental and CFD

For the test case the total pressure was predicted well, Figure D.1 and D.3,showing the right trends at all the test stations. As can be seen the values predicted by the code for the total pressure were the same as the measured ones. Only a small error, typically between 10 Pa and 15 Pa, resulted from the CFD results. At places the total pressure exceeded the ambient conditions, which is physically impossible, but the maximum value is only about 4 Pa above atmosphere stagnation conditions. The error here can be attributed to numerical error, but can be neglected for practical purposes.

At the inlet the static pressure was acceptably predicted, the predicted values are close to the true values (Figure D.1). The profile itself was however not that well modelled. It shows the pressure

clearly dropping off towards the outside, contrary to the experimental data. No swirl is present in the inlet flow and the static pressure must thus be uniform over the span. The static pressure behind the IGV (Figure D.3) was accurate in the inner sections of the duct and under predicted on the outer section. The error is about 30 Pa at this point, but the profile showed the characteristic hump on the outside, which results from the lower velocity of the air entering the outer section further downstream. Looking upstream again at the static pressure in the inlet section, the drop in the profile on the outer sections here was also in the region of 30 Pa. It would appear that the error experienced behind the IGV was induced by the differences further upstream in the duct, and that the flow was modelled accurately around the IGV geometry.

Looking at the velocity predictions (Figures D.2 and D.4), the simulations gave good answers, especially ahead of the IGVs. Here the answers coincided exactly with the experiments; only at the edges could some differences be seen. Behind the IGV blades (Figure D.4) there was a slight over prediction of the velocity. The reason here was what appeared to be an over prediction of the wake from the IGV blades. As a result there is a higher blockage and a corresponding higher velocity behind the IGVs. The velocity profile does however follow the experimental trend closely.

The verification exercise showed that the code used was accurate enough and that it could be used for further design evaluations. Sufficiently accurate answers could only be expected if a higher order advection scheme was used to solve the mass and momentum equations in the simulation. The methods used here, both analytical and iterative, can be used to define an appropriate grid spacing to start off with. Defining the grid in this way simplifies the set-up process without going through an extended set of grid sensitivity analyses.

Further Interpretations

A spin-off of these CFD simulations was a further analysis of the flow entering the fan rotor. By comparing a specified single mass flow for the entire fan to the split mass flow condition as used in the verification, a comparison could be made to the relative throttling of each section of the experimental fan.

For the single, total specified mass flow case the velocity profile behind the IGV blades was uniform. This is the assumption that was made in the design stages of the fan. Care will have to be taken to consider the phenomenon of a possibly skewed velocity profile entering the fan. It does however appear that the performance of the fan sections was not degraded because of this.

The total pressure distribution ahead of the fan was still uniform as it was for the experimental tests. As the total pressure distribution is the most critical affecting the fan performance, the fan still showed the acceptable performance, despite a non-uniform velocity profile.

When implementing the split mass flow condition, the velocity profile shifted, and resembled the measured flow profiles closely. The change in the axial velocity showed that the two fan sections were not throttled properly relative to each other. The performance tests conducted with these settings showed that the outer fan was over throttled. As a result the outer mass flow reduced with a corresponding reduction in the axial velocity. A streamline plot of the CFD results also showed the streamlines diving inwards into the core section, Figure D.5, further supporting the analysis of an over throttled outer fan.

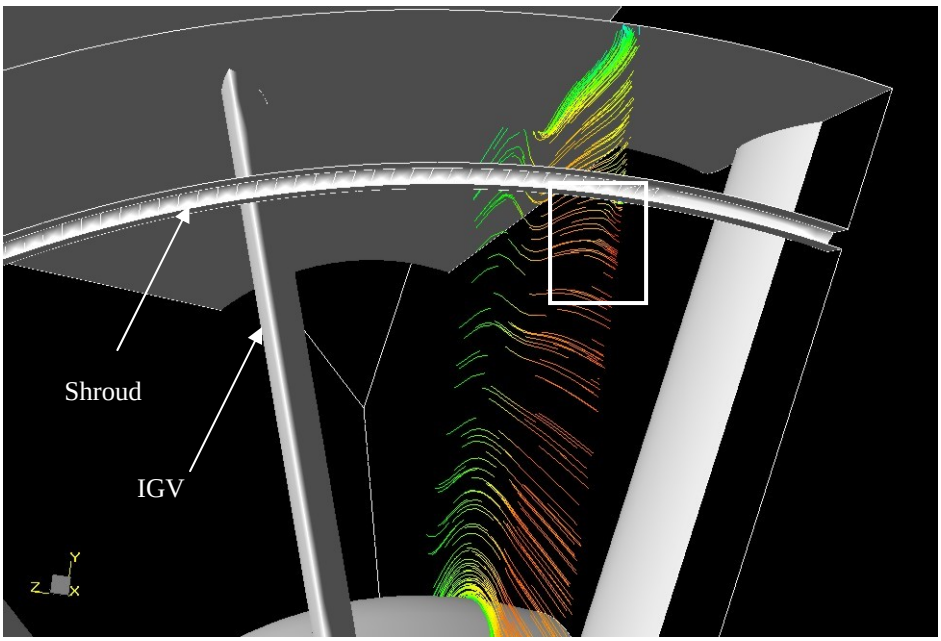

Figure D.5 Streamlines entering the fan, looking from the fan upstream, with the forward section of the shroud and the IGVs visible. The white square shows the area where the streamlines dive into the core section

APPENDIX E

DEFINITION OF THE MODIFIED ROBIN CONFIGURATION

A generic fuselage was used for the investigation of the intake concepts. The fuselage used was created by modifying the original ROBIN configuration (Freeman et al.[36]) for the current purpose. The fuselage was adapted to be representative of a tail-rotor-less helicopter fuselage. The forward section of the fuselage up to x/R = 0.8 is identical to the original ROBIN. The fuselage then tapers off to a constant diameter tail boom to represent the circulation control section. This section extends from the nondimensional coordinates of x/R = 1.2 to x/R = 1.9.

The cowlings were modified to be representative of single- and twin-engine helicopters. The single-engine version, (shown in Figure 9.1) had the gearbox cowling extended to x/R = 1.2 from the original to accommodate the exhaust duct into the tail boom. The twin-engine helicopter on the other hand had the gearbox cowling shortened to x/R = 0.88, with an additional cowling added to form the engine bay cowling, extending from x/R = 0.6 to x/R = 1.2 (shown in Figure 9.2).

The ROBIN fuselage is defined analytically with super-ellipse equations[53]. In nondimensional form the fuselage cross section (y/R and z/R) at a given longitudinal station x/R is given by a super-elliptical function with the parameters for height (H), width (W), fuselage camber line (Z_o) and an elliptical power (N). Each fuselage section is described by a function in the same form, with the coefficients (C_1 to C_8) being defined for each section. The form of the function is defined as follows:

$$\begin{bmatrix} H(x/R) \\ W(x/R) \\ Z_o(x/R) \\ N(x/R) \end{bmatrix} = C_6 + C_7\left(C_1 + C_2\left(\frac{x/R + C_3}{C_4} \right)^{C_5} \right)^{\frac{1}{C_8}} \qquad \text{(E.1)}$$

Here R is the rotor radius, thus being the parameter that defines the overall dimension of the fuselage. The coordinates at a given longitudinal station of the fuselage are defined using polar coordinates. The nondimensional radius for the desired cross section is defined as follows:

$$r = \left(\frac{\left(\frac{H}{2}\frac{W}{2}\right)^N}{\left(\frac{H}{2}\sin\phi\right)^N + \left(\frac{W}{2}\cos\phi\right)^N} \right)^{\frac{1}{N}} \qquad \text{(E.2)}$$

The nondimensional coordinates on the cross section can then be determined by varying φ from 0 to 2π with the following transformation back into Cartesian coordinates:

$$\begin{aligned} y/R &= r\sin\phi \\ z/R &= r\cos\phi + Z_o \end{aligned} \qquad \text{(E.3)}$$

Fuselage Coefficients

The following tables list the coefficients for the fuselage that is common to both versions of the modified ROBIN.

Nose Cone 0.00 < x/R < 0.40

	C_1	C_2	C_3	C_4	C_5	C_6	C_7	C_8
H	1.00	-1.00	-0.40	0.40	1.80	0.00	0.25	1.80
W	1.00	-1.00	-0.40	0.40	2.00	0.00	0.25	2.00
Z_o	1.00	-1.00	-0.40	0.40	1.80	-0.08	0.08	1.80
N	2.00	3.00	0.00	0.40	1.00	0.00	1.00	1.00

Mid Fuselage 0.40 < x/R < 0.80

	C_1	C_2	C_3	C_4	C_5	C_6	C_7	C_8
H	0.25	0.00	0.00	0.00	0.00	0.00	0.00	0.00
W	0.25	0.00	0.00	0.00	0.00	0.00	0.00	0.00
Z_o	0.00	0.00	0.00	0.00	0.00	0.00	0.00	0.00
N	5.00	0.00	0.00	0.00	0.00	0.00	0.00	0.00

Rear Fuselage 0.80 < x/R < 1.20

	C_1	C_2	C_3	C_4	C_5	C_6	C_7	C_8
H	1.00	-1.00	-0.80	0.40	1.50	0.13	0.12	0.60
W	1.00	-1.00	-0.80	0.40	1.50	0.13	0.12	0.60
Z_o	1.00	-1.00	-0.80	0.40	1.50	0.025	-0.025	0.60
N	5.00	-3.00	-0.80	0.40	1.50	0.00	0.00	0.00

Tail Boom 1.20 < x/R < 1.90

	C_1	C_2	C_3	C_4	C_5	C_6	C_7	C_8
H	0.13	0.00	0.00	0.00	0.00	0.00	0.00	0.00
W	0.13	0.00	0.00	0.00	0.00	0.00	0.00	0.00
Z_o	0.025	0.00	0.00	0.00	0.00	0.00	0.00	0.00
N	2.00	0.00	0.00	0.00	0.00	0.00	0.00	0.00

Tail Cone 1.90 < x/R < 2.00

	C_1	C_2	C_3	C_4	C_5	C_6	C_7	C_8
H	1.00	-1.00	-1.90	0.10	2.00	0.00	0.13	2.00
W	1.00	-1.00	-1.90	0.10	2.00	0.00	0.13	2.00
Z_o	0.025	0.00	0.00	0.00	0.00	0.00	0.00	0.00
N	2.00	0.00	0.00	0.00	0.00	0.00	0.00	0.00

Cowling Coefficients

Single Gearbox/Engine Cowling

The following tables lists the coefficients for the single engine helicopter gearbox/engine cowling

Forward Cowling 0.40 < x/R < 0.80

	C_1	C_2	C_3	C_4	C_5	C_6	C_7	C_8
H	1.00	-1.00	-0.80	0.40	3.00	0.00	0.145	3.00
W	1.00	-1.00	-0.80	0.40	3.00	0.00	0.1656	3.00
Z_o	0.125	0.00	0.00	1.00	1.00	0.00	1.00	1.00
N	5.00	-3.00	-0.80	0.40	1.00	0.00	1.00	1.00

Rear Cowling 0.80 < x/R < 1.20

	C_1	C_2	C_3	C_4	C_5	C_6	C_7	C_8
H	1.00	-1.00	-0.80	0.40	2.00	0.00	0.145	2.50
W	1.00	-1.00	-0.80	0.40	2.00	0.00	0.1656	2.50
Z_o	1.00	-1.00	-0.80	0.40	2.00	0.09	0.035	2.00
N	5.00	-3.00	-0.80	0.40	1.00	0.00	1.00	0.00

Twin Gearbox Cowling

The following tables lists the coefficients for the twin engine helicopter gearbox cowling

Forward Cowling 0.40 < x/R < 0.70

	C_1	C_2	C_3	C_4	C_5	C_6	C_7	C_8
H	1.00	-1.00	-0.70	0.30	3.00	0.00	0.145	3.00
W	1.00	-1.00	-0.70	0.30	3.00	0.00	0.1656	3.00
Z_o	0.125	0.00	0.00	1.00	1.00	0.00	1.00	1.00
N	5.00	-3.00	-0.70	0.30	1.00	0.00	1.00	1.00

Rear Cowling 0.70 < x/R < 0.88

	C_1	C_2	C_3	C_4	C_5	C_6	C_7	C_8
H	1.00	-1.00	-0.70	0.18	2.00	0.00	0.145	2.50
W	1.00	-1.00	-0.70	0.18	2.00	0.00	0.1656	2.50
Z_o	0.125	0.00	0.00	1.00	1.00	0.00	1.00	1.00
N	5.00	-3.00	-0.70	0.18	1.00	0.00	1.00	0.00

Twin Engine Cowling

The following tables lists the coefficients for the twin engine helicopter engine cowling

Forward Engine Cowling 0.60 < x/R < 0.75

	C_1	C_2	C_3	C_4	C_5	C_6	C_7	C_8
H	1.00	-1.00	-0.75	0.15	2.00	0.00	0.10	2.00
W	1.00	-1.00	-0.75	0.15	2.00	0.00	0.22	2.00
Z_o	0.00	0.00	0.00	1.00	1.00	0.10	1.00	1.00
N	5.00	-3.00	-0.75	0.15	1.00	0.00	1.00	1.00

Mid Engine Cowling 0.75 < x/R < 0.90

	C_1	C_2	C_3	C_4	C_5	C_6	C_7	C_8
H	0.10	0.00	0.00	0.00	0.00	0.00	0.00	0.00
W	0.22	0.00	0.00	0.00	0.00	0.00	0.00	0.00
Z_o	0.10	0.00	0.00	0.00	0.00	0.00	0.00	0.00
N	5.00	0.00	0.00	0.00	0.00	0.00	0.00	0.00

Rear Engine Cowling 0.90 < x/R < 1.20

	C_1	C_2	C_3	C_4	C_5	C_6	C_7	C_8
H	1.00	-1.00	-0.90	0.30	1.50	0.00	0.10	1.10
W	1.00	-1.00	-0.90	0.30	1.50	0.00	0.22	1.10
Z_o	1.00	-1.00	-0.90	0.30	1.50	0.075	0.025	1.00
N	5.00	-3.00	-0.90	0.30	1.00	0.00	1.00	0.00